Scalable Spark Ablation Synthesis of Nanoparticles
Fundamental Considerations and Application in Textile Nanofinishing

Feng, Jicheng

Scalable Spark Ablation Synthesis of Nanoparticles:

Fundamental Considerations and Application in Textile Nanofinishing

◎ Jicheng FENG

冯继戌

50 nm

Scalable Spark Ablation Synthesis of Nanoparticles:

Fundamental Considerations and Application in Textile Nanofinishing

JICHENG FENG

Scalable Spark Ablation Synthesis of Nanoparticles:

Fundamental Considerations and Application in Textile Nanofinishing

Proefschrift

ter verkrijging van de graad van doctor
aan de Technische Universiteit Delft,
op gezag van de Rector Magnificus prof.ir. K.C.A.M. Luyben;
voorzitter van het College voor Promoties,
in het openbaar te verdedigen op
donderdag 3 november 2016 om 12:30 uur

door

Jicheng FENG

Master of Science in Materials Processing and Engineering
Shanghai University of Engineering Science, China,
geboren te Shandong, China

This dissertation has been approved by the:

promotor: Prof. dr. A. Schmidt-Ott and

copromotor: Dr. G. Biskos

Composition of the doctoral committee:

Rector Magnificus	chairman
Prof. dr. A. Schmidt-Ott	Technische Universiteit Delft, promotor
Dr. G. Biskos	The Cyprus Institute, Cyprus, copromotor

Independent members:

Prof. dr. S. E. Pratsinis	ETH Zürich, Switzerland
Prof. dr.-ing F. E. Kruis	Universität Duisburg-Essen, Germany
Prof. dr. A. P. Weber	Technische Universiteit Clausthal, Germany
Prof. dr. M. T. M. Koper	Leiden Universiteit
Prof. dr. ir. J. R. van Ommen	Technische Universiteit Delft
Prof. dr. F. M. Mulder	Technische Universiteit Delft, reservelid

Cover design by Jicheng Feng, combining the TEM images of collected nanoparticles with ancient Chinese Ink & Brush painting (see Chapter 8 for more details).

To my beloved family

献给我亲爱的家人

玉吾于成

No pain no gain

Abstract (English)

A major challenge in nanotechnology is that of determining how to introduce green principles when assembling individual nanoscale elements to create multifunctional working devices. This dissertation focuses on fundamentals (Part A), scaling-up (Part B) and application (Part C) of nanoparticles with sub-10 nm in size produced by ambient spark ablation, which is a scalable and environmentally benign process, providing great versatility in producing inorganic nanoparticles consisting of a wide variety of conducting or semiconducting materials with virtually unlimited mixing possibilities. In Part A, a new 'singlet' concept has been introduced, which rules out the pseudo-paradigm: continuous gas-phase synthesis of nanoparticles is associated with rapid agglomeration. Subsequently, a general approach has been developed to describe the size distributions of singlet particles as a function of the process conditions. In Part B, a newly developed high-frequency spark yields a series of monometallic and bimetallic nanoparticles, sub-10 nm (primary) particles and well-defined chemical composition, providing a green and versatile platform for manufacturing key building blocks toward industrial scale. To improve the uniformity of nanoparticles, inhibition of 'splashing' particles (larger than 100 nm) has been successfully achieved by using an external magnetic field within the inter-electrode gap. The resulting Lorenz force deflects the continuous glowing current, onto which sparks are superimposed, thereby avoiding the sparks to strike the same point of electrode surface. To explore internal nanoparticle mixing, a model developed here links the composition of nanoparticles to spark oscillations. In Part C, by integrating gas-phase nanoparticle syntheses into textile nanofinishing, a number of constraints encountered in traditional wet-finishing processes, can be circumvented while creating a new class of fabrics. As proof of this concept, Ag nanoparticles are deposited onto a range of textiles, imparting high antimicrobial activities and exhibiting good washing durability. Accounting for the green, scalability and versatility of the technique used here as well as its compatibility with the existing fabrication processes, the generated nanoparticles bear a great potential for creating multifunctional working devices.

Abstract (Dutch)

Een grootte uitdagingen in de nanotechnologie is vaststellen hoe groene principes kunnen worden geïntroduceerd in de assemblage van individuele elementen op nanoschaal tot multifunctionele working devices. Dit proefschrift richt zich op de fundamenten (deel A), het opschalen (deel B) en de toepassingen (deel C) van sub-10 nm nanodeeltjes geproduceerd met vonk ablatie onder kamertemperatuur en druk. Dit is een schaalbare en milieuvriendelijke methode die aanzienlijke veelzijdigheid verschaft bij de productie van anorganische nanodeeltjes, bestaande uit uiteenlopende geleiders en halfgeleiders en met praktisch onbeperkte mengmogelijkheden. In deel A is een nieuw 'singlet' concept geïntroduceerd die het pseudo-paradigma dat de continue synthese van nanodeeltjes in de gasfase is geassocieerd met snelle agglomeratie uitsluit. Vervolgens is er een algemene benadering ontwikkeld om de grootteverdelingen van singlet deeltjes te beschrijven als functie van de procesomstandigheden. Deel B behandeld een onlangs ontwikkelde high-frequency spark waarmee een serie monometallische en bimetallische nanodeeltjes, sub-10 nm (primary) en met duidelijke chemische samenstelling, is geproduceerd. Hiermee wordt een groen en veelzijdig platform verstrekt voor de productie van belangrijke bouwstenen voor industriële schaal. Uniformiteit van de deeltjes is succesvol verbeterd door de productie van 'splashing' deeltjes te remmen met behulp van een extern magnetisch veld tussen de elektrodes. Door de resulterende Lorentz kracht wijkt de continu gloeiende stroom, waarop de vonken zijn gesuperponeerd, uit en wordt voorkomen dat de vonk dezelfde positie treft. Om interne menging in nanodeeltjes te onderzoeken, werd een model ontwikkeld die de samenstelling van de nanodeeltjes aan de vonk oscillatie verbindt. In deel C, door synthese van nanodeeltjes in de gasfase te integreren in 'textile nanofinishing', konden een aantal beperkingen van traditionele wet-finishing processen worden omzeild en werd een nieuwe klasse stof gecreëerd. Als bewijs voor dit concept werden Ag nanodeeltjes gedeponeerd op textiel. Dit resulteerde in hoge antimicrobiële activiteiten en goede wasbestendigheid. In het kader van het groene, de schaalbaarheid en veelzijdigheid van de technieken die hier worden gebruikt, evenals de compatibiliteit met bestaande fabricage processen, bieden de gegenereerde nanodeeltjes veel mogelijkheden voor het maken van multifunctionele working devices.

Table of Contents

3. General Approach to the Evolution of Singlet Nanoparticles from a Rapidly Quenched Point Source   69

Part B Scaling-up

4. A Green and Versatile Method for High-yield Synthesis of Metallic Nanoparticles   117

5. Internal Nanoparticle Mixing by Oscillatory Spark Ablation between Electrodes of Different Materials

6. Inhibition of 'Splashing' in High Frequency Sparks for Nanoparticle Synthesis

Part C Application

7. Scalable and Environmentally Benign Process for Smart Textile Nanofinishing

List of Figures

Graphical Abstract of Chapter 4

Graphical Abstract of Chapter 5

Graphical Abstract of Chapter 6

Graphical Abstract of Chapter 7

List of Tables

List of Abbreviations and Symbols

Abbreviations

AA	Antimicrobial Activity
AEM	Aerosol Electrometer
APCP	Acrylic-Polyester-Cotton-Polyamide
a.u.	arbitrary unit
BUONAPART-e	Better Upscaling and Optimization of Nanoparticle and Nanostructure Production by Means of Electrical Discharges
CFU	Colony Forming Unit
CPC	Condensation Particle Counter
DMA	Differential Mobility Analyser
EDX	Energy-dispersive X-ray spectroscopy
ESP	Electrostatic Precipitator
FFT	Fast Fourier Transform
GMD	Geometrical Mean Diameter
GSD	Geometric Standard Deviation
HFS	High Frequency Sparks
HRTEM	High Resolution Transmission Electron Microscopy
HRSEM	High Resolution Scanning Electron Microscopy
HV	High Voltage
ICP-MS	Inductively Coupled Plasma Mass Spectrometry
KP	Klebsiella Pneumoniae
LYS	Lyocell rayon (Safari)
LYZ	Lyocell rayon (Zen)
MPS	Mini-Particle Sampler
NP	Nanoparticle
PES	Polyester
ppm	mg per kg
PSD	Particle Size Distribution

RLCS	Resistance-Inductance-Capacitance based Spark
SA	Staphylococcus Aureus
SDG	Spark Discharge Generator
SEM	Scanning Electron Microscopy
SI	Supplementary Information
slm	standard litre per minute
SMPS	Scanning Mobility Particle Sizer
SAXS	Small Angle X-ray Scattering
TEM	Transmission Electron Microscopy
WAXS	Wide Angle X-ray Scattering
XPS	X-ray Photoelectron Spectrometer

Symbols

Greek symbols

α	fraction of spark energy consumed for NP production
α_A	the fraction of spark energy consumed for anode ablation
α_C	the fraction of spark energy consumed for cathode ablation
α_s	solidity
ξ	deposition parameter
μ	dynamic viscosity
λ_m	mean free path
λ	the wavelength of the X-ray beam
ζ	$=Q_a/Q_{sh}$
ρ	material density
ρ_g	the density of carrier gas
β	coagulation kernel or coagulation coefficient
ε_0	electric permittivity
τ	spark duration
θ	half of the scattering angle
φ	a correction factor accounting for the fact that the aerosol is polydisperse
φ'	composition of arbitrary particle

$\overline{\varphi}'$	mean composition of particles
$\overline{\varphi}_C$	mean nanoparticle composition (in the form of cathode material)
φ_i	fraction of one component in one nanoparticle
ε	an enhancement factor due to van der Waals forces between particles
σ_g	geometric stand deviation
σ_{sp}	sample standard deviation
η	fitting parameter for the volume of initial vapour cloud
η_D	single fibre deposition efficiency
δ	fitting parameter for the volume of initial vapour cloud
γ	proportionality factor between K_{df1} and Q_q
γ_s	surface tension of the NPs
Ω	atomic volume
τ_D	damping factor
ω	the natural frequency of the oscillations
$\mathcal{E}$	deposition parameter

Fundamental constants

σ	Stefan−Boltzmann constant 5.67×10^{-8} W m^{-2} K^{-4}
γ_p	empirical constant 7.69
e	elementary charge 1.60×10^{-19} C
N_A	Avogadro's number 6.02×10^{23} mol^{-1}
R	universal gas constant 8.31 J mol^{-1} K^{-1}
k	Boltzmann constant 1.38×10^{-23} m^2 kg s^{-2} k^{-1}

Other symbols

A_s	the area of the substrate
A	deposition area of textiles
A_{cs}	cross section area of the glow current
b	a constant embedded in the enhancement factor due to the poly-dispersity
c_g	specific heat capacity of the carrier gas
c_{ps}	heat capacity of the solid material
c_{pl}	heat capacity of the liquid material

c_p	particle velocity as a function of temperature and colliding particle masses
C_m	material-dependent constant
C_{mA}	material-dependent constant for the cathode
C_{mC}	material-dependent constant for the anode
C_c	Cunningham slip correction factor
C_{ca}	capacitance
C_1	unity
C_t	CFU of untreated samples at time 18 h
C_0	CFU of untreated samples at time 0 h
C_{Pd}	Pd material constant
C_{Au}	Au material constant
C_{Ag}	Ag material constant
D	diffusion coefficient
D_f	mass-mobility exponent
D_c	critical size of the singlet particles or the mean primary particle size
d	nozzle diameter
d_a	atom diameter
d_p	particle size
d_{pp}	primary particle size
$d_{\overline{m}}$	particle diameter of average mass
d_{tube}	tube inner diameter
d^*	critical nucleus size
d_f	fibre diameter
d_s	surface fractal dimension
d_{mb}	mobility diameter
d_{gap}	electrode gap distance
d_{mf}	mass fractal dimension by SAXS
D_f	mass mobility exponent
D_{pf}	final particle diameter
D_{pi}	the initial diameter of small cluster before mixing
E	spark energy
E_0	threshold energy
E_{th}	thermal energy

E_{dis}	energy dissipation
E_{dep}	deposition efficiency
f	spark repetition frequency
f_{sc}	the increased factor for the electric field inside the DMA due to space charge effect
g	transition parameter
G_F	a flow rate and geometry dependent parameter
H_e	vaporization enthalpy J kg^{-1}
H_v	vaporization enthalpy J mol $^{-1}$
H_m	melting enthalpy
I	current
I_i	scattering intensity in SWAXS
I_{peak}	peak current in the current waveform
I_{GC}	glowing current
k_a	thermal conductivity of carrier gas
k_e	thermal conductivity of the electrode
k_r	ratio of energies absorbed by the cathode and the anode
K_{dl}	dilution rate
K_{df1}	diffusional transport rate in turbulent flow
K_{df2}	laminar diffusional transport rate
l	representative distance as a function of particle diffusion coefficient and velocity
L_t	particle travel distance at the horizontal
L_{tube}	tube length
L_i	inductance
L	thickness of textiles
L_d	depth of textiles
$\dot{m}$	mass production rate of NPs
Δm	ablated mass per spark
m_g	the mass of the gas in V_o
M	molar weight
M_A	the mass per unit area of the textile
M_{ag}	mass density of the aerosol

m	particle mass
m_{Ai}	the mass of one component in one nanoparticle
m_{Bi}	the mass of the other component in one nanoparticle
m_{pp}	mass of one primary particle
$m_{Au=C}$	mass of Au in particles when Au is the cathode
$m_{Pd=C}$	mass of Pd in particles when Pd is the cathode
$m_{Pd=A}$	mass of Pd in particles when Pd is the anode
$m_{Au=A}$	mass of Au in particles when Au is the anode
Δm	mass ablated per spark
Δm_A	mass ablated per spark from the anode
Δm_C	mass ablated per spark from the cathode
N	particle concentration
N_{ag}	the concentration of agglomerates
N_0	initial concentration of the vapour
$N(t_f)$	final particle concentration
N_{tot}	total particle number concentration
Q	quenching gas flow rate
Q_q	quenching gas flow rate
Q_a	aerosol flow rate
Q_{sh}	sheath flow rate
P	surface fractals
P_s	the power of spark
P_p	penetration
p_a	actual pressure
p_s	saturated pressure
p_0	atmospheric pressure
p_{dep}	the probability of particle deposition
P_{st}	sticking probability after particle collision
p	charge probability
Δp	pressure drop
q	scattering vector
r	half of the plume width
r_s	radius of the spark channel

r_c	the amount materials ablated from cathode to that of both electrodes
R	interception parameter
Re	Reynold number
R_g	gyration radius of the particles
R_{spark}	spark resistance
R_{extra}	extra resistance
R_{tot}	total resistance
R_{GC}	resistance of glowing current
S	supersaturation
St	Stokes number
T_c	carrier gas temperature
T_b	boiling point of the electrode
T_m	melting point of the electrode
t_B	duration in Stage B
t_C	duration in Stage C
t_D	duration in Stage D
t_d	turbulent time
t	time
T_g	temperature of mixed cloud containing metallic vapour and gas molecular
T_t	CFU of nanofinished samples at time 18 h
T_o	CFU of nanofinished samples at time 0 h
ΔT	temperature change of the carrier gas
U	face velocity through textiles
u_a	time-averaged fluid speed
U_0	mean fluid velocity
U_c	potential difference over the electrodes
U_{gap}	gap voltage
V_b	breakdown voltage
V_g	gas volume
V_{mean}	mean gap voltage
V_0	the volume of initial vapour cloud
V	DMA voltage
V_{geo}	characteristic volume of SDG

V_{eff} effective volume of the plume

w a dimensionless quantity introduced in this thesis

w_{f} the natural frequency of the oscillation

x horizontal direction in the cone

x_{g} proportionality between the geometry and characteristic volume of SDG

Z_{psc} electrical mobility with consideration of the space charge effect

Z_{p} electrical mobility without consideration of the space charge effect

1. Introduction

"There's Plenty of Room at the Bottom."

— by Richard P. Feynman

1. 1 General information on nanoparticles

The term 'nanoparticle' (NP) is commonly used to indicate particles with diameters smaller than 100 nm, which is approximately three orders of magnitude smaller than the diameter of a human hair. In the literatures, atomic (<1 nm) and nano clusters (1~2 nm) are often used to describe particles with dimeters smaller than 2 nm. A number of approaches are used to categorize the NPs. From the aspect of types of materials that NPs consist of, inorganic and organic particles are frequently mentioned. On the basis of chemical composition, development in NP synthesis has achieved to mix two or more materials to obtain binary, ternary or multicomponent particles[1–3]. In terms of configuration of the NPs, there are a variety of shapes such as spherical, cubic NPs, nanowires, or other different nanostructures (onion-like core-shell particles, Janus particles that have two heads composed of different materials)[4].
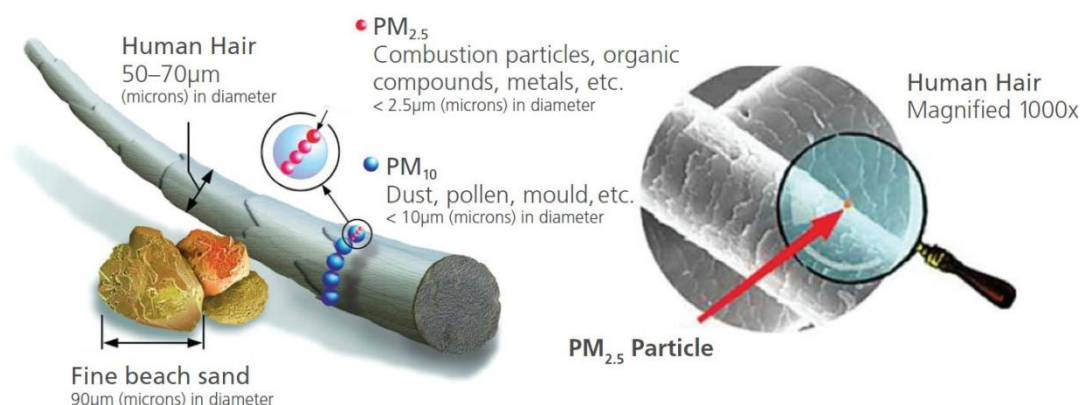
Figure 1.1 Comparing different particle sizes with a human hair (resource: http://www.dustoutus.com/resources/definitions/#lightbox/0/).

Generally, there are two basic techniques to produced NPs. The first approach is commonly referred to as top-down, which starts with bulk material split into nanosized pieces by applying mechanical, electrical, or other forms of energy. On the contrary, the bottom-up process enables atomic or molecular species to grow to NPs.

1.2 Interesting applications of NPs

The NPs have provided fascinating applications for our life because of their unique electronic, optical, or magnetic properties that differ substantially from their corresponding bulk counterparts. The most important variables determining their properties are size (distribution), composition, shape, and the degree of agglomeration.

One application has been realized in nanofinishing smart textiles[5,6], which have huge capacity in global markets. Fashion and apparel industries were valued at $1.2 trillion globally in 2014, and the market size is expected to have a compound annual growth rate of 4.8% until 2025, mainly driven by emerging markets. In 2014, the global smart textiles market was assessed at $795 million, which is anticipated to reach $4.72 billion by 2020 with a compound annual growth of 33%. Military related sectors occupies about 27% of the total market of smart textiles. The nanofiber-based products can reach over $1 billion by 2020. Silver and palladium NPs distributed within a dress or jacket impart antimicrobial, air purifying, or virtually unlimited colour-changing properties. These metallic NPs are assembled over the fibre surface of the textiles. One can also control the colour by manipulating the light interactions with the coated textiles by plasmonic NPs. Fashion-shows may not only be propelled by designers to please the eye, but also provide unprecedented research opportunities.

Magnetic materials expel heat in the presence of a magnetic field due to the alignment of the magnetic moments and cool down when removing this field[7]. In the light of this principle, magnetic refrigerants are the ideal candidates to revolutionize conventional refrigeration based on vapor-compression, providing ca. 30 % better energy efficiency and less noisy, eliminating detrimental refrigerant gases as well as creating more compact systems[8]. Great efforts to explore new magnetic materials have been focused on maximizing their cooling effects by manipulating the composition[9,10], size[11,12] and crystal structure[9,13−18]. The interactions between the

single magnetic domains can be minimized by using NPs smaller than this domain size, thereby increasing their magnetoanisotropy[12]. Further reducing the size of NPs, the thermal energy exceeds the magnetoanisotropy energy, quickly randomizing the magnetic dipoles[19,20]. As a result, supermagnetism occurs, thus not showing the undesired hysteresis above the blocking temperature in the typical magnetization measurements [20,21]. Another interesting feature of these superparamagnetic NPs lies in their switching behavior, triggering tremendous new possibilities[13,19–23].

Cancer might be treated more efficiently by properly functionalizing magnetic NPs, to make them biocompatible and target-specific[19,24,25]. The superparamagnetic NPs have no net magnetization at body temperature. They can be magnetized in the presence of an external magnetic field, and guided to the target in the human body. Being able to guide the particles independently can reduce drug dosages, so that therapies are more efficient and less harmful to patients. Magnetism can be switched off after delivering the drug to the target and the nonmagnetic particles can safely be removed from the blood in the liver and the kidneys.

A rapidly growing demand for catalysis is stimulating the manufacturing of large quantities of well-defined NPs, since the catalytic properties are enhanced by the large surface area of the very small NPs. The market of gold NPs is expected to reach $ 4.86 billion by 2020, according to a new study[1]. This means that producing of well-defined NPs is not only interesting for academic purposes but also to a global business. 'Making money by going green' has to be realized by using a sustainable manufacture method.

1.3 A need for scaling up

1.3.1 Challenges

The commercial production of high-performing nanomaterial-based applications, such as antimicrobial textiles[26,27], products in medicine[28,29], and nanocatalysis[30,31], requires scalable fabrication processes that are simple and do not use expensive and toxic chemicals[32–34]. These applications have attracted growing interest in exploring a new scalable method of synthesizing NPs with a directly-controlled size, well-defined composition and high purity[22,35–37], which are the most important variables

determining the properties of the products. One of the challenging tasks in nanotechnology is to increase the NP mass production rate with an accurately controlled size distribution down to the atomic scale. For example, methods with high throughput tend to exhibit limited size control and vice versa[38–40].

The conventional wet-chemistry processes for synthesizing NPs allow a homogeneous and narrow size and shape distribution, yet present a number of drawbacks[41–43]. Their scalability is severely inhibited by slow kinetics in the liquid phase as well as their batch type operations. Additionally, such batch operations commonly result in a wide variability in terms of physicochemical properties of the synthesized NPs. Moreover, liquid-phase methods generally require a number of chemicals for synthesizing one specific nanomaterial. Consequently, impurities and hazardous wastes are inextricably linked to these techniques, and some of the waste products are detrimental to both environment and products.

1.3.2 A green and versatile synthesis method

Gas-phase processes, on the other hand, are continuous, rapid, and environmentally friendly, and therefore they have been identified as chemical manufacturing techniques for a wide range of nanomaterials at the industrial scale. Flame processes[44], for example, have been used for producing oxide materials[45–47], such as pigmentary titania, silica and carbon black at several magatons per year. Fast kinetics of particle formation in gas phase, however, is not only an advantage in scaling-up; but it also tends to form fractal-like structures (i.e., agglomerates). The agglomerates result from collisions among particles, which remain joined by strong adhesive forces after colliding. The agglomeration is favoured at high particle concentrations. As a result, it usually occurs in industrial aerosol processes. The primary nanoscale particles, which build up the agglomerates, are usually the major determinant of the unique/novel properties of the final nanomaterials. The primary particle size could be controlled by manipulating the temperature profile downstream of the particle source. The surface state of the primary particles determines their size. This is because the trace amount of some constituent gas molecules reacts with the surface of these small particles. In contrast to the wet-chemistry methods, the purification of the resulting NPs can be generally avoided due to using a limited number of chemical precursors.

Among the numerous gas-phase methods, micro-second pulsed spark ablation operated at ambient pressure[48] provides the great versatility of synthesizing many ultrapure NPs with virtually unlimited mixing possibilities[34,49–52], and easy-to-control particle sizes ranging from that of atomic clusters to non-agglomerated 'singlets' (cf. Chapter 2) and agglomerated particles[49,53,54]. Furthermore, the absence of solvents and other toxic chemicals allows it to be an inherently environmentally benign process. In this method, repeated microsecond-pulsed sparks formed between two electrodes with desired composition locally heat their surface to produce vapor clouds[34], which are drastically quenched and carried away by a high-purity gas flow. As a result, the vapors become extremely supersaturated[55,56], thereby leading to the formation of NPs by homogeneous nucleation and subsequent condensation. This fast quenching also facilitates the internal mixing in spark ablation (cf. Chapter 5) and makes this method feasible to produce thermodynamically metastable materials[57].

The mass production rate of NPs produced by means of spark ablation is proportional to the spark repetition frequency and to the mass ablated per spark that is linearly related to the spark energy[54,58]. Spark discharges using resistance-inductance-capacitance (RLC) circuits (referred to this circuit based spark as RLCS from this point onwards)[34,59] have an upper operating frequency threshold of a few hundred Hz. Above that a continuous arc discharge develops[60], thereby yielding much larger particles[61]. Alternatively, the NP production rate can also be raised by increasing the spark energy. However, increasing the spark energy above a certain level leads to undesired 'splashing particles' (i.e., large particles ejected from a molten pool that are momentarily formed due to repeatedly striking the same hot-spot on the electrode surface; cf. Chapter 6)[62]. As deduced from the above discussion, maximizing the spark repetition frequency is a reliable approach to scale up this method (cf. Chapter 4).

1.4 Compatibility with existing fabrication processes

This spark ablation (cf. Section 1.3), which produces well-defined NPs with high throughput, is compatible with existing fabrications processes. The resulting NPs suspended in the gas-phase can be deposited and immobilized onto various (flat or

porous) substrates (e.g., silicon wafers, glass slides, polymeric, filter membranes, ceramics, textiles), opening a wealth of new possibilities for producing hierarchically patterned coatings and membranes[51,55,63–65]. For instance, 3D patterned nanostructures have been created with the help of focused aerosol deposition[66–73]. The representative applications of these nanostructures include printable electronics[73], perovskite solar cells[69,74], and sensors[26]. In addition, dry gas-phase methods can also be coupled with wet-chemistry routes, which enables the synthesis of an even broader range of new building blocks[51,75–78].

1.5 Goal of this thesis

The goal of this thesis is to use spark ablation for producing well-defined NPs that fulfill the requirements for the applications in the field of smart textiles, and magnetic materials in a green and scalable manner. To achieve this goal, several sub-tasks must be combined as discussed in Section 1.6. Ultimately, knowledge about the scaling-up of NPs production will be shared with other industry partners within our project (BUONAPART-e). It is expected that this environmentally benign and versatile method (regarding virtually unlimited mixing possiblities, controllable particle sizes, and high purity) will be applied in a large number of industrial processes in the next decades. This thesis will therefore contribute to identifying these new possibilities and intends to inspire new research activities on nanostructured materials in connection with gas phase methods. It also strives to form a bridge between the aerosol and the materials community, from which fruitful results can be obtained.

1.6 Thesis outline

This thesis is organized as follows. There are three main parts, namely fundamentals (**Part A**, i.e., Chapters 2 and 3), scaling up NP production (**Part B**, i.e., Chapters 4 ~6), and their associated applications (**Part C**, i.e., Chapter 7). In order to keep the conciseness of the main body of some chapters, Supplementary Information (SI) is therefore appended at the end of the associated chapters. These SI materials include additional technical details, some necessary specifications, further elaborations, compelling evidence, which may be of interest to certain readers. To discriminate

between the main body and SI, a different number system starting with an upper-case lettering "S" (e.g. S5.1) is adopted in the SI materials.
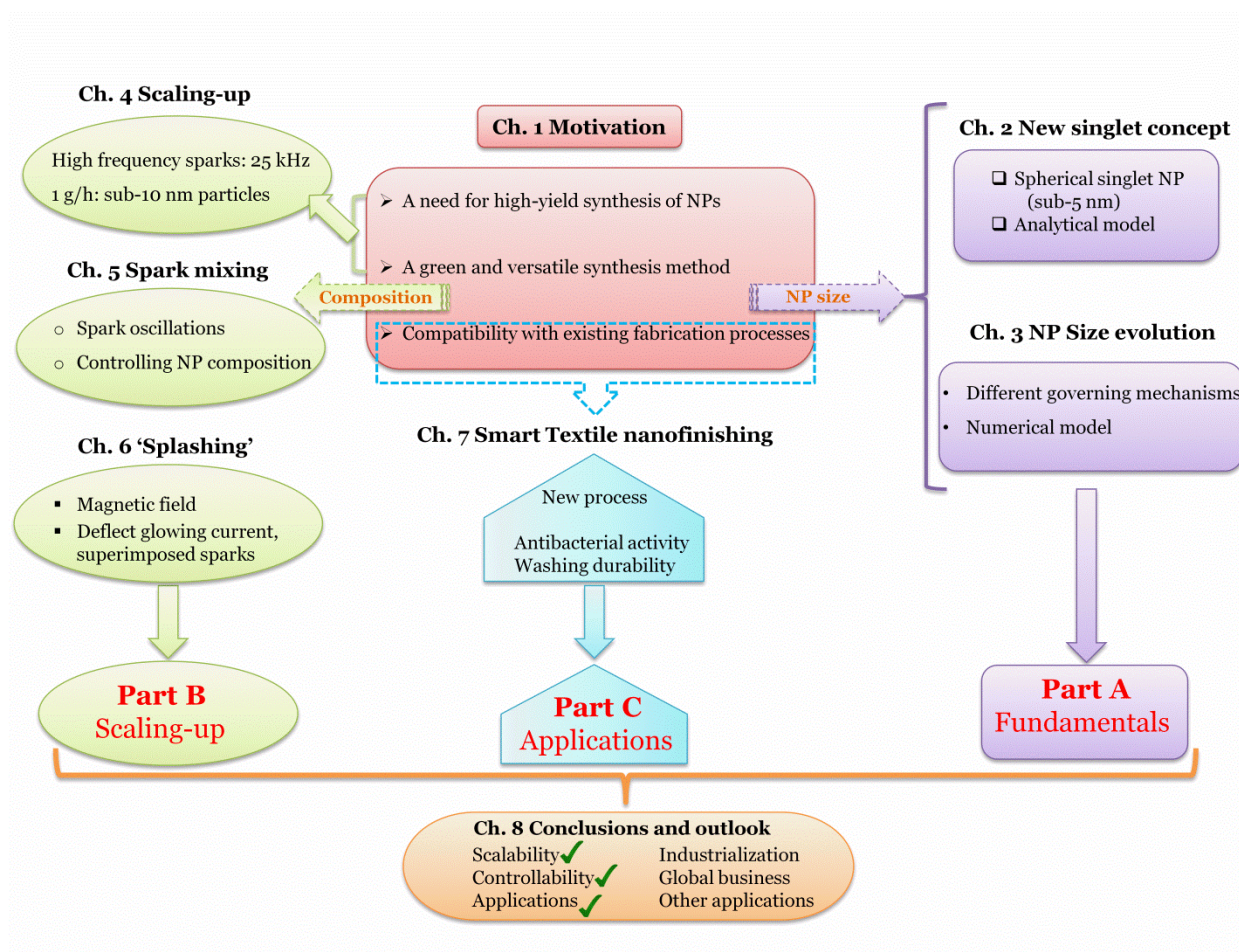
Figure 1.2 Visual outline of this thesis.

Part A: fundamental considerations

Continuous gas-phase synthesis of NPs is commonly associated with rapid agglomeration, which can be a limiting factor for numerous applications. In **Chapter 2**, experimental evidence is provided to demonstrate that gas-phase methods can be used to produce ultrapure non-agglomerated "singlet" NPs with tunable sizes under atmospheric conditions. By controlling the temperature in the particle growth zone to guarantee complete coalescence of colliding entities, the size of singlets in principle can be regulated from that of single atoms to any desired value.

Besides introducing the new concept of singlet NPs in Chapter 2, a general model is also developed to predict the size distribution of the generated NPs as a function of

the process conditions in **Chapter 3**. Despite the complexity of the entire process, the concentration and size evolution of particles can be adequately described by a first-order differential equation accounting for coagulation, turbulent dilution, and diffusional deposition to the walls. This model provides a simple and practical tool that can be generally used to design and control particle generators for the synthesis of NPs with tunable sizes.

Part B: scaling up

After the fundamental studies have been described in Chapters 2 and 3, scaling up of this method is subsequently conducted. Besides, to meet the industrial demands, there is an urgent need to deliver large quantities of well-defined NPs. **Chapter 4** presents a newly developed high frequency spark (HFS; see more details[79]) which achieves a frequency as high as 25 kHz[34]. Such a high frequency, which is proportional to the mass production rate, is two orders of magnitude higher than the RLCS. In order to avoid producing noticeable 'splashing particles', small and constant spark energy is used in the HFS system. The singlet NPs described in Chapters 1 and 2 can in principle be produced on an industrial scale by using this HFS when appropriate quenching gas flow rates are achieved.

Chapter 5 shows that polarity reversal of micro-second pulsed sparks between electrodes of different materials enables synthesis of mixed NPs with a controllable composition distribution. To examine this influence, a model is developed in this chapter. This model provides a tool for tuning the ablation ratio between the electrodes by adjusting the electric characteristics of the spark circuit, thereby controlling the mean composition of the resulting NPs. Model predictions are in accordance with measurements obtained here and earlier works, proving the feasibility of producing mixed NPs with a desirable composition.

The operating conditions of the HFS are optimized to deliver a constant NP output and to suppress 'splashing particles' in **Chapter 6.** Inhibition of 'splashing particles' has been successfully suppressed by employing an external magnetic field in the electrode gap. The resulting Lorentz force can deflect a low-power and continuous glowing current, onto which sparks are superimposed, thereby avoiding the sparks to strike the same point of the electrode surface.

Part C: application

In this part, the focus lies on the applications of the NPs on the basis of fundamental studies of Chapters 2 and 3, and these NPs can also be produced in large quantities by employing the HFS described in Chapter 4. As deduced from Chapters 5 and 6, the resulting NPs also possess improved uniformity and desired mixing ratio.

Chapter 7 proposes a scalable and environmentally benign process of embedding NPs onto textiles that act as filters. A range of textiles has been demonstrated to have high antibacterial activity and good washing durability. In view of the deposition of a wide range of NPs onto numerous textiles, this universal approach to 'smart textile nanofinishing' can be generalized and industrialized, such as self-cleaning textiles for upholstery with TiO_2 NPs and shielding radiation textiles with Fe_2O_3 NPs.

Chapter 8 closes with the most important conclusions, followed by some recommendations for future studies on the basis of the work described in this thesis. The main goal of this thesis is to describe a versatile and green method for producing well-defined NPs (in terms of controlled size and chemical composition) with high throughput. After fundamental studies and scaling-up of the NP production method have been outlined in **Part A** (Chapters 2 and 3) and **Part B** (Chapters 4, 5 and 6), **Part C** (Chapter 7) goes on to introduce a new process for smart textile nanofinishing, showing the antibacterial activity of resulting textiles. The future users can critically select the desired NPs by appropriately tuning the operating conditions of spark ablation. This work can stimulate more interesting applications, thereby driving its industrialization. It is hoped that this thesis compliments some previous work focused on specific facets, and the results obtained here therefore are expected to provide minor contributions to the development of our society.

References

1   W. Shi, H. Zeng, Y. Sahoo, T. Y. Ohulchanskyy, Y. Ding, Z. L. Wang, M. Swihart and P. N. Prasad, *Nano Lett.*, 2006, **6**, 875–881.

2   X.-J. Liu, C.-H. Cui, H.-H. Li, Y. Lei, T.-T. Zhuang, M. Sun, M. N. Arshad, H. a. Albar, T. R. Sobahi and S.-H. Yu, *Chem. Sci.*, 2015, **6**, 3038–3043.

3   K. Hur, R. G. Hennig, F. A. Escobedo and U. Wiesner, *Nano Lett.*, 2012, **12**, 3218–23.

4   Y. Xia, Y. Xiong, B. Lim and S. E. Skrabalak, *Angew. Chemie - Int. Ed.*, 2009, **48**, 60–103.

5   B. Simoncic and D. Klemencic, *Text. Res. J.*, 2016, **86**, 210–223.

6   A. K. Yetisen, H. Qu, A. Manbachi, H. Butt, M. R. Dokmeci, J. P. Hinestroza, M. Skorobogatiy, A. Khademhosseini and S. H. Yun, *ACS Nano*, 2016, **10**, 3042–3068.

7   O. Tegus, E. Brück, K. H. J. Buschow and F. R. de Boer, *Nature*, 2002, **415**, 150–152.

8   O. Gutfleisch, M. a. Willard, E. Bruck, C. H. Chen, S. G. Sankar and J. P. Liu, *Adv. Mater.*, 2011, **23**, 821–842.

9   K. A. Gschneidner Jr, V. K. Pecharsky and A. O. Tsokol, *Reports Prog. Phys.*, 2005, **68**, 1479–1539.

10   S. Li, R. Huang, Y. Zhao, W. Wang and L. Li, *Phys. Chem. Chem. Phys.*, 2015, **17**, 30999–31003.

11   A. M. Tishin and Y. I. Spichkin, *Int. J. Refrig.*, 2014, **37**, 223–229.

12   D. Vollath, *Nanoparticles-Nanocomposites-Nanomaterials: An introduction for beginners*, Wiley-VCH, 2013.

13   U. Jeong, X. Teng, Y. Wang, H. Yang and Y. Xia, *Adv. Mater.*, 2007, **19**, 33–60.

14   J. Liu, T. Gottschall, K. P. Skokov, J. D. Moore and O. Gutfleisch, *Nat. Mater.*, 2012, **11**, 620–6.

15   E. Brück, *J. Phys. D. Appl. Phys.*, 2005, **38**, R381–R391.

16   B. G. Shen, J. R. Sun, F. X. Hu, H. W. Zhang and Z. H. Cheng, *Adv. Mater.*, 2009, **21**, 4545–4564.

17   L. F. Bao, F. X. Hu, L. Chen, J. Wang, J. R. Sun and B. G. Shen, *Appl. Phys. Lett.*, 2012, **101**, 162406.

18   L. Jia, J. R. Sun, F. W. Wang, T. Y. Zhao, H. W. Zhang, B. G. Shen, D. X. Li, S. Nimori, Y. Ren and Q. S. Zeng, *Appl. Phys. Lett.*, 2008, **92**, 101904.

19   M. Latorre and C. Rinaldi, *J. Phys. D. Appl. Phys.*, 2003, **36**, R167–R181.

20   A. Kolhatkar, A. Jamison, D. Litvinov, R. Willson and T. Lee, *Tuning the Magnetic Properties of Nanoparticles*, 2013, vol. 14.

21   A.-H. Lu, E. L. Salabas and F. Schüth, *Angew. Chemie Int. Ed.*, 2007, **46**, 1222–1244.

22   N. A. Frey, S. Peng, K. Cheng and S. Sun, *Chem. Soc. Rev.*, 2009, **38**, 2532–2542.

23   D. L. Huber, *Small*, 2005, **1**, 482–501.

24   C. Alexiou, R. J. Schmid, R. Jurgons, M. Kremer, G. Wanner, C. Bergemann, E. Huenges, T. Nawroth, W. Arnold and F. G. Parak, *Eur. Biophys. J.*, 2006, **35**, 446–450.

25   A. Ito, M. Shinkai, H. Honda and T. Kobayashi, *J. Biosci. Bioeng.*, 2005, **100**, 1–11.

26   N. A. Isaac, P. Ngene, R. J. Westerwaal, J. Gaury, B. Dam, A. Schmidt-Ott and G. Biskos, *Sensors Actuators B Chem.*, 2015, **221**, 290–296.

27   Q. Kuang, C. Lao, Z. L. Wang, Z. Xie and L. Zheng, *J. Am. Chem. Soc.*, 2007, **129**, 6070–6071.

28   J. B. Goodenough and K.-S. Park, *J. Am. Chem. Soc.*, 2013, **135**, 1167–1176.

29   S. Kondrat, P. Wu, R. Qiao and A. A. Kornyshev, *Nat. Mater.*, 2014, **13**, 387–393.

30   T. V. Pfeiffer, J. Ortiz-Gonzalez, R. Santbergen, H. Tan, A. Schmidt-Ott, M. Zeman and A. H. M. Smets, *Energy Procedia*, 2014, **60**, 3–12.

31   B. D. Yuhas and P. Yang, *J. Am. Chem. Soc.*, 2009, **131**, 3756–3761.

32   F. E. Kruis, H. Fissan and A. Peled, *J. Aerosol Sci.*, 1998, **29**, 511–535.

33   A. Gutsch, H. Mühlenweg and M. Krämer, *Small*, 2005, **1**, 30–46.

34   T. V. Pfeiffer, J. Feng and A. Schmidt-Ott, *Adv. Powder Technol.*, 2014, **25**, 56–70.

35   H. T. Chung, J. H. Won and P. Zelenay, *Nat. Commun.*, 2013, **4**, 1922.

36   J. Chang, X. Huang, G. Zhou, S. Cui, P. B. Hallac, J. Jiang, P. T. Hurley and J. Chen, *Adv. Mater.*, 2014, **26**, 758–764.

37   Y. Xia, T. D. Nguyen, M. Yang, B. Lee, A. Santos, P. Podsiadlo, Z. Tang, S. C. Glotzer and N. A. Kotov, *Nat. Nanotechnol.*, 2011, **6**, 580–587.

38   C. A. Charitidis, P. Georgiou, M. A. Koklioti, A.-F. Trompeta and V. Markakis, *Manuf. Rev.*, 2014, **1**, 1–19.

39   M. T. Swihart, *Curr. Opin. Colloid Interface Sci.*, 2003, **8**, 127–133.

40   A. Gutsch, M. Krämer, G. Michael, H. Mühlenweg, M. Pridöhl and G. Zimmermann, *KONA Powder Part. J.*, 2002, **20**, 24–37.

41   J.-G. Park, J. D. Forster and E. R. Dufresne, *J. Am. Chem. Soc.*, 2010, **132**, 5960–1.

42   T. K. Sau and C. J. Murphy, *J. Am. Chem. Soc.*, 2004, **126**, 8648–5649.

43   G. H. Jeong, Y. W. Lee, M. Kim and S. W. Han, *J. Colloid Interface Sci.*, 2009, **329**, 97–102.

44   K. Wegner, S. Vinati, P. Piseri, A. Antonini, A. Zelioli, E. Barborini, C. Ducati and P. Milani, *Nanotechnology*, 2012, **23**, 185603.

45   H. K. Kammler, L. Mädler and S. E. Pratsinis, *Chem. Eng. Technol.*, 2001, **24**, 583–596.

46   R. Strobel and S. E. Pratsinis, *J. Mater. Chem.*, 2007, **17**, 4743.

47   S. E. Pratsinis, *Prog. Energy Combust. Sci.*, 1998, **24**, 197–219.

48   S. Schwyn, E. Garwin and A. Schmidt-Ott, *J. Aerosol Sci.*, 1988, **19**, 639–642.

49   J. Feng, G. Biskos and A. Schmidt-Ott, *Sci. Rep.*, 2015, **5**, 15788.

50   J. H. Byeon, J. H. Park, K. Y. Yoon and J. Hwang, *Nanoscale*, 2009, **1**, 339–343.

51   J. H. Byeon and Y.-W. Kim, *Nanoscale*, 2012, **4**, 6726–6729.

52   J. H. Byeon, J. H. Park and J. Hwang, *J. Aerosol Sci.*, 2008, **39**, 888–896.

53   A. Maisser, K. Barmpounis, M. B. Attoui, G. Biskos and A. Schmidt-Ott, *Aerosol Sci. Technol.*, 2015, **49**, 886–894.

54 J. Feng, L. Huang, L. Ludvigsson, M. E. Messing, A. Maisser, G. Biskos and A. Schmidt-Ott, *J. Phys. Chem. C*, 2016, **120**, 621–630.

55 C. Peineke, *PhD thesis*, Delft University of Technology, 2008.

56 G. Biskos, V. A. Vons, C. U. Yurteri and A. Schmidt-Ott, *KONA Powder Part. J.*, 2008, **26**, 13–35.

57 V. Sebastian, M. Arruebo and J. Santamaria, *Small*, 2014, **10**, 835–853.

58 F. Llewellyn Jones, *Br. J. Appl. Phys.*, 1950, **1**, 60–65.

59 A. Anastasopol, T. V Pfeiffer, J. Middelkoop, U. Lafont, R. J. Canales-Perez, A. Schmidt-Ott, F. M. Mulder and S. W. H. Eijt, *J. Am. Chem. Soc.*, 2013, **135**, 7891–7900.

60 B. O. Meuller, M. E. Messing, D. L. J. Engberg, A. M. Jansson, L. I. M. Johansson, S. M. Norlén, N. Tureson and K. Deppert, *Aerosol Sci. Technol.*, 2012, **46**, 1256–1270.

61 E. Hontañón, J. M. Palomares, M. Stein, X. Guo, R. Engeln, H. Nirschl and F. E. Kruis, *J. Nanoparticle Res.*, 2013, **15**, 1957.

62 N. S. Tabrizi, M. Ullmann, V. A. Vons, U. Lafont and A. Schmidt-Ott, *J. Nanoparticle Res.*, 2009, **11**, 315–332.

63 D. M. King, X. Liang and A. W. Weimer, *Powder Technol.*, 2012, **221**, 13–25.

64 S. K. Sengar, B. R. Mehta, R. Kumar and V. Singh, *Sci. Rep.*, 2013, **3**, 2814.

65 M. Heurlin, M. H. Magnusson, D. Lindgren, M. Ek, L. R. Wallenberg, K. Deppert and L. Samuelson, *Nature*, 2012, **492**, 90–94.

66 K. Jung, H.-J. Song, G. Lee, Y. Ko, K. Ahn, H. Choi, J. Y. Kim, K. Ha, J. Song, J.-K. Lee, C. Lee and M. Choi, *ACS Nano*, 2014, **8**, 2590–2601.

67 H. Choi, S. Kang, W. Jung, Y. Jung, S. J. Park, D. S. Kim and M. Choi, *J. Aerosol Sci.*, 2015, **88**, 90–97.

68 K. Jung, J. Hahn, S. In, Y. Bae, H. Lee, P. V Pikhitsa, K. Ahn, K. Ha, J.-K. Lee, N. Park and M. Choi, *Adv. Mater.*, 2014, **26**, 5924–5929.

69 S. Jang, J. Yoon, K. Ha, M. Kim, D. H. Kim, S. M. Kim, S. M. Kang, S. J. Park, H. S. Jung and M. Choi, *Nano Energy*, 2016, **22**, 499–506.

70 S. You, K. Han, H. Kim, H. Lee, C. G. Woo, C. Jeong, W. Nam and M. Choi, *Small*, 2010, **6**, 2146–2152.

71 H. Lee, S. You, P. V Pikhitsa, J. Kim, S. Kwon, C. G. Woo and M. Choi, *Nano Lett.*, 2011, **11**, 119–124.

72   H. Kim, J. Kim, H. Yang, J. Suh, T. Kim, B. Han, S. Kim, D. S. Kim, P. V
      Pikhitsa and M. Choi, *Nat. Nanotechnol.*, 2006, **1**, 117–121.

73   J. J. Cole, E. C. Lin, C. R. Barry and H. O. Jacobs, *Small*, 2010, **6**, 1117–1124.

74   S. M. Kang, S. Jang, J.-K. Lee, J. Yoon, D.-E. Yoo, J.-W. Lee, M. Choi and N.-G.
      Park, *Small*, 2016, **12**, 2443–2449.

75   Z. Jin, M. Xiao, Z. Bao, P. Wang and J. Wang, *Angew. Chem. Int. Ed. Engl.*,
      2012, **51**, 6406–6410.

76   R. G. Sanedrin, D. G. Georganopoulou, S. Park and C. A. Mirkin, *Adv. Mater.*,
      2005, **17**, 1027–1031.

77   J. M. Tour, *Nature*, 2014, **512**, 30–31.

78   C. Boissiere, D. Grosso, A. Chaumonnot, L. Nicole and C. Sanchez, *Adv. Mater.*,
      2011, **23**, 599–623.

79   T. V. Pfeiffer, *PhD thesis*, Delft University of Technology, 2014.

Part A

Fundamental Considerations

2. Toward Industrial Scale Synthesis of Ultrapure Singlet Nanoparticles with Controllable Sizes in a Continuous Gas-phase Process

Continuous gas-phase synthesis of nanoparticles is associated with rapid agglomeration, which can be a limiting factor for numerous applications. In this chapter, this pseudo-paradigm is challenged by providing experimental evidence to support that gas-phase methods can be used to produce ultrapure non-agglomerated "singlet" nanoparticles having tunable sizes at room temperature. For drastically quenched processes, the temperature in the particle growth phase can be decoupled from the localized vaporization, and can be set to a value guaranteeing complete coalescence. By controlling the temperature to guarantee complete coalescence of colliding entities, the singlet particle size in principle can be regulated to any desired value. The results are assessed in the context of a simple analytical model, assuming a constant room temperature and a uniform residence time distribution, to explore the dependence of singlet size on the operating conditions. Agreement of the model with experimental measurements shows that these methods can be effectively used for producing singlets that can be processed by many alternative approaches. Combined with the capabilities of upscaling and unlimited mixing that spark ablation enables, this study provides an easy-to-use concept for producing the key building blocks for low-cost nanofabrication of advanced materials toward industrial scale.

Graphical Abstract
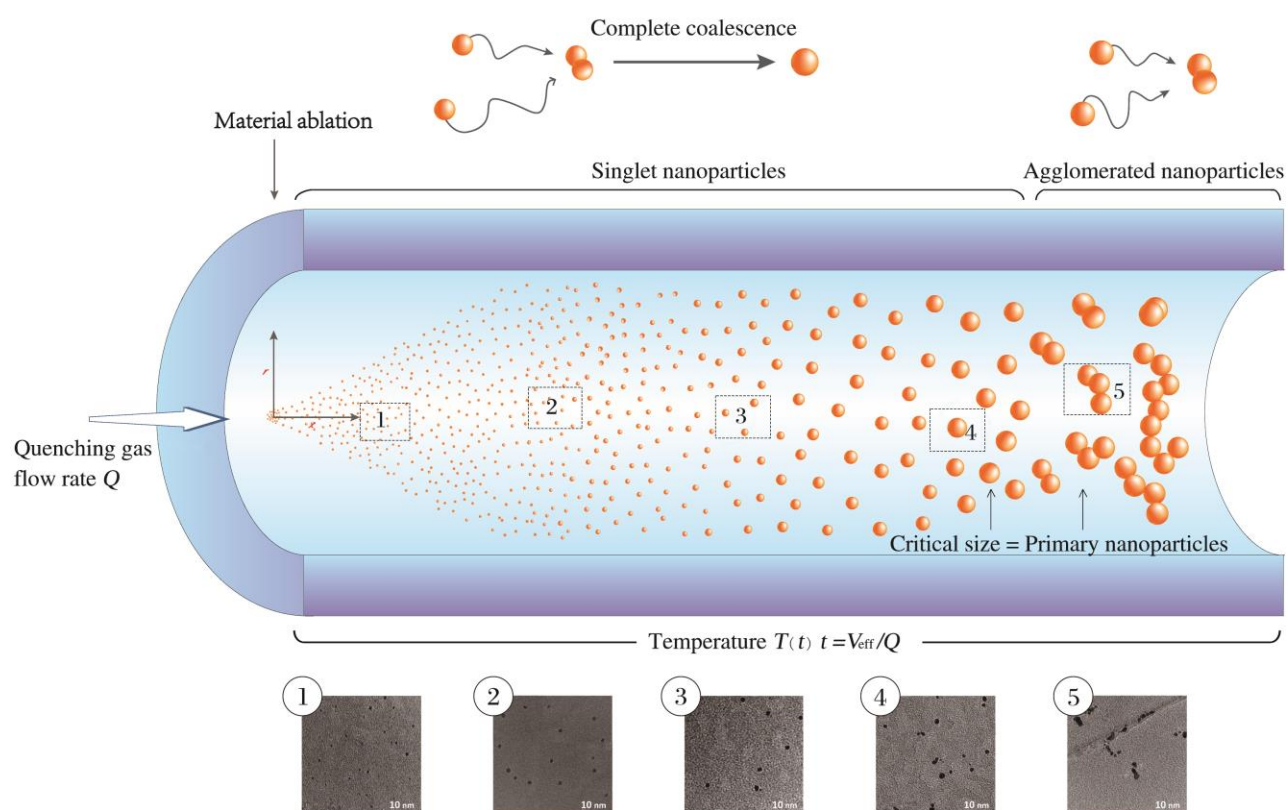
2.1 Introduction

Gas-phase methods for nanoparticle (NP) synthesis exhibit fast kinetics because the relevant diffusion coefficients are three orders of magnitude larger than those encountered in wet-chemistry techniques. Although the fast kinetics enable effective continuous processes, which are gaining significant ground in view of industrial applications over the recent years[1,2], they commonly lead to agglomerated particles which are undesirable in some cases. These agglomerates consist of primary particles (typically regarded as the smallest size the particles can have) that are difficult to take apart[3].

A number of previous works have therefore focused on ways to avoid the collisions of these particles before deposition or immobilization. In spark discharges, for example, agglomeration can be reduced by using the high space charge density[4], although this can be a limiting factor for its scalability. For flame aerosol synthesis, it has been shown that the associated elevated temperatures lead to non-agglomerated particles having sizes in the micron range[5]. Imposing harsh conditions in the gas-phase processes can also produce atomic clusters[6–8].

This chapter provides a general concept of continuous gas-phase synthesis of ultrapure singlet particles ranging from atomic clusters to particles in the nanometre range. The essence of this concept is illustrated in Figure 2.1. Vapours are produced by localized material ablation using lasers or electric discharges. The vapours are strongly quenched by an inert gas flow of variable temperature, thereby producing particles by condensation. As the supersaturations reached in the rapidly quenched vapour cloud are extremely high, the critical nucleus size is pushed down to the atomic scale. As a result, the growth governed by particle-particle collisions can be considered to start from the atomic scale, and therefore particle-particle collisional growth represents a valid model for the description of the size distribution evolution[7,9–12]. Note that this simplification is only valid in the case of rapidly

quenched vapours emitted from point sources. If the quenching flows are low (and thus the cooling rates are substantially low) as in most NP production methods in the gas phase, more sophisticated models will be required to describe particle formation and growth[13]. The atomic clusters and smallest NPs that are formed at the early stages of the process are liquid-like even at room temperature[14], and therefore fully coalesce into singlets when colliding with each other. Growth of singlets to a critical size above which coalescence only partly occurs or ceases for the selected operating temperature (see below), signals the onset of agglomeration which leads to non-spherical/agglomerated particles. For drastically quenched processes, the temperature in the particle growth phase can be decoupled from the localized vaporization, and can be set to a value guaranteeing complete coalescence (cf. Figure 2.1). In contrast to other high temperature aerosol synthesis methods[5,15], this feature provides great flexibility in controlling the size of the resulting NPs.
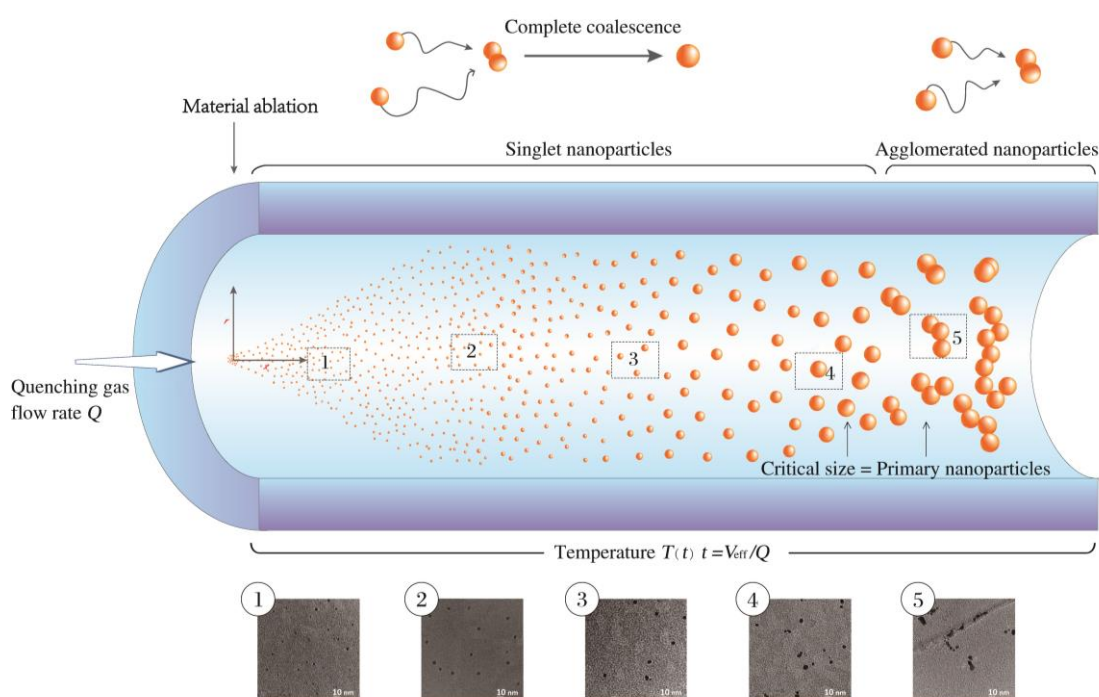
Figure 2.1 Schematic representation of the formation of singlet and agglomerated aerosol NPs resulting from material ablation at atmospheric pressure.

This chapter challenges the pseudo-paradigm that "nanoparticle synthesis in the gas phase leads to agglomerates"[3] by coining a scalable concept of "singlet" particle production. Using spark ablation as an example of the vapour point source, the results show that the concept can lead to singlets ranging from clusters of a few atoms

to particles of any desired size by tuning the operating conditions in Section 2.2. Using first principles this section also develops an analytical model, which is based on the Smoluchowski coagulation, for predicting the size of the singlet particles under different operating conditions. Collisional growth of particles can be simply described by the monodisperse aerosol dynamics under a number of simplifications, which have also been used by others[16,17]. Section 2.3 demonstrates that the proposed approach exhibits enormous flexibility for high-throughput and ultrapure production[18], thereby advancing NP synthesis and enabling low-cost fabrication of nanomaterials on an industrial scale as concluded in Section 2.4. Section 2.5 shows the experimental setup, which consists of units for the generation, collection, and online size distribution measurement of NPs (cf. Figure S2.3 in the SI).

2.2 Results

2.2.1 An analytical approach

In order to exclusively produce singlet particles, the process must be controlled in a way that particle growth does not exceed the critical size, which in turn depends on the material of the particles and temperature[15,19], and is relatively insensitive to other process parameters. In practice, singlets of any diameter can be achieved by controlling the temperature of the aerosol (i.e., particles dispersed within the carrier gas), so that coalescence is guaranteed up to the desired size. To further ensure that coalescence is not hindered by unwanted oxidation of particles due to the presence of trace amounts of oxygen and/or water in the carrier gas, extremely clean conditions are required throughout the production line. Such conditions can be achieved using suitable absorbers (i.e., molecular sieves and catalysts) to purify the carrier gas upstream the particle generator[20].

In the next paragraphs, a simple model is developed to predict the evolution of singlet NPs produced by material ablation in the gas-phase under conditions that guarantee complete coalescence (see Section S2.1). According to Smoluchowski's theory[9], the decay rate of particle concentration $dN(t)/dt$ is proportional to the square of $N(t)$. Any particle losses by diffusional transport to the walls, where van der Waals forces normally guarantee sticking, can be approximated by a linear term in $N(t)$ [21,22]. For

sufficiently high concentrations during particle evolution, losses by diffusion to the walls as well as rapid turbulent dilution (cf. Figure S2.1 for additional details) can be neglected compared to the vigorous coagulation. $N(t)$ can therefore be described by:

$$\frac{\mathrm{d}N}{\mathrm{d}t} = -\frac{1}{2}\beta N^2 \tag{2.1}$$

where β is the coagulation kernel, which changes with time depending on the momentary particle size distribution and temperature, gas flow conditions, and inter-particle forces[23,24]. For the early stages of atomic cluster formation, β is unknown because the sticking probability after each collision depends largely on the stability of the atomic clusters[25]. Turbulent flow conditions that are not well enough defined in practical cases of particle coagulational growth, lead to yet another intractable problem in deriving any rigorous model for predicting the evolution of the particles. For tackling these problems, it is therefore instructive to evaluate the general behaviour of coagulating systems, governed by equation (2.1).

As the initial concentration N_0 of the vapour atoms produced by material ablation is many orders of magnitude larger than the final concentration $N(t_f)$ of the particles (i.e., $N_0 >> N(t_f)$), equation (2.1) implies that $N(t_f)$ is independent of N_0. In fact, $N(t_f)$ is only determined by the evolution of $N(t)$ during approximately the last decade concentration reduction (cf. Figure S2.2)[26]. This stage, referred to as the "the final coagulation stage" in the following, covers most of the total coagulation time. Therefore, the complex turbulent flow conditions and the uncertainties in using an appropriate value for β (associated with the early stages of atomic clusters growth) can be reasonably excluded as explained further in the SI (cf. Sections S2.1 and S2.2 therein). For suitable ablation methods, the temperature in the particle growth region can be decoupled from that in the vaporization stage, and set to a well-defined value during the final coagulation stage. For a specific mass ablation rate, the particles grow approximately by a factor of two during the final coagulation stage due to the proportionality of particle size d_p to $N(t)^{-\frac{1}{3}}$. Coagulation models show that β does not vary by more than a factor of two when particle size doubles, and its dominating value corresponds to the final size.

It is therefore reasonable to assume that β is constant and solve equation (2.1) considering $N_o \gg N(t_f)$ to yield:

$$N(t_f) = \frac{2}{\beta V_{eff}} Q \qquad (2.2)$$

where Q is the gas volumetric flow rate and V_{eff} the effective volume corresponding to the volume incorporating most of the flow and occupied by the coagulating aerosol. In a continuous flow arrangement, the residence time of the particles is then $t_f = V_{eff}/Q$ and represents the duration for an aerosol parcel to travel from the vapour source to the point of measurement or further particle processing, where coagulation is inhibited by immobilization or adequate dilution. A good estimation for the relevant β can be based on the final particle size as explained above.

The increase of particle size due to coagulation is related to the decrease in number concentration. As the average particle size increased, the measured particle concentration drops while the total particle mass concentration $\frac{dm}{dV}$ remains approximately constant[27]. Considering that the mass production rate $\dot{m}$ can be expressed as $\frac{dm}{dt} = \frac{dm}{dV}\frac{dV}{dt} = Q\frac{dm}{dV}$, the particle size d_p can be calculated by:

$$d_p = \left(\frac{3\beta V_{eff}\dot{m}}{\rho\pi Q^2}\right)^{1/3} \qquad (2.3)$$

where ρ is the material density. This expression can be used to determine the particle size as a function of gas flow rate Q and particle mass production rate $\dot{m}$. Equation (2.3) is generally valid for any material ablation process or similar processes where vaporization is localized enough for the coagulation temperature, defining β, to be decoupled from the vaporization temperature, at least during the final coagulation stage. Evidently, rapid dilution (i.e., dilution time $t_d \ll t_f$; cf. Figure S2.1) and high enough temperature for complete coalescence as mentioned above, must also be ensured.

If the particle losses are neglected, equation (2.3) will generally lead to an overestimation of particle size. However, the effect of losses on particle size is moderate for most systems because $\dot{m}$ enters equation (2.3) as the cube root. The

ensuring text will show that the model can be applied to a microsecond-pulsed particle source where in practice the system is mixed well enough to provide a uniform concentration during the final coagulation stage. The particle size predicted by equation (2.3) remains an approximation, but the elegance of the approach lies in the fact that uncertainties are circumvented because the final size depends on the final stage of the process, where the system is well defined.

From this point onwards spark ablation will be considered as the source of vapours for particle formation. As a scalable technique, mixing is remarkably simple with spark ablation as compared to other evaporation-condensation methods[1,28]. Being applicable to many inorganic materials[18], and virtually allowing unlimited mixing combinations at atomic and nanometre scale[29,30], it represents a powerful approach for synthesizing advanced materials with multiple functionalities[31,32].

Details of the spark ablation setup are described in the experimental section (cf. Section S2.3 and Figure S2.3 in the SI). In brief, repeated microsecond-pulsed sparks initiated between two electrodes ablate electrode materials to produce vapour clouds. These vapours are subsequently quenched by a high-purity gas flow and condensed to form atomic clusters and NPs. Depending on the process variables (i.e., quenching gas flow rate Q, spark energy E, and spark repetition frequencies f), the resulting particles can have sizes that range from clusters of a few atoms up to any desired size. For the sake of completeness, it must be noted here that if agglomerates are produced by spark ablation, or by any other similar gas-phase method, they can be converted to singlet particles by heating in gas suspension after growth has essentially ceased[15,33,34]. This technique has been applied in diluted laboratory setups with particle mass production rates in the range of mg h^{-1}. By contrast, the concept presented in this work, where coalescence is induced in the particle growth phase, is only limited by the vapour mass production rate from the spark ablated electrodes. Considering that the measurements of ablated mass per spark indicate that a production rate of the order of 1 g h^{-1} is feasible (cf. Section S2.4 in the SI), the concept can lead up to three orders of magnitude higher singlet particle production rate than other commonly used techniques[18]. Additionally, the possibility of numbering up the generators can further increase the production rate of the desired particles to meet industrial demands[1].

The mass produced by a single spark is given by:

$$\Delta m = C_{\mathrm{m}}(E - E_0) \tag{2.4}$$

Here C_{m} is a material-dependent constant (cf. equation (S2.6)), E the spark energy, and E_0 is the minimum spark energy for producing particles (cf. equation (S2.7)). C_{m} and E_0 can be calculated by the evaporation model, which is derived by the energy balance of the evaporation process (cf. equation (S2.5))[35].

The mass production rate is given by $\dot{m} = \Delta m f$ (cf. Figure S2.4), where f is the spark repetition frequency. Pulsed sparks can be regarded as a continuous particle source given that sufficient mixing guarantees a uniform concentration before the final coagulation stage is reached. Combining equations (2.3) and (2.4) yields:

$$d_{\mathrm{p}} = \left(\frac{3\beta V_{\mathrm{eff}}C(E - E_0)f}{\pi \rho Q^2}\right)^{1/3} \tag{2.5}$$

Recipes and sources for determining sufficiently accurate values for the required quantities of $C_{\mathrm{m}}, E_0, \beta$, and V_{eff} are given in the SI (cf. Section S2.4 and S2.5). In the following, the proposed model is validated (i.e., equations (2.2) and (2.3) that give the evolution of particle concentration and size) with the measurements.

2.2.2 Experimental validation

Figure 2.2 (a-e) shows TEM images of particles collected using the experimental setup (cf. Section S2.3 and Figure S2.3 in the SI) under different quenching gas flow rates at a fixed spark energy E (=16 mJ) and frequency f (=60 Hz), which allows variation of the singlet particle size from ca. 2 nm upwards. Evidently, the coalescence is complete up to sizes between 5 and 6 nm (cf. Figure S2.6 for more details in the SI). Larger particles are agglomerates, indicating that the selected coagulation temperature of ca. 20 ℃ is adequate for generation of Au singlet particles up to ca. 6 nm.

In coagulation with full coalescence, the size distribution approaches a lognormal self-preserving distribution with geometric standard deviation (GSD) ranging from ca. 1.33 to 1.35[36]. Figure 2.2f shows that the geometrical mean diameter (GMD) of the singlet particles measured by the scanning mobility particle sizer (SMPS) is ca.10 %

larger than that determined by the TEM images when Q = 9.9 standard litres per minute (slm). This discrepancy can be explained by the larger representation of the small particles (having large diffusion coefficients) collected by diffusion on the TEM grids. The limited number of particles (ranging from 20 to 50) counted in TEM images also adds a minor statistical error in the microscopy observations.
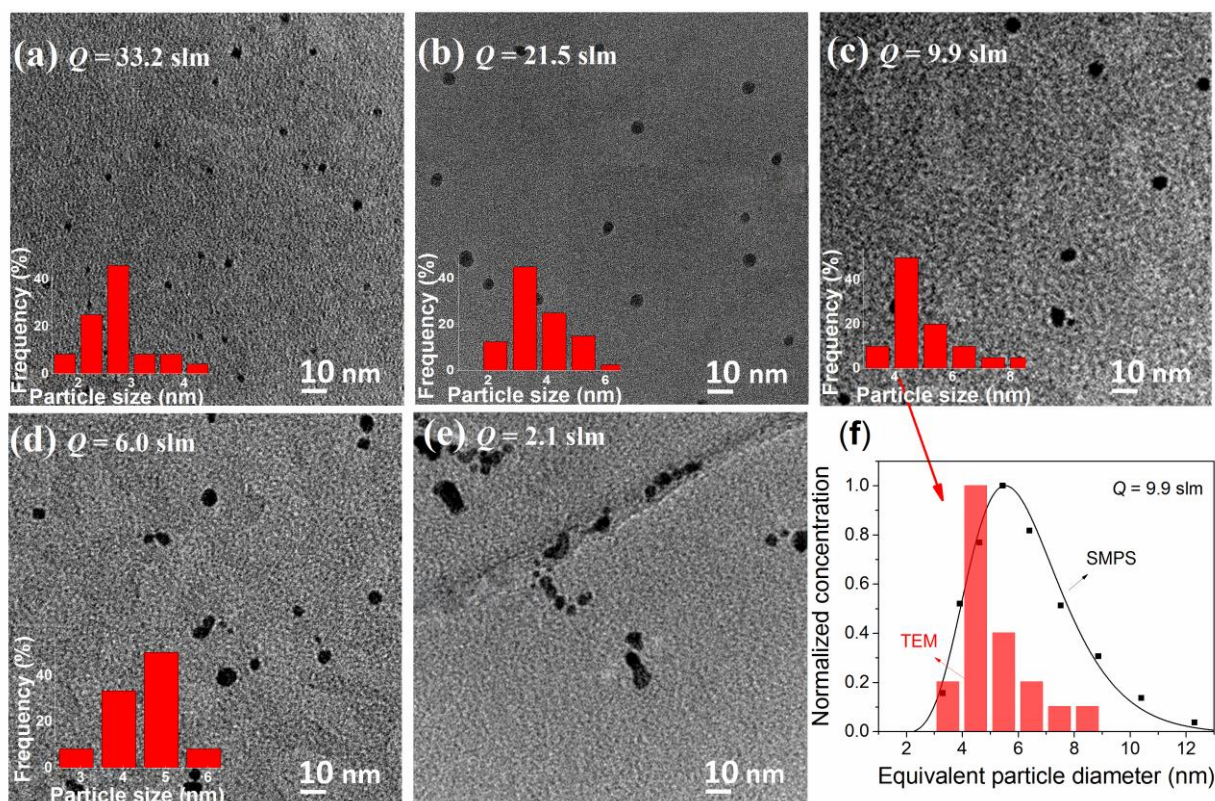
Figure 2.2 Electron Micrographs of Au singlets (a-c) and partly agglomerated particles (d and e) produced by spark ablation and collected downstream of the DMA, and particle size distributions determined by the SMPS and TEM image at Q = 9.9 slm (f). Geometric standard deviations of the particles sampled on the TEM images of (a-d) are 1.10 (52 particles), 1.07 (32 particles), 1.10 (20 particles) and 1.08 (40 particles), respectively. Therefore, the particles can be considered as quasi-monodisperse. Figure 2.2d and 2.2e show that the size of primary particle is ca. 6 nm, which corresponds to the largest singlet particles of Au.

Figure 2.3 shows how the total number concentration of the particles at the exit of the particle generator varies with quenching gas flow rate. It should be noted here that the concentration is derived from the particle sizes measured by the SMPS with the assumption that there are no diffusional losses, i.e., mass of ablated material per unit

volume is conserved (cf. Figure S2.2 and equation (S2.4) in the SI). It should be pointed out that in order to derive the particle size distributions at the exit of the particle generator, the space charge effect in the differential mobility analyser (DMA)[37] is neglected as it affects the particle size measurements by less than 4% assuming the highest possible concentration of charged particles observed here (ca. 10^7 cm^{-3}; cf. Section S2.7 in the SI). Moreover, for particle concentrations of the order of 10^{10} cm^{-3}, coagulation within the DMA can also be neglected during the short residence time of 0.15 s, as discussed in Section S2.2 in the SI (cf. Figure S2.2).
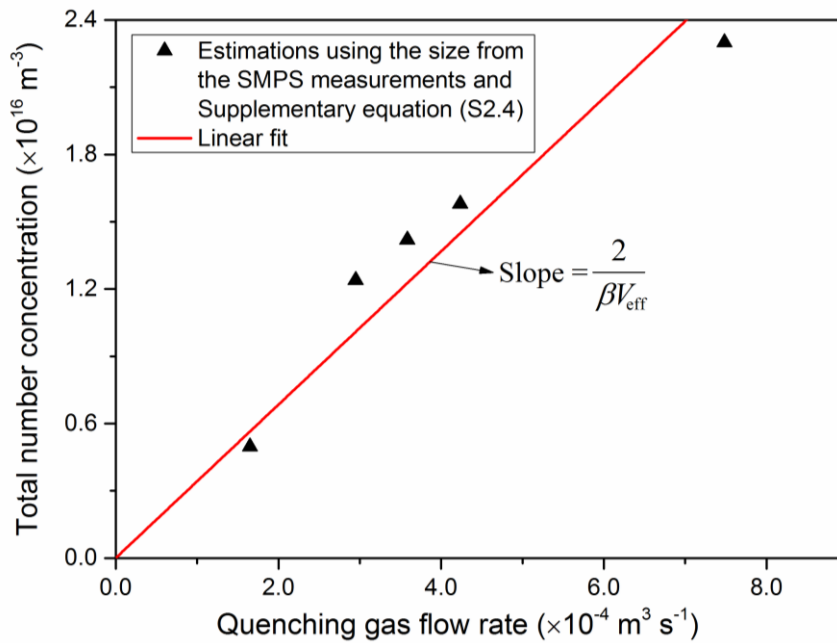
Figure 2.3 Concentration of Au singlet particles as a function of quenching gas flow rate at spark energy of 16 mJ and a spark repetition frequency of 60 Hz

The estimation of singlet particle concentration confirms the dependence of $N(t_f)$ on Q predicted by equation (2.2), which has been derived using a constant β and assuming that $N_0 \gg N(t_f)$. The slope (i.e., $\frac{2}{\beta V_{eff}}$) of the best-fitted straight line through the measurements indicates that the product βV_{eff} is 5.93×10^{-20} m^6 s^{-1}. This value is in line with a theoretical value for β that considers poly-dispersity as well as van der Waals forces between the particles (cf. Section S2.5.1 and S2.5.2 in the SI)[24,38]. Note that the image potential described by Ouyang *et al.*[24], can be neglected for our low concentration of charged particles (cf. Section S2.5.3). The value of β is in the order of 10^{-16} m^3 s^{-1} (cf. equation (S2.8)) based on the final (desired) size and an

estimated effective volume V_{eff} of 10^{-4} m³ corresponding to an adequate fraction of the volume of the spark chamber (cf. Figure S2.5).
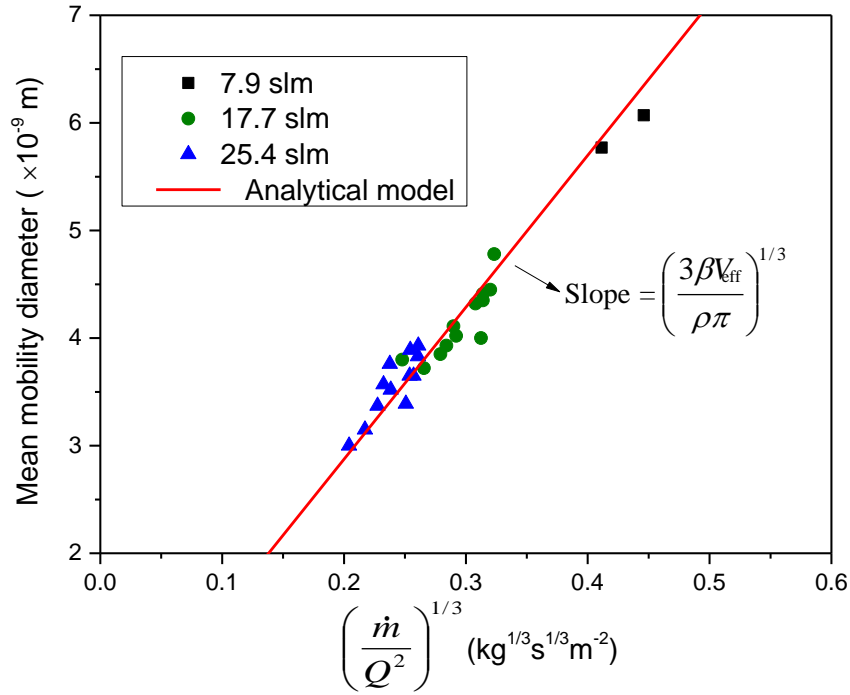
Figure 2.4 Mean mobility diameter of particles produce by spark ablation as a function of mass production rate and quenching gas flow rate.

Figure 2.4 shows the variation of the GMD with the term $(\frac{\dot{m}}{Q^2})^{1/3}$, which is linear according to equation (2.3). The slope (i.e., $(\frac{3\beta V_{eff}}{\rho\pi})^{1/3}$) of the best-fitted solid line through the experiments is 1.42×10^{-9} kg$^{-1/3}$ s$^{-1/3}$ m³. For a density of 19.3 g cm^{-3} for Au, the product βV_{eff} derived from this slope is 5.78×10^{-20} m⁶ s^{-1}, which is in good agreement with the value derived from Figure 2.3, and thus also with the theoretical value of β and an estimate of V_{eff} from the geometry of the confinement (see details in Section S2.5 in the SI). The value of V_{eff} has the highest uncertainty. For systems of similar geometry to that used here $V_{eff} \approx (0.2\sim0.3)V_{geo}$ is recommend, where V_{geo} is the geometric volume of the confinement (details are provided in Figure S2.5). Note that an error in V_{eff} within a factor of two would only alter the predicted d_p by 25%. Only the experimental values for particles having sizes below 7 nm are plotted in Figure 2.4, since larger particles are agglomerates (cf. Figure 2.2e) due to incomplete coalescence.

2.3 Discussion

2.3.1 Dependence of operating conditions on the particle size

In principle, the GMD of singlet particles produced via spark ablation (and any other similar gas-phase process) can be tuned from atomic clusters to any desired size by carefully varying the gas flow rate Q, and the mass production rate $\dot{m}$, which in turn is defined by the spark energy E and the spark repetition frequency f. Of course, full coalescence must be guaranteed by choosing a sufficiently high operating temperature and a high-purity carrier gas. In order to up-scale singlet NPs production process, one needs to increase the production rate $\dot{m}$. This can be achieved by numbering up the particle generators, with each of them delivering a mass rate in the order of 1 g h^{-1}.

The model can estimate the singlet size distribution at the outlet of the NP generator used in this work. The GMD is given by equation (2.3) while the lognormal size distribution has a self-preserving GSD of ca. 1.45[36]. Mobility size classification in the gas-phase can easily be applied for applications requiring narrower size distributions[39], although it should be noted that doing so will lead to substantial particle losses and will therefore limit scalability.

2.3.2 Deposition of well-defined singlets

Deposition of well-defined singlets on a substrate can yield films and materials of unique properties. Avoiding coalescence of the colliding particles on the substrate is a prerequisite to retain these properties. An elegant way to hinder coalescence is by coating the particles (e.g., with an oxidized layer) while they are still suspended in the gas (i.e., before deposition)[40,41]. For deposited uncoated particles, coalescence on the substrate can be avoided by keeping the surface coverage low enough (cf. Figure S2.8) or by manipulating charge effects between particles[4,42]. Low surface coverage is sufficient to improve the conversion efficiency of solar cells and photo catalysts for water splitting[43,44]. In the case of high surface coverage, where the particles are in contact, the substrate temperature should be controlled below the threshold temperature to avoid the coalescence of the arriving singlets[45,46]. Integrating gas-phase synthesis of singlets into wet-chemistry routes can also be used for supressing

particle collisions, since the collision rate is decreased by three orders of magnitude in the liquid phase, and opens numerous possibilities of further processing[47].

2.4 Conclusions

This chapter has introduced a general concept for continuous gas-phase synthesis of well-defined singlet particles in the nanometre size regime and even below that. The concept of promoting coalescence by using an ultrapure carrier gas and a sufficiently high temperature in the particle growth zone has been tested on the example of synthesizing Au NPs smaller than ca. 6 nm using spark ablation. For drastically quenched processes (e.g., spark ablation), the temperature in the particle growth phase can be decoupled from the localized vaporization, and can then be set to a value guaranteeing complete coalescence. Based on the drastic quenching rate of spark ablation, this study simply assumed a constant room temperature in the entire particle growth, and this temperature can lead to complete coalescence of colliding particles smaller than the critical size ca. 6 nm. To obtain singlet particles larger than this critical size, one can increase the temperature downstream of the material ablation by using a tube oven. In addition, this work has developed an analytical model that can be used to determine the combination of process parameters required to obtain singlet NPs of a desired size. The model can be applied to predict the size of singlet NPs (consisting of any material; cf. Figure S2.9 of the Ag singlets) produced by rapidly quenched gas-phase processes, provided isothermal conditions and uniform residence time in particle growth processes.

Combined with the various advantages of continuous gas-phase processes, including their scalability, high particle purity and high versatility (i.e., particles of virtually any inorganic composition or mixture that spark ablation enables), the method used as an example here (spark ablation) exhibits enormous flexibility for high-throughput production of ultrapure singlets, especially in the size regime below 10 nm. Consequently, the technique enables the advancement of NP synthesis and paves the way towards cost-effective fabrication of novel nanomaterials for numerous applications (cf. Section S2.8) [18,30,40,43,44,47−59].

2.5 Methods

2.5.1 Spark Discharge Generator

A spark discharge generator consists of a pair of electrodes with a gap of ca. 1 mm between them, connected to an electric circuit (see Figure S2.3 in the SI). The circuit induces microsecond pulsed discharges in a typical range of energy per spark from 0.3 to 200 mJ and a repetition frequency ranging from 0.1 to 25 kHz[18]. An inert gas flow continuously flushes the inter-electrode gap carrying away the produced vapors and particles to the point where they can be processed.

2.5.2 Experimental Set-up

The system consists of units for the generation (I), collection (II), and online size distribution measurement (III) of NPs (cf. Figure S2.3). The size distributions of the resulting aerosols are measured with a scanning mobility particle sizer (SMPS) system[60], consisting of a differential mobility analyzer (DMA), and a Faraday cup aerosol electrometer (AEM), but avoiding an aerosol neutralizer. The singlet NPss produced by the spark ablation were collected on TEM grids, using a custom-made electrostatic precipitator (ESP) placed at the DMA outlet. The DMA classifies the particles according to their mobility. The resulting NPs are led to the SMPS through a ca. 0.4-m long stainless steel tube with an inner diameter of 4 mm.

Supplementary Information in Chapter 2

Supplementary Information in Chapter 2 contains the following contents of material: experimental details, the features of materials ablation in gases, detailed explanation of governed final coagulation stage, the calculation of mass ablated by a single spark, the enhancement of coagulation rate, the example of critical size of singlets described in this report, the space-charge effect inside the DMA, the applications of these singlets and expanding to other materials by using the introduced concept, which accompanies this chapter in the following pages.

S2.1 Material ablation in high purity gas

Localized material ablation guarantees a high purity of the resulting NPs, and allows decoupling of the high temperature required for vaporization from the system temperature $T(t)$ where particle growth takes place[61–63]. This advantageous feature allows that the system temperature $T(t)$ can be regulated in order to ensure full coalescence of colliding particles to any desired size.

Another important feature of ablation processes is that they yield an initial particle or vapor atom concentration N_o that is several orders of magnitude higher than the final particle concentration $N(t_f)$, i.e., $N_o >> N(t_f)$[3]. This feature allows for analytical estimation of particle concentration evolution by excluding uncertainties at the early stage of particle formation process (*e.g.*, sticking probability, turbulence).

The quenching gas flowing through the electrode gap causes turbulent dilution of the initial vapours and particles. The time period t_d that the vapour atoms and particles spend in this dilution stage is much shorter than the total period of particle growth and thus can be reasonably neglected as discussed in Section S2.1.1 below.

S2.1.1 Turbulent dilution time t_d

The flow downstream the spark ablation can be split into two regions: the first that exhibits turbulent dilution and the second where particles reach the tube walls. To understand which process is more dominating, an estimate of the residence time of the particles is needed in each of these two regions. This section uses the simplest description that assuming the jet region flares out linearly in the x direction. The time-averaged turbulent flow pattern is a conical volume with an angle of roughly $20°$[64]. In the time-averaged turbulent jet, x is measured from the virtual origin of the cone and is proportional to the plume width $2r$ ($dr/dx \approx \tan(10°)$). The plume is developing before its boundaries reach the walls of the spark chamber. The inner diameter of the spark chamber is about 3.5 cm as shown below.
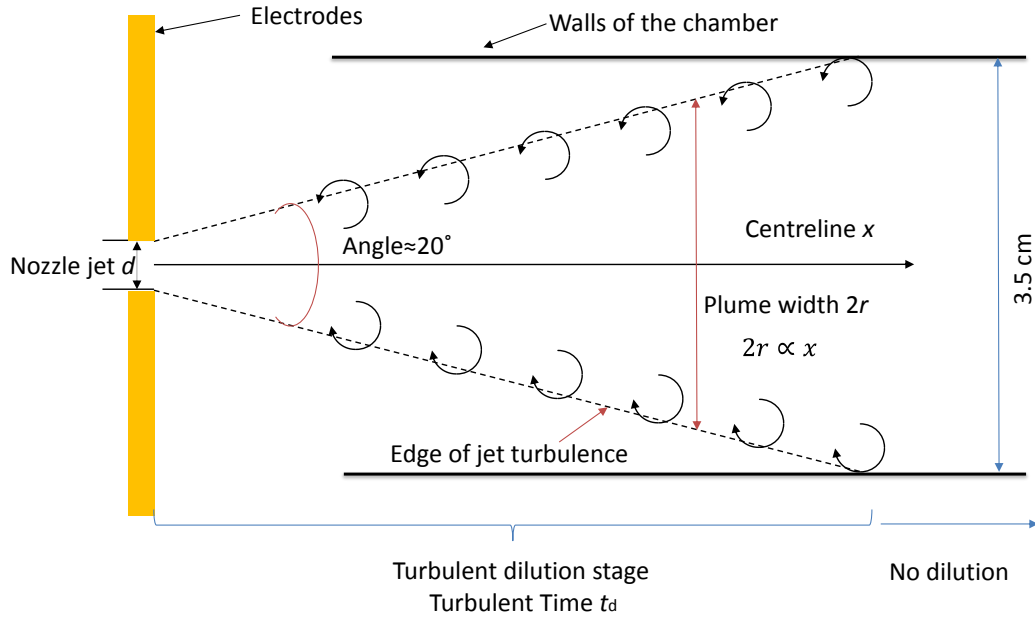
Figure S2.1 Illustration of the flow structure in the turbulent dilution and the convective region immediately downstream the spark discharge.

The travelling distance of the particles flowing through the jet is estimated as $L_t = r/\tan(10°) \approx 9.9$ cm, and the time of travel along the x direction is obtained by $dt = dx/u_a$. u_a is the time-averaged fluid speed at the centreline given by[64]:

$$u_a = U_0 \left(\frac{x}{x_0}\right)^{-1/2} \tag{S2.1}$$

where U_0 is the mean fluid velocity at the nozzle and x_0 is given by[64]:

$$x_0 = \frac{3}{4} \gamma_p d \tag{S2.2}$$

where d is the nozzle diameter, $\gamma_p = 7.67$ the empirical constant accounting for the growth rate of the jet region. Combining equation (S2.1), (S2.2) and $dt = dx/u_a$ yields $dt = \frac{\left(\frac{x}{x_0}\right)^{1/2}}{U_0} dx$ which can integrate for 0 to t_d and for x_0 to L the left and right hand of the equation, respectively, yields:

$$t_d = \frac{2}{3 U_0 x_0^{1/2}} \left(L_t^{3/2} - x_0^{3/2} \right) \tag{S2.3}$$

Using a quenching gas flow rate of 10 standard litres per minute (slm), the turbulent time is $t_d = 6.7$ ms. In contrast, the total residence time of particles in the apparatus is in the order of 1 s. Hence, the turbulent dilution time can be reasonably neglected. This further justifies the assumption of mass density conservation in the total period of particle growth.

S2.2 Final coagulation stage

Figure S2.2 shows the evolution of the number concentration predicted by equation (2.1) of Chapter 2 with time due to poly-disperse coagulation. In the case of the straight line on the logarithmic plot marked "$N_0 \to \infty$" was calculated using equation (2.2) of the main text assuming a constant coagulation kernel β calculated by the final particle size. The residence time V_{eff}/Q in equation (2.2) is simply replaced by the residence time t. Note that β has been enhanced by a self-preserving size distribution with respect to mono-disperse case. Given that the self-preserving value of the geometric standard deviation (GSD) is reached approximately after the time of the first reduction of the concentration by a factor of 10, equation (2.2) can also be applied for the case of arbitrary size distributions[65], if the enhancement factor of a certain poly-dispersity for β is considered with respect to the mono-disperse case[38]. At the moment the curves for different initial concentrations reach this straight line (i.e., $N_0 \to \infty$), the concentration becomes independent of the initial concentration.

However, β depends on the particle size. For a specific mass ablation rate, the particles grow approximately by a factor of two during the final coagulation stage due to the proportionality of particle size d_p with $N(t)^{-\frac{1}{3}}$. Because β does not vary more than a factor of two in the final coagulation stage, and its dominating value corresponds to the final size, a constant β can be assumed for a given mean particle size. Although assuming a constant β of a final particle size remains an approximation, Figure S2.2 illustrates a general feature: any coagulation process approaches a state where the particle concentration is independent of its initial value. If β spreads out to have high-variability with size, only the line for "$N_0 \to \infty$" will be curved. Regarding the poly-disperse coagulation, the end of the turbulent dilution period can be regarded as the initial state.

If the general concentration evolution of self-preserving size distribution according to Figure S2.2 is applied to this case, the time interval between 0.2 to 2 s is marked in the figure. It is seen that $N(t_f)$ evolves into the same line of $N_0 \to \infty$ regardless of its initial concentration, if only $N_0 \geq 10^{17}$ m^{-3}. It also becomes clear that the concentration $N(t_f)$ is mostly determined by the evolution of $N(t)$ during approximately the last decade of N-reduction or the last decade in time.
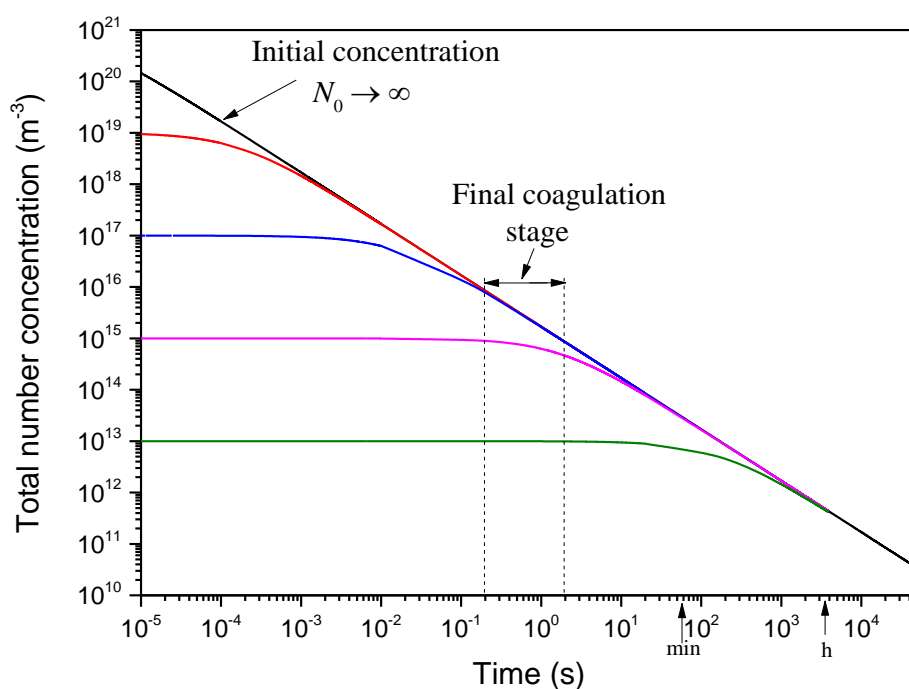
Figure S2.2 Particle number concentration versus time for various initial concentrations N_0. The constant coagulation kernel β used in these predictions accounts for poly-dispersity (i.e., self-preserving distribution) that increases the final particle size as compared to the mono-disperse coagulation (cf. equation (S2.8) and Section S2.5).

S2.3 Experimental materials

Figure S2.3 shows the details of the experimental setup described in the Methods section of Chapter 2. The system consists of components for the generation (I), collection (II), and online size distribution measurements (III) of NPs. Some acronyms are shown in the following subsection. The electrode rods (99.99% purity, Au and Ag, 3 mm diameter, 25 mm long) used in the spark generator were purchased

from MaTecK Material-Technologie Kristalle GmbH. For all experiments discussed in this paper, N₂ (purity 99.999%) is used as a carrier gas.
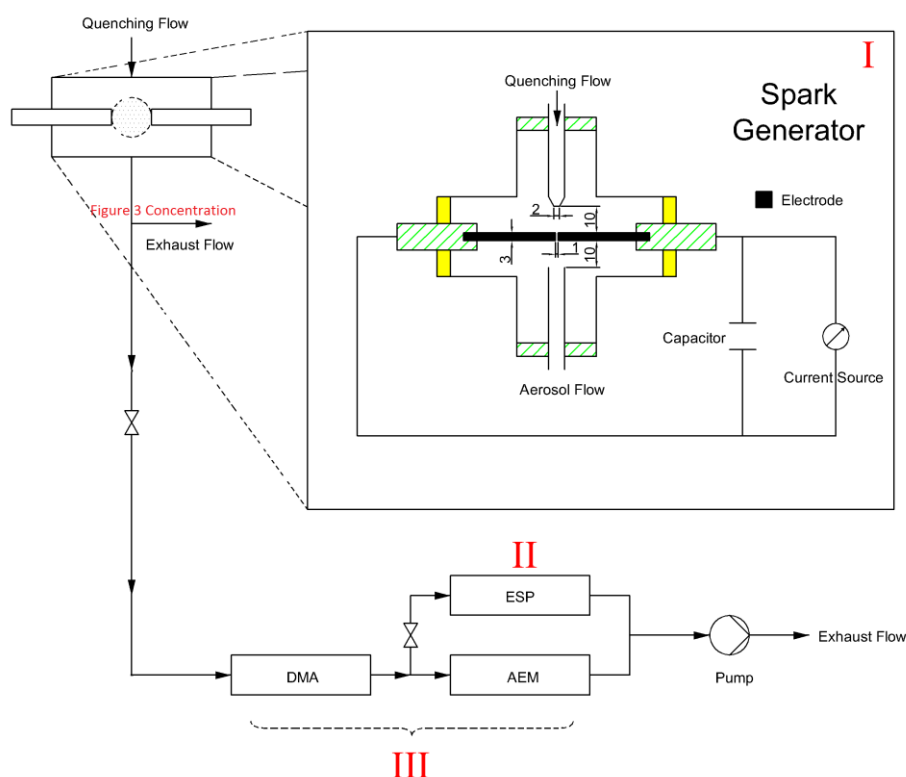
Figure S2.3 Schematic diagram of the experimental setup. All dimensions are expressed in mm. Key: DMA, differential mobility analyzer; ESP, electrostatic precipitator; AEM, aerosol electrometer.

The measured concentrations plotted in Figure 2.3 are derived from the geometric mean particle diameter measured by SMPS and assuming negligible wall losses, i.e., mass conservation per unit volume. The total particle concentration is therefore given by:

$$N_{\text{tot}} = \frac{6\dot{m}}{\rho d_{\text{p}}{}^3 Q} \tag{S2.4}$$

While particle size can reliably be determined by means of the SMPS, this is not the case for the absolute particle concentration, as explained below. An SMPS system, generally consists of a bipolar charger (also called "neutralizer"), a DMA and an AEM. However, a neutralizer would increase the residence time of the NPs before

entering the DMA by ca. 7 s. This long residence time leads to strong coagulation and agglomerate formation, which has been avoided in the present study.

Another reason for not using the bipolar charger is that it would not give any additional information given that a fraction of particles produced by spark ablation is already bipolarly charged. At the high particle concentration here, a bipolar charger would not deliver the well-defined equilibrium charge distribution which would be necessary for an absolute particle concentration measurement[66], providing another reason to avoid using it.

The bipolar charger is frequently omitted by people routinely characterizing particles produced by spark production. Tabrizi *et al.* have shown that the total particle size distribution can be represented by the charged particles directly from the spark discharge in a relative sense[60], which means that the mean sizes are correctly reflected. This can be explained by the fact that spark ablation produces a high concentration of ions of both polarities similarly to the bipolar charger. For small particles, it can easily be shown that this rule is even valid if charge equilibrium is not reached. It can also be shown that coagulational growth of these small particles alters the size distribution of the neutral particles and the charged particles in a very similar way. The detailed explanations for the aforementioned points are described in the next paragraph.

The measurement-based values for the charged particle concentration and the total particle concentration imply that the particle collision frequency of the charged particles among each other, leading to recombination and thus loss of charges, must be negligible during the period between completion of charging near the spark and measurement. Thus the charged particles retain their charge but grow in size by colliding with neutral particles. Originally, the relative charging probabilities corresponding to different sizes within the self-preserving distribution are proportional to d_p^2,[67] which would lead to the correct derivation of the total particle size distribution by the SMPS system regarding the position of the geometric mean size (see above). The growth of the geometric mean size of this self-preserving distribution by a factor c_{sp} retains the said proportionality with d_p^2, because each size within the self-preserving distribution grows by the same factor (this makes it self-

preserving). So the particles of a size d_{p1} grow to the size $d_{1g} = c_{sp}d_{p1}$, and the particles of a size d_{p2} grow to the size $d_{2g} = c_{sp}\ d_{p2}$. The corresponding initial charging probabilities $P_1 \propto d_{p1}^2$ and $P_2 \propto d_{p2}^2$ remain unchanged after growth[67], thus $P_{1g} \propto d_{p1}^2$ and $P_{2g} \propto d_{p2}^2$. The SMPS system assumes $P_{1g} \propto c_{sp}^2\ d_{p1}^2$ and $P_{2g} \propto c_{sp}^2\ d_{p2}^2$, but the ratio P_{1g}/P_{2g} remains constant, which means that the SMPS system indicates a distribution that correctly represents the geometric mean size but underestimates the total particle number concentration.

S2.3.1 Characterization methods

S2.3.1.1 Online characterization

The DMA selects particles based on their different sizes, whereas the AEM measures the current of all the singly charged particles downstream the DMA. This current, which depends on the aerosol flow rate used in the measurements, defines the concentration of charged particles of the polarity chosen by the DMA (negative in our case). Note that a bipolar charger typically used in SMPS system is not employed in the measurements. One reason is that the spark produced particles are already bipolarly charged and represent the total particle size distributions as explained above[60]. The other reason is that the longer residence time (ca. 7 s) inside a bipolar charger would have led to considerable agglomeration, which is desired to be avoided in the present study.

S2.3.1.2 Offline characterization

Transmission electron microscopy (TEM) and scanning electron microscopy (SEM) were used to image the particles produced by the spark generator. An electrostatic precipitator (ESP) was used to collect the charged particles produced by the spark generator and classified by the DMA. TEM grids (Van Loenen Instruments, S143-3 Q'foil 1.2/1.3 400 Cu) and substrates covered by TiO_2 layer were inserted into the ESP. The DMA voltage is fixed at the peak of the particle size distribution.

S2.4 Ablated mass per spark

Equation (2.4) from Chapter 2 is expanded below. The mass ablated from one spark can be estimated by the Llewellyn Jones model given by[35]:

$$\Delta m = \frac{\alpha E - 2\pi r_s^2 \sigma \tau (T_b^4 - T^4) - 2\pi r_s \tau k_e (T_b - T) - 2\pi r_s \tau k_a (T_b - T)}{c_{ps}(T_m - T) + c_{pl}(T_b - T_m) + H_m + H_e} \tag{S2.5}$$

where E is the energy per spark (J); α is the fraction of spark energy used for evaporation; c_{ps} and c_{pl} (J K^{-1} kg^{-1}) are the heat capacities of the solid and liquid material, respectively; τ (s) is the spark duration; r_s (m) is the radius of the spark channel; k_e and k_a (W m^{-1} K^{-1}) are the thermal conductivity of the electrode material and carrier gas (N$_2$, $k_a = 25.83 \times 10^{-3}$ W m^{-1} K^{-1}), respectively; T, T_b, and T_m (K) are the carrier gas temperature at 293 K (e.g., room temperature), the boiling and melting points of the electrode materials, respectively; H_m and H_e (J kg^{-1}) are the enthalpies of melting and vaporization of electrode materials; and σ (5.67×10^{-8} W m^{-2} K^{-4}) is the Stefan–Boltzmann constant. Values of all material properties (for Au and Ag) are given in Table S2.1.
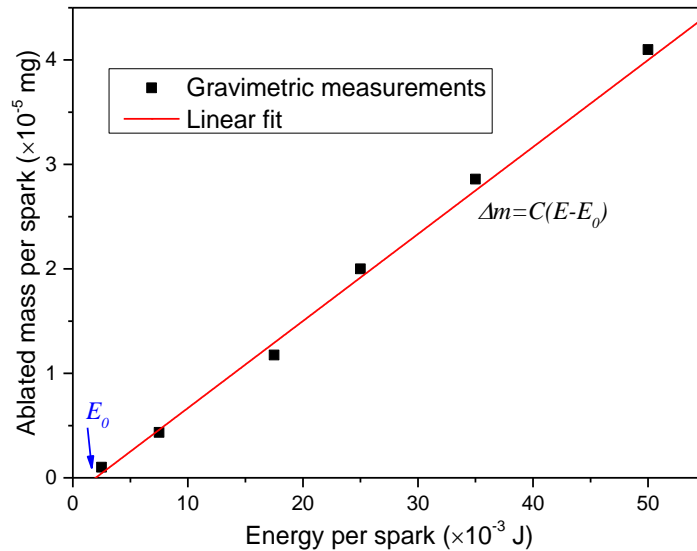
Figure S2.4 Mass ablated from the electrodes by one spark as a function of the spark energy.

Figure S2.4 shows measurements of the mass ablation by one spark from the electrodes as a function of the spark energies. The result is consistent with

proportionality between Δm and $(E\text{-}E_o)$. This justifies the fraction of energy α consumed for production of NPs is constant for identical gap distances. Note that the value of α is validated for all materials[60]. Threshold energy E_0 and the slope C are derived from the fitted straight line through the experiments shown in Figure S2.4. The material-dependent constant C_m is given by:

$$C_m = \frac{\alpha}{c_{ps}(T_m - T) + c_{pl}(T_b - T_m) + H_m + H_e} \tag{S2.6}$$

Its value is derived as 8.33×10^{-10} kg J^{-1} when $\alpha = 0.1819\%$ from the slope of the straight line in Figure S2.4, which can be considered independent of the electrode materials for identical spark gaps[35,60].

Table S2.1 Physical constants at atmospheric conditions

Parameters	Au	Ag
c_{ps} (J K^{-1} kg^{-1})	129	235
c_{pl} (J K^{-1} kg^{-1})	129	235
k_e (W m^{-1} K^{-1})	318	429
T_b (K)	3243	2435
T_m (K)	1337	1235
H_m (J kg^{-1})	6.37×10^4	1.04×10^5
H_e (J kg^{-1})	1.74×10^6	2.35×10^6

The threshold energy E_0 to produce NPs via spark ablation is:

$$E_0 = \frac{2\pi r^2 \sigma\tau(T_b^4 - T^4) + 2\pi r\tau k_e(T_b - T) + 2\pi r\tau k_a(T_b - T)}{\alpha} \tag{S2.7}$$

Assuming that the radius of spark ablated hot-spot r is 0.51 μm and the spark duration τ is 1.2 μs, equation S2.6 yields $E_0 = 1.98$ mJ. This value is in agreement, within experimental uncertainty, with the estimated value of 1.97 mJ by the fitted line through the experiments shown in Figure S2.4.

A newly developed switching circuit delivers high frequency sparks ranging from 1 to 25 kHz described in the previous publication[18]. Based on the data in Figure S2.4 at spark energy of 50 mJ and 25 kHz repetition frequency, the mass production rate $\dot{m} = \Delta m f$ of single synthesis unit can go up to 25 kHz × 4 × 10^{-5} mg × 3600 s = 3.6 g/h. Arrays of these units could be used to scale up production to any desired rate.

S2.5 Enhancement of the coagulation

This section discusses the enhancement of coagulation by both poly-dispersity, van der Waals forces between particles and image potentials between net neutral NPs and charged ones based on the Fuchs' interpolation model for mono-disperse particles.

S2.5.1 Mono-disperse coagulation

Fuchs' coagulation theory[23], gives the Brownian coagulation kernel β for particles of equal size as follows:

$$\beta = 8\pi D d_{\mathrm{p}} \left(\frac{d_{\mathrm{p}}}{d_{\mathrm{p}} + g} + \frac{8D}{c d_{\mathrm{p}}} \right)^{-1} \tag{S2.8}$$

Here D is the particle diffusion coefficient, g the transition parameter, and c a function of temperature and the mass of colliding particles (cf. Table S2.2). Equation (S2.8) assumes sticking at every collision and no forces between the particles. Because $N(t_{\mathrm{f}})$ is sensitive only to the value of β in the final coagulation stage as discussed above, equation (S2.8) can be used to estimate the constant value used in the model by using the desired particle size. For 5 nm particles, β is 3.29×10^{-16} m^3 s^{-1}.

S2.5.2 Poly-dispersity enhanced coagulation

Apart from the particle size, the coagulation rate depends on the broadness of the size distribution and inter-particle forces. The coagulation rate for aerosols having a log-normal size distribution is enhanced with respect to the mono-disperse case, so a correction factor has to be used to predict the resulting size distribution more accurately[26,38]. The fact that a coagulating aerosol rapidly approaches a self-preserving size distribution can be directly used to most cases, as the self-preserving distribution is certainly reached in the final coagulation stage (as indicated by the size distribution measurements shown in Figure 2.2f in Chapter 2), which is crucial for $N(t_{\mathrm{f}})$ and d_{p}. Based on this fact and assuming a singlet particle diameter of 5 nm,

β can be estimated as 3.94×10^{-16} m³ s⁻¹ [38], which is ca. 20% larger than the value given by equation (S2.8).

S2.5.3 van der Waals forces enhanced coagulation

Although previous studies have showed that the majority of particles produced by spark ablation is uncharged[60], ignoring inter-particle forces leads to inaccurate predictions of coagulational growth. For metal particles in the free molecular regime, the effect of van der Waals forces on coagulation is significantly pronounced[24]. For example gold particles in the size range of 1~20 nm require an enhancement factor of ca. 2.2 to match observations with predictions[24,68,69]. This factor is directly applied to the particle size distribution shown in Figure 2.2f and Figure 2.4 of Chapter 2. The coagulation kernel enhanced by van der Waals forces then increases to $\beta = 8.67 \times 10^{-16}$ m³ s⁻¹.

Table S2.2 Fuchs form of the coagulation kernel β

Coagulation Kernel[23]	$\beta = 8\pi D d_{\mathrm{p}} \left(\dfrac{d_{\mathrm{p}}}{d_{\mathrm{p}} + g} + \dfrac{8D}{c_{\mathrm{p}} d_{\mathrm{p}}} \right)^{-1}$
Diffusion coefficient[26]	$D = \dfrac{kTC_{\mathrm{c}}}{3\pi\mu d_{\mathrm{p}}}$
Cunningham slip correction factor[26]	$C_{\mathrm{c}} = 1 + \dfrac{\lambda_{\mathrm{m}}}{d_{\mathrm{p}}}(2.34 + 1.05\exp(-0.39\dfrac{d_{\mathrm{p}}}{\lambda_{\mathrm{m}}})$
Particle velocity [23]	$c_{\mathrm{p}} = (\dfrac{8kT}{\pi m})^{1/2}$
Transition parameter [23]	$g = \dfrac{1}{3 d_{\mathrm{p}} l}[(d_{\mathrm{p}} + l)^3 - (d_{\mathrm{p}}^2 + l^2)^{3/2}] - d_{\mathrm{p}}$
	$l = \dfrac{8D}{\pi c_{\mathrm{p}}}$

S2.5.3 Image potential enhancement

Image potential is frequently the dominant factor of potential energy in collisions between net neutral particles and charged particles[24]. Assuming that the concentration of the charged particles is ca. 1% of the total particle number concentration, the image potential term is only 2% of the concentration decay rate

determined by equation (2.1), and can therefore be neglected for even lower charge particle fraction in this work (considerably lower than the equilibrium state).

Dividing βV_{eff} derived from the data shown in Figure 2.3 and Figure 2.4 by this value, the estimated effective volume V_{eff} is around 66 cm³, which is 1/5~3/10 of the total geometric volume of the spark chamber (cf. Figure S2.5).
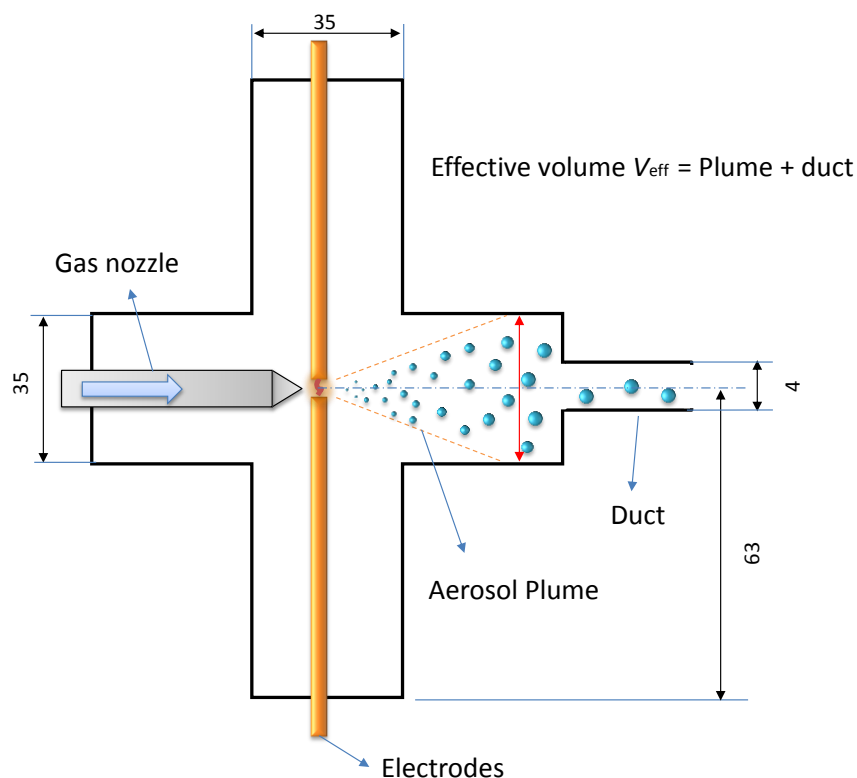
Figure S2.5 Schematic illustration of particle generator indicating the effective volume V_{eff} taken up by the aerosol plume within and downstream of the generator, where V_{eff} = (0.2~0.3)V_{geo}. Here the geometric volume of spark chamber V_{geo} is ca. 210 cm³. A gas nozzle is fixed upstream the gap between the two electrodes. The dimension of the duct, which was connected the spark chamber to the DMA, has an inner diameter of 4 mm and a length of 40 cm. All the detailed geometries are specified with the unit of mm.

S2.6 The critical size of singlets

Figure S2.6 shows the primary particles of agglomerates having a critical size of about 5~6 nm. Comparing with the particles shown in Figure 2.2, the size is the critical size for Au singlets. Subsequent collisions of particles larger than the critical

size lead to the formation of agglomerates due to incomplete coalescence. The primary particles embedded in the agglomerates are the smallest round units, which have typically been considered as the minimum attainable size for NPs.
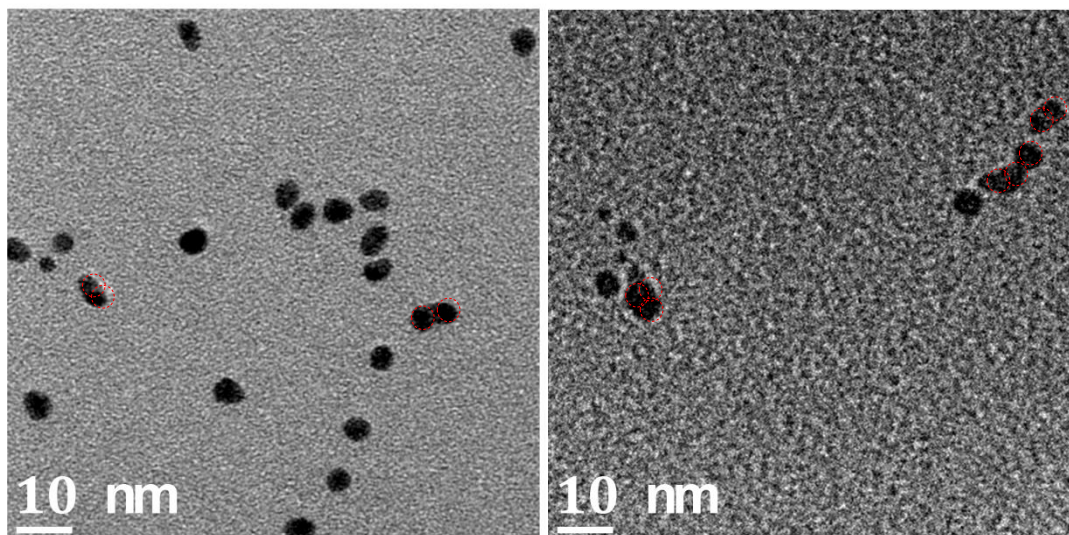
Figure S2.6 TEM images of the critical size of Au singlets. The particles were produced by spark ablation using spark energy of 16 mJ, repetition frequency of 60 Hz, and quenching gas flow rate of 10 slm. The aerosol particles with a flow rate 1.4 slm were sampled by using a custom-made electrostatic precipitator placed 5 cm downstream of the DMA.

S2.7 Space-charge effect inside the DMA

The space charge effect is caused by the cumulative effects of the electric fields of all of the charged particles in the classification region, which can influence the DMA measurements when particle concentration is significantly high. According to Camata *et al.*, space charge increases the electric field in the particle-free region near the aerosol inlet by a factor given by[37]:

$$f_{sc} = 1 + \frac{Ne}{\varepsilon_0 V} G_F \tag{S2.9}$$

where N is the concentration of charged particles, e the elementary charge, ε_0 electric permittivity, V the DMA voltage, and G_F is a flow rate and geometry dependent parameter. All the relevant parameters are summarized in the Table S2.3.

The space charge-effects are superimposed on the electrical field in the DMA, thereby changing the electrical mobility of the particles. Combining the work of Knutson *et al.*[70], and Camata *et al.*[37], the electrical mobility of the particle classified by a DMA when consider the space charge effect can be expressed as[70]:

$$Z_{\text{psc}} = \frac{Z_{\text{p}}}{f_{\text{sc}}} \tag{S2.10}$$

where Z_{psc} and Z_{p} represent with and without considering the space charge effect inside the DMA, respectively.

Table S2.3 Quantities required in equation (S2.9).

Parameters	Expression or value	Note
ε_0 (F m^{-1})	8.85×10^{-12}	-
G_{F} (m^2)	$\frac{1}{4}r_2{}^2\left(1 - \left(\frac{r_a}{r_2}\right)^2\left(1 - \ln\left(\frac{r_a}{r_2}\right)^2\right)\right)$	-
r_1 (m)	0.935×10^{-2}	diameter of the inner electrode of DMA
r_2 (m)	1.936×10^{-2}	diameter of the outer electrode of DMA
r_a (m)	$\sqrt{\frac{\zeta}{1+\zeta}\left(r_1{}^2 + \frac{1}{\zeta}r_2{}^2\right)}$	-
ζ	$\frac{Q_a}{Q_{\text{sh}}}$	-
Q_a (slm)	1	Aerosol flow rate
Q_{sh} (slm)	14	Sheath flow rate

Figure S2.7 shows the space charge effect on the mobility diameters for a concentration of negatively charged particles of 10^7 cm^{-3}. The mobility diameter increases from 1 to 4 % as the particle size decreases from 6 to 3 nm (i.e., the particle size range investigated in this work). The concentration derived from the measurements using the DMA and the AEM was always below this value. It should also be pointed out that Camata *et al.* have assumed a unipolarly charged aerosol[37]. Given that this work uses a bipolarly charged aerosol (as produced by spark ablation), these errors are overestimated because in this case the space charge only has an effect after the particles of the two polarities have been separated in the entrance zone of the DMA.
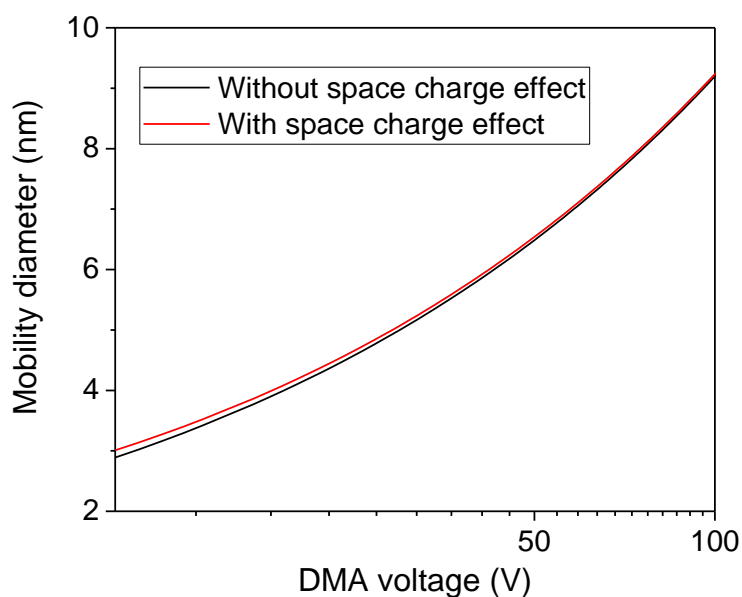
Figure S2.7 Mobility diameter of particles selected by the DMA as a function voltage applied between its two electrodes with (red line) and without (black line) consideration of the space charge effect. The concentration of charged particles in these calculations is assumed to be 10^7 cm^{-3}, which is the maximum charged particle concentration derived from the measurements of the DMA and AEM.

S2.8 Au singlet NPs deposited on substrates
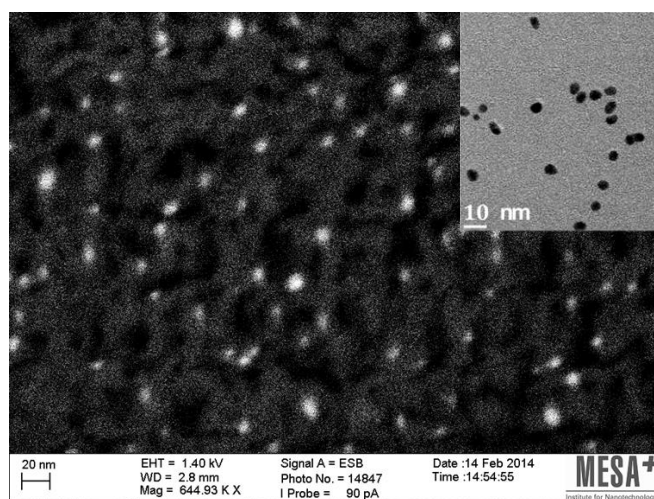
Figure S2.8 SEM Micrograph of Au singlet particles deposited on a well-defined TiO$_2$ layer substrate. The inset is the corresponding TEM micrograph. The conditions for particle production and collection are the same as those used in Figure S2.6.

Figure S2.8 shows SEM image of Au singlet NPs produced by spark ablation distributed on a TiO$_2$ coated substrate, which was placed in the custom-made

electrostatic precipitator at 5 cm downstream of the DMA. A represent TEM micrograph of particles is shown in the insert. The resulting singlet NPs can be used for many applications, particularly for nanocatalysis[71]. Properly altering the process variables of spark ablation permits the ultrapure singlet Au NPs to be deposited on the substrate, without using any chemical precursors or post-treatment[18].

S2.9 Production of Ag singlet particles

Figure S2.9 shows singlet Ag particles having diameters of ca. 6 nm produced by spark ablation. Due to the material properties, the production rate of Ag vapour atoms (Δmf) is ca. 1.4 times greater than that of Au (cf. equation (S2.5)), which leads to particles that are approximately 1.1 times larger when using the same experimental conditions with those used for the measurements shown in Figure 2.2f (cf. equation (2.5) in the main text) under the assumption of the same value of β for both metals. The same factor is determined by comparing the singlet particles of both metals from TEM micrographs, which shows TEM analysis is in agreement with predictions using equation (2.5) and equation (S2.5). The comparison between model prediction and TEM analysis justifies the simple model can be expanded to other materials.
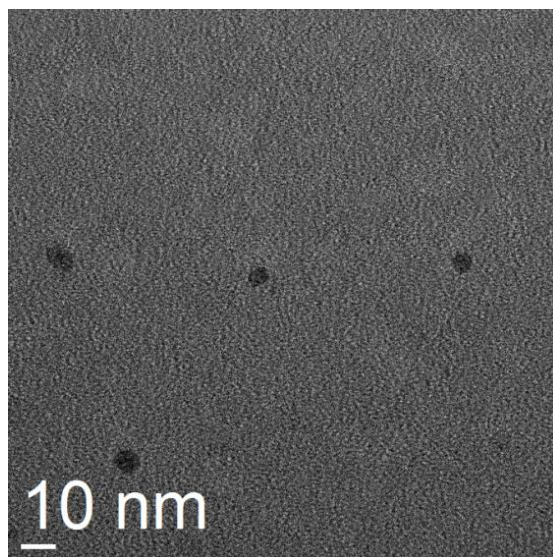
Figure S2.9 TEM image of Ag singlet particles produced by spark ablation. The particle producing and sampling conditions were the same as those used in Figures S2.6 and S2.8.

References

1   C. A. Charitidis, P. Georgiou, M. A. Koklioti, A.-F. Trompeta and V. Markakis, *Manuf. Rev.*, 2014, **1**, 1–19.

2   L. Mädler, H. K. Kammler, R. Mueller and S. E. Pratsinis, *J. Aerosol Sci.*, 2002, **33**, 369–389.

3   A. Gutsch, H. Mühlenweg and M. Krämer, *Small*, 2005, **1**, 30–46.

4   K.-T. Park, M. M. Farid and J. Hwang, *J. Aerosol Sci.*, 2014, **67**, 144–156.

5   S. E. Pratsinis, *Prog. Energy Combust. Sci.*, 1998, **24**, 197–219.

6   Y. Wang, J. Fang, M. Attoui, T. S. Chadha, W.-N. Wang and P. Biswas, *J. Aerosol Sci.*, 2014, **71**, 52–64.

7   J. Fang, Y. Wang, M. Attoui, T. S. Chadha, J. R. Ray, W.-N. Wang, Y.-S. Jun and P. Biswas, *Anal. Chem.*, 2014, **86**, 7523–7529.

8   C. Peineke, M. Attoui, R. Robles, A. C. Reber, S. N. Khanna and A. Schmidt-Ott, *J. Aerosol Sci.*, 2009, **40**, 423–430.

9   M. von Smoluchowski, *Z. phys. Chem*, 1917, **92**, 129–168.

10   T. Thajudeen, R. Gopalakrishnan and C. J. Hogan, *Aerosol Sci. Technol.*, 2012, **46**, 1174–1186.

11   R. Gopalakrishnan, T. Thajudeen and C. J. Hogan, *J. Chem. Phys.*, 2011, **135**, 054302.

12   R. Gopalakrishnan and C. J. Hogan, *Aerosol Sci. Technol.*, 2011, **45**, 1499–1509.

13   P. Biswas, C. Y. Wu, M. R. Zachariah and B. McMillin, *J. Mater. Res.*, 1997, **12**, 714–723.

14   A. B. Bourlinos, R. Herrera, N. Chalkias, D. D. Jiang, Q. Zhang, L. A. Archer and E. P. Giannelis, *Adv. Mater.*, 2005, **17**, 234–237.

15   F. E. Kruis, H. Fissan and B. Rellinghaus, *Mater. Sci. Eng. B*, 2000, **69-70**, 329–334.

16   J. Chun and D. L. Koch, *J. Aerosol Sci.*, 2006, **37**, 471–482.

17   F. E. Kruis, K. A. Kusters, S. E. Pratsinis and B. Scarlett, *Aerosol Sci. Technol.*, 1993, **19**, 514–526.

18   T. V. Pfeiffer, J. Feng and A. Schmidt-Ott, *Adv. Powder Technol.*, 2014, **25**, 56–70.

19   K. E. J. Lehtinen and M. R. Zachariah, *J. Aerosol Sci.*, 2002, **33**, 357–368.

20   V. A. Vons, L. C. P. M. de Smet, D. Munao, A. Evirgen, E. M. Kelder and A. Schmidt-Ott, *J. Nanoparticle Res.*, 2011, **13**, 4867–4879.

21   M. Alonso, *Rev. Metal.*, 1998, **34**, 413–415.

22   U. Uhrner, S. von Löwis, H. Vehkamäki, B. Wehner, S. Bräsel, M. Hermann, F. Stratmann, M. Kulmala and A. Wiedensohler, *Atmos. Environ.*, 2007, **41**, 7440–7461.

23   J. H. Seinfeld and S. N. Pandis, *Atmospheric Chemistry and Physics: From Air Pollution to Climate Change*, John Wiley & Sons, New York, 2006.

24   H. Ouyang, R. Gopalakrishnan and C. J. Hogan, *J. Chem. Phys.*, 2012, **137**, 064316.

25   M. Schmidt, R. Kusche, B. von Issendorff and H. Haberland, *Nature*, 1998, **393**, 238–240.

26   W. C. Hinds, *Aerosol Technology: Properties, Behavior, and Measurement of Airborne Particles*, John Wiley & Sons, New York, 1999.

27   L. Ravi and S. L. Girshick, *Phys. Rev. E*, 2009, **79**, 026408.

28   M. T. Swihart, *Curr. Opin. Colloid Interface Sci.*, 2003, **8**, 127–133.

29   N. S. Tabrizi, Q. Xu, N. M. Pers and A. Schmidt-Ott, *J. Nanoparticle Res.*, 2010, **12**, 247–259.

30   A. Anastasopol, T. V Pfeiffer, J. Middelkoop, U. Lafont, R. J. Canales-Perez, A. Schmidt-Ott, F. M. Mulder and S. W. H. Eijt, *J. Am. Chem. Soc.*, 2013, **135**, 7891–7900.

31   U. Banin, Y. Ben-Shahar and K. Vinokurov, *Chem. Mater.*, 2014, **26**, 97–110.

32   H. T. Chung, J. H. Won and P. Zelenay, *Nat. Commun.*, 2013, **4**, 1922.

33   A. Schmidt-Ott, *Appl. Phys. Lett.*, 1988, **52**, 954–956.

34   A. Schmidt-Ott, *J. Aerosol Sci.*, 1988, **19**, 553–563.

35   F. Llewellyn Jones, *Br. J. Appl. Phys.*, 1950, **1**, 60–65.

36   S. Vemury and S. E. Pratsinis, *J. Aerosol Sci.*, 1995, **26**, 175–185.

37   P. R. Camata, A. H. Atwater and C. R. Flagan, *J. Aerosol Sci.*, 2001, **32**, 583–599.

38   K. W. Lee and H. Chen, *Aerosol Sci. Technol.*, 1984, **3**, 327–334.

39   G. Biskos, V. A. Vons, C. U. Yurteri and A. Schmidt-Ott, *KONA Powder Part. J.*, 2008, **26**, 13–35.

40   T. Pfeiffer, P. Kedia, M. E. Messing, M. Valvo and A. Schmidt-Ott, *Materials*, 2015, **8**, 1027–1042.

41   J.-T. Kim and J.-S. Chang, *J. Electrostat.*, 2005, **63**, 911–916.

42   A. C. Zonnevylle, C. W. Hagen, P. Kruit and a. Schmidt-Ott, *Microelectron. Eng.*, 2009, **86**, 803–805.

43   T. V. Pfeiffer, J. Ortiz-Gonzalez, R. Santbergen, H. Tan, A. Schmidt-Ott, M. Zeman and A. H. M. Smets, *Energy Procedia*, 2014, **60**, 3–12.

44   M. Valenti, D. Dolat, G. Biskos, A. Schmidt-ott and W. A. Smith, *J. Phys. Chem. C*, 2015, **119**, 2096–2104.

45   E. Thimsen and P. Biswas, *AIChE J.*, 2007, **53**, 1727–1735.

46   P. Biswas and T. Elijah, *Aerosol Measurement: Principles, Techniques, and Applications*, John Wiley & Sons, New York, Third edit., 2011.

47   J. H. Byeon and Y.-W. Kim, *Nanoscale*, 2012, **4**, 6726–6729.

48   M. E. Messing, R. Westerström, B. O. Meuller, S. Blomberg, J. Gustafson, J. N. Andersen, E. Lundgren, R. van Rijn, O. Balmes, H. Bluhm and K. Deppert, *J. Phys. Chem. C*, 2010, **114**, 9257–9263.

49   J. H. Byeon and J.-W. Kim, *ACS Appl. Mater. Interfaces*, 2014, **6**, 3105–3110.

50   Y. H. Joe, W. Ju, J. H. Park, Y. H. Yoon and H. Jungho, *Aerosol air quaility Res.*, 2013, **13**, 1009–1018.

51   J. Byeon, D. Park and J. Kim, *Nanoscale*, 2015, **7**, 2271–2275.

52   J. H. Byeon and J.-W. Kim, *ACS Appl. Mater. Interfaces*, 2010, **2**, 947–951.

53   D. Z. Pai, K. Ken Ostrikov, S. Kumar, D. A. Lacoste, I. Levchenko and C. O. Laux, *Sci. Rep.*, 2013, **3**, 1221.

54   J. Feng, G. Biskos and A. Schmidt-Ott, *Sci. Rep.*, 2015, **5**, 15788.

55   J. Feng, L. Huang, L. Ludvigsson, M. E. Messing, A. Maisser, G. Biskos and A. Schmidt-Ott, *J. Phys. Chem. C*, 2016, **120**, 621–630.

56   V. A. Vons, H. Leegwater, W. J. Legerstee, S. W. H. Eijt and A. Schmidt-Ott, *Int. J. Hydrogen Energy*, 2010, **35**, 5479–5489.

57   N. A. Isaac, P. Ngene, R. J. Westerwaal, J. Gaury, B. Dam, A. Schmidt-Ott and G. Biskos, *Sensors Actuators B Chem.*, 2015, **221**, 290–296.

58   S. K. Sengar, B. R. Mehta, R. Kumar and V. Singh, *Sci. Rep.*, 2013, **3**, 2814.

59   J. H. Park, K. Y. Yoon, H. Na, Y. S. Kim, J. Hwang, J. Kim and Y. H. Yoon, *Sci. Total Environ.*, 2011, **409**, 4132–4138.

60   N. S. Tabrizi, M. Ullmann, V. A. Vons, U. Lafont and A. Schmidt-Ott, *J. Nanoparticle Res.*, 2009, **11**, 315–332.

61   H. Martinen and H. Tholl, *Zeitschrift für Naturforsch. A*, 1970, **25**, 430–439.

62   N. T. Jenkins and T. W. Eagar, *JOM*, 2003, **55**, 44–47.

63   A. E. Berkowitz and J. L. Walter, *J. Mater. Res.*, 1987, **2**, 277–288.

64   A. Bejan, *Convection Heat Transfer*, John Wiley & Sons, Hoboken, 2013.

65   F. S. Lai, S. K. Friedlander, J. Pich and G. M. Hidy, *J. Colloid Interface Sci.*, 1972, **39**, 395–405.

66   J. L. de La Verpilliere, J. J. Swanson and A. M. Boies, *J. Aerosol Sci.*, 2015, **86**, 55–68.

67   W. a. Hoppel and G. M. Frick, *Aerosol Sci. Technol.*, 1986, **5**, 1–21.

68   I. M. Kennedy and S. J. Harris, *J. Colloid Interface Sci.*, 1989, **130**, 489–497.

69   H. Burtscher and A. Schmidt-Ott, *Surf. Sci.*, 1985, **156**, 735–740.

70   E. O. Knutson and K. T. Whitby, *J. Aerosol Sci.*, 1975, **6**, 443–451.

71   B. D. Fraters, *PhD thesis*, University of Twente, 2015.

3. General Approach to the Evolution of Singlet Nanoparticles from a Rapidly Quenched Point Source

Among the numerous point vapour sources, microsecond-pulsed spark ablation at atmospheric pressure is a versatile and environmentally friendly method for producing ultrapure inorganic nanoparticles ranging from singlets having sizes smaller than 1 nm to larger agglomerated structures. Due to its fast quenching and extremely high supersaturation, coagulational growth already begins at the atomic scale at room temperature. Based on this knowledge, a simple semi-empirical yet versatile model is developed for predicting the size distribution of singlet particles as a function of the process conditions. The model assumes that a plume of a turbulent aerosol flow flares out from a concentrated point source, eventually reaching the walls of the confinement where a fraction of the particles is deposited. Despite the complexity of the entire process, the concentration and size evolution of particles can be adequately described by a first-order differential equation accounting for coagulation, turbulent dilution, and diffusional deposition to the walls. The model provides a simple and practical tool that can generally be used to design and control point vapour source reactors for the synthesis of singlets with tunable sizes.

Graphical Abstract
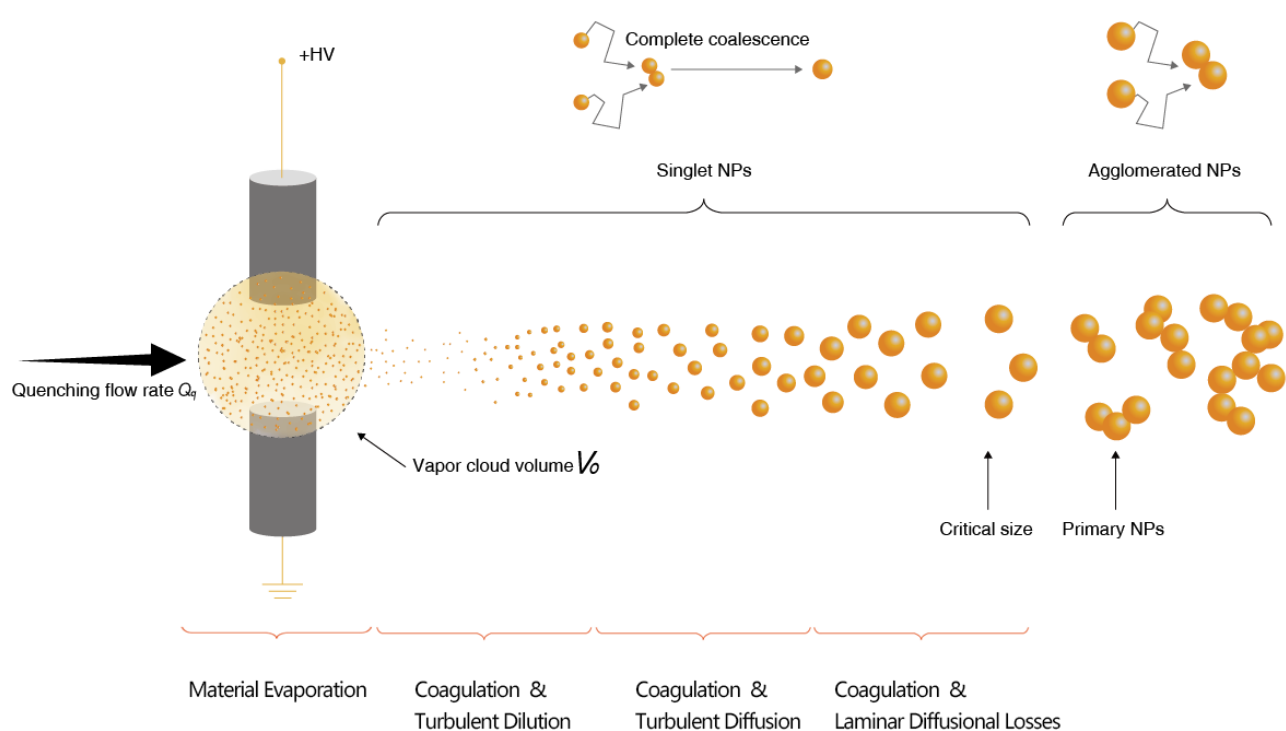
3.1 Introduction

Chapter 2 introduced a new concept of singlet production incorporated with an analytical model explaining their controllable sizes. This chapter proposes a general approach to describe the size distributions of singlet particles as a function of the process conditions.

Synthesis of high-purity inorganic nanoparticles (NPs) of well-defined size, composition and morphology is paramount for developing a number of novel materials and products[1–8]. To meet the required industrial scale fabrication rates, there is an urgent need to develop efficient and robust processes for the synthesis of NPs[9,10]. Microsecond-pulsed sparks, which is one of the typical examples of rapidly quenched point sources, repeatedly form between two electrodes at a frequency ranging from 10^{-4} to 25 kHz (cf. Chapter 5), locally heating the surface of the electrodes resulting in vapour clouds[11], which are drastically quenched and carried away by a high-purity gas flow. As a result, the vapours are brought to the carrier gas temperature T_c (typically room temperature) while an infinitely large supersaturation is reached through instantaneous quenching from boiling temperature to T_c (cf. Table S3.1 in the SI). This extremely high supersaturation pushes the critical nucleus size down to the atomic scale, indicating that irreversible coagulational growth starting from the atomic scale can be used to describe the particle growth process[12].

This chapter develops a simple yet versatile model that predicts the size distributions of the singlet particles produced from a rapidly-quenched point vapour source. The model assumes that the primary particle size is larger than the desired singlet size[16]. A discrepancy exists between theoretical predictions and measurements for the size of primary particles, as the coalescence process is extremely sensitive to the state of the particle surface, which can be significantly influenced by gas impurities even in or below the ppb range. To the best of our knowledge, the prior studies have not considered this point appropriately, and thus the theoretical prediction of the NP size

evolution in realistic systems presents a major impediment[13–15]. In this chapter, the chosen temperature in the particle growth phase guarantees complete coalescence to the desired size. Spark ablation, a representative point vapour source technique, its operating parameters are easily incorporated into the model.

The rest of this chapter is organized as follows: Section 3.2 describes the details of the experimental setup and the procedures used in the measurements, while Section 3.3 provides the theoretical framework for predicting the size distribution evolution of NPs. Section 3.4 explains the calibration of the model based on experimental observations. Model predictions are further compared to those of a simple analytical model proposed in Chapter 2 [17]. Section 3.5 discusses its easy applicability to acquire a complete size distribution. Finally, Section 3.6 concludes that this simple, yet versatile approach can generally be used to describe the evolution of particle size and concentration from rapidly-quenched point vapour sources such as spark discharges and laser ablation (see details in Section S3.1.1). This model provides a simple tool for designing and controlling spark generators or similar point sources with the aim of tuning singlet NP sizes.

3.2 Experimental section

Figure 3.1 shows a schematic layout of the experimental setup that consists of a spark discharge generator (SDG), an online particle size spectrometer and a particle collection system. The SDG has been used with a pair of Au rod electrodes (MaTecK GmbH, Germany; 99.99% purity) having a diameter of 3 mm and length of 25 mm. Results using Ag rod electrodes are also provided in the SI (cf. Figure S3.1). The two electrodes, placed ca. 1 mm apart are connected in parallel to a variable capacitor and a high voltage power supply (TECHNIX, Model: CCR10-R-750-OP) operated in a constant current mode[18]. A continuous N_2 gas flow (99.999% purity) ranging from ca. 2 to 45 standard litres per minute (slm) is passed through the inter-electrode gap. When the breakdown voltage of the carrier gas is reached, a short spark discharge (e.g., a few microseconds) forms in the gap. A high voltage probe is connected to an oscilloscope (HAMEG Instruments, Model HMO1024) for recording the breakdown voltage V_b and the spark repetition frequency f. The spark energy $E = 0.5 C_{ca} V_b^2$, is varied by changing capacitance C_{ca} from 3 nF to 31 nF.
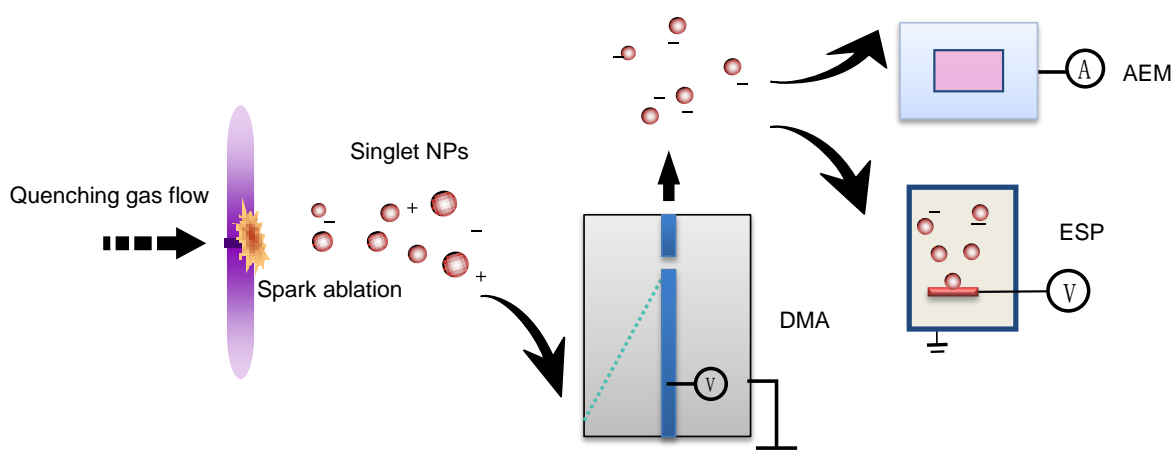
Figure 3.1 Schematic layout of the continuous gas phase NP synthesis setup. In brief, NPs formed in the spark generator are subsequently passed through a tube and size selected in the differential mobility analyser (DMA) before their concentration is measured by the Faraday cup aerosol electrometer (AEM), or deposited on a desired substrate by the electrostatic precipitator (ESP).

A custom-made scanning mobility particle sizer (SMPS) consisting of a differential mobility analyser (DMA), and an aerosol electrometer (AEM) was used for online measurements of the size distribution of the resulting particles[19,20]. Transmission electron microscopy (TEM) was used to image the resulting NPs. An electrostatic precipitator (ESP) placed downstream of the DMA was employed to collect particles from the monodisperse aerosol flow onto TEM grids (Van Loenen Instruments, S143-3 Q'foil 1.2/1.3 400 Cu)[21]. A Philips CM30T microscope operated at 300 kV with a LaB6 filament as the electron source was used for the imaging, whereas high-resolution TEM (HRTEM) images were acquired with a JEOL 3000F equipped with a field emission gun.

3.3 Theoretical framework

Figure 3.2a shows a schematic representation of the evolution of the singlet and agglomerated NPs from a rapidly-quenched point vapour source, while Figure 3.2b illustrates the dominant mechanisms at each stage (i.e., from Stage *A* to *D*) before the particles become agglomerates. A vapour cloud is drastically quenched while carried away by the gas flow. The instantaneous quenching of the vapour cloud from boiling

temperature to T_c (i.e., ranging from 10^6 to 10^9 K s^{-1}) [22–24], causes an infinitely large supersaturation (cf. SI Section S3.1). As a result, the extremely high supersaturation pushes the critical nucleus size to the atomic range which subsequently grow to NPs by particle-particle collisions and sticking; a process commonly referred to as coagulation[12]. Turbulent dilution and/or particle diffusional losses to the walls of the generator also affect the evolution of the particles downstream of the point source when the plume reaches the walls of the confinement (i.e., at stages *B*, *C* and *D* shown in Figure 3.2b).

The surface of pure particles in the size range of a few nanometres is liquid-like[30–32]. For Au NPs suspended in a high-purity gas as in the present case, this is valid even at room temperature. This liquid-like surface of the NPs is attributed to the contraction of the ionic radii of the atoms with reduced coordination number[33], as confirmed by a number of other publications[32–35]. The liquid-like surface of very small NPs (with diameters < 5 nm) is essential to achieve complete coalescence and its driving force is surface energy minimization, associated with dangling bond density and distribution. Furthermore, the Laplace pressure inside sufficiently small NPs, which is inversely proportional to the particle size, permits plastic deformation through the slip of edge defects, thereby promoting further coalescence. The NPs therefore completely coalesce to form larger spherical singlet NPs upon collision with each other. Once the NP diameter exceeds a critical size D_c, further inter-particle collisions lead to non-spherical fractal-like agglomerates (cf. Figure 3.2a). For a given material, D_c depends on temperature[14,36–40], and can therefore be influenced by the carrier gas temperature T_c. Due to the fast quenching, T_c can easily be decoupled from the material ablation (cf. Stage *A* in Figure 3.2b), which allows easy control over D_c (singlet size ranges from one single atom to D_c.).
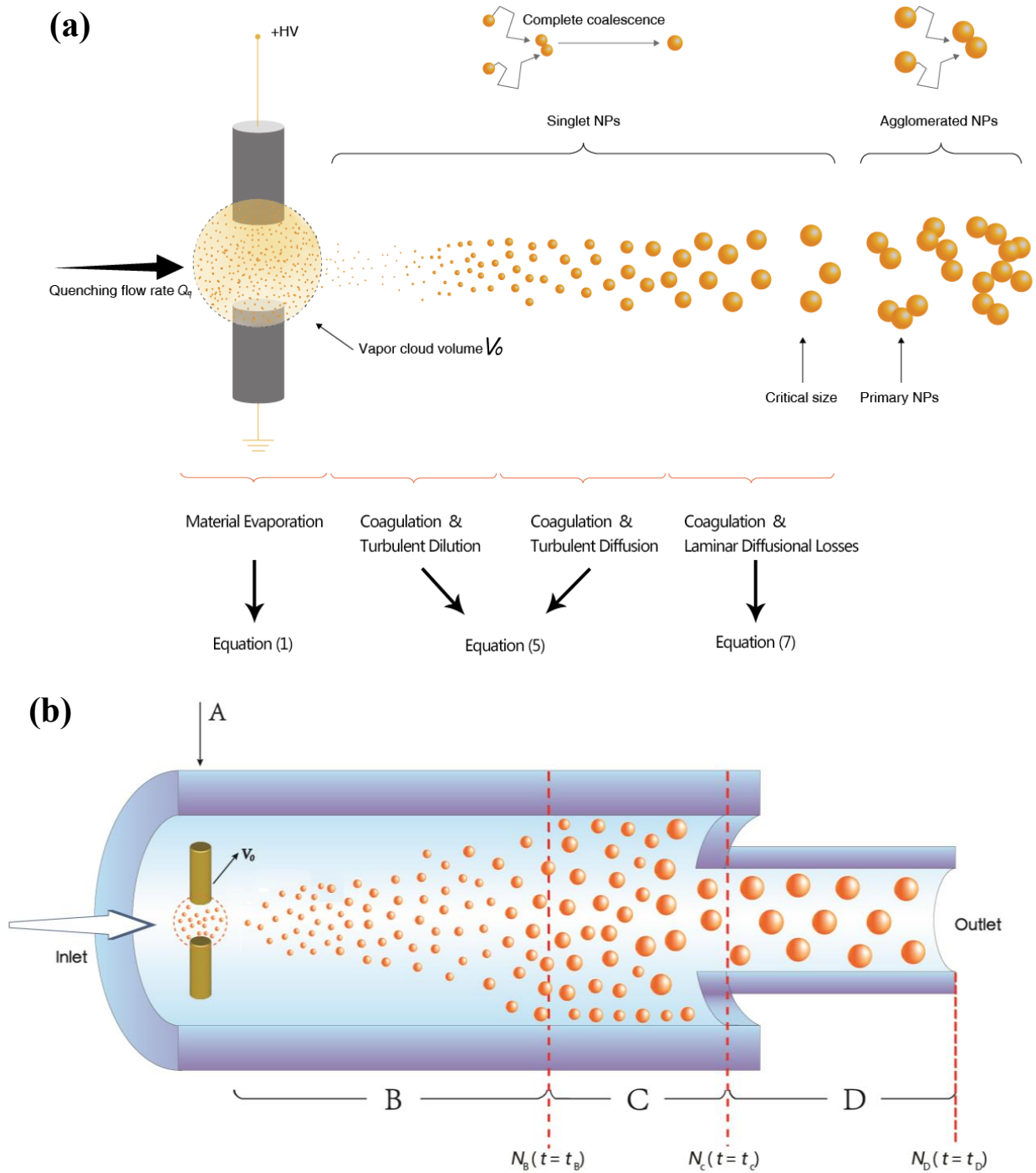
Figure 3.2 (a) Schematic representation of the particle formation process from a rapidly-quenched point source. (b) The main stages of the process considered in the model. Vapour clouds having initial volume V_0 produced from a rapidly-quenched point source (Stage *A*) are subsequently carried away and cooled down to form NPs. The dominant mechanisms defining the size and concentration of the particles immediately after the point source are coagulation and turbulent dilution (Stage *B*).

When the aerosol plume eventually reaches the boundaries of the generator, the dominant mechanisms become coagulation and turbulent diffusional deposition (Stage *C*; within the generator). At the exit of the generator, the particle growth process can be stopped by diluting the aerosol[25], by depositing the NPs onto a substrate with a low coverage[26,27], by suspending them in a liquid for further processing[28], or by coating them rapidly[29], depending on the applications. In other cases, including that of the present experimental setup, a tube is added to the generator to lead the aerosol to a device for characterizing. Stage *D* is therefore added, where diffusional losses and further coagulation take place under laminar flow conditions.

The model is based on the following main assumptions:

(1) At $t = 0$ (initial conditions) the temperature of the vapour cloud is equal to that of the carrier gas temperature T_c and remains constant throughout the particle growth process (cf. Figures S3.2 and S3.3 as well as Section S3.9.1 in the SI).

(2) The selected temperature T_c guarantees full coalescence for the desired singlet size.

(3) The sticking probability for every particle-particle collision is unity, and therefore particle growth is solely determined by collisions[12,41].

The entire concentration evolution of the particles can be described by Smoluchowski's coagulation theory at T_c [12], extended to account for turbulent dilution and particle diffusional losses onto the walls[42]. The whole process can be presented by four distinct stages. Stage *A* represents a point vapour source that produces a certain amount of vapour atoms. Subsequently, in Stage *B* (i.e., the expanding plume), the size and concentrations of the forming NPs are determined by coagulation and turbulent dilution, while Stage *C* and *D* where the aerosol flows in a confinement, the size distribution is determined by coagulation and diffusional losses to the walls.

3.3.1 Material ablation (Stage *A*)

A single spark or laser produces a vapour cloud (Stage *A*) as shown in Figure 3.2b. Based on the energy balance, the mass of the produced vapour can be expressed as a function of the energy per spark *E* or the applied energy for other similar processes as follows[43]:

$$\Delta m = C_{\mathrm{m}}(E - E_0) \tag{3.1}$$

where E_0 is the threshold energy for particle production and the material-dependent constant C_{m}. Values of all the physical parameters related to C_{m} and E_0 in equation (3.1) are given in Tables S3.2, S3.3 and S3.4 in the SI. It is worthwhile to point out that C_{m} constitutes an empirical factor α, which is determined by gravimetrical analysis (cf. Table S3.2 in the SI). Its value of α = 0.18% can generally be used for similar setups, independent of the gap distance (cf. Table S3.5, SI). Using this constant α for C_{m} in equation (3.1) has been shown to hold for a wide range of materials[18].

3.3.2 Particle Concentration Evolution

In Stage *B* (i.e., close to the point source) an aerosol plume flares out from a point vapour source[44]. As a result, apart from the coagulational term that scales the concentration decay rate d*N*/d*t* with the square of the number concentration *N(t)*, a turbulent dilution term has to be introduced[42,45]. Since the plume is not in contact with the chamber walls yet, diffusional deposition does not have to be considered at this stage. Assuming for the moment that all particles have the same size, the decay rate of particle number concentration can therefore be described by:

$$\frac{\mathrm{d}N}{\mathrm{d}t} = -\frac{1}{2}\beta N^2 - K_{\mathrm{dl}}N \qquad (t \leq t_{\mathrm{B}}) \tag{3.2}$$

where N (m-3) is the particle concentration at time t (s), β the size dependent coagulation kernel (m3 s-1), K_{dl} the dilution rate (s-1) and t_{B} the turbulent dilution time (s) which is of the order of millisecond[17].

As turbulence occurs on length scales much larger than the particle-particle distance, it has no relevance for the particle-particle collision rate[41]. The coagulation kernel required to solve equation (3.2) is given by:

$$\beta = 8\pi\varphi\varepsilon D d_{\mathrm{p}} \left(\frac{d_{\mathrm{p}}}{d_{\mathrm{p}} + g} + \frac{8 P_{\mathrm{st}} D}{c_{\mathrm{p}} d_{\mathrm{p}}} \right)^{-1} \tag{3.3}$$

where φ is a correction factor accounting for the fact that the aerosol is polydisperse[46]; ε is an enhancement factor due to van der Waals forces between particles[47]; D is the particle diffusion coefficient; g is the transition parameter; c_{p} is particle velocity as a function of temperature and colliding particle masses, and P_{st} is the sticking probability after collisions. All the parameters in equation (3.3) are provided in Table S3.6 in the SI.

The coagulation kernel β depends on the sizes of both colliding particles, and its effective value rises when the broadness of the particle size distribution widens. This increase is due to the fact that particles differing in sizes have a higher collision probability than equally sized ones, because the bigger particles provide a larger target for smaller ones having higher diffusion coefficients. Under this circumstance, the geometric standard deviation (σ_{g}) of particle size distribution is constrained to the self-preserving value[48]. Accordingly, Lee and Chen have shown that the coagulation rate for a polydisperse aerosol of arbitrary size distribution can be expressed by the monodisperse model introducing an enhancement factor[46]. The data below confirms that the self-preserving distribution is reached already when the particles grow to ca. 5 nm.

In practice, van der Waals forces between particles enhance the coagulation rate through increased collision frequency[47]. Particularly, for metal NPs in the free molecular regime, the effect of van der Waals forces becomes considerably pronounced[41], and according to prior work[49], the associated enhancement factor can be regarded as a constant when the particle size is below 20 nm.

The dilution term $K_{\mathrm{dl}}N$ in equation (3.2) is negligible due to rapid coagulation at high concentration in Stage B. Equation (3.3) yields values of β that are in the order of 10^{-16} m^3 s^{-1} for particle diameters ranging from 1 to 100 nm. In addition, aerosol dynamic

simulations suggest that K_{dl} in equation (3.2) is in the range of 10 s^{-1} [42,45]. As turbulent dilution time t_B is a few ms, $N(t = t_B) \approx \frac{2}{\beta t_B}$ is estimated to be in the order of 10^{19} m^{-3} [17]. Considering the aforementioned approximations, the dilution rate K_{dl} is only ca. 1% of the term $\frac{1}{2}\beta N$ in equation (3.2), which can therefore be simplified to:

$$\frac{dN}{dt} = -\frac{1}{2}\beta N^2 \quad (t \leq t_B) \tag{3.4}$$

Particle diffusional losses to the walls become important in Stage *C* where dilution stops. In a turbulent flow system, a thin laminar boundary layer is formed near the confinement wall where diffusion becomes the only transport mechanism onto the walls[50]. This layer separates a turbulently well-stirred volume with the concentration $N(t)$ from the wall where the concentration is zero. Based on this information, the diffusional transport rate is driven by a concentration gradient $N(t)$, and thus introduce a linear term $K_{df1}N$ to account for the diffusional losses under turbulent flow[51]. The particle number concentration continues to fall rapidly due to coagulation, eventually reaching a point where K_{df1} is comparable with $\frac{1}{2}\beta N$. In this case, the linear term representing diffusional losses cannot be neglected and equation (3.4) can be modified to:

$$\frac{dN}{dt} = -\frac{1}{2}\beta N^2 - K_{df1}N \quad (t \leq t_C) \tag{3.5}$$

Equation (3.5) can be used to describe the particle concentration evolution along the entire particle generator in both Stages *B* and *C*. Because K_{df1} is an order of magnitude smaller than K_{dl} (negligible compared to $\frac{1}{2}\beta N$ in Stage *B*), adding the term $K_{df1}N$ in equation (3.4) is not detrimental to the concentration evolution. The turbulent diffusional deposition of the particles to the walls (Re ranges from 4000 to 20000 and these estimations are shown in Section S3.8.1 in the SI) is difficult to determine theoretically. For this reason, K_{df1} is estimated by fitting the measurements to the model as discussed in Section 3.4 further below.

The residence time in the particle generator, including Stages B and C, is expressed by

$$t_{\mathrm{C}} = \frac{V_{\mathrm{eff}}}{Q_{\mathrm{q}}}$$ (3.6)

where Q_{q} is the quenching gas flow rate and $V_{\mathrm{eff}} = x_{\mathrm{g}} V_{\mathrm{geo}}$ ($x_{\mathrm{g}} \leq 1$) is the characteristic volume that the main aerosol flow occupies in the confinement of geometry volume V_{geo}. For systems of similar geometry (e.g., $V_{\mathrm{geo}} = 210$ cm³) as used in this work $x_{\mathrm{g}} = 0.2$ is recommended, which is based on the estimations from the analytical model in Chapter 2 and the best fit to the measurements in the simulations. As an alternative, V_{eff} of any arbitrary chamber can be determined empirically by turning the point source on (or off) and measuring the time the concentration takes to rise (or fall) to the 50% value at the outlet.

Measuring the size distribution of the particles immediately downstream of the particle generator has practical constraints with the most important being the tube connecting the particle generator to the SMPS system. In Stage D (i.e., the stage where the evolution of the particles takes place in the tube), the coagulation and particle diffusional losses continue. Laminar flow (Re $\approx$ 500) conditions allow one to directly derive the relation between the concentrations at the inlet and outlet of the output tube ($N_{\mathrm{C}} = N(t_{\mathrm{C}})$ and $N_{\mathrm{D}} = N(t_{\mathrm{D}})$), respectively). In analogy to equation (3.5), Stage D can be described by:

$$\frac{\mathrm{d}N}{\mathrm{d}t} = -\frac{1}{2}\beta N^2 - K_{\mathrm{df2}}N \quad (t_{\mathrm{C}} < t \leq t_{\mathrm{D}})$$ (3.7)

where K_{df2} is a laminar diffusional loss rate derived from Fick's second law (see Section S3.7 in the SI) given by:

$$K_{\mathrm{df2}} = \frac{2\pi \left(\frac{DQ_{\mathrm{a}}}{L_{\mathrm{tube}}}\right)^{1/2}}{d_{\mathrm{tube}}{}^2} \exp\left(\frac{\pi L_{\mathrm{tube}} d_{\mathrm{tube}}{}^2}{4Q_{\mathrm{a}}} K_{\mathrm{df2}}\right)$$ (3.8)

where d_{tube} and L_{tube} are the diameter and the length of the tube through which the aerosol flows, and Q_{a} is the aerosol flow rate. The residence time in Stage D is calculated by $\pi L_{\mathrm{tube}} d_{\mathrm{tube}}{}^2/4Q_{\mathrm{a}}$.

The number of vapour atoms produced by each spark or laser, i.e., the product of the initial atom concentration N_0 and the initial volume of the vapour cloud V_0 is an important parameter determining the final particle size, which is related to the mass Δm of vapour produced by each spark or other patterns of pulsed heating sources:

$$N_0 V_0 = N_A \frac{\Delta m}{M} \tag{3.9}$$

Here N_A is Avogadro's number (mol^{-1}), and M is the molar weight (Kg mol^{-1}). The unknown parameter V_0 can be derived by matching the measurements with equation (3.5) as described in Section 3.4.

3.3.3 Evolution of Particle Size

In Stage B, the reduction of NP mass per unit volume is driven only by dilution (cf. Section S3.8 in SI), and therefore one can write:

$$\frac{d(\rho \frac{\pi}{6} d_{\overline{m}}^3 N)}{dt} = -K_{dl} N \rho \frac{\pi}{6} d_{\overline{m}}^3 \qquad (t \leq t_B) \tag{3.10}$$

where $d_{\overline{m}}$ is the diameter of average mass and ρ is the particle material density. As the distribution is log-normal and σ_g can be estimated by the constant self-preserving value $\sigma_g = 1.35$ as shown below[52], $d_{\overline{m}}$ and the geometric mean diameter d_p can be converted by the Hatch-Choate relation (i.e., $d_{\overline{m}} = d_p \exp(1.5 \ln^2 \sigma_g)$) for any log-normal size distribution (cf. Section S3.8 in the SI). Equation (3.10) is also valid for replacing $d_{\overline{m}}$ by d_p because the proportionality constant (i.e., $\exp(1.5 \ln^2 \sigma_g)$) can be cancelled out.

Likewise, the reduction of mass per unit volume due to diffusional losses in Stages C and D are given by:

$$\frac{d(d_p^3 N)}{dt} = -K_{df1} N d_p^3 \qquad (t_B \leq t \leq t_C) \tag{3.11}$$

$$\frac{d(d_p^3 N)}{dt} = -K_{df2} N d_p^3 \qquad (t_C \leq t \leq t_D) \tag{3.12}$$

From equations (3.2), (3.5), (3.7), (3.10), (3.11) and (3.12), it follows that:

$$\frac{\mathrm{d}d_\mathrm{p}}{\mathrm{d}t} = \frac{1}{6}\beta N d_\mathrm{p} \qquad (t \leq t_\mathrm{D}) \tag{3.13}$$

Equation (3.13) is therefore valid for all the stages. Considering that the initial size (i.e., $d_\mathrm{p}(t = 0) = d_\mathrm{A}$) is the atomic diameter, equations (3.5) (3.7) and (3.13) can be solved to predict the singlet particle size distributions as well as the total particle concentration.

To summarize, material vaporization (cf. Stage *A*) is described by the evaporation model (cf. equation (3.1)). In Stage *B*, the initial atomic vapour plume coagulates so rapidly that the simultaneous turbulent dilution can be neglected with regard to the number concentration and size evolution. In Stage *C*, where the emerging aerosol cloud reaches the wall of the confinement, turbulent wall deposition must be considered besides coagulation. Despite the complexity of the process, the evolution of NP concentration in Stages *B* and *C* can be described by a differential equation (equation (3.5)) with a square term accounting for coagulation and a linear one accounting for turbulent deposition. In Stage *D* linking the generator to the characterizing device, coagulation and diffusional losses continue under laminar flow conditions (cf. equation (3.7)). The mean size evolution can be expressed by equation (3.13) for all stages.

3.4 Calibration of the model and its interpretations

Figure 3.3 shows NP size distributions measured by the SMPS at a specific point (the distance from the DMA to the exit of spark generator is 40 cm) downstream of the spark discharge generator at different quenching gas flow rates. An increase of the quenching flow drastically decreases the size of particles as a result of the decreased residence time t_D and the inhibited coagulation[45]. By further increasing the quenching flow rate, the particle size would ultimately get down to atomic size[53,54]. The equally sized vapour atoms with $\sigma_\mathrm{g} = 1$ gradually agglomerate to approach an increasingly broader size distribution (cf. σ_g in Table 3.1) that reaches the self-preserving size distribution[52,55]. As the value of σ_g of 1.35 is normally obtained, when forcing a lognormal function to fit the data, which can be taken as a general feature

for the case of complete coalescence. The larger value of σ_g for particle sizes above ca. 5 nm (cf. Table 3.1) signals the onset of agglomeration.
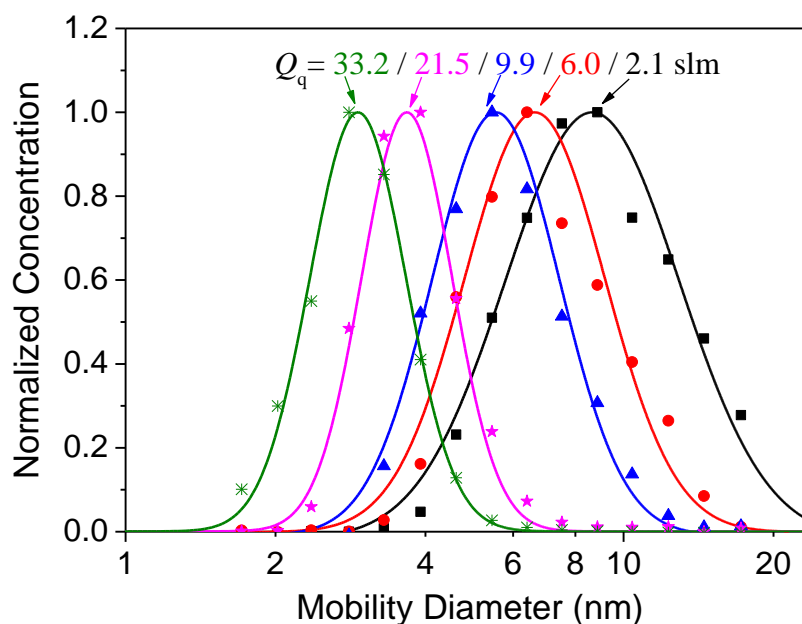
Figure 3.3 Measured size distributions of particles produced by spark ablation using various quenching gas flow rates and fixed energy per spark (15.74 mJ).

Table 3.1 Mean mobility diameter and geometry standard deviation of the size distributions of the particles generated by spark ablation at different quenching gas flow rates. The values of different parameters correspond to the measurements shown in Figure 3.3. d_p denotes the mean mobility diameters, which are presented in Figure 3.4.

Q_q (slm)	d_p (nm)	σ_g
33.2	2.8	1.25
21.5	3.6	1.25
9.9	5.4	1.37
6.0	6.3	1.39
2.1	8.0	1.43

Figure 3.4 shows the dependence of the mean particle diameter on the quenching flow rate at a fixed spark repetition frequency and energy per spark, together with TEM images of collected NPs in some cases (cf. insets). The numerical solution for d_p (Q_q) (red dashed line) derived from equations (3.5), (3.7) and (3.13), taking into account equations (3.8) and (3.9), yields the best fit to the measurements in Figure 3.4 for an initial vapour cloud volume of $V_0 = 56$ mm^3. Interestingly, this predicted volume is corroborated by emission spectroscopy experiments performed by Geretovszky's group[56]. Model predictions consider $V_0 = 56 \pm 23$ % mm^3 (grey shaded region) and the values of K_{df1} are independently derived from Figure 3.6.
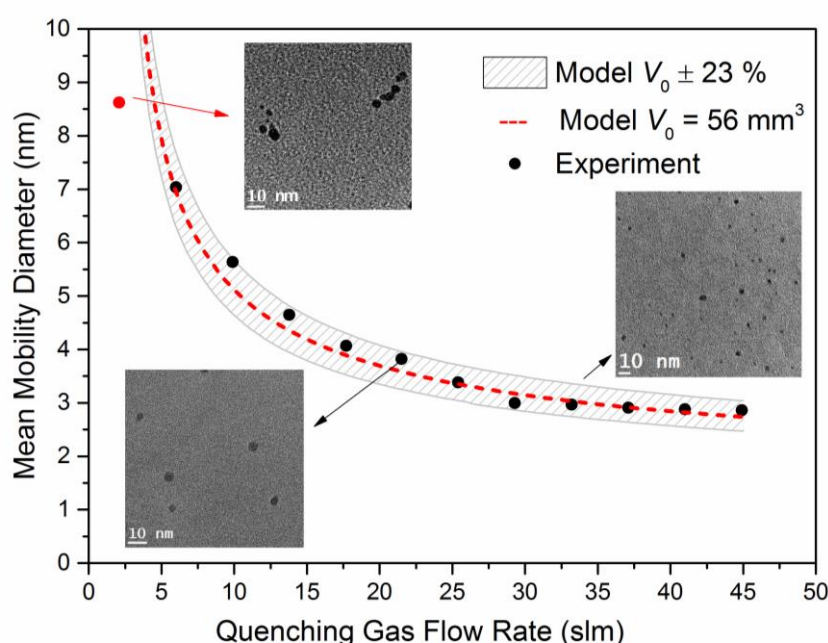
Figure 3.4 Measured and predicted mean mobility diameters of the particles produced by spark ablation, together with model predictions using $V_0 = 56$ mm^3 that best fits the data, as a function of quenching gas flow rates. For all measurements presented here, the spark energy (15.74 mJ) and repetition frequency (60 Hz) stay constant. Model predictions consider $V_0 = 56 \pm 23$ % mm^3 (grey shaded region) and values of K_{df1} are independently derived from the fit shown in Figure 3.6. The insets display TEM images of the particles produced at specific conditions.

The mean size of singlet NPs ranges from ca. 2 to 6 nm based on the TEM images, which are associated with the size distributions shown in Figure 3.3. At gas flow rates higher than 6.0 slm, the NPs are fully coalesced singlets having diameter smaller than

ca. 6 nm (cf. insets). For a given material, the critical size of the singlets (i.e., primary particle size) can be controlled by the carrier gas temperature T_c. Therefore, singlet sizes ranging from a single atom to any desired diameter can in principle be obtained by adjusting T_c that is high enough to guarantee complete coalescence[57]. At a flow rate of 2.1 slm and at room temperature T_c, the formation of agglomerates consists of primary particles of this critical size (D_c), indicating that particles larger than ca. 5 nm do not fully coalesce upon collisions. The measurement corresponding to the agglomerated particles in Figure 3.4 (red colour) was not included in the calibration of our model.
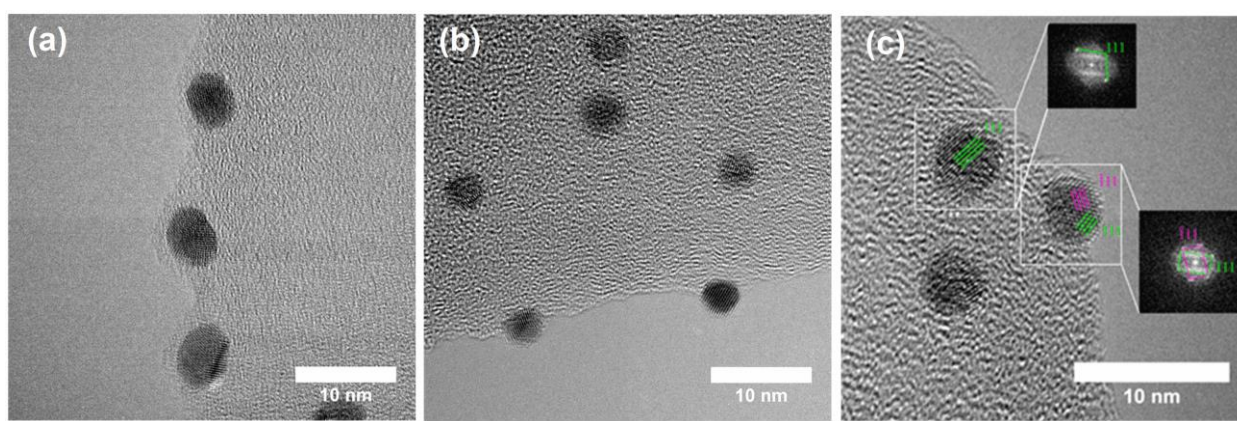
Figure 3.5 High-resolution TEM (HRTEM) images (a, 15 slm; b and c, 30 slm) of the resulting particles, which were collected at spark energy of 15.76 mJ and spark repetition frequency of 60 Hz. Facets are indicated by solid lines in (c) and its insets show fast Fourier transform (FFT) patterns of the selected particles.

High-resolution TEM (HRTEM) images show the shape and configuration of the resulting particles and confirm the crystal structure of gold. Particles shown in Figure 3.5a were sampled at a flow rate of 15 slm, while particles in Figure 3.5b and 3.5c were deposited at a flow rate of 30 slm. The spark energy and repetition frequency are the same with those described in Figure 3.4 (i.e., E = 15.74 mJ, and f = 60 Hz; Using the same spark energy and repetition frequency, the particles shown in Figure S2.6 were collected at a gas flow rate of 10 slm). Figure 3.5a and 3.5b contain a mixture of particles that are single crystalline and polycrystalline. The particles shown in Figure 3.5b are slightly more spherical than in Figure 3.5a with some of them being more elongated. Formation of these spherical shaped NPs is driven by solid-state diffusion[58], mainly by relocation of surface atoms. The insets in Figure

3.5c show fast Fourier transform (FFT) patterns of the selected particles that indicate lattice directions <111> and <$\bar{1}$11> with a reciprocal spacing of 0.24 nm. This correlates well with the lattice distance of the {111} planes in crystalline gold (0.236 nm).

Physical and chemical stability are critical issues, mainly in nanosuspensions (colloids) but also in aerosols. The physical stability issues include agglomeration, crystal growth and the change of crystallinity state. In the present case, the singlet particles are deposited onto a TEM grid, where they are immobilized due to van der Waals forces. This avoids further agglomeration. At room temperature, the crystallinity state of most metallic NPs remains unchanged, even though their surface is liquid-like[30,58]. The chemical stability of singlet particles depends on their material and storage conditions, namely the temperature and the surrounding medium. In the case of dry gas-phase deposition, Au NPs exposed to the atmosphere remain highly pure and crystalline, as confirmed by HRTEM measurements (cf. Figure 3.5).
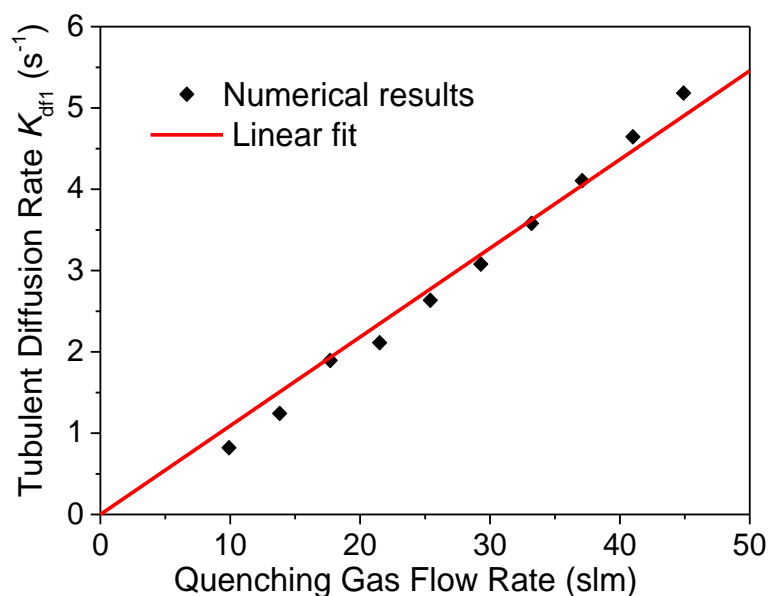
Figure 3.6 Turbulent diffusional deposition rate K_{df1} as a function of quenching gas flow rate Q_q. The empirical value K_{df1} is derived from matching the model (i.e., the solution of equations (3.5) and (3.7)) with the measured particle mean sizes at different quenching gas flow rates.

The turbulent diffusional loss rate K_{df1} is estimated by fitting the model (i.e., the solution of equations (3.5) and (3.7)) to the measurements of particle mean sizes

under different quenching gas flow rates. Figure 3.6 shows the resulting particle diffusional loss rate as a function of the quenching gas flow rate. The measurements fit well to a linear relation for all sizes, which is in line with the findings from Nomura et al[50]. The diffusional loss rate increases with the flow rates as a result of the enhanced turbulent deposition (in other words, the increase of the diffusional loss rate is equivalent to the increase of turbulent intensity), which yields:

$$K_{df1} = \gamma \, Q_q \tag{3.14}$$

with $\gamma = 6.534 \times 10^3$ m^{-3}. This linearity holds in general, as long as the gas flow is turbulent[50]. To generalize to any point vapour source for NP production, γ can be calibrated by measuring the particle number concentration or particle size only at two different quenching gas flow rates for any reactor geometry. In contrast to the complication of turbulent deposition[52], the observation of the linearity shown in equation (3.14) represents an elegant means of expressing wall deposition of NPs in a turbulent flow despite its simplicity.
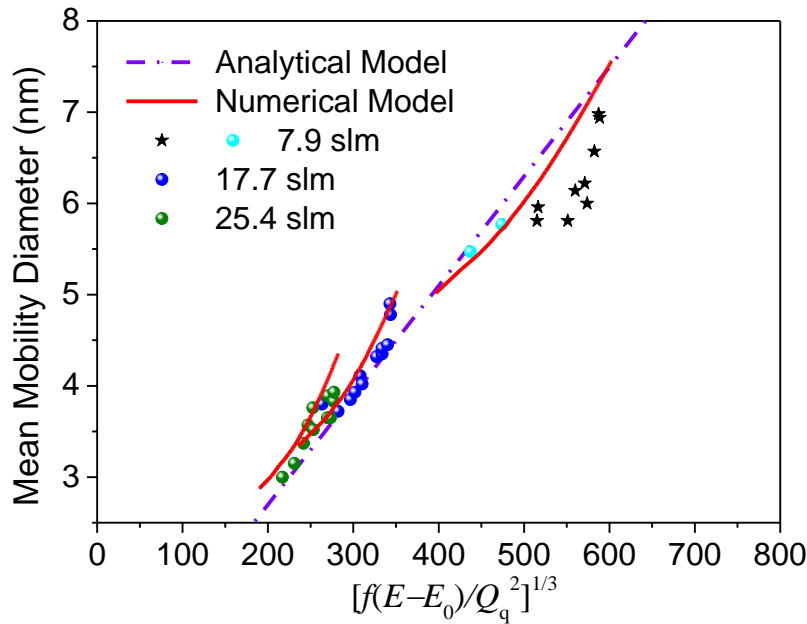
Figure 3.7 Particle size dependence on $\left(\frac{f(E-E_0)}{Q_q^2}\right)^{1/3}$ that includes the operating spark energy (E-E_0), repetition frequency f, and quenching gas flow rate Q_q. Solid circles and stars denote experimental measurements where singlets and agglomerates are observed respectively. Red curves and the dot-dashed line represent the model described in this chapter and the analytical model proposed in our recent work[17].

Figure 3.7 shows how the particle size varies with $(\frac{f(E-E_0)}{Q_q^2})^{1/3}$, where E is the energy per spark that in turn directly determines the ablated mass Δm (cf. equation (3.1)) and E_0 (cf. Table S3.2) is a threshold spark energy for producing NPs[17], f the spark repetition frequency and Q_q the quenching gas flow rate. The reason for using this coupled term in the horizontal axis is that it is approximately linearly related to the particle mean sizes[17]. The dots in Figure 3.7 correspond to the measured sizes at different operating conditions, while the curves are the predictions from the model described in Section 3.3. For a fixed Q_q, the predictions are derived by varying the spark energy E and/or repetition frequency f. E is related to the initial conditions as shown in equation (3.1) and (3.9), whereas f influences the concentration evolution of the particles downstream of the point source as described by Tabrizi et al[18]. In addition, the product of f and Δm (cf. equation (3.1) connects f and E) gives the mass production rate $\dot{m}$ of the NPs from the point source. Therefore, Figure 3.7 also simply implies the relation between the mass production rate and particle size. Predictions using the analytical model proposed in the earlier work are also shown in Figure 3.7[17]. This analytical model assumes negligible particle diffusional losses and a constant coagulation kernel from which the size of singlet particles can be estimated. The discrepancy between the analytical model and the model described in this work becomes apparent for large values of Q_q. This is because higher quenching flows lead to increase of particle losses by turbulent diffusion (cf. dependence of K_{df1} with Q_q in Figure 3.6), which is not captured by the analytical model.

For any given material, the size of the vapour cloud V_0 depends on the ablated mass per spark. An empirical relation is derived from back calculating the size and concentration evolution of NPs (as shown in Figure 3.7) from equations (3.5), (3.7) and (3.13) for different values of Δm (corresponding to different applied spark energy) determined by equation (3.1), and it is expressed as:

$$V_0 = \frac{\delta}{M} \Delta m^{\eta} \tag{3.15}$$

where η and δ are derived from the fit yielding 0.75 and 1.76 $m^3 Kg^{1-\eta} mol^{-1}$. Equation (3.15) thus suggests that $V_0 \propto \Delta m^{0.75}$, which means that the initial vapour cloud volume varies almost linearly with the vapour mass emitted per spark. This finding is

88   **Size Evolution** |

plausible because a linear dependence is found according to the ideal gas law (cf. Section S3.9, SI). Combining equations (3.9) and (3.15) yields that $N_0 \propto E^{0.25}$, which means that the initial atomic concentration in the vapour cloud is relatively insensitive to the energy per spark.

3.5 Discussion

Model simulations only consider the influence of gas flow rate and energy per spark on particle size distributions, whereas the influence of frequency is coupled with spark energy through the spark power $P_s = 2E f$, the product of current and the breakdown voltage (both can be obtained experimentally). It is also assumed that the spark repetition is high enough to guarantee homogeneous aerosol particle concentrations downstream of sparks, while very low spark repetition frequency will lead to divergence of this model.

3.5.1 Analytic solution for Stage D

Stage D is described by an analytical approach of practical value, which to the best of our knowledge have not been presented before. This model is applied to predict the mean particle size at the exit of particle generator. Equation (3.7) gives the concentration evolution in Stage D, i.e. in a tube under laminar flow conditions. For applications where such a tube is necessary, as in our case for driving the aerosol particles from the generator to characterizing system, an expression relating the size $d_p(t_C)$ and concentration $N(t_C)$ of the particles at the outlet of the generator to the measured size $d_p(t_D)$ and concentration $N(t_D)$ is desired. Since particle growth during Stage D is generally not enormous, there is only a minor error by assuming constant K_{df2} and β[17], which enables an analytical solution of equation (3.7) for $N(t_C)$:

$$N(t_C) = \frac{N(t_D)}{\exp\left(-K_{df2}\dfrac{\pi d_{tube}{}^2 L_{tube}}{4Q_a}\right)(1+\omega) - \omega} \tag{3.16}$$

where $\omega = \frac{\beta N(t_D)}{2K_{df2}}$, is a dimensionless quantity. K_{df2} is calculated by equation (3.8) on the basis of the measured $d_p(t_D)$, whereas the residence time t can be expressed as

$\frac{\pi d_{\text{tube}}{}^2 L_{\text{tube}}}{4Q_{\text{a}}}$. Combining equations (3.13) and (3.16), one can integrate equation (3.13) from $d_{\text{p}}(t_{\text{C}})$ to $d_{\text{p}}(t_{\text{D}})$, which leads to the desired relation between the size at the outlet of the particle generator:

$$d_{\text{p}}(t_C) = \frac{d_{\text{p}}(t_{\text{D}})}{\left(\dfrac{\omega}{\dfrac{1}{\exp\left(K_{\text{df2}}\dfrac{\pi d_{\text{tube}}{}^2 L_{\text{tube}}}{4Q_{\text{a}}}\right) - 1} - \omega} + 1\right)^{\frac{1}{3}}} \tag{3.17}$$

Equation (3.17) expresses the particle size $d_{\text{p}}(t_{\text{C}})$ at the inlet of an arbitrary duct as a function of w, $d_{\text{p}}(t_D)$ at the outlet and the particle penetration $P_{\text{p}} = \exp(-K_{\text{df2}}\, t)$. The expression of P_{p} is grossly simplified compared to the Gormley-Kennedy equation (cf. Figure S3.6 in the SI) [59]. Note that the dimensionless quantity $\frac{\beta N\,(t_{\text{D}})}{2K_{\text{df2}}}$ introduced here expresses the importance of coagulation with respect to diffusional losses.

As can be seen from the above, under conditions similar to our experiment, the analytical results for the correction factor $N(t_{\text{D}})/N(t_{\text{C}})$ based on the values of K_{df2} and β at time t_{D} only varies between ca. 3% from the respective value derived numerically with the correct size dependence of these quantities. For the size correction, $d_{\text{p}}(t_{\text{D}})/d_{\text{p}}(t_{\text{C}})$, the analytical value reproduces the numerical one only within an error of about 0.1%.

It is worthwhile pointing out that equations (3.16) and (3.17) are evidently valid at any point in Stage D as long as this point is placed downstream of the generator exit. This purpose can be easily achieved by adjusting the tube length L_{tube}. With respect to the geometry of the tube, one can simply adjust the calculation of the residence time accordingly in equations (3.16) and (3.17).

3.5.2 Recipes for applying the model

Summarizing the findings examined above, these parameters required for applying the model are determined by the following recipes. First, one needs to determine the mass of vapour emitted per spark or other similar rapidly-quenched point sources

such as laser ablation through equation (3.1) and numerically solve the equations (3.5) and (3.13). The complex problem of turbulent particle wall loss is tackled by inserting the turbulent diffusion rate K_{df1} as a value proportional to the flow rate Q_q according to equation (3.14), where the proportionality constant γ has to be calibrated by two different quenching gas flow rates. The initial concentration N_0 is given through equation (3.9) by the initial vapour volume V_0 empirically determined by equation (3.15). The value for N_0 remains an approximation, but the present observations imply that it is relatively insensitive to the energy applied to the point source. On the other hand, the concentration evolution continues in the form of equation (3.7) under a well-defined laminar flow, where K_{df2} is calculated by equation (3.8). For the entire process, the coagulation kernel β is calculated by equation (3.3). The residence time t_D is expressed through the quenching gas flow rate Q_q and an effective volume V_{eff} according to equation (3.6) in addition to the time flowing through Stage D (e.g., $\pi L_{tube} d_{tube}^2 / 4 Q_a$)

3.5.3 Acquisition of a complete particle size distribution

The experiment shows that the size distributions can all be fitted to log-normal functions and that the self-preserving geometric standard deviation of 1.35 is reached at the size of ca. 6 nm, which can be regarded as a general feature. For sizes above this value it will therefore be safe to assume the self-preserving value, if complete coalescence is guaranteed. Narrower distributions are observed below ca. 6 nm, as equally sized atoms exist in the initial vapour cloud. Log-normal distributions for the type of processes treated here allow the simple approach of monodisperse coagulation to be used when the coagulation kernel β is appropriately modified (cf. equation (3.3)). As the value of σ_g of 1.35 is normally obtained, when forcing a lognormal function to fit the data, which can be taken as a general feature for the case of complete coalescence. The larger value of σ_g for particle sizes above ca. 5 nm (cf. Table 3.1) signals the beginning of agglomeration. In order to obtain the complete singlet size distribution, one can thus safely assume a well-defined log-normal distribution having the geometric standard deviation of self-preserving value (in most cases) and the mean size calculated by equation (3.13).

The recipes summarized above can be generally used to predict the particle size distribution from any highly quenched point vapour source, and to design the particle generator. It is relevant for applications, where the growth process is stopped, for example, by dilution, or by rapid deposition of the particles onto a substrate, or by combining with wet chemistry routes to open a great number of new possibilities[28], or by rapid coating[29]. In other cases, including the experimental setup employed here, a tube is added to the generator to lead the aerosol to a device for characterization (cf. Figure 3.2b). Coagulation and wall losses continue within Stage *D*. Here, well-defined laminar flow conditions lead to easily modelling this stage (cf. equations (3.7) and (3.13)). As a practical alternative, analytical formulae are also derived for Stage *D* (cf. equations (3.16) and (3.17)). To our best knowledge, such expressions have not been presented in this form before and involve a new dimensionless quantity $\frac{\beta N(t)}{K_{df2}}$ expressing the importance of coagulation with respect to diffusional losses. The analytical results have been shown sufficiently accurate and can be applied to predict the particle size distribution at the generator exit in combination with the SMPS measurements (cf. equation (3.17)).

3.6 Conclusions

This chapter has described a simple, yet versatile approach that can generally be used to describe the evolution of particle size and concentration from rapidly-quenched point vapour sources such as spark discharges, which should have high enough spark repetition frequency, guaranteeing a homogenous particle concentration downstream of the spark source. The model assumes solely coagulational growth based on the extremely high supersaturations where the vapour atoms start to coagulate and subsequently grow to fully coalesced singlet NPs at room temperature. The mean size of singlet NPs can be easily controlled by adjusting the operating conditions. The experiment shows that the size distributions can all be fitted to log-normal functions and that the self-preserving of ca. 1.35 is reached at a size of ca. 6 nm, which can be regarded as a general feature. The larger value of geometric standard deviation for particle sizes above ca. 6 nm (cf. Table 3.1) signals the beginning of agglomeration. As a result, a log-normal particle size distribution is acquired by using a mean size calculated by equation (3.13) and a geometric standard deviation of the self-

preserving value. In addition, analytical formulae express the phenomena occurring in Stage D (equations (3.16) and (3.17)), providing a useful tool for further processing of the NPs exiting particle generators. To the best of our knowledge, this is the first simplified particle evolution model that includes a dimensionless quantity $\frac{\beta N}{K_{df2}}$, which expresses the importance of coagulation with respect to diffusional losses. The approach described in this work is versatile and applicable to the singlet NPs of any material; it is also compatible with existing fabrication processes, thereby enabling a non-disruptive methodology for the generation of functional materials.

Supplementary Information in Chapter 3

Supplementary Information in Chapter 3 consists of the following contents: the estimation of supersaturation and critical nucleus size (Table S3.1), material properties and constants (Tables S3.2, S3.3 and S3.4), the required parameters for calculating an appropriately modified coagulation kernel (Table S3.6), generalization of our model to other materials (Figure S3.1), the experimental justification of assumption 1), detailed procedures to derive the laminar diffusional loss rate K_{df2} and particle size evolution, linearity between vapour volume and its mass, and comparison of the penetration estimated by Gormley-Kennedy theory and our grossly simplified method. This material is available in the new few pages.

S3.1 Estimation of the vapour cloud supersaturation

Quantitative prediction for the critical nucleus size is often not possible as the data for supersaturation and surface tension are not well known. The surface tension of these NPs are directly used from the literatures[60–62], whereas the supersaturation is approximated by equation (S3.1) further below.

The supersaturation S can be approximated as:

$$S = \frac{p_a}{p_s} \tag{S3.1}$$

where p_a and p_s are the actual pressure and saturated pressure, respectively.

The saturated pressure can be determined from Clausius–Clapeyron equation assuming that the enthalpy of vaporisation H_v is independent of temperature given by:

$$p_s = p_0 \exp\left(\frac{H_v}{R}\left(\frac{1}{T_b} - \frac{1}{T_c}\right)\right) \tag{S3.2}$$

where p_o is the atmospheric pressure, T_b the boiling temperature, R is universal gas constant, and T_c is the room temperature.

Assuming the ideal gas law for the vapour cloud, p_a can be estimated as:

$$p_a = N_0 k T_c \tag{S3.3}$$

where k is the Boltzmann constant and N_o is the initial number concentration, which is in the order of 10^{20} m^{-3}. The critical nucleus size d^* can be derived from Kelvin equation:

$$d^* = \frac{4\gamma_s \Omega}{k T_c \ln(S)} \tag{S3.4}$$

where Ω is the atomic volume and γ_s is the surface tension.

Taking the examples Au and Ag, the supersaturation and critical nucleus sizes are shown in Table S1. Values of their physical properties are provided in Table S3.2 and S3.3 further below.

Table S3.1 The supersaturation and critical nucleus size for Au and Ag.

	Au	Ag
S	1.24×10^{50}	2.86×10^{34}
d^* (nm)	0.86	0.85~1.03

S3.1.1 Coagulational growth of particles in spark discharge and laser ablation

A spark discharge starts from streamer formation and propagation between electrodes where high voltage is applied. The initial electrons are directed to the anode, during which they gain energy in the electric field, thereby ionizing the ambient gas molecules by collision. During ionization, new electrons are also created. Due to the larger mass of ions than electrons, the ions are considered to be at the end of streamer propagation, while the electrons are deposited on the anode. When the steamer reaches the opposite electrode, the cathode, electron emission increases dramatically, and the streamer grows into a conductive plasma column. The gas is then heated and cylindrical expansion takes place, leading to electrode evaporation and erosion. In laser ablation, laser heating of the surface leads to the material evaporation. The vaporized material absorbs part of laser power, leading to hemispherical expansion. In spark ablation, the vapour is quenched very rapidly to quasi-room temperature, and this is also the case for laser ablation, if the dilution gas stream is pointed at the point of ablation and sufficiently high. The vapour cloud that is cooled and diluted by mixing with the quenching gas marks the starting point of the coagulation model described in Chapter 3.

S3.2 Material properties and constants

Based on the energy balance, the mass of the produced vapour can be expressed as a function of the energy per spark E as follows[43]:

$$\Delta m = \frac{\alpha E - 2\pi r_s^2 \sigma \tau (T_b^4 - T_c^4) - 2\pi r_s \tau k_e (T_b - T_c) - 2\pi r_s \tau k_a (T_b - T_c)}{c_{ps}(T_m - T_c) + c_{pl}(T_b - T_m) + H_m + H_e} \tag{S3.5}$$

Here α is the fraction of spark energy consumed for NP production, c_{ps} and c_{pl} (J K^{-1} kg^{-1}) the heat capacities of the solid and liquid material, τ (s) the spark duration, r_s (m) the radius of the spark channel, k_e and k_a (W m^{-1} K^{-1}) the thermal conductivity of the electrode material and carrier gas, respectively, T_c, T_b, and T_m (K) the temperatures of the carrier gas, the boiling and melting points of the electrode materials, respectively, H_m and H_e (J kg^{-1}) are the enthalpies of melting and vaporization of electrode materials, and σ (5.67×10^{-8} W m^{-2} K^{-4}) is the Stefan–Boltzmann constant. The constant portion of spark energy α = 0.18% has been empirically determined by gravimetric measurement for all gap distances (see Section S3.6).

Table S3.2 Constants used in the calculations

Stefan–Boltzmann constant	σ = 5.67×10^{-8} W m^{-2} K^{-4}
Avogadro constant	N_A = 6.02×10^{23} mol^{-1}
Boltzmann constant	k =1.38 × 10^{-23} J K^{-1}
Universal gas constant	R = 8.31 J K^{-1} mol^{-1}
Material-dependent constant C_m in equation (3.1)	$\dfrac{\alpha}{c_{ps}(T_m - T) + c_{pl}(T_b - T_m) + H_m + H_e}$
The threshold energy E_o to produce NPs in equation (3.1)	$\dfrac{2\pi r^2 \sigma\tau(T_b^4 - T^4) + 2\pi r\tau k_e(T_b - T) + 2\pi r\tau k_a(T_b - T)}{\alpha}$

Table S3.3 Material properties at atmospheric conditions

Material properties	symbol	Au	Ag
Surface tension	γ_s (N m^{-1})	8.78[60]	5.9~7.20[61,63]
Heat capacities of the solid	c_{ps} (J K^{-1} kg^{-1})	129	235
and liquid materials	c_{pl} (J K^{-1} kg^{-1})	129	235
Thermal conductivity	k_e (W m^{-1} K^{-1})	318	429
Boiling point	T_b (K)	3243	2435
Melting point	T_m (K)	1337	1235
Enthalpies of melting	H_m (J kg^{-1})	6.37×10^4	1.04×10^5
Enthalpies of vaporizing	H_e (J kg^{-1})	1.74×10^6	2.35×10^6
	H_v (J mol^{-1})	3.42×10^5	2.54×10^5
Molar weight	M (Kg mol^{-1})	0.197	0.108
Atom diameter	d_a (nm)	0.288	0.288
	N$_2$		
Thermal conductivity	k_a (W m^{-1} K^{-1})	25.83 × 10^{-3}	
Temperature	T_c (K)	293	
Dynamic viscosity	μ (Kg m^{-1} s^{-1})	1.75×10^{-5}	
Mean free path	λ_m (nm)	58.80	

Table S3.4 Characteristics of the sparks

Energy per spark	$E = 0.15 \sim 180$ mJ
Spark duration	$\tau = 1.2$ μs
Radius of the spark channel	$r_s = 1.5$ μm

S3.3 Independence of the portion of the spark energy on gap distances

Table S3.5 Energy consumed to a hot-spot and dissipated by radiation, metallic thermal conduction, and convection and conduction in the gas

Terms	Au (J)	Ag (J)
Radiation: $2\pi r_s^2 \sigma \tau (T_b^4 - T_c^4)$	1.06×10^{-10}	3.38×10^{-11}
Electrode thermal conduction: $2\pi r_s \tau k_e (T_b - T_c)$	1.06×10^{-5}	1.04×10^{-5}
Convection and conduction in the gas: $2\pi r_s \tau k_a (T_b - T_c)$	8.62×10^{-10}	6.26×10^{-10}

Based on the energy balance, the mass of the vapor can be expressed as a function of energy per spark given by equation (S3.5) [43].

Using the constants provided in Tables S3.2, S3.3 and S3.4 and equation (S3.5), the value of the individual terms, namely radiation, metallic thermal condition as well as convection and conduction in the gas, for Au and Ag are summarized in Table S3.5.

Table S3.5 shows that the metallic conduction contrasting to radiation and convection in the gas, is largely dominate in equation (S3.5). This finding suggests that the electrode gap distance is independent of the portion of spark energy (i.e., α in equation (S3.5)) consumed for NP production. In the case of larger distance, the spark energy distributes over a larger volume where the radiation is emitted.[18] However, radiation is only 0.001 % of metallic conduction. On the contrary, changes of the gap distance do influence the passing gas flow conditions and lead to different efficiency of material transportation. The thermal conduction of Au and Ag is similar as shown in Table S3.3. Therefore, constant α probably validates for all the gap

distances. The other processes, for instance, the energy absorbed as heat by evaporation of electrons (cathode) and positive ions (anode) can also affect α.

S3.4 Fuchs form of the coagulation kernel

Table S3.6 Fuchs form of the coagulation kernel β which considers the enhancement of van der Waals forces, and particle polydispersity.

Coagulation Kernel[41]	$$\beta = 8\pi\epsilon\varphi D d_{\mathrm{p}} \left(\frac{d_{\mathrm{p}}}{d_{\mathrm{p}} + g} + \frac{8 P_{\mathrm{st}} D}{c_{\mathrm{p}} d_{\mathrm{p}}} \right)^{-1}$$
Diffusion coefficient[64]	$$D = \frac{k T_{\mathrm{c}} C_{\mathrm{c}}}{3\pi\mu d_{\mathrm{p}}}$$
Cunningham slip correction factor[64]	$$C_{\mathrm{c}} = 1 + \frac{\lambda_{\mathrm{m}}}{d_{\mathrm{p}}} (2.34 + 1.05\exp(-0.39\frac{d_{\mathrm{p}}}{\lambda_{\mathrm{m}}}))$$
Particle velocity [41]	$$c_{\mathrm{p}} = (\frac{48 k T_{\mathrm{c}}}{\pi^2 \rho d_{\mathrm{p}}^3})^{1/2}$$
Transition parameter [41]	$$g = \frac{1}{3 d_{\mathrm{p}} l} [(d_{\mathrm{p}} + l)^3 - (d_p{}^2 + l^2)^{3/2}] - d_{\mathrm{p}}$$ $$l = \frac{8D}{\pi c_{\mathrm{p}}}$$
Enhancement factor by van der Waal forces[47,65,66]	$\varepsilon \approx$ 2.2 for size ca. 5 nm from references[47,66]
Enhancement factor by poly-dispersity[46]	$$\varphi = 3\sqrt{3} b \left(\frac{\mu^2 d_{\mathrm{p}}}{\rho k T_{\mathrm{c}}} \right)^{1/2} \left[\exp\left(\frac{25}{8} \ln^2 \sigma_{\mathrm{g}} \right) + 2 \exp\left(\frac{5}{8} \ln^2 \sigma_{\mathrm{g}} \right) \right.$$ $$\left. + \exp\left(\frac{1}{8} \ln^2 \sigma_{\mathrm{g}} \right) \right]$$ b ranges from $\frac{1}{\sqrt{2}}$ for σ_{g} =1.0 to 0.8755 for σ_{g}=3.0
Sticking probability[41]	$P_{\mathrm{st}} = 1$

Table S3.7 Specific values for b and φ. Here b is calculated based on the linear relations to σ_g, using the source from Lee et al[46]. According to previous work[67], enhancement by van der Waal forces is insensitive to particles smaller than 20 nm. Therefore, ε was taken as a constant of 2.2. Since the volume of initial vapour cloud is found to be only related to the energy per spark, as shown in equation (3.15) with $\eta = 0.75$ and $\delta = 1.76$ m^3 Kg$^{1-\eta}$ mol^{-1}. Figure 3.4 was only using spark energy of 15.76 mJ, thus providing $V_0 = 56$ mm^3 for the best fit to the measurements. The influence of deviations of V_0 in model predictions is shown in the grey shaded region of Figure 3.4.

d_p (nm)	Q_q (slm)	σ_g	b	φ
2.8	33.2	1.25	0.7365	1.62
3.6	21.5	1.25	0.7365	1.62
5.4	9.9	1.37	0.7507	1.67
6.3	6.0	1.39	0.7529	1.68
8.0	2.1	1.43	0.7578	1.70

S3.5 Comparison between the predicted and measured mean diameter of Ag NPs
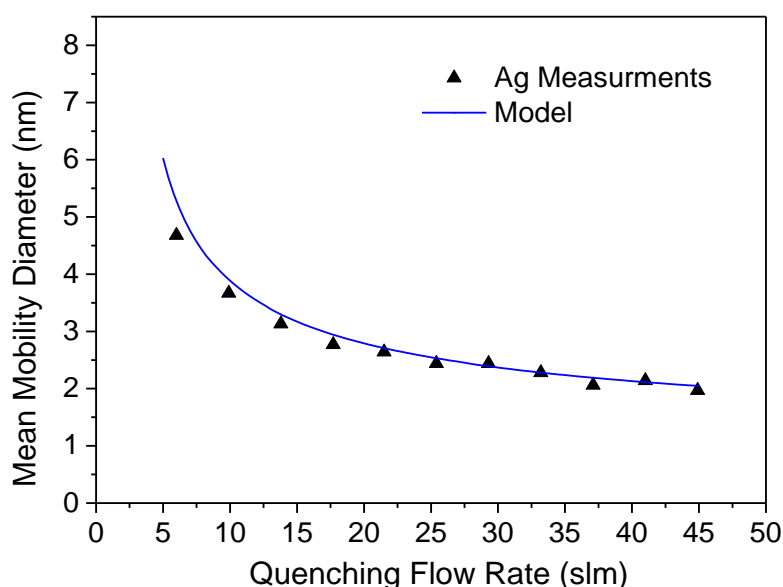
Figure S3.1 Measured and predicted geometric mean diameter of Ag singlet particles as a function of quenching gas flow rate.

Figure S3.1 shows a comparison between measured and predicted Ag particles as a function of quenching gas flow rate and provides the evidence to generalize our model to other materials, e.g., Ag, while main manuscript uses Au particles (cf.

Figure 3.4). For the predictions shown in Figure S3.1, the same system parameters was used as for Au, with the only exception of the η in equation (3.15), which was 0.715 instead of 0.75.

S3.6 Proximity collection of the early stage clusters

To verify the assumption 1) in the main manuscript and compare the volume of initial vapour cloud to the model, NPs were collected close to the spark by a Mini-Particle Sampler (MPS) [68], which carries a TEM grid with holes, through which the aerosol flow passes. Particle collection can thus be described as a filtration process.
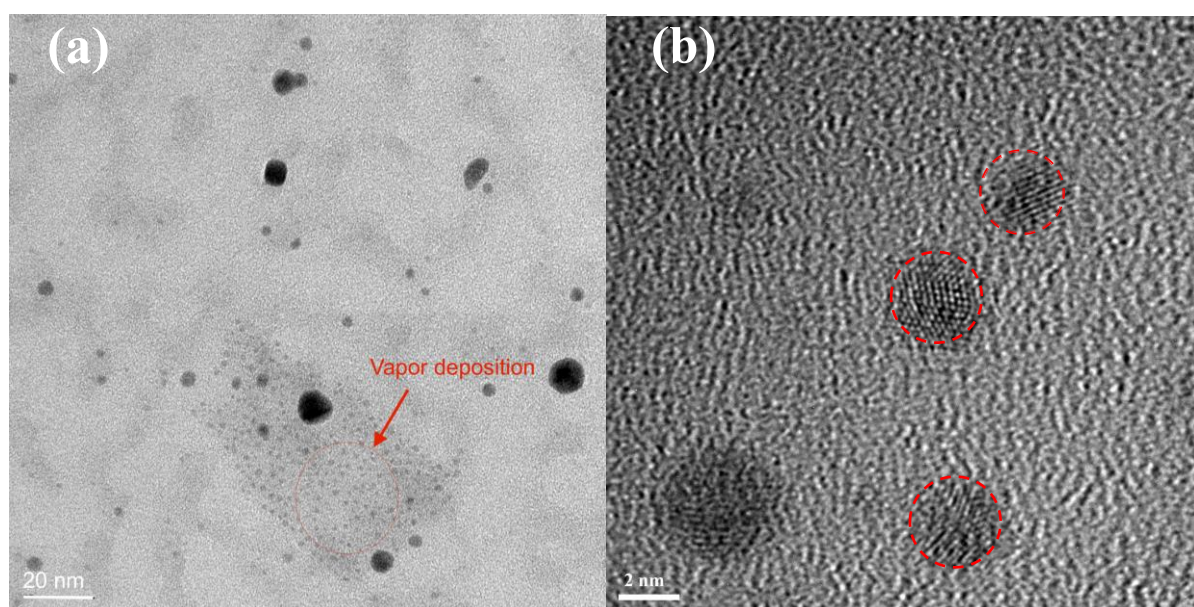
Figure S3.2 TEM images for Au NPs collected at a distance of ca. 8 mm downstream of the spark with different scale bar, (a) 20 nm and (b) 2 nm. The collection time was 5 s, while the spark energy, frequency and flow rate were fixed as ca. 16 mJ, 60 Hz and 7 slm, respectively.

Figure S3.2 shows TEM image of MPS sampled NPs close to the spark (cf. a distance of ca. 8 mm from spark, which is in the range of model prediction for the initial vapour cloud volume) and the grey areas seems to be a deposited film, which indicates the TEM grid is positioned in the vapour domain. Because thin films or very small particles are liquid-like at room temperature, surface tension leads to the formation of patches, within which small droplets form, similar to what happens with a water film on glass. In the area indicated of Figure S3.2a by the solid circle,

enough material has accumulated for these droplets to grow to a size between 1 and 2 nm, and become visible in TEM. The micrograph thus indicates that the depositing species are smaller than 1 nm (vapour atoms or small clusters). Thus at the distance of ca. 8 mm from the spark (i.e., the vapour from a 1 mm gap having flow rate of 10 slm needs ca. 0.4 ms to reach TEM grid), the plume is still in a vapour-like state. The estimated quenching rate from boiling point to room temperature during 0.4 ms is 7.5×10^6 K s^{-1}, which agrees to the literatures ($10^6 \sim 10^9$ K s^{-1})[22–24]. The micrograph thus justifies the assumption 1) that the cooling time from the boiling point to the carrier gas temperature T_c (usually room temperature) is so short that the starting condition in Stages B and C (i.e., the entire spark chamber) is a vapour at T_c, and collisional growth occurs under this constant temperature T_c throughout the system. The large particles (i.e., a few nm in size) shown in Figure S3.2a are due to the recirculation of the aerosol in the particle generator.
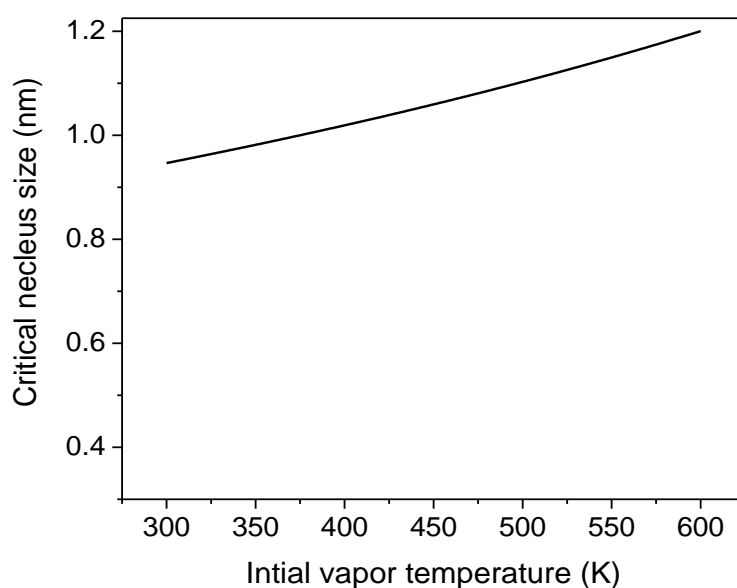
Figure S3.3 Dependence of the vapour temperature on the critical nucleus size.

Due to very short spark duration (<10 μs), the temperature downstream of the discharge, where the TEM grid is located (ca. 8 mm away from the spark) hardly exceeds room temperature. Multiple crystalline domains within the sampled NPs are observed by HRTEM images (cf. Figure S3.2b). This observation confirms that the temperature downstream of the spark stays low. Otherwise, in-flight collisions of hot, newly-formed clusters would lead to full epitaxial crystallization, assisted by the high temperature. Grammatikopoulos *et al.* also reported that multiple domains will be

formed if the NPs coalesce at room temperature[33]. Sparks or laser ablation configurations with a higher energy per pulse or a higher repetition frequency than the one used here would still fulfil this condition of 'rapid quenching' when the gas flow rate is increased accordingly. In addition, the results of Chapter 2 have shown that assuming single atoms in the initial state does not have to be fulfilled in a strict sense, as the final particle size is insensitive to the initial one at a given mass loading[17]. This means that even if quenching is not drastic enough to disable classical nucleation, the simple assumption of a vapour condensing at room temperature leads to correct results (cf. Figures 3.4 and 3.7 in Chapter 3).

S3.7 Laminar deposition rate K_{df2}

Diffusion of aerosol particles on the walls leads to a concentration gradient from left to right through a circular tube with a length of dl. The number of particles dn deposited per unit area of surface during a time dt is given by[64]:

$$dn = N_0 \left(\frac{D}{\pi t}\right)^{1/2} dt \tag{S3.6}$$
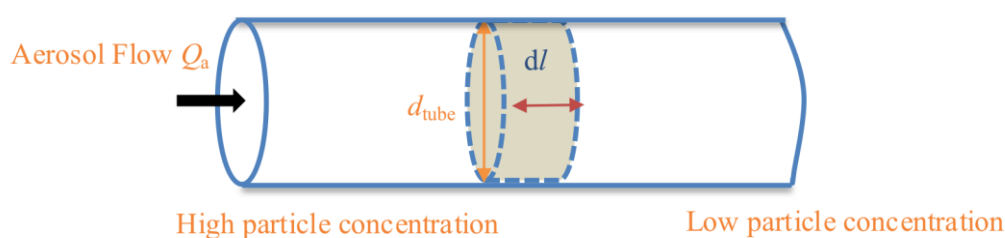
Figure S3.4 Schematic diagram of a circular tube, through which the aerosol NPs pass. A differential variable is used to estimate the diffusional loss rate under laminar flow conditions.

For a tube with the diameter d_{tube} and the length of dl during time dt, the total number of deposited particles Σ onto the walls can be expressed as:

$$\Sigma = \pi d_{tube} \, dl \, dn \tag{S3.7}$$

Under laminar flow conditions, the concentration decay by diffusional losses can be described by:[64]

$$dN = -K_{df2} N dt \tag{S3.8}$$

In this case, Σ can be calculated by:

$$\Sigma = -\frac{\pi}{4} d_{\text{tube}}{}^2 \text{d}l \, \text{d}N \tag{S3.9}$$

Combining equations (S3.6)-(S3.9), one can arrive at:

$$\Sigma = \pi d_{\text{tube}} \, \text{d}l \, N_0 \left(\frac{D}{\pi t}\right)^{1/2} \text{d}t = -\frac{\pi}{4} d_{\text{tube}}{}^2 \, \text{d}l \, (-K_{\text{df2}} N \, \text{d}t) \tag{S3.10}$$

Equation (S3.10) can be simplified to:

$$\frac{4 \left(\frac{D}{\pi t}\right)^{1/2}}{d_{\text{tube}}} = K_{\text{df2}} \frac{N}{N_0} \tag{S3.11}$$

Integrating equation (S3.8), the penetration is given by:

$$P_{\text{p}} = \frac{N}{N_0} = \exp(-K_{\text{df2}} t) \tag{S3.12}$$

Combining equation (S3.11) and (S3.12), the laminar deposition rate can be implicitly expressed as:

$$K_{\text{df2}} = \exp(K_{\text{df2}} t) \frac{4 \left(\frac{D}{\pi t}\right)^{1/2}}{d_{\text{tube}}} \tag{S3.13}$$

Equation (S3.13) can also be rewritten by replacing $t = \frac{\pi d_{\text{tube}}{}^2 L_{\text{tube}}}{4 Q_{\text{a}}}$ as:

$$K_{\text{df2}} = \exp\left(K_{\text{df2}} \frac{\pi d_{\text{tube}}{}^2 L_{\text{tube}}}{4 Q_{\text{a}}}\right) \frac{2 \pi \left(\frac{D Q_{\text{a}}}{L_{\text{tube}}}\right)^{1/2}}{d_{\text{tube}}{}^2} \tag{S3.14}$$

S3.8 Size evolution of particles

The procedures of size evolution for other stages based on the mass conservation are analogous to Stage B where turbulent dilution and coagulation occur, because the reduction of NP mass in per unit volume is only driven by dilution or diffusion. Here only Stage B is used as an example to describe the procedures to get the geometric mean size evolution of the particles. The concentration decay rate in Stage B can be described as:

$$\frac{dN}{dt} = -\frac{1}{2}\beta N^2 - K_{dl}N \qquad (t \le t_B) \tag{S3.15}$$

In order to use the mass conservation, the diameter of the particle with average mass $d_{\overline{m}}$, however, must be converted from the geometric mean diameter d_p by Hatch-Choate conversion equation given by:

$$d_{\overline{m}} = d_p \exp(1.5 \ln^2 \sigma_g) \tag{S3.16}$$

where σ_g is the geometric standard deviation and can be regarded as a self-preserving value of 1.35. Therefore, the conversion factor is a constant and it is generally valid for any log-normal size distribution.

In Stage B, the NP mass in per unit volume is reduced only by dilution so the reduction rate can be expressed as:

$$\frac{d\left(\rho\frac{\pi}{6}(\exp(1.5\ln^2\sigma_g)d_p)^3 N\right)}{dt} = -K_{dl}\,\rho\frac{\pi}{6}(\exp(1.5\ln^2\sigma_g)d_p)^3 N \ (t \le t_B) \tag{S3.17}$$

Cancelling out the constants on both sides of equation (S3.17), it is thus simplified to:

$$\frac{3d_p^2 N d(d_p) + d_p^3 dN}{dt} = -K_{dl}\,d_p{}^3 N \qquad (t \le t_B) \tag{S3.18}$$

Substituting equation (S3.15) in equation (S3.18), the mean size evolution is finally obtained:

$$\frac{dd_p}{dt} = \frac{1}{6}\beta N d_p \tag{S3.19}$$

S3.8.1 Estimating Re in Stage B

As shown in Figure S2.1, the flow rate exits from a nozzle with a rectangular shape having dimension of 2×3 mm². With consideration of rapid turbulent time (in the order of ms as estimated in Section S2.1), using 10 slm flow rate gives a velocity of ca. 10 m/s, which is approximated to the velocity around the walls. Inserting this value in Re formula (gas density is in the order of 1 kg/m³, N_2 viscosity $1.75×10^{-5}$ pa s, hydraulic diameter $3.5×10^{-2}$ m), one can obtain a value of ca. 20 000, whereas a flow rate of 2 slm corresponds to Re around 4000.

S3.9 Relation between the volume and mass of initial vapour cloud

The vapour produced by the point source has adiabatically expanded to ambient pressure p_0, and reached a temperature T_A. Its thermal energy E_{th}, a fixed fraction of the spark energy E, is proportional to nT_A ($E_{th} \propto nT_A$), where n is the number of moles. Applying the ideal gas law to this vapour cloud leads to $E_{th} \propto p_0 V_A$, which means that V_A is proportional to the spark energy E and thus approximately to the mass per spark, Δm, considering equation (S3.5) and Figure 3.4. The vapour cloud is subsequently cooled and diluted by mixing with the quenching gas (room temperature T_c). Cooling to a given temperature T_s means expansion of V_A by a given factor to V_0, which is named as the initial volume, as it marks the starting point of the coagulation model. These considerations are in line with a value of $\eta = 0.75$ close to 1. Note that in practise T_S is close to T_c, and it has been assumed coagulation at the quenching gas temperature.

S3.9.1 Estimating the temperature increase of the gas downstream of spark ablation

The model assumes constant temperature during the "final coagulation stage", in which the final concentration and particle size can be estimated via mass balance. It is assumed that the particulate material is completely mixed with the quenching gas in this determining phase. The following considerations justify the assumption of a constant temperature during the final coagulation stage. Basically, the temperature

of the whole process can be considered to be ambient temperature, which is also the temperature of the inflow of quenching gas. Note that this process temperature could be increased with respect to room temperature to guarantee complete coalescence up to the largest particle size desired, but room temperature is sufficiently high in the experiment. In reality, the temperature at the final coagulation stage may not be strictly constant, because the spark heats up the gas by ΔT, and subsequently the walls of the system, which are at ambient temperature, cool back towards ambient. In order to support the assumption of constant temperature during the final coagulation stage, the temperature increase by the spark is estimated, as it represents the maximum temperature drop possible during that stage.

The spark is assumed to release all its energy to the gas. This neglects heat transfer to the electrodes and radiation loss and leads to an upper limit for the temperature increase. At a given energy per spark E and a spark repetition frequency f, the energy released during the time t into a volume $V_g = Q_q t$ of flowing gas (flow rate Q_q, density ρ_g) is given by:

$$Eft = c_g \rho_g Q_q \, t \, \Delta T \tag{S3.20}$$

Here c_g is the specific heat capacity of the quenching gas, considered as constant. With the parameters of the experiment given in the table below, the result is $\Delta T = 4.4$ K. As reasoned above, this is the maximum possible value and it is certainly negligible with respect to its effect on coagulation, justifying the assumption 1) made in Chapter 3.

Table S3.8 Values of various parameters used in equation (S3.20). Values of some parameters are specifically provided under atmospheric conditions at a N_2 gas flow rate of 10 slm.

Parameters	E ($\times 10^{-3}$ J)	f (Hz)	Q_q ($\times 10^{-4}$ m³/s)	N_2 density (kg/m³)	c_g (J/(kg K))	T_c (K)
Values	16	60	1.67	1.25	1040	293

S3.10 Estimation of the penetration

In contrast to Gormley-Kennedy theory[59], the elegance of our method to estimate the penetration through a circular tube lies in the simplicity of calculating K_{df2} (cf. equation (S3.14)). Since the residence time is always easy to calculate, one can easily use equations (S3.12) and (S3.14) to estimate the penetration for any geometry. The penetration predicted by Gormley-Kennedy theory, is comparable to that predicted using equations (S3.12) and (S3.14) (cf. Figure S3.6).

Figure S3.6 compares the penetration predicted by equation (S3.8) and Gormley-Kennedy model as a function of deposition parameter ($\xi = \frac{D L_{tube}}{Q_a}$) for circular tubes with a length L_{tube}. The points in Figure S3.6 are chosen in a laminar circular tube with an inside diameter of 4 mm and length of 40 mm. The residence time is 0.181 s based on an aerosol flow rate Q_a = 1.67 slm and the dimensions of this circular tube. For easy calculations, particle growth was not considered in this short time. Briefly, equation (S3.12) was used to estimate the penetration, where K_{df2} is estimated by equation (S3.14) for the mean size of particles.
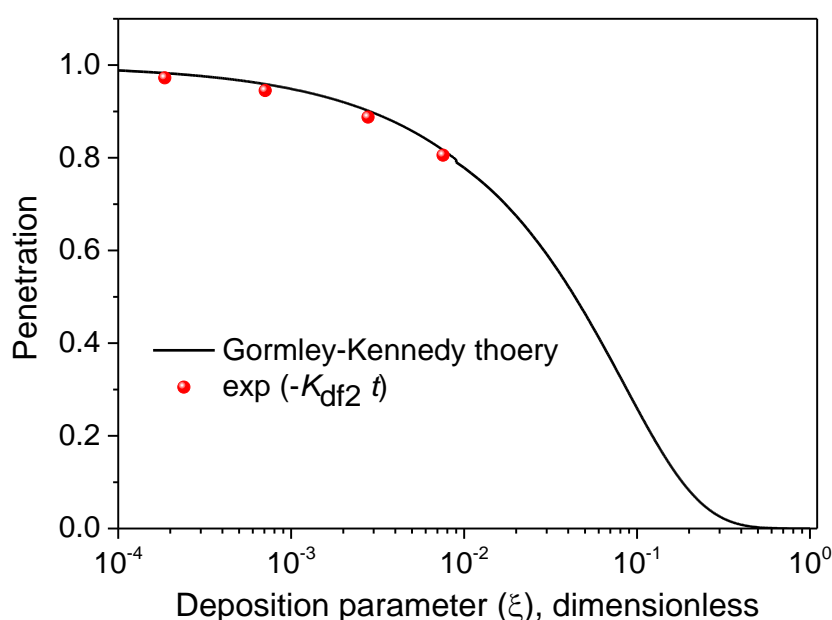
Figure S3.6 Penetration versus deposition parameter for circular tubes and the comparison between Gormley-Kennedy theory and our method (cf. using equations (S3.12) and (S3.14)).

References

1   J. F. Gomes, A. C. Garcia, C. Pires, E. B. Ferreira, R. Q. Albuquerque, G. Tremiliosi-Filho and L. H. S. Gasparotto, *J. Phys. Chem. C*, 2014, **118**, 28868–28875.

2   K. Linehan and H. Doyle, *Small*, 2014, **10**, 584–590.

3   M. E. Messing, K. A. Dick, L. R. Wallenberg and K. Deppert, *Gold Bull.*, 2009, **42**, 20–26.

4   J. Chang, X. Huang, G. Zhou, S. Cui, P. B. Hallac, J. Jiang, P. T. Hurley and J. Chen, *Adv. Mater.*, 2014, **26**, 758–764.

5   A. Anastasopol, T. V Pfeiffer, J. Middelkoop, U. Lafont, R. J. Canales-Perez, A. Schmidt-Ott, F. M. Mulder and S. W. H. Eijt, *J. Am. Chem. Soc.*, 2013, **135**, 7891–7900.

6   V. A. Vons, H. Leegwater, W. J. Legerstee, S. W. H. Eijt and A. Schmidt-Ott, *Int. J. Hydrogen Energy*, 2010, **35**, 5479–5489.

7   W. Yan, W. Ma, H. Kuang, L. Liu, L. Wang, L. Xu and C. Xu, *J. Phys. Chem. C*, 2013, **117**, 17757–17765.

8   T. Li and G. Galli, *J. Phys. Chem. C*, 2007, **111**, 16192–16196.

9   U. K. Krieger, C. Marcolli and J. P. Reid, *Chem. Soc. Rev.*, 2012, **41**, 6631–6662.

10   X. Shan, I. Díez-Pérez, L. Wang, P. Wiktor, Y. Gu, L. Zhang, W. Wang, J. Lu, S. Wang, Q. Gong, J. Li and N. Tao, *Nat. Nanotechnol.*, 2012, **7**, 668–672.

11   T. V. Pfeiffer, J. Feng and A. Schmidt-Ott, *Adv. Powder Technol.*, 2014, **25**, 56–70.

12   M. von Smoluchowski, *Z. phys. Chem*, 1917, **92**, 129–168.

13   A. Voloshko, J.-P. Colombier and T. E. Itina, *Appl. Surf. Sci.*, 2015, **336**, 143–149.

14   A. Gutsch, H. Mühlenweg and M. Krämer, *Small*, 2005, **1**, 30–46.

15   T. E. Itina and A. Voloshko, *Appl. Phys. B*, 2013, **113**, 473–478.

16   S. N. Rogak, *Aerosol Sci. Technol.*, 1997, **26**, 127–140.

17   J. Feng, G. Biskos and A. Schmidt-Ott, *Sci. Rep.*, 2015, **5**, 15788.

18   N. S. Tabrizi, M. Ullmann, V. A. Vons, U. Lafont and A. Schmidt-Ott, *J. Nanoparticle Res.*, 2009, **11**, 315–332.

19   S. C. Wang and R. C. Flagan, *Aerosol Sci. Technol.*, 1990, **13**, 230–240.

20   G. Biskos, V. A. Vons, C. U. Yurteri and A. Schmidt-Ott, *KONA Powder Part. J.*, 2008, **26**, 13–35.

21   N. S. Tabrizi, *PhD thesis*, Delft University of Technology, 2009.

22   H. Martinen and H. Tholl, *Zeitschrift für Naturforsch. A*, 1970, **25**, 430–439.

23   N. T. Jenkins and T. W. Eagar, *JOM*, 2003, **55**, 44–47.

24   A. E. Berkowitz and J. L. Walter, *J. Mater. Res.*, 1987, **2**, 277–288.

25   K.-T. Park, M. M. Farid and J. Hwang, *J. Aerosol Sci.*, 2014, **67**, 144–156.

26   T. V. Pfeiffer, J. Ortiz-Gonzalez, R. Santbergen, H. Tan, A. Schmidt-Ott, M. Zeman and A. H. M. Smets, *Energy Procedia*, 2014, **60**, 3–12.

27   M. Valenti, D. Dolat, G. Biskos, A. Schmidt-ott and W. A. Smith, *J. Phys. Chem. C*, 2015, **119**, 2096–2104.

28   J. H. Byeon and Y.-W. Kim, *Nanoscale*, 2012, **4**, 6726–6729.

29   T. Pfeiffer, P. Kedia, M. E. Messing, M. Valvo and A. Schmidt-Ott, *Materials*, 2015, **8**, 1027–1042.

30   J. Sun, L. He, Y.-C. Lo, T. Xu, H. Bi, L. Sun, Z. Zhang, S. X. Mao and J. Li, *Nat. Mater.*, 2014, **13**, 1007–1012.

31   A. B. Bourlinos, R. Herrera, N. Chalkias, D. D. Jiang, Q. Zhang, L. A. Archer and E. P. Giannelis, *Adv. Mater.*, 2005, **17**, 234–237.

32   M. José-Yacamán, C. Gutierrez-Wing, M. Miki, D. Q. Yang, K. N. Piyakis and E. Sacher, *J. Phys. Chem. B*, 2005, **109**, 9703–9711.

33   P. Grammatikopoulos, C. Cassidy, V. Singh and M. Sowwan, *Sci. Rep.*, 2014, **4**, 5779.

34   J. F. van der Veen, *Surf. Sci.*, 1999, **433-435**, 1–11.

35   Q. S. Mei and K. Lu, *Prog. Mater. Sci.*, 2007, **52**, 1175–1262.

36   F. E. Kruis, H. Fissan and B. Rellinghaus, *Mater. Sci. Eng. B*, 2000, **69-70**, 329–334.

37   K. Nanda, F. Kruis and H. Fissan, *Phys. Rev. Lett.*, 2002, **89**, 256103.

38   K. E. J. Lehtinen, R. S. Windeler and S. K. Friedlander, *J. Aerosol Sci.*, 1996, **27**, 883–896.

39   K. Lehtinen, *J. Colloid Interface Sci.*, 1996, **182**, 606–608.

40   S. H. Ehrman, M. I. Aquino-Class and M. R. Zachariah, *J. Mater. Res.*, 1999, **14**, 1664–1671.

41   J. H. Seinfeld and S. N. Pandis, *Atmospheric Chemistry and Physics: From Air Pollution to Climate Change*, John Wiley & Sons, New York, 2006.

42   U. Uhrner, S. von Löwis, H. Vehkamäki, B. Wehner, S. Bräsel, M. Hermann, F. Stratmann, M. Kulmala and A. Wiedensohler, *Atmos. Environ.*, 2007, **41**, 7440–7461.

43   F. Llewellyn Jones, *Br. J. Appl. Phys.*, 1950, **1**, 60–65.

44   A. Bejan, *Sci. Rep.*, 2012, **2**, 594.

45   P. Jiang, D. O. Lignell, K. E. Kelly, J. S. Lighty, A. F. Sarofim and C. J. Montgomery, *J. Air Waste Manag. Assoc.*, 2005, **55**, 437–45.

46   K. W. Lee and H. Chen, *Aerosol Sci. Technol.*, 1984, **3**, 327–334.

47   H. Ouyang, R. Gopalakrishnan and C. J. Hogan, *J. Chem. Phys.*, 2012, **137**, 064316.

48   C. . Wang and S. . Friedlander, *J. Colloid Interface Sci.*, 1967, **24**, 170–179.

49   A. Schmidt-Ott and H. Burtscher, *J. Colloid Interface Sci.*, 1982, **89**, 353–357.

50   Y. Nomura, P. K. Hopke, B. Fitzgerald and B. Mesbah, *Aerosol Sci. Technol.*, 1997, **27**, 62–72.

51   M. Alonso, *Rev. Metal.*, 1998, **34**, 413–415.

52   S. K. Friedlander, *Smoke, Dust, and Haze Fundamentals of Aerosol Dynamics*, Oxford University Press, New York, 2 edition., 2000.

53   C. Peineke, M. Attoui, R. Robles, A. C. Reber, S. N. Khanna and A. Schmidt-Ott, *J. Aerosol Sci.*, 2009, **40**, 423–430.

54   A. Maisser, K. Barmpounis, M. B. Attoui, G. Biskos and A. Schmidt-Ott, *Aerosol Sci. Technol.*, 2015, **49**, 886–894.

55   J. D. Landgrebe and S. E. Pratsinis, *Ind. Eng. Chem. Res.*, 1989, **28**, 1474–1481.

56   Zs. Geretovszky. personal communication, June 2015. The performed emission spectroscopic experiments, served the purpose of creating a distribution map of the (excited) species having a sphere-like volume (e.g., a few mm in diameter) in and around the electrode gap during discharge operation. This finding is in line with the volume of initial vapor cloud predicted in this chapter.

57   K. E. J. Lehtinen and M. R. Zachariah, *J. Aerosol Sci.*, 2002, **33**, 357–368.

58   B. Cheng and A. H. W. Ngan, *Int. J. Plast.*, 2013, **47**, 65–79.

59   D. B. Ingham, *J. Aerosol Sci.*, 1975, **6**, 125–132.

60   K. K. Nanda, A. Maisels and F. E. Kruis, *J. Phys. Chem. C*, 2008, **112**, 13488–13491.

61   K. K. Nanda, A. Maisels, F. E. Kruis, H. Fissan and S. Stappert, *Phys. Rev. Lett.*, 2003, **91**, 106102.

62   S. C. Vanithakumari and K. K. Nanda, *J. Phys. Chem. B*, 2006, **110**, 1033–1037.

63   H. Hofmeister, S. Thiel, M. Dubiel and E. Schurig, *Appl. Phys. Lett.*, 1997, **70**, 1694.

64   W. C. Hinds, *Aerosol Technology: Properties, Behavior, and Measurement of Airborne Particles*, John Wiley & Sons, New York, 1999.

65   W. H. Marlow, *Surf. Sci.*, 1981, **106**, 529–537.

66   I. M. Kennedy and S. J. Harris, *J. Colloid Interface Sci.*, 1989, **130**, 489–497.

67   H. Burtscher and A. Schmidt-Ott, *Surf. Sci.*, 1985, **156**, 735–740.

68   B. R'mili, O. L. C. Le Bihan, C. Dutouquet, O. Aguerre-Charriol and E. Frejafon, *Aerosol Sci. Technol.*, 2013, **47**, 767–775.

69   V. Vons, *PhD thesis*, Delft University of Technology, 2008.

Part B

Scaling-up

4. A Green and Versatile Method for High-yield Synthesis of Metallic Nanoparticles

High-yield and continuous synthesis of ultrapure inorganic nanoparticles (NPs) of well-defined size and composition has invariably been one of the major challenges in nanotechnology. Employing green techniques that avoid the use of poisonous and expensive chemicals has been realized as a necessity for the production of NPs on an industrial scale. This chapter shows that a newly developed high-frequency spark (HFS) quenched by a high-purity gas yields large quantities of various monometallic and bimetallic NPs, well-defined with respect to the primary particle size (a few nm) and chemical composition. Given that the mass production rate is linearly dependent on the operating frequency, the method proposed in this work can reach up to 1 g h^{-1}, providing chemists with a versatile tool producing multicomponent metallic NPs only in one single step. Considering that the methodology neither requires any specialized machinery, nor any chemical reagents, product purification, or any further waste processing, it provides a green and versatile platform for manufacturing key building blocks toward industrial scale.

Graphical Abstract

4.1 Introduction

Part A (Chapters 2, 3) of this thesis focuses on the theoretical facets and provides key parameters to control the particle size and nanostructures at surfaces. This chapter concentrates on scaling up of this production method while maintaining a small primary particle size.

Commercial production of high-performing nanomaterial-based devices[1–7], requires scalable fabrication processes that are robust, rapid and avoid the use of expensive and toxic chemicals[8]. These applications have attracted growing interest in conjunction with the synthesizing of diverse inorganic NPs with small primary particles, only a few nm in size and a well-defined chemical composition, and high purity[9–12]. Achieving high enough mass production rates of such NPs has invariably been one of the challenging tasks in nanotechnology.

Conventional wet-chemistry processes allow manipulating the shape of NPs with homogeneous and narrow size distributions[13–15]. Their scalability, however, is limited by the batch operation and slow kinetics. The former commonly results in undesirable variability of NP physicochemical properties[16]. In addition, liquid-phase methods generally require a number of chemical precursors, which can lead to the contaminations of the resulting nanomaterial surface and, in some cases, hazardous wastes that have to be released to the environment.

Rapidly quenched gas-phase spark ablation operated at ambient pressure provides great versatility in the synthesis of metallic NPs consisting of a wide variety of conducting or semiconducting materials including rare earths (that are difficult to produce with traditional wet-chemistry methods), thermodynamically metastable materials[17], and alloys (e.g., steel) or other nanocomposite patterns with virtually unlimited mixing possibilities[8,18–21]. In addition, the method offers good control over particle size which ranges from that of atomic clusters to that of singlets (cf. Chapter 1) or agglomerates consisting of primary particles a few nm in diameter[18,22,23]. This

technique can produce oxide and non-oxide NPs, when appropriate gases and electrodes are available. As a result, recent research efforts have focused on fabricating NPs using spark ablation (at low frequencies) for a host of new applications (Table S4.1)[3,6,8,18,20,23–35]. Although the energy required by the system is high (i.e., on the order of 10^6 J g^{-1}, exclusively in the form of electricity), the advantage of avoiding any solvents, toxic chemicals and wastes makes this method inherently environmentally benign. Purifying the electrodes is beyond the scope of this production line. Therefore, the energy used for purifying electrodes is not considered. It should be noted that wet-chemistry manufacturing processes may have a comparable demand of energy for processing the waste stream, producing the precursors, and purifying the nanomaterials. To make the process also sustainable with respect to its energy consumption, one could couple it with a source of renewable energy (e.g., solar panels).

Apart from the importance of having small enough primary particles (a few nm)[23], achieving a high yield in NP synthesis is a vital prerequisite for numerous applications. The mass production rate of spark ablation is proportional to the spark repetition frequency and to the mass ablated per spark, which is linearly related to the spark energy as have been recently demonstrated both experimentally and theoretically[23]. Spark discharges using resistance-inductance-capacitance (RLC) circuits (referred to as RLCS from this point onwards; cf. Figure S4.1)[8,30] have an upper operating frequency threshold of a few hundred Hz. A continuous arc discharge develops above that threshold, which yields undesirable larger primary particles associated with a higher mass production rate[36]. Above a certain level of the spark energy, however, undesired 'splashing particles' (cf. Chapter 6) are ejected from molten pools that are momentarily formed on the electrode surface during the spark discharges[37].

This chapter shows that a newly developed high frequency spark (HFS; cf. Figure S4.1 and previous work[8,38,39]) can enormously increase the NP production rate while maintaining the small size of their primary particles. The core concept of the HFS is to decouple the charge and discharge cycles driven by the RLC circuit by adding a number of fast electronic switches, allowing spark frequencies to be controlled up to 25 kHz[8]. Switching prevents transition into the continuous arc mode, and facilitates a

constant low-energy per spark set independently of gas characteristics (type, purity, and flow rate) and electrode gap spacing. This constant spark energy reduces the differences in the ablated mass from spark to spark and also avoids 'splashing', guaranteeing a consistent output when operating multiple HFSs in parallel[23]. The maximum frequency of 25 kHz corresponds to a duty cycle of 25% (i.e., typical spark duration of ca. 10 μs over a period of 40 μs for the entire cycle), thereby allowing adequate quenching between successive sparks. In contrast to continuous arc discharges, the gas quenching is sufficient to cause a sharp temperature drop downstream of the spark zone favoring the formation of small (primary) particles[36].

This chapter expounds, for the first time, the HFS (operating frequencies > 1 kHz) on high-yield synthesis of a series of monometallic Au, Ag, Ni, Zn, Cu, Al and bimetallic Cu-Ni (95-5 at.%) NPs. Since producing non-agglomerated singlets has been demonstrated in Chapters 2 and 3[18,23], this chapter allows the agglomeration. In Section 4.2, the size distributions of the resulting agglomerated NPs are characterized by a scanning mobility particle sizer (SMPS; cf. Section S4.3 in the SI), whereas the size of the primary particles of the agglomerates is analyzed by transmission electron microscopy (TEM) and small-angle X-ray scattering (SAXS). In addition, wide-angle X-ray scattering (WAXS) is used to determine the crystal phases of the resulting particles. Section 4.3 summarizes the most important findings: HFSs can achieve a high-yield in a wide range of NP syntheses, while maintaining small primary particles, and identifies some future directions. This chapter closes with a brief description of experimental setup in Section 4.4.

4.2 Results and discussion

4.2.1 NP mass production rate determined by gravimetric measurements

Gravimetric measurements of the electrodes were used to determine the mass production rate $\dot{m}$ of the resulting particles. Figure 4.1 shows the mass production rates of NPs consisting of a number of different materials, namely Au, Zn, Ag, Cu, Cu-Ni (95-5 at.%), Ni and Al, produced at frequencies from 1 to 4.5 kHz. A high-purity carrier gas (Ar, 99.999%) at a total flow rate of 20 standard liters per minute (slm) was used for all the measurements carried out in this chapter (cf. Figure S4.2 in the

SI). A low-enough constant spark energy of 32 mJ is fixed throughout the experiments (cf. Section S4.3 described in the SI) to avoid the formation of notable 'splashing particles'. The red arrow (cf. Figure 4.1) indicates that the maximum frequency of RLCS corresponds to a maximum $\dot{m}$ which lies below 20×10^{-3} g h^{-1}. The measured linear relations between $\dot{m}$ and f imply that the mass ablated per spark Δm is constant and independent of frequency, and $\dot{m}$ can therefore be written as:

$$\dot{m} = \Delta m \, f \qquad (4.1)$$

Note that Δm is material dependent (cf. equation (S4.1) and Table S4.2) [18].
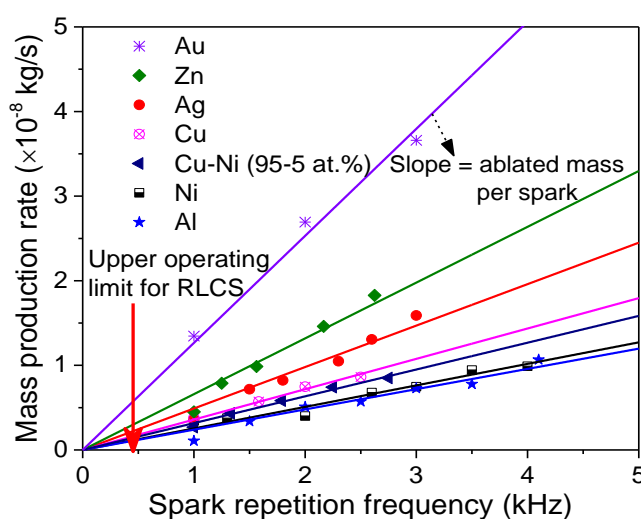
Figure 4.1 Mass production rates of HFS-produced Au, Zn, Ag, Cu, Cu-Ni (95-5 at.%), Ni, and Al NPs, as a function of spark repetition frequencies. Symbols denote the gravimetric measurements of the electrodes, while the lines are fits to the measurements. The red arrow indicates the upper operating limit of the RLCS.

In view of these linear relations and based on the data shown in Figure 4.1, the mass production rate of Au NPs can be extrapolated to ca. 1.1 g h^{-1} when the spark frequency is raised to 25 kHz. Operating at such high frequencies, however, would require a quenching gas flow rate higher than 100 slm in order to sufficiently cool the electrodes. The present system only allows flow rates of the order of a few tens slm. The HFS could therefore be operated at 25 kHz only for a short period, and stable operation was feasible only up to 4.5 kHz at the flow rate used here (20 slm). A recycling flow system capable of handling the flow rate of a few hundred slm has been designed (cf. Figure S4.3 in the SI). Continuous and stable operation at 25 kHz would

also require a gap control system, since the electrodes are rapidly consumed (see more details in Section S4.6 in the SI).

4.2.2 Deposition of individual non-agglomerated NPs

Figure 4.2 shows the non-agglomerated spherical Au NPs with high crystallinity, which were deposited (using only ca. 1 s) on a TEM grid (placed in the custom-made filter holder) at a flow rate of 20 slm and spark repetition frequency of 1 kHz, corresponding to a production rate of ca. 60 mg h^{-1}. Formation of these spherical NPs is driven by solid-state diffusion[23], mainly by relocation of surface atoms. However, it is observed that the agglomerates inevitably form for high coverage on the surface of substrates (cf. TEM images in the SI). This is attributed to the incomplete coalescence of the colliding particles on substrates. Further annealing these agglomerates yields spherical particles having larger sizes than the primary particles within the as-deposited agglomerates. If particle growth or post-heat treatment is to be avoided, coalescence could be hindered by forming a protecting layer on the particle surface, such as coating particles by introducing a trace amount of oxygen in the carrier gas, which has been reported as 'pinning' effect by Seipenbusch *et al*.[40]. Alternatively, decreasing the temperature below the threshold can avoid triggering coalescence. In addition, guiding the aerosol NPs to the liquid phase opens numerous possibilities to stabilize them, which, however, results in impurities and expensive/tedious washing procedures.

Besides the applications shown in Table S4.1, nonagglomerated singlet particles have been shown to increase the conversion efficiency of solar cells and photocatalysts for water splitting[6,32], whereas agglomerated particles have been used to nanofinish a number of antibacterial textiles with high antibacterial activity and good washing durability[41]. With respect to nanocatalysis, it was found that the agglomerated NPs at surface can be reconstructed to spheres by annealing. Even at 900 ^{o}C for 100 h, particle size distributions remain the same, showing high stability and improved methane conversion efficiency[42].
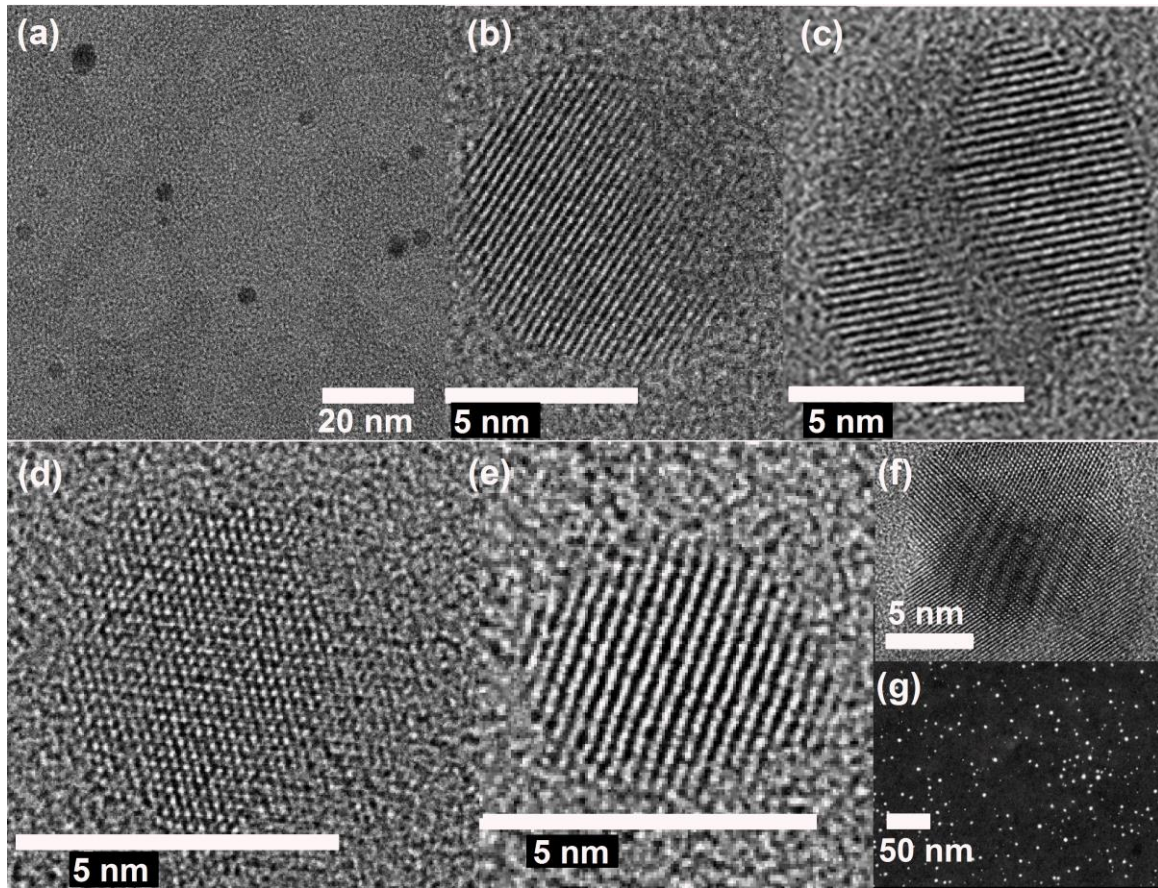
Figure 4.2 TEM images of Au (a, b, c) and Ag NPs (d, e, f, g: STEM) generated by the HFS at 1 kHz, showing their shape and configuration and confirming their crystal structures.

4.2.3 NP mass production rate estimated by aerosol density

Apart from the determination of $\dot{m}$ by gravimetric measurements, $\dot{m}$ is derivable through the mass density of the aerosol M_{ag} given by:

$$\dot{m} = M_{ag}Q \tag{4.2}$$

where Q is the quenching gas volume flow rate. M_{ag} is estimated from the measured particle size distributions (Figure 4.3) by means of a simple model that assumes a scaling relation between the mass of freshly formed agglomerates and their mobility diameter (cf. Section S4.7 in the SI). $\dot{m}$ estimated by equation (4.2) are consistent with the gravimetric measurements, thereby verifying that the mass ablated from the electrodes is essentially converted to NPs (cf. Section S4.4 and Table S4.3 and S4.4 shown in the SI).
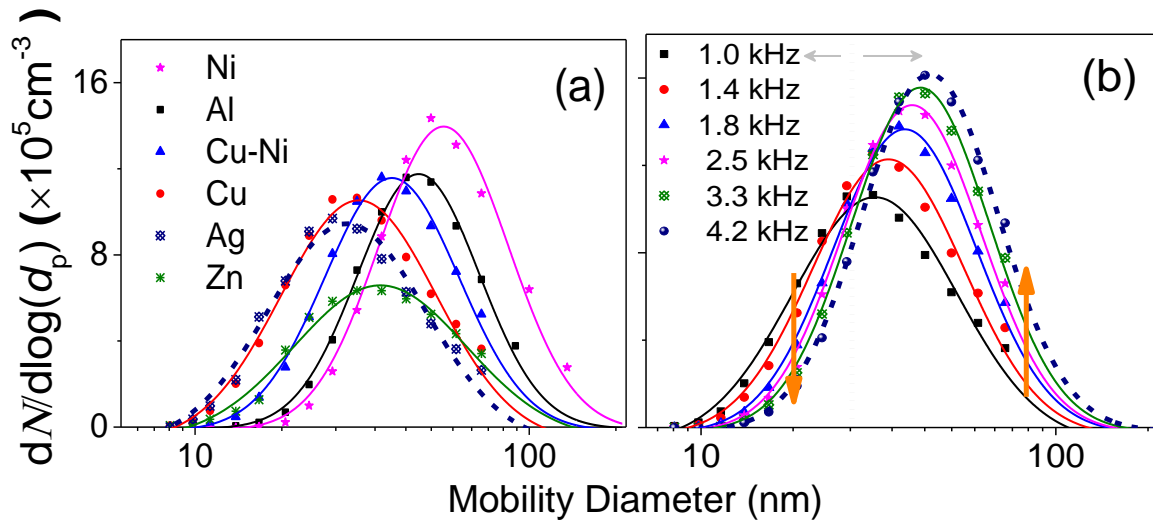
Figure 4.3 Size distributions of agglomerated NPs produced by the HFS for (a) Ni, Al, Cu-Ni (95-5 at.%), Cu, Ag, and Zn NPs produced at 1 kHz, and (b) Cu NPs produced using different spark repetition frequencies. The symbols denote the SMPS measurements and the curves are fitted log-normal distributions to the data.

Figure 4.3a shows the particle size distributions for Zn, Ag, Cu, Cu-Ni (95-5 at.%), Ni and Al, measured by the SMPS[18]. Note that the SMPS measures the agglomerate size (agglomeration is allowed here), and not the primary particle size, which can only be determined by TEM imaging or SAXS (cf. Figures S4.6 and S4.8 shown in the SI). Details of the measurements and the size distributions of different particle materials are summarized in Table S4.3. In Figure 4.3a, Ni shows a relatively large particle concentration and size despite its low production rate (cf. Figure 4.1). This is attributed to the small primary particle size and the tendency of magnetic materials to form chain-like agglomerates (small fractal dimension; Figure S4.6a in the SI), leading to a larger mobility diameter for a given mass per agglomerate (cf. Section S4.7 in the SI) and reduced losses. Figure 4.3b shows the size distributions of agglomerated Cu NPs generated at frequencies ranging from 1.0 to 4.2 kHz. The size distributions shift to larger sizes as the spark frequency increases, correlating well with coagulation theory. If Q is increased linearly in accordance with f, M_{ag} will remain unchanged for a specific material (cf. equations (4.1) and (4.2)) as indicated by size distribution measurements discussed in Section S4.9 in the SI.

4.2.4 Determination of the primary particle size

The primary particle size has greater relevance than the agglomerate size for the majority of technological applications. Concerning the invariance of the agglomerate size distribution when f/Q stays constant, it is hypothesized that the particle formation process remains similar. The TEM observations confirm that there is a strong similarity to the primary particle sizes under these conditions (cf. Figure S4.8 presented in the SI).

It should be mentioned that using TEM to quantitatively determine the primary particle size is difficult here, since boundaries among them are unclear. Therefore, TEM images can only be used to qualitatively compare the primary particle size. To combat this difficulty, SAXS is used for determining the primary particle sizes, thereby achieving the comparison of primary particle sizes of different materials. This technique usually provides particle size in terms of the radius of gyration (the root-mean-square of the distances of all the electrons in the particle from their center of gravity), using Guinier's law, as well as particle surface area from the Porod constant and the scattering invariant[43]. In contrast to using TEM for estimating particle size, SAXS data represent an average over a large number of particles because all particles located within the illuminated volume contribute to the scattering.

To further understand this empirical result, as well as the different primary particle sizes observed for the materials investigated in the present study (cf. Table 4.2), it is instructive to qualitatively identify the major determinants of primary particle size. Growth of NPs in the rapidly quenched gas-phase synthesis is dominated by particle collisions and sticking. The particles formed at the early stage are liquid-like[44], and therefore fully coalesce into singlets when colliding with each other until they attain a critical size, above which coalescence only partly occurs or ceases, thus forming non-spherical agglomerated particles[18]. This critical size is essentially the primary particle size in the agglomerates, and is temperature and material dependent. A higher surface diffusion coefficient (usually indicated by a lower melting point) yields larger primary particles. For example, the primary Zn NPs are larger than those of Ni. Together with the growth history of the particles, the temperature history is particularly influential in the primary particle size. If f/Q stays constant for a given

material and specific spark energy, the particulate volume produced by each spark will be distributed over the same gas volume, suggesting a similar temperature history, as the same energy is dissipated per spark. Considering that f/Q remains unchanged, the gas impurity concentration also stays constant with respect to the particle mass concentration, thereby forming a similar surface diffusion barrier (through gas impurities reacting with the particles, usually forming an oxide layer, if non-oxide NPs are desired) hindering further coalescence. In addition, material with a higher $\Delta m/\rho$ (ρ: bulk material density) yields a greater particulate volume while maintaining identical operating conditions. This implies the tendency of forming larger primary particles, as they grow faster in the initial hot "coalescence zone".

Table 4.1 Qualitative rules for controlling primary particle size.

Increasing the below factors	increase (↑) or decrease (↓)
Quenching gas volume flow rate Q	↓
Spark repetition frequency f	↑
Particulate volume $\Delta m/\rho$	↑
Surface diffusion coefficient	↑
Reactivity with gas impurities	↓

The aforementioned considerations highlight the difficulty in predicting the primary particle size due to the complexity of the process and due to the fact that gas impurity is unknown unless a purification system is adopted. Table 4.1 summarizes the criteria of controlling primary particle size, which allows us to keep the primary particle size small as their production rate increases. The primary particle sizes of Ni, Cu, Cu-Ni, Al, and Zn determined by SAXS measurements (cf. Table 4.2) correlate well with $\Delta m/\rho$ (cf. Table S4.2). The surface diffusion coefficient does not correspond to the melting point for alloys. In Cu-Ni (95-5 at.%), the NP surface state tends to behave similarly to that of pure Ni due to segregating Ni to the surface[45], thereby forming smaller primary particles than Cu and alike to Ni (cf. Table 4.2). Ag NPs apparently make an exception, showing a primary particle size "too large" with respect to the rules in Table 4.1. This is ascribed to strong coalescence on the substrate and/or under the electron beam that it has been frequently observed for noble metal NPs (cf. Figure S4.6a for Ag and Au in the SI). It is believed that this is not so for most other

metals because traces of reactive species exert a stabilizing effect (i.e., hindering particle coalescence).
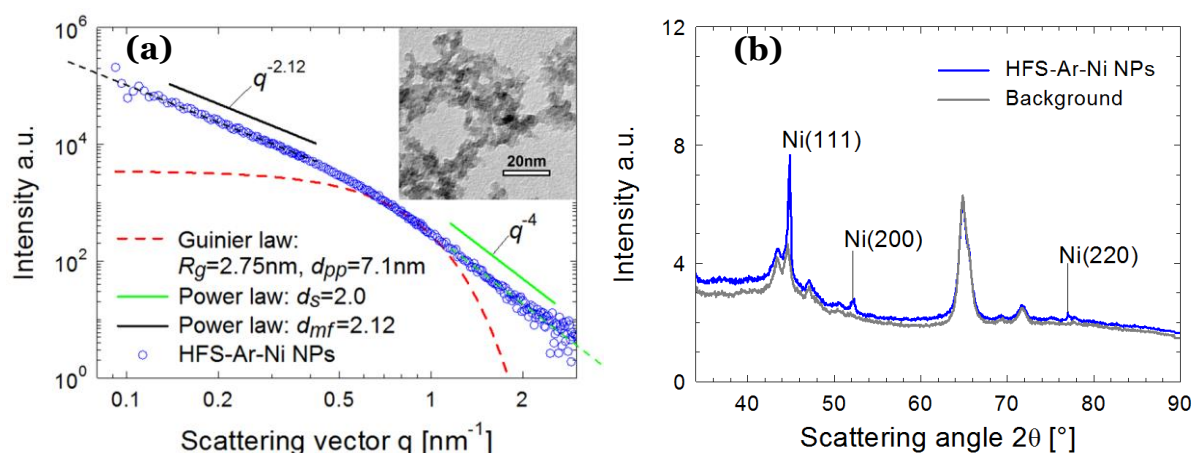
Figure 4.4 SAXS/WAXS and TEM measurements of Ni NPs generated at 3 kHz. (a) SAXS curve and TEM image (inset), which provides the small primary particles of a few nm in size. (b) WAXS curves.

In the SAXS/WAXS observations, the scattering intensity of deposited particles is measured as a function of scattering angle 2θ or scattering vector $q = (4\pi/\lambda)\sin\theta$ (the wavelength of the X-ray beam $\lambda = 0.154$ nm). Figure 4.4 shows the SAXS/WAXS results for Ni NPs generated at 3 kHz, whereas the data for other NPs are summarized in Table 4.2. The SAXS curve in a log-log plot shows two power-law regimes, and the values of their exponents P can be determined from the slopes of the linear parts (black and green lines). Due to the growth mechanism, the particle samples have fractal surfaces and form a mass fractal structure. The mass fractal describes the 3D network structure of agglomerates, whereas the surface fractal describes roughness of particle surface. In general, for surface fractals (with exponents $3<P<4$) the surface fractal dimension d_s is given by $d_s = 6-P$. For the two-phase structure with sharp boundaries and smooth surfaces, P is equal to 4. For mass fractals (with $1<P<3$) the mass-fractal dimension d_{mf} is equal to P, which describes the mass-fractal scaling inside the aggregates or agglomerates[46,47]. Ni agglomerates have d_{mf} of 2.12 and a smooth surface ($d_s = 2.0$). A "shoulder" occurs between two power-law regimes, as marked by a red-dash curve, yielding the gyration radius of the particles ($R_g = 2.75$ nm), thereby determining $d_{pp} \simeq 7$ nm ($d_{pp} = 2\sqrt{5/3}\,R_g$) [46,47]. This estimation is in line with the TEM observations (cf. inset in Figure 3a). Simultaneous

WAXS measurements identify the crystal phases of the resulting Ni NPs (cf. Figure 4.4b) by comparing them with the background peaks. The mean primary particle sizes d_{pp} and crystal phases of Cu, Al, Zn, Ag and Cu-Ni NPs generated at 3 kHz are reported in Table 4.2.

Table 4.2 The structural properties of HFS-generated (at ca. 3 kHz) monometallic and bimetallic NPs characterized by SAXS/WAXS.

Metallic NPs	SAXS	WAXS
	d_{pp} (nm)	Crystal phase
Ni	7.13	Ni
Cu	8.58	Cu, CuO [a)]
Al	11.53	Al
Zn	14.70	Zn, ZnO [a)]
Ag	26.51	Ag
CuNi	7.28	Cu, Ni, CuO[a)]

[a)] Occurrence of oxide crystal phases (e.g. CuO and ZnO) is probably due to the partial oxidation of NPs during the transport and handling as well as the presence of trace amounts of oxygen and/or water in the carrier gas during NP production.

4.3 Summaries

To summarize, this chapter has presented that a newly developed HFS allows the preparation of various metallic NPs of well-defined primary particles size and composition at yields of up to 130×10^{-3} g h^{-1} (operated at 3 kHz). Such yields of small NPs have never been achieved before by gas-phase spark ablation. The mass production rates for the NPs consisting of different materials increase linearly with spark frequency. As a result, HFS can achieve NP mass production rates of the order of 1 g h^{-1} as extrapolated from the results reported here. Considering that the generic process is easily scalable by parallelizing, the HFSs can achieve mass production rates to meet industrial demands. Besides the production capacity, the method also maintains consistency in product quality attributed to good kinetic control in a continuous manner.

In addition, the fast quenching makes this method feasible to produce thermodynamically metastable materials and to achieve efficient mixing on the

atomic or nanometer scale. In contrast to chemical routes, the system avoids using any precursor solutions, thereby allowing single-step synthesis of complex multicomponent metallic nanomaterials with high purity in a predictable and green manner. The present findings pave the way of upscaling an extensive variety of nanomaterial syntheses with respect to virtually unlimited mixing possibilities, providing a green and versatile approach to nanofabrication due to the compatibility of the method with existing fabricating processes. The produced NPs (many types, desirable composition) will be of interest to diverse fields such as material science, chemistry, and physics as well as applications from industrial partners.

4.4 Experimental section

The experimental setup includes a NP production system, online measurement system, and collection systems. The SDG consists of a pair of electrodes connected to a newly developed HFS. The SMPS system constitutes an [241]Am bipolar charger, a custom-made differential mobility analyzer (DMA), and a condensation particle counter (CPC; TSI Model 3775) [18]. Additional details of the experiments can be found in Section S4.3 in the SI.

Supplementary Information in Chapter 4

Supplementary Information is provided in the following pages, including applications of the spark produced NPs, the comparison between RLCS and HFS, experimental details, mass ablated per spark, the design of recycling flow system, electrode gap control system, the estimation of mass production rate, TEM images, and particle size distributions with a fixed Q/f, and the evidences for producing non-agglomerated singlet particles when utilizing an appropriate ratio Q/f.

S4.1 Applications of the spark produced nanoparticles (NPs)

Table S4.1 Representative applications of spark produced NPs (using frequencies < 1 kHz).

Nanomaterials	Reference(s)	Applications	Notes
Mg-Ti	30	H_2 storage	alloy NPs
Pd-Au	3	optical H_2 sensing	nanoparticulate films
Au	32	water splitting	plasmonic effect
Ag	6	solar cells	nanoparticle film
Cu	48	catalysis	catalysing Ag deposition on a polymer substrate
Pd-Ag, Pt-Ag, Au-Ag	25	catalysis	bimetallic nanostructures for catalytic CO conversion
TiO_2/Graphite oxide	49	photocatalysis	nanocomposites for photocatalytic hydrogenation
Ag	27	spectroscopic	nano dots and nano rings
Ag	26	antibacterial	bioaerosol filtration
Au	50–52	growing nanowires	nano seeds
Pd (Cu)/graphene	34	synthesizing core-shell NPs	metal core, multilayer graphene shell
Au/Ag	20	synthesizing core-shell NPs	Au-core, Ag shell; Au nano-seed injected into Ag precursor solution
Au/Ag, Au/polystyrene latex	31	synthesizing core-shell NPs	coagulational deposition

S4.2 Comparison between RLCS and HFS

Figure S4.1 shows a simple RLC spark (RLCS) circuit and a newly developed switching circuit that decouples charge and discharge cycles by adding a number of fast electronic switches. In the RLCS, the capacitors are charged by a constant current supply. A spark discharge between the two electrodes is formed when the voltage over the capacitor reaches the breakdown voltage. After this discharge, the charging of the capacitor starts again and this process repeats itself at a certain frequency.

RLCS

Maximum frequency : ca. 500 Hz

HFS

Maximum frequency: 25 kHz
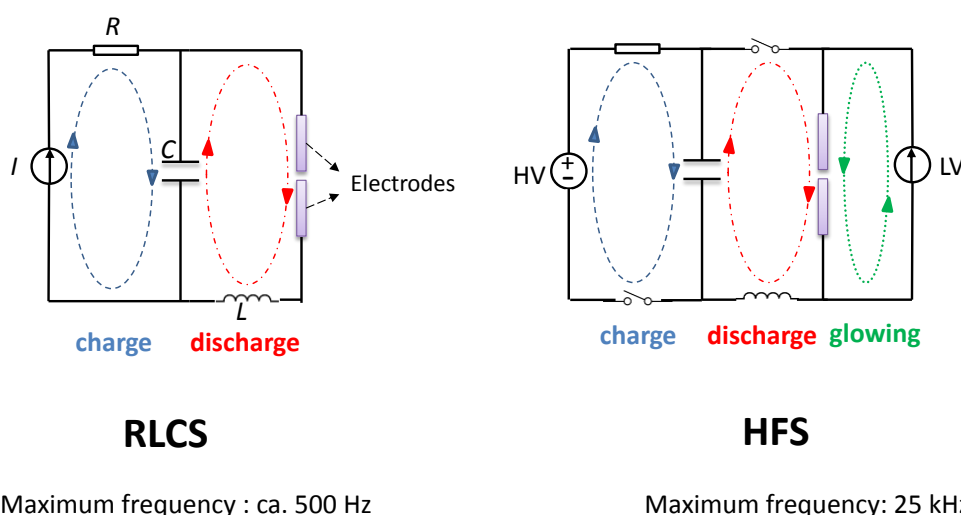
Figure S4.1 Schematic representation of RLC spark circuit (RLCS) and the high frequency sparks (HFS; i.e., a switching spark circuit) decoupling charge and discharge cycles. Current paths during charge and discharge processes as well as for the continuous glow current are presented by the dashed cycles of different colours (dark blue: charge; red: discharge; green: glow current).

By contrast, the HFS separates charge and discharge in the RLC circuit and the sparks are superimposed onto a continuous low glow current between consecutive sparks[39]. This glow current is three orders of magnitude lower compared to that needed to sustain an arc[38]. As a result, it does not result in the ablation of a significant amount of mass from the electrodes[53] and guarantees that the plasma between the electrodes does not extinguish completely between two successive

sparks. The applied voltage required for igniting each spark discharge is also kept low because of this current. The spark energy is proportional to the capacitance and to the square of the discharge voltage. Considering that the HFS has a fixed capacitance and applies a constant voltage, constant and low spark energy can thus be well maintained for each spark[8,18,37]. By keeping a low and constant spark energy and simply increasing the spark repetition frequency, it is easy to increase the mass production rate of NPs.

S4.3 Experimental

Figure S4.2 shows the schematic layout of the experimental setup that was used to investigate the mass production rate of NPs. It consists of a NP production system (i.e., a spark discharge generator; SDG), online measurement system (i.e., a scanning mobility particle sizer[54]; SMPS), and collection systems (i.e., a filter, and a mini-particle sampler;[55] MPS). The SDG consists of a pair of electrodes connected to a newly developed HFS. The SMPS system[37] constitutes an [241]Am bipolar charger, a custom-made differential mobility analyzer (DMA), and a condensation particle counter (CPC; TSI Model 3775) [54].

S4.3.1 NP production: SDG

The SDG consists of a pair of electrodes connected to a newly developed HFS[8]. The HFS can achieve a spark repetition frequency up to 25 kHz. In contrast to the RLCS[18], the HFS with a fixed capacitance C_{ca} of 45 nF decouples charge and discharge cycles[8]. Doing so in the HFS allows the applied voltage U_C between the electrodes set independent of the breakdown voltage. A low current source in the switch circuit provides a continuous low current in the discharge gap. The continuous low-power discharge within the gap reduces the breakdown voltage of the carrier gas, allowing stable operation at $U_C = 1.2$ kV for gap distances up to 2 mm. For all the experiments, the energy per spark was fixed to 32.4 mJ (estimated by $E = 0.5\ C_{ca}U_C^2$). In order to obtain the spark repetition frequency and monitor the spark oscillation, an oscilloscope (HAMEG instruments GmbH, HMO1024) was connected to the HFS using 1:100 HV probes (Testec HV250).
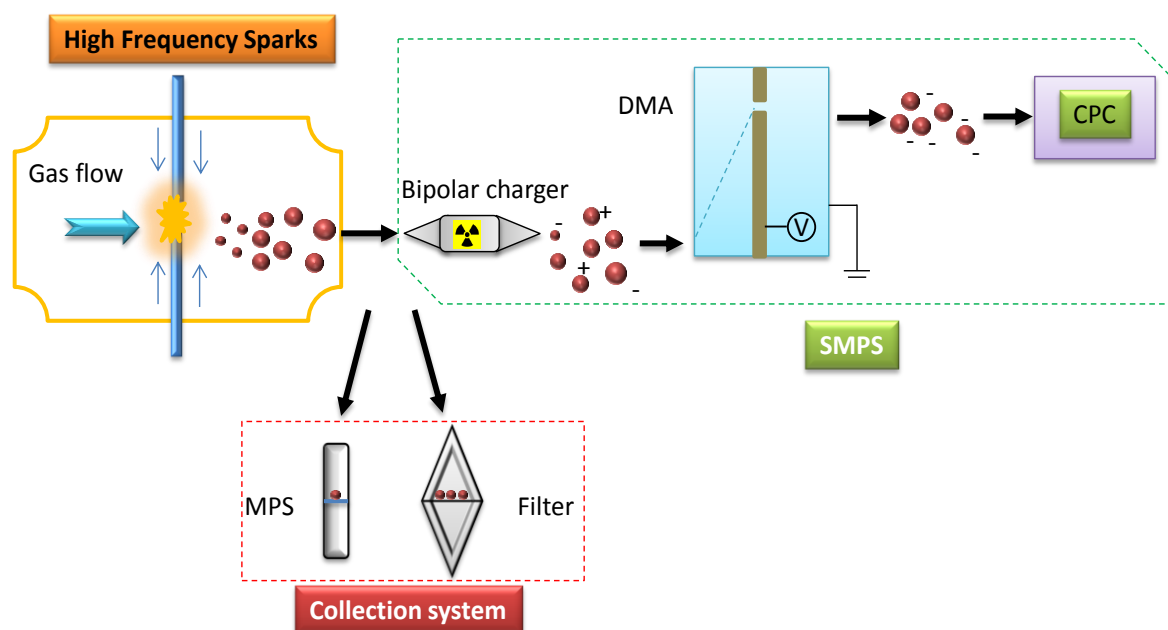
Figure S4.2 Schematic layout of the experimental setup. Key: DMA, differential mobility analyser; CPC, condensation particle counter; MPS, mini-particle sampler.

S4.3.2 Experimental materials

The SDG has been used with pairs of solid electrodes made of Au, Al, Cu, Ag, Ni, Cu-Ni (95-5 at.%), or Zn (all of them have 99.99% purity) having a diameter of 3 mm and a length of 25 mm (MaTecK GmbH) as shown in Figure S4.2. In all cases, the two electrodes were facing each other with a gap length variable up to 2 mm. A continuous inert gas (Ar, purity 99.999%) flushed through the gap at a rate of 13 standard litres per minute (slm) and a coaxial flow rate of 7 slm (cf. four blue arrows around the pair of electrodes).

S4.3.3 Online measurement system: SMPS

An SMPS was used to measure the size distribution of the NPs produced by the HFSs[56]. The system consists of an aerosol charge neutralizer, a differential mobility analyser (DMA) and a condensation particle counter (CPC). The neutralizer located upstream of the DMA brings the particles into a charge equilibrium[57]. The DMA operated with a closed-loop sheath flow system classifies particles based on their

electrical mobility. Subsequently, the CPC measures particle concentrations (up to 10^7 cm^{-3}).

S4.3.4 Collection systems for offline characterization

The samples from the collection systems are characterized by transmission electron microscope (TEM; JEOL JEM-1400, and Philips CM12), and a custom-built small- and wide-angle X-ray scattering (SAXS/WAXS) laboratory camera[46]. TEM measurements provide the information of particle morphologies. The MPS was used to collect NPs onto the TEM grids (S143-3 Q'foil 1.2/1.3 400 Cu) with holes, through which the aerosol flow passed, and some particles were subsequently collected[55]. The non-destructive SAXS/WAXS technique allows simultaneous measurements of the primary particle, as well as quantitative determination of the crystallite properties, such as the co-existence of crystal phases, and their fractions[46,47]. The samples for SAXS/WAXS were collected on membrane filters (HVHP09050 Durapore PVDF with 0.45 µm pore size and 90 mm in diameter) using a custom-made filter holder[58].

S4.4 Mass ablated per spark

Table S4.2 Physical constants of the applied electrode materials and Δm determined by the slopes of linear relations shown in Figure 4.1 as well as $\Delta m'$ estimated gravimetrically

Materials	Density (g/cm^3)	H_e ($\times 10^6$ J/kg)	H_m ($\times 10^5$ J/kg)	T_b (K)	T_m (K)	C_{ps} (J/(K kg))	Δm ($\times 10^{-6}$ mg)	$\Delta m/\rho$ ($\times 10^{-10}$ cm^3)	α (%)	$\Delta m'$ ($\times 10^{-6}$ mg)
Zn	7.14	1.8	1.1	1180	693	392	6.6	9.24	0.045	4.5
Ag	10.49	2.4	1.0	2435	1235	234	4.9	4.67	0.043	3.6
Al	2.70	1.1	4.0	2743	933	896	2.4	8.89	0.097	1.9
Cu	8.96	4.7	2.1	2835	1358	382	3.6	4.02	0.065	3.4
Au	19.30	1.7	6.4	3243	1337	129	13	6.74	0.088	13
Ni	8.91	6.4	1.7	3003	1728	442	2.5	2.81	0.061	3.8

The mass ablated per spark can be estimated by the evaporation model expressed as[59]:

$$\Delta m \approx \frac{\alpha E}{c_{ps}(T_b - T) + H_m + H_e} \tag{S4.1}$$

Here, E is the energy per spark (J); α is the fraction of spark energy consumed for particle production, which can be empirically estimated to be in the order of ca. 0.1 %[23]; c_{ps} (J K^{-1} kg^{-1}) is the heat capacity of the solid material; T and T_b are the room temperature, and the boiling point of the materials, respectively; H_m and H_e (J kg^{-1}) are the enthalpies of melting and vaporization of the materials. Values of the properties of all material used in this study are given in Table S4.2. Δm represents the slope of the linear fittings to the measurements as shown in Figure 4.1 in Chapter 4.

The linear relations between production rate and frequency of different materials (Figure 4.1) demonstrate that Δm is unchanged. This also indicates that the averaged values of α is also unchanged (cf. equation (S4.1)) for a given composition of electrode material and carrier gas. The values of α were derived from equalizing the slopes of linearity shown in Figure 4.1 to equation (S4.1). Its values, in principle, can be directly used for estimating the mass production rates of different materials. It should be noted that this unknown parameter α can also be theoretically obtained with precise calculation of the multi-events of the energy transfer[60]. However, even if theoretical determination is available, it can only represent one single spark, as shown in equation (S4.1). Since not all the sparks behave unchangeably under real operations (the influence from electrode surface, carrier gas conditions within the inter-electrode gap, irregular participation of generated clusters in the plasmas), the empirical determination of its value seems more practical.

$\Delta m'$ determined gravimetrically at spark repetition of 1 kHz, which assumed that each spark behaves the same during the time of operation, is smaller than that of using equation (S4.1). This can be attributed to the change of α at higher f, where a fraction of splashing particles can be formed. In contrast to $\Delta m'$, Δm is derived from the slopes of the linear relations between mass production rate and spark repetition frequencies.

S4.5 The design of recycling flow system

Figure S4.3 depicts the recycling flow system in the HFS NP production, which can be capable of handling a high flow rate of ca. 500 slm. A gas supply is placed upstream of the HFS. This gas quenches the spark and carries away the aerosol NPs to the collection system. Pressure and temperature of the gas are monitored. The pump system drives the flow and also defines the flow rate. A cooling system is used to remove heat generated by the pump system and the HFS. In addition, there is an outlet for online measurement of the produced NPs. In principle, this recycling flow system also allows the operation of multiple HFSs that can deliver the NPs on an industrial scale.
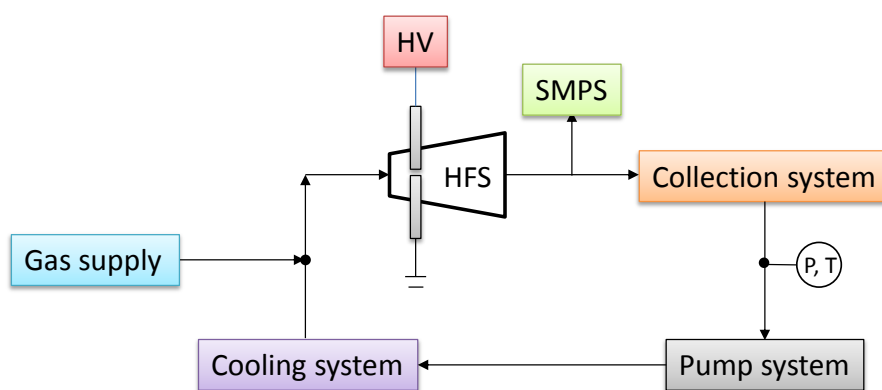
Figure S4.3 Schematic layout of the recycling flow system. Such setup configuration can also allow the operation of the multiple HFSs in parallel.

S4.6 Electrode gap control system

In order to enable continuous and stable operation of HFS, a robust electrode feeder system needs to be designed. For example, when the HFS is operated at 25 kHz, the consumption rate of Au solid electrodes with a diameter of 3 mm is estimated to be 8 mm h^{-1}. Such a rapid electrode consumption rate leads to discontinuous production mode, since the gap distance for a stable spark is only below ca. 2 mm for a given voltage of 1.2 kV in the HFS.

Considering that a constant voltage U_c over the electrodes has been applied in the HFS, it is not feasible to control the gap distance from a direct measurement of this voltage signal as the RLCS does. In addition, the spark resistance R_{spark} is

independent of the gap distance[61]. This means that the peak current $I_{peak} = U_c/R_{spark}$ is also constant. As a result, both the voltage and peak current cannot be used to control the gap distance.

The resistance of the glow current R_{GC} (cf. Figure S4.1) between the successive sparks can be expressed as:

$$R_{GC} \propto \frac{d_{gap}}{A_{cs}} \tag{S4.2}$$

where A_{cs} is the cross sectional area of the glow current, and d_{gap} is the electrode gap distance. The gap voltage U_{gap} must also depend on d_{gap}, which can be written as:

$$U_{gap} \propto \frac{I_{GC}}{A_{cs}} d_{gap} \tag{S4.3}$$

where I_{GC} is the glow current between two successive sparks, and I_{GC}/A_{cs} is the glow current density, which can be assumed as a constant[61]. Therefore, equation (S4.3) is simplified to:

$$U_{gap} \propto d_{gap} \tag{S4.4}$$

This linear relation is further confirmed by the measurements shown in Figure S4.4.

Figure S4.4 shows that the mean gap voltage of the glow current between successive sparks is linearly dependent on the gap distance. A custom-made electrical device (cf. Figure S4.5) is applied to derive the control signal V_{mean} from the voltage U_{gap} across the sparks. It forms the difference between the potentials of the electrodes and integrates the potentials over the time to form the averaged values. Consequently, the electrode gap can be monitored by V_{mean} that varies monotonically with the gap distance as shown in equation (S4.4).
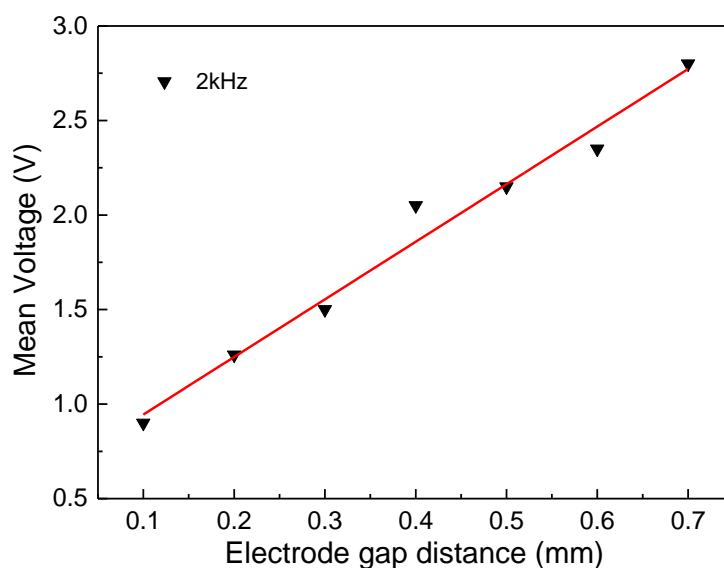
Figure S4.4 Mean gap voltage V_{mean} of the glow current as a function of gap distance between two Al electrodes in Ar at the spark frequency of 2 kHz. The measurements (points) are matched with the line.
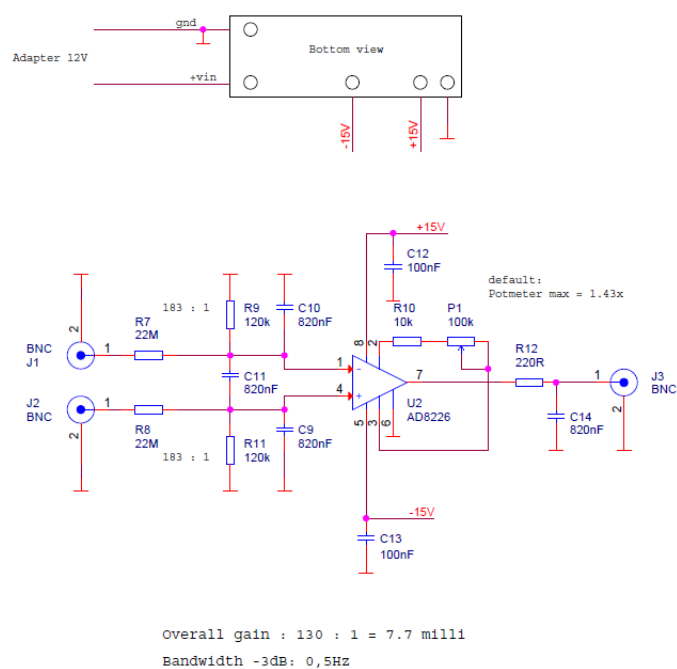
Figure S4.5 Differential amplifier measuring the mean (time averaged) gap voltage. The amplifier gain is set to 130:1. Maximum output voltage is ±15 V. The bandwidth is 0.5 Hz.

S4.7 The mass production rate estimated by the size distribution of the particles

A scaling relation describing an agglomerate with a mobility diameter d_{mb} consisting of primary particles with a mean primary particle size d_{pp} is given by[62]:

$$\frac{M_{\text{ag}}(d_{\text{mb}})}{m_{\text{pp}}} = C_1 \left(\frac{d_{\text{mb}}}{d_{\text{pp}}}\right)^{D_{\text{f}}} N_{\text{ag}}(d_{\text{mb}}) \tag{S4.5}$$

where C_1 can be approximated with unity[63]; D_{f} is the mass-mobility exponent[64]; m_{pp} is the mass of one primary particle, and $M_{\text{ag}}(d_{\text{mb}})$ and $N_{\text{ag}}(d_{\text{mb}})$ are the mass density and the number concentration of the agglomerates as a function of a mobility diameter d_{mb}. Assuming that the primary particles have the density of the bulk material ρ, the sum of the mass of agglomerates M_{ag} is given by:

$$M_{\text{ag}} = \rho \frac{\pi}{6} d_{\text{pp}}^{3} \int_{0}^{\infty} \left(\frac{d_{\text{mb}}}{d_{\text{pp}}}\right)^{D_{\text{f}}} \frac{\mathrm{d}N_{\text{ag}}(d_{\text{mb}})}{\mathrm{d}d_{\text{mb}}} \mathrm{d}d_{\text{mb}} \tag{S4.6}$$

Assuming that D_{f} is a constant for a specific size distribution and a constant d_{pp}, the size distribution of the aerosol NPs can always be fitted to a lognormal function with a total particle number concentration N_{tot}, a geometry mean diameter d_{pm}, and a geometric standard deviation σ_{g} [65]. Therefore, the solution of equation (S4.6) is given by:

$$M_{\text{ag}} = \frac{\pi}{6} \rho d_{\text{pp}}^{3-D_{\text{f}}} N_{\text{tot}} \exp\left(\frac{D_{\text{f}}^{2}\left(\ln\sigma_{\text{g}}\right)^{2}}{2}\right) (d_{\text{pm}})^{D_{\text{f}}} \tag{S4.7}$$

Assuming particle losses are negligible during aerosol NP transport, the mass production rate $\dot{m}$ can be expressed as:

$$\dot{m} = M_{\text{ag}} Q \tag{S4.8}$$

Substituting equation (S4.7) to equation (S4.8), one can obtain:

$$\dot{m} = \frac{\pi}{6} Q \rho d_{pp}^{3-D_f} N_{tot} \exp\left(\frac{D_f^2 (\ln\sigma_g)^2}{2}\right) (d_{pm})^{D_f} \tag{S4.9}$$

N_{tot}, σ_g and d_{pm} are known quantities determined by a lognormal particle size distribution (i.e., SMPS measurements), whereas d_{pp} can be obtained by analysing TEM images or SAXS measurements. The only unknown parameter D_f can be estimated by matching equation (S4.9) to the gravimetric measurements.

The SMPS measurements show that the Ni NPs have the highest concentration among the materials tested in this study (cf. Figure 4.3a in Chapter 4), while their mass production rate is relatively low (cf. Figure 4.1 in Chapter 4). This apparent discrepancy can be attributed to that the larger surface area of Ni agglomerates resulting from their smaller primary particles (see Table 4.2 in Chapter 4) leads to a larger mobility diameter for the same mass per agglomerate. Another likely reason for the larger mobility diameter is that Ni NPs probably tend to form linear chain-like structures (cf. Figure S4.8a) due to their magnetism[66]. Larger particles results in fewer diffusional losses when transported through the tubing of the experimental setup, explaining its higher concentration.

Table S4.3 Comparison of the mass production rates $\dot{m}$ estimated on the basis of the size distributions of the particles (i.e., SMPS measurements), and that is determined by the gravimetric measurements at a spark repetition frequency of 1 kHz.

Materials	d_{mp} (nm)	σ_g	N_{tot} (#/cm³)	D_f	M_{ag} (mg/cm³)	$\dot{m}$ (mg/h)
Al	56	1.52	6.34×10^7	2.26	0.73×10^{-5}	8.8
Ni	68	1.56	9.68×10^7	1.95	0.78×10^{-5}	9.5
CuNi	48	1.59	5.90×10^7	2.11	0.93×10^{-5}	11.3
Cu	41	1.71	5.36×10^7	2.24	1.09×10^{-5}	13.3
Ag	38	1.72	4.59×10^7	2.37	1.43×10^{-5}	17.5
Zn	51	1.81	4.55×10^7	2.21	1.98×10^{-5}	24.2
Au	--	--	-	-	-	46.5

Table S4.4 The mass production rate $\dot{m}$ determined by the size distributions of Cu NPs generated at different frequencies ranging from 1.0 to 4.2 kHz.

Frequency (kHz)	M_{ag} (mg/cm³)	$\dot{m}$ (mg/h)	D_f	D_f (15% losses)
1.0	1.09×10^{-5}	13.3	2.24	2.18
1.4	1.50×10^{-5}	18.4	2.35	2.29
1.8	1.95×10^{-5}	23.9	2.35	2.29
2.5	2.70×10^{-5}	32.4	2.44	2.37
3.3	3.32×10^{-5}	41.8	2.44	2.39
4.2	4.38×10^{-5}	53.6	2.47	2.41

Table S4.4 shows the mass production rate determined by size distributions of Cu NPs produced at different frequencies (from 1.0 to 4.2 kHz). The substantially increased concentrations of agglomerated NPs at higher spark frequency (cf. Figure 4.3b in Chapter 4) and the value of mass-mobility exponent, which correlates well with previous publications[64,67], imply that equation (4.2) can be used to estimate the mass production rate. The mass-mobility exponent ranges from 2.24 to 2.47 (cf. Table S4.4). Assuming that particle losses are in the order of 15% during particle transport to the SMPS system, this range accordingly changes from 2.18 to 2.41. The values of M_{ag} and the mass-mobility exponent of different materials at 1 kHz (cf. Figure 4.3a in Chapter 4) and Cu NPs at different spark frequencies (cf. Figure 4.3b in Chapter 4) are summarized in Tables S4.3 and S4.4.

S4.8 TEM images of NPs consisting of different materials

Figure S4.6 shows TEM images of Au, Zn, Al, Ag, Ni, and Al NPs produced by HFS at the frequency of 1 kHz. The purpose of TEM images of different materials is to show the primary particles within the agglomerates. To produce non-agglomerated singlet particles can be found in the earlier work (cf. Chapter 2)[18]. Combining the TEM imaging with the SMPS measurements (cf. Figure 4.3 in Chapter 4), it is seen that the number concentration profile in the large size range (> 100 nm) is mostly attributed to the agglomerates rather than the 'splashing particles'.
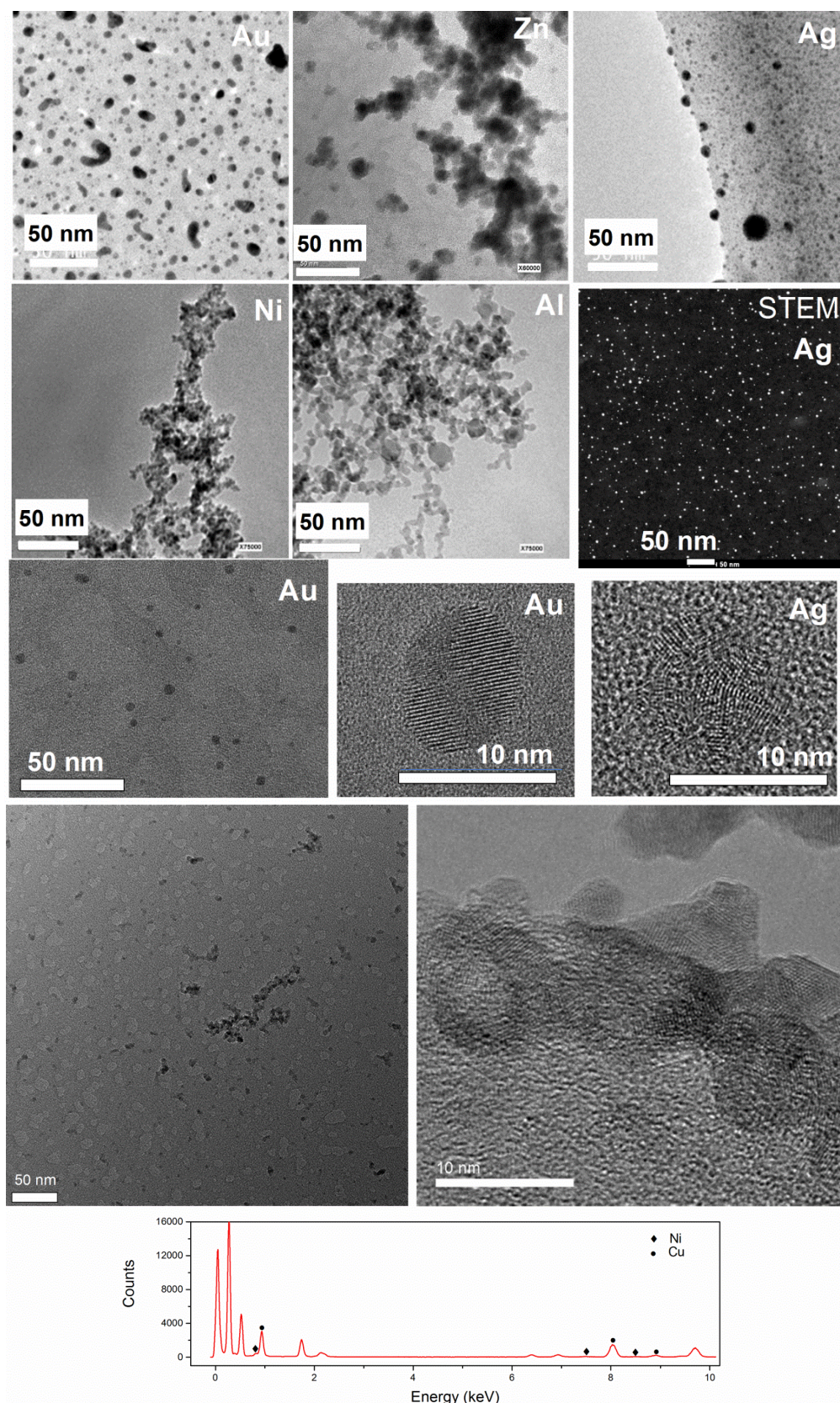
Figure S4.6. TEM images of Au, Zn, Al, Ag, Ni, and Al NPs generated by HFS at the frequency of 1 kHz, the spark energy of 32.4 mJ and the flow rate of 20 slm. The TEM grids were attached on the filter membrane inside a custom-made filter. The distance

between the filter membrane and the sparks is ca. 20 cm. Due to long deposition (i.e., high NP surface coverage on substrates; ca. 20 min), the agglomerates form on the TEM grid (the images in the first row and Ni, Al in the second row). The micrographs for Zn, Ni and Al show the small primary particles within the agglomerates. To show the non-agglomerated NPs, HRTEM and STEM images are provided for Au and Ag NPs (the third row) with highly crystalline structure collected in a short time (ca. 1 s, to guarantee a low surface coverage of NPs on substrates). TEM images of CuNi NPs (the fourth row) and the associated EDS (assembled at the bottom) show that the composition of Cu-Ni NPs (97:3) is similar to that of the starting electrodes (95:5), and their crystal structure is also exhibited here.

The primary particle sizes of both Al and Ni NPs are ca. 5 nm. Note that the primary particle size of Zn NPs is disproportionately large (ca. 15 nm), which can be attributed to its lowest melting point out of the materials tested in this work, indicating a lower solid-state surface diffusion coefficient. Another reason for this is that the larger amount of material ablation makes the effective density of gas-vapour mixture higher (flow rate is the same as other materials), which promotes further coalescence in a hotter initial zone. Zn also possesses a larger value of $\Delta m/\rho$ among other materials tested in this chapter.

From the micrographs obtained from agglomerates in Figure S4.6, it can be seen that for the primary particle diameters d_{pp} for Ni, Al and Zn: d_{pp} (Ni) < d_{pp} (Al) < d_{pp} (Zn), corresponding well with the indication of $\Delta m/\rho$ (cf. Table S4.2), which provides the order of the materials tested in this work: d_{pp} (Cu-Ni) < d_{pp} (Ni) < d_{pp} (Cu) < d_{pp} (Ag) < d_{pp} (Au) < d_{pp} (Al) < d_{pp} (Zn). In the case of Ag and Au, the criteria lead to opposite trends due to the fact that the noble metallic NPs are prone to coalesce after the deposition and the observation of particle coalescence under electron beam of TEM. Concerning the comparison of Cu with CuNi (95-5 at.%), both indicators (e.g., $\Delta m/\rho$ and surface diffusion coefficient) are similar, but CuNi exhibits a smaller primary particle size (cf. Table 4.2). This may be due to the Ni segregating to the surface and reducing the surface diffusion coefficient. The melting point of a given material can only be considered as a reliable indicator of surface diffusion for pure NPs.

The non-agglomerated Au and Ag NPs were collected in a short time (ca. 1 s), indicating that the agglomerates are formed on substrates rather than in the gas phase. This makes the deposition of non-agglomerated singlet particle possible. Note that such singlet particles should maintain the low surface coverage. In the case of high surface coverage, one can either rapidly coat the NPs in the gas phase before deposition or drastically decrease the temperature below the threshold one for hindering particle coalescence.

S4.9 Particle size distributions with a fixed *Q/f*

Figure S4.7 shows the size distributions of Ag particles at two different spark repetition frequencies and gas flow rates, i.e., by keeping the same ratio *Q/f*. Thus similar particle size distributions are obtained. The slightly low concentration at higher flow rate is due to the fact that the resulting turbulence leads to substantial diffusional losses as reported in Chapter 3[23]. It should be mentioned that each size distribution measurement was repeated at least five times to assure repeatability. The uncertainties in the measurements were below 5%.
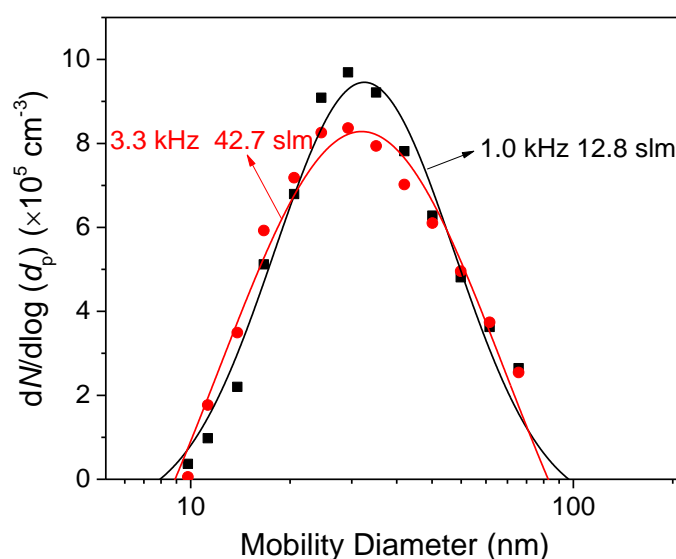
Figure S4.7 Size distributions of Ag particles at different carrier gas flow rates that linearly increased with the spark repetition frequency at a fixed spark energy of 32.4 mJ.
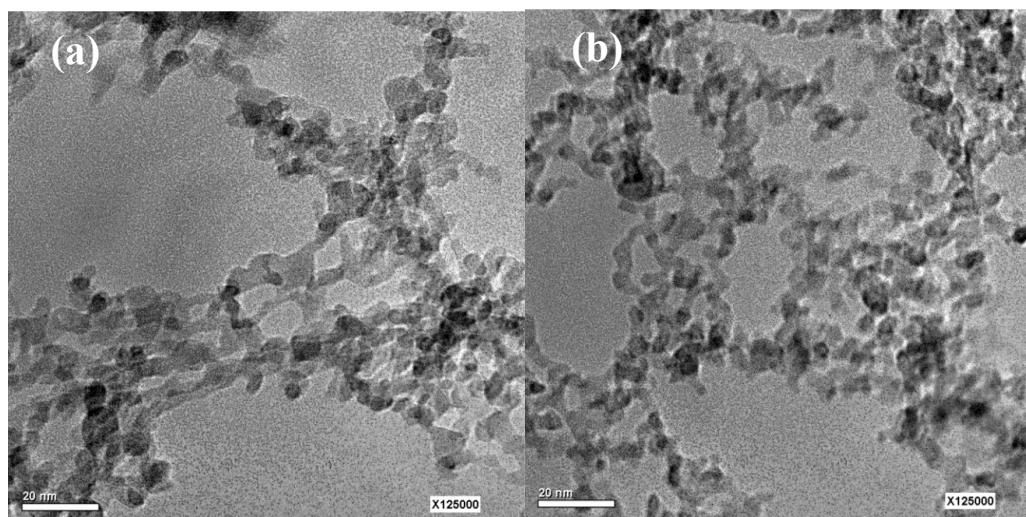
Figure S4.8 TEM images of Al agglomerates produced by the HFS at f = 2 kHz, Q = 30 slm and E = 32.4 mJ (a), and at f = 3 kHz, Q = 45 slm and E = 32.4 mJ (b). The TEM grids were attached on the filter membrane inside a custom-made filter and the deposition was conducted for 10 min. The distance between the filter membrane and the sparks is ca. 20 cm.

S4.10 Mass production rate of NPs in dry gas-phase synthesis methods

In principle, any production rate is feasible, because spark ablation, in contrast to most other methods, is easily scalable by simply numbering up the electrode pairs while maintaining consistency in product quality, attributed to good kinetic control in a continuous manner. Scalable methods for high-yield synthesis of particles a few nm in size hardly exist, especially when avoiding any liquid precursors and post-processing is desired. In addition, the method enables the production of thermodynamically metastable materials due to the associated rapid quenching[17,23]. Table S4.5 compares the nanoparticle production rates of the method with those of other scalable techniques that come close to the size range of this work. It should be noted that it is much easier to achieve a high production rate for larger particle sizes, which explains the high rates reported for arc discharges[69]. Table S4.5 does not include flame and laser ablation methods, because the former employs liquid precursors and the latter requires expensive laser sources which inhibit further scalability.
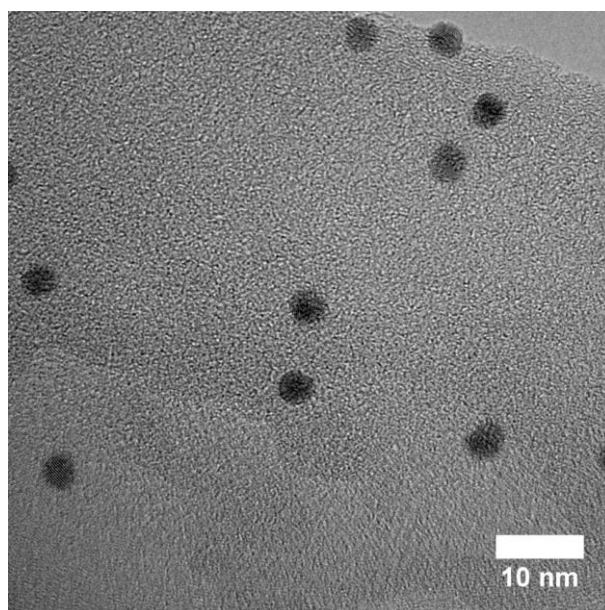
Figure S4.9 HRTEM image of non-agglomerated Au singlet NPs generated by low-frequency spark ablation (Q = 50 slm, f = 60 Hz and E = 16 mJ). The particle deposition was carried out by custom-made electrostatic precipitator downstream of the DMA for ca. 2 h. The distance from the TME gird to the sparks was ca. 50 cm.

Table S4.5 Mass production of NPs in gas-phase synthesis methods except flame aerosol technology and laser ablation.

Techniques	Pressure (Pa)	Production rate (g/h)	Particle size (nm)	Material
Plasma[68]	180-1860	0.014-0.052	2-8	Si
Arc discharge[69]	ambient pressure	10	~100	Metals
Spark ablation	ambient pressure	~1(one electrode pair)	0.5-20	Conducting, semiconducting and mixed NPs
hot-wall aerosol reactors[70–72]	2500~15000	0.005~1	ca. 10-1000	Si-based
inert gas condensation[73–75]	10^{-7}~10^{-5}	0.005~0.5	2-100	metals and ceramics

Figure S4.9 evidences the production of non-agglomerated singlet particles when utilizing an appropriate ratio Q/f in the HFS. On the other hand, the coverage on substrates is also a major determinant for collecting individual singlet particles. This is because high purity singlets strongly coalesce due to collisions, forming the agglomerates. Due to the absence of any liquid chemicals, the prevention of further

coalescence is difficult here. However, in combination with insights from the chemists, this should be easily addressed by using some gaseous chemicals, which can form a protecting layer on the particle surfaces.

S4.11 SAXS/WAXS measurements for different NPs

(g)

(h)

(i)

(j)

(k)

(l)
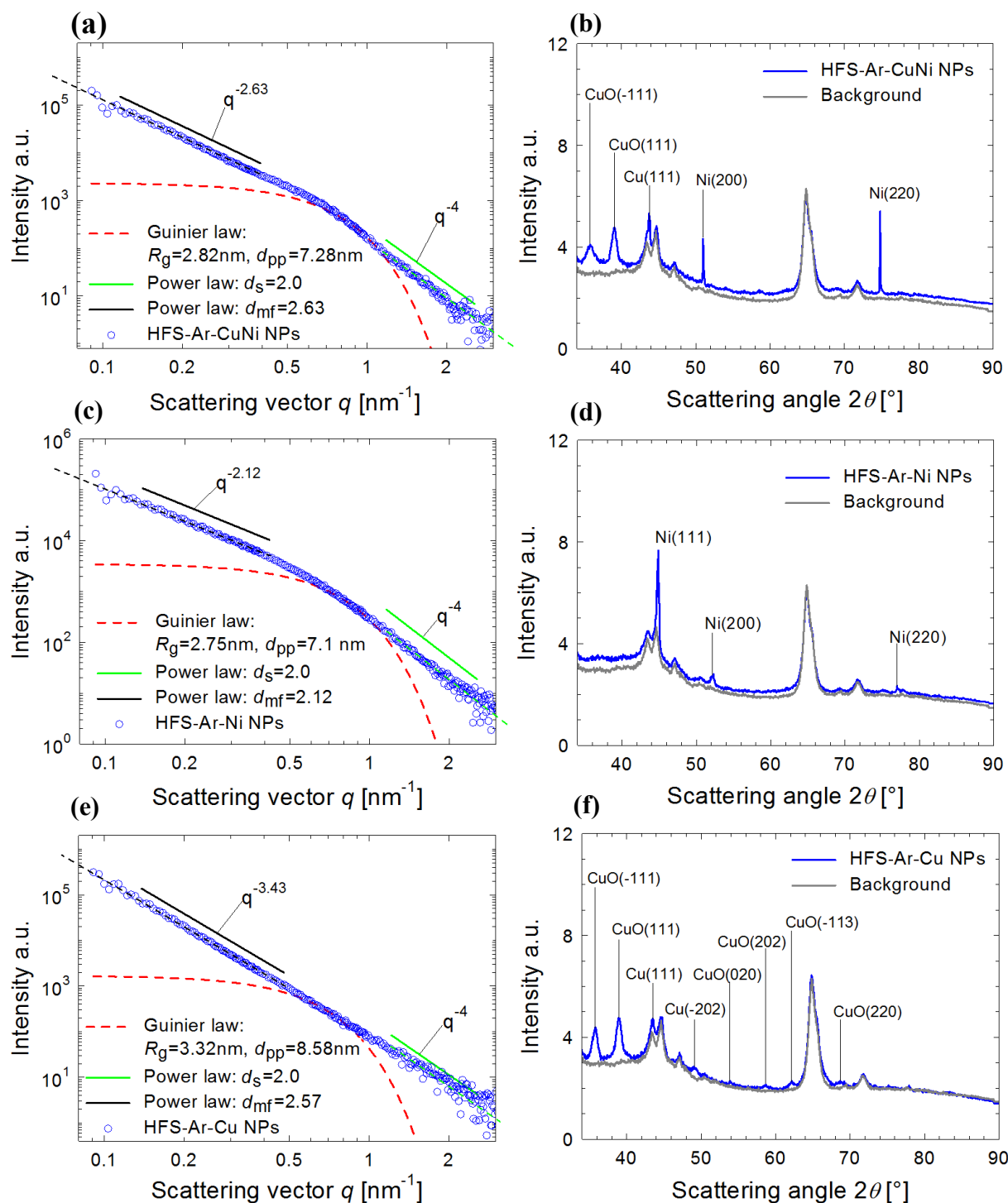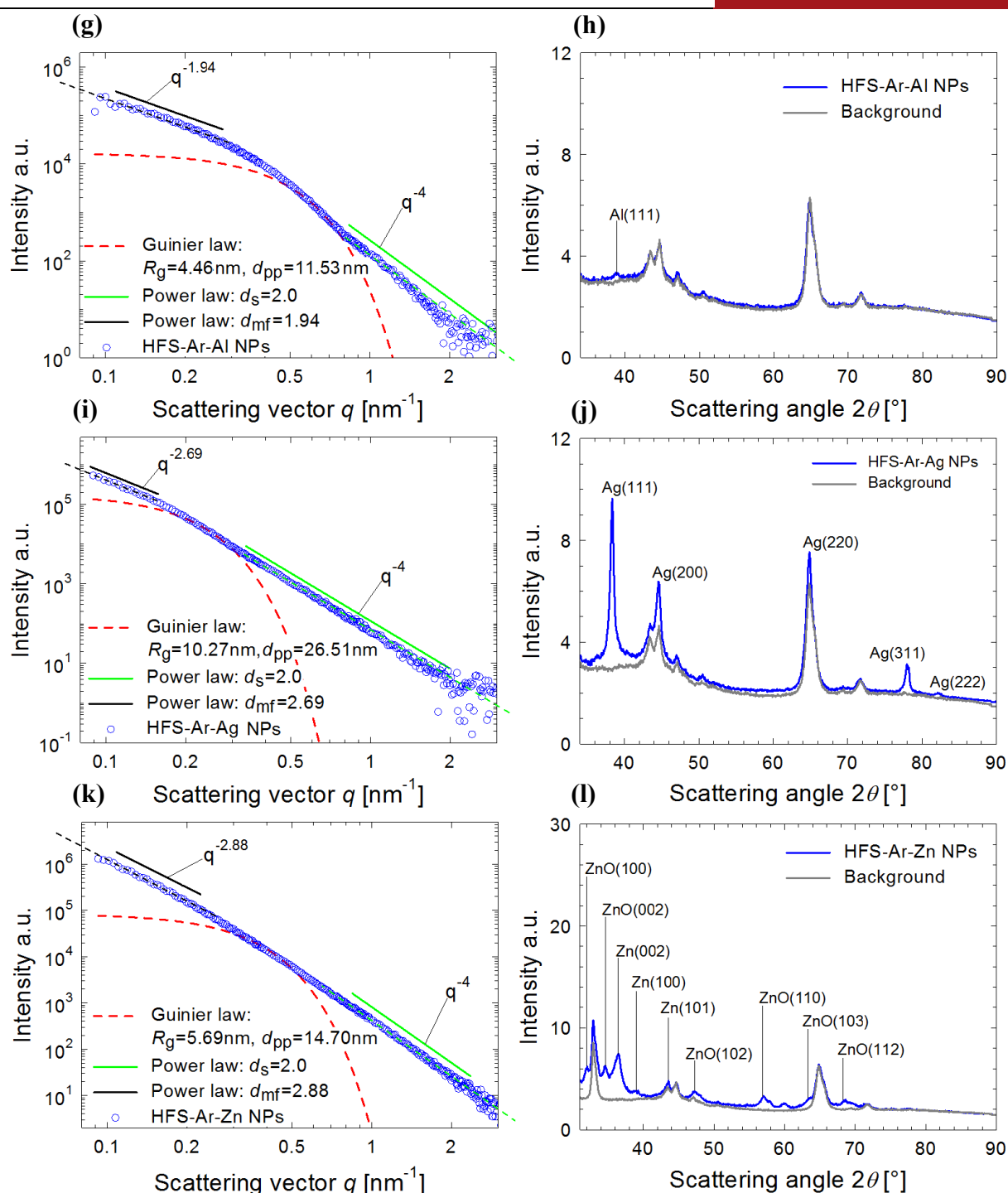
Figure S4.10. SAXS/WAXS measurements for various NPs. (a, b) CuNi, (c, d) Ni, (e, f) Cu, (g, h) Al, (i, g) Ag, (k, l) Zn. This figure is summarized in Table 4.2 in Chapter 4.

References

1   Q. Zhang, Y. Yan and G. Chen, *Adv. Sci.*, 2015, **2**, 1500176.

2   S. Kondrat, P. Wu, R. Qiao and A. A. Kornyshev, *Nat. Mater.*, 2014, **13**, 387–393.

3   N. A. Isaac, P. Ngene, R. J. Westerwaal, J. Gaury, B. Dam, A. Schmidt-Ott and G. Biskos, *Sensors Actuators B Chem.*, 2015, **221**, 290–296.

4   C. Kuru, C. Choi, A. Kargar, D. Choi, Y. J. Kim, C. H. Liu, S. Yavuz and S. Jin, *Adv. Sci.*, 2015, **2**, 1500004.

5   P. Thoniyot, M. J. Tan, A. A. Karim, D. J. Young and X. J. Loh, *Adv. Sci.*, 2015, **2**, 1400010.

6   T. V. Pfeiffer, J. Ortiz-Gonzalez, R. Santbergen, H. Tan, A. Schmidt-Ott, M. Zeman and A. H. M. Smets, *Energy Procedia*, 2014, **60**, 3–12.

7   C. Zuo, H. J. Bolink, H. Han, J. Huang, D. Cahen and L. Ding, *Adv. Sci.*, 2016, 1500324.

8   T. V. Pfeiffer, J. Feng and A. Schmidt-Ott, *Adv. Powder Technol.*, 2014, **25**, 56–70.

9   H. T. Chung, J. H. Won and P. Zelenay, *Nat. Commun.*, 2013, **4**, 1922.

10   N. A. Frey, S. Peng, K. Cheng and S. Sun, *Chem. Soc. Rev.*, 2009, **38**, 2532–2542.

11   J. Chang, X. Huang, G. Zhou, S. Cui, P. B. Hallac, J. Jiang, P. T. Hurley and J. Chen, *Adv. Mater.*, 2014, **26**, 758–764.

12   Y. Xia, T. D. Nguyen, M. Yang, B. Lee, A. Santos, P. Podsiadlo, Z. Tang, S. C. Glotzer and N. A. Kotov, *Nat. Nanotechnol.*, 2011, **6**, 580–587.

13   T. K. Sau and C. J. Murphy, *J. Am. Chem. Soc.*, 2004, **126**, 8648–8649.

14   G. H. Jeong, Y. W. Lee, M. Kim and S. W. Han, *J. Colloid Interface Sci.*, 2009, **329**, 97–102.

15   M. R. Buck and R. E. Schaak, *Angew. Chemie Int. Ed.*, 2013, **52**, 6154–6178.

16   J.-M. Lim, A. Swami, L. M. Gilson, S. Chopra, S. Choi, J. Wu, R. Langer, R. Karnik and O. C. Farokhzad, *ACS Nano*, 2014, **8**, 6056–6065.

17   V. Sebastian, M. Arruebo and J. Santamaria, *Small*, 2014, **10**, 835–853.

18   J. Feng, G. Biskos and A. Schmidt-Ott, *Sci. Rep.*, 2015, **5**, 15788.

19   J. H. Byeon, J. H. Park, K. Y. Yoon and J. Hwang, *Nanoscale*, 2009, **1**, 339–343.

20   J. H. Byeon and Y.-W. Kim, *Nanoscale*, 2012, **4**, 6726–6729.

21   J. H. Byeon, J. H. Park and J. Hwang, *J. Aerosol Sci.*, 2008, **39**, 888–896.

22   A. Maisser, K. Barmpounis, M. B. Attoui, G. Biskos and A. Schmidt-Ott, *Aerosol Sci. Technol.*, 2015, **49**, 886–894.

23   J. Feng, L. Huang, L. Ludvigsson, M. E. Messing, A. Maisser, G. Biskos and A. Schmidt-Ott, *J. Phys. Chem. C*, 2016, **120**, 621–630.

24   M. E. Messing, R. Westerström, B. O. Meuller, S. Blomberg, J. Gustafson, J. N. Andersen, E. Lundgren, R. van Rijn, O. Balmes, H. Bluhm and K. Deppert, *J. Phys. Chem. C*, 2010, **114**, 9257–9263.

25   J. H. Byeon and J.-W. Kim, *ACS Appl. Mater. Interfaces*, 2014, **6**, 3105–3110.

26   Y. H. Joe, W. Ju, J. H. Park, Y. H. Yoon and H. Jungho, *Aerosol air quaility Res.*, 2013, **13**, 1009–1018.

27   J. Byeon, D. Park and J. Kim, *Nanoscale*, 2015, **7**, 2271–2275.

28   J. H. Byeon and J.-W. Kim, *ACS Appl. Mater. Interfaces*, 2010, **2**, 947–951.

29   D. Z. Pai, K. Ken Ostrikov, S. Kumar, D. A. Lacoste, I. Levchenko and C. O. Laux, *Sci. Rep.*, 2013, **3**, 1221.

30   A. Anastasopol, T. V Pfeiffer, J. Middelkoop, U. Lafont, R. J. Canales-Perez, A. Schmidt-Ott, F. M. Mulder and S. W. H. Eijt, *J. Am. Chem. Soc.*, 2013, **135**, 7891–7900.

31   T. Pfeiffer, P. Kedia, M. E. Messing, M. Valvo and A. Schmidt-Ott, *Materials*, 2015, **8**, 1027–1042.

32   M. Valenti, D. Dolat, G. Biskos, A. Schmidt-ott and W. A. Smith, *J. Phys. Chem. C*, 2015, **119**, 2096–2104.

33   V. A. Vons, H. Leegwater, W. J. Legerstee, S. W. H. Eijt and A. Schmidt-Ott, *Int. J. Hydrogen Energy*, 2010, **35**, 5479–5489.

34   S. K. Sengar, B. R. Mehta, R. Kumar and V. Singh, *Sci. Rep.*, 2013, **3**, 2814.

35   J. H. Park, K. Y. Yoon, H. Na, Y. S. Kim, J. Hwang, J. Kim and Y. H. Yoon, *Sci. Total Environ.*, 2011, **409**, 4132–4138.

36   E. Hontañón, J. M. Palomares, M. Stein, X. Guo, R. Engeln, H. Nirschl and F. E. Kruis, *J. Nanoparticle Res.*, 2013, **15**, 1957.

37   N. S. Tabrizi, M. Ullmann, V. A. Vons, U. Lafont and A. Schmidt-Ott, *J. Nanoparticle Res.*, 2009, **11**, 315–332.

38   T. V. Pfeiffer, *PhD thesis*, Delft University of Technology, 2014.

39   A. Schmidt-Ott and T.V. Pfeiffer, WO 2013/115644, 2013.

40   M. Seipenbusch, A. P. Weber, A. Schiel and G. Kasper, *J. Aerosol Sci.*, 2003, **34**, 1699–1709.

41   J. Feng, E. Hontañón, M. Blanes, J. Meyer, X. Guo, L. Santos, L. Paltrinier, N. Ramlawi, L. C. P. M. de Smet, H. Nirschl, F. E. Kruis, A. Schmidt-Ott and G. Biskos, *ACS Appl. Mater. Interfaces*, 2016, **8**, 14756–14765.

42   C. Denonville and H. Malerød-Fjeld, Personal communication on Ni nanoparticles as catalysis in catalytic reactors, Duisburg, January, 2016.

43   G. Beaucage, H. K. Kammler and S. E. Pratsinis, *J. Appl. Crystallogr.*, 2004, **37**, 523–535.

44   A. B. Bourlinos, R. Herrera, N. Chalkias, D. D. Jiang, Q. Zhang, L. A. Archer and E. P. Giannelis, *Adv. Mater.*, 2005, **17**, 234–237.

45   Q. Wu, L. D. L. Duchstein, G. L. Chiarello, J. M. Christensen, C. D. Damsgaard, C. F. Elkjaer, J. B. Wagner, B. Temel, J.-D. Grunwaldt and A. D. Jensen, *ChemCatChem*, 2014, **6**, 301–310.

46   X. Guo, A. Gutsche and H. Nirschl, *J. Nanoparticle Res.*, 2013, **15**, 2058.

47   X. Guo, M. Wagner, A. Gutsche, J. Meyer, M. Seipenbusch and H. Nirschl, *J. Aerosol Sci.*, 2015, **85**, 17–29.

48   J. H. Byeon and J. T. Roberts, *ACS Appl. Mater. Interfaces*, 2012, **4**, 2515–2520.

49   J. H. Byeon and J.-W. Kim, *J. Mater. Chem. A*, 2014, **2**, 6939–6944.

50   M. Heurlin, M. H. Magnusson, D. Lindgren, M. Ek, L. R. Wallenberg, K. Deppert and L. Samuelson, *Nature*, 2012, **492**, 90–94.

51   M. E. Messing, K. A. Dick, L. R. Wallenberg and K. Deppert, *Gold Bull.*, 2009, **42**, 20–26.

52 M. E. Messing, K. Hillerich, J. Bolinsson, K. Storm, J. Johansson, K. A. Dick and K. Deppert, *Nano Res.*, 2010, **3**, 506–519.

53 A. Fridman, *Plasma Chemistry*, Cambridge University Press, Cambridge, 2012.

54 S. C. Wang and R. C. Flagan, *Aerosol Sci. Technol.*, 1990, **13**, 230–240.

55 B. R'mili, O. L. C. Le Bihan, C. Dutouquet, O. Aguerre-Charriol and E. Frejafon, *Aerosol Sci. Technol.*, 2013, **47**, 767–775.

56 G. Biskos, V. A. Vons, C. U. Yurteri and A. Schmidt-Ott, *KONA Powder Part. J.*, 2008, **26**, 13–35.

57 W. C. Hinds, *Aerosol Technology: Properties, Behavior, and Measurement of Airborne Particles*, John Wiley & Sons, New York, 1999.

58 N. S. Tabrizi, *Generation of Nanoparticles by Spark Discharge*, TUDelft, Delft, 2009.

59 F. Llewellyn Jones, *Br. J. Appl. Phys.*, 1950, **1**, 60–65.

60 T. Itina. Personal communication, June 2015. The theoretical values of α has been obtained ranging from 0.04% to 0.1% while spark energy varies from a few mJ to 600 mJ.

61 V. Vons, *PhD thesis*, Delft University of Technology, 2008.

62 A. Schmidt-Ott, *J. Aerosol Sci.*, 1988, **19**, 553–563.

63 A. Schmidt-Ott, U. Baltensperger, H. . Gäggeler and D. . Jost, *J. Aerosol Sci.*, 1990, **21**, 711–717.

64 D. Broßell, M. Valenti, S. Bezantakos, A. Schmidt-Ott and G. Biskos, *Aerosol Sci. Technol.*, 2015, **49**, 495–507.

65 J. Heintzenberg, *Aerosol Sci. Technol.*, 1994, **21**, 46–48.

66 S. Lösch, G. N. Iles, B. Schmitz and B. H. Günther, *J. Phys. Conf. Ser.*, 2011, **327**, 012036.

67 C. R. Svensson, L. Ludvigsson, B. O. Meuller, M. L. Eggersdorfer, K. Deppert, M. Bohgard, J. H. Pagels, M. E. Messing and J. Rissler, *J. Aerosol Sci.*, 2015, **87**, 38–52.

68 L. Mangolini, E. Thimsen and U. Kortshagen, *Nano Lett.*, 2005, **5**, 655–659.

69 C. A. Charitidis, P. Georgiou, M. A. Koklioti, A.-F. Trompeta and V. Markakis, *Manuf. Rev.*, 2014, **1**, 1–19.

70   C. Mehringer, C. Kloner, B. Butz, B. Winter, E. Spiecker and W. Peukert, *Nanoscale*, 2015, **7**, 5186–5196.

71   L. Mangolini, *J. Vac. Sci. Technol. B Microelectron. Nanom. Struct.*, 2013, **31**, 020801.

72   D. M. Holunga, R. C. Flagan and H. a. Atwater, *Ind. Eng. Chem. Res.*, 2005, **44**, 6332–6341.

73   M. B. Ward, R. Brydson and R. F. Cochrane, *J. Phys. Conf. Ser.*, 2006, **26**, 296–299.

74   C. G. Granqvist and R. a. Buhrman, *J. Appl. Phys.*, 1976, **47**, 2200–2219.

75   G. W. Nieman, J. R. Weertman and R. W. Siegel, *Scr. Metall.*, 1989, **23**, 2013–2018.

5. Internal Nanoparticle Mixing by Oscillatory Spark Ablation between Electrodes of Different Materials

Growing demands for engineered mixed nanoparticles (NPs) have spurred efforts to explore efficient and versatile synthesis methods. Spark ablation provides a viable alternative for producing widely different types of mixed NPs in a scalable and environmentally friendly manner. Importantly, implementing the spark mixing concept can create a new class of nanomaterials with components that are immiscible in their bulk counterparts. This chapter shows that polarity reversal of micro-second pulsed sparks between electrodes consisting of different materials enables synthesis of mixed NPs with a controllable composition distribution. A model developed in this work provides a tool for tuning the ablation ratio between the electrodes by adjusting the electric characteristics of the spark circuit, thereby controlling the mean composition of the resulting NPs. The model predictions are in accordance with measurements obtained here and earlier works, proving the feasibility of producing mixed NPs with a desirable composition. Considering that a composition distribution exists among the mixed NPs, controlling its broadness can be achieved by changing the operating conditions. This research therefore can be used to produce unique nanomaterials in an efficient and scalable fashion, especially when the starting electrode materials do not allow forming alloy or powder-mixture form.

Graphical Abstract
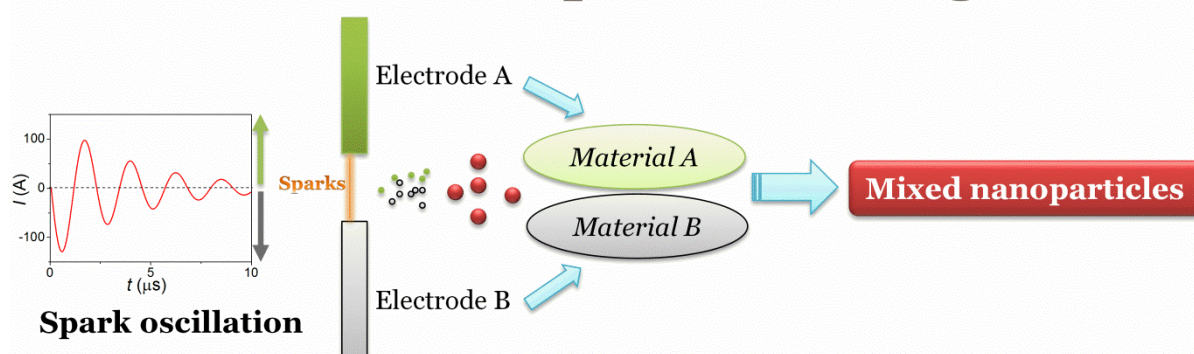
5. 1 Introduction

Efficient production of nanocomposites is essential for the development of industrial scale applications[1–5]. Spark ablation is a green and scalable gas phase method enabling the manufacturing of a range of nanoparticles (NPs)[6]. Its unique feature lies in the capability of manufacturing NPs with virtually unlimited mixing combinations in a single step[6–11]. Importantly, spark ablation has been used to create crystalline phases that only exist in the nanoparticulate state[12–14], and this is because a large fraction of the atoms occupies the material interface, thereby influencing their miscibility[13]. Together with the ability to accurately control the size of the resulting NPs, this feature can enormously extend the scope of manufacturing diverse nanomaterials[15–22].

In spark ablation, a pair of electrodes is connected to a pulse-forming electrical circuit that periodically initiates a spark discharge, evaporating electrode material, which subsequently condenses to form NPs[9,23]. Rapid condensation of mixed vapours and subsequent collisional particle growth leads to the formation of mixed NPs[2,8,12,23]. To produce mixed NPs, the starting electrode materials can consist of alloys or sintered micron-sized particles[23], which, however, may not exist or may be difficult to obtain for some material combinations. A way out of this situation is to use two electrodes consisting of different materials. In light of this concept, successful NP mixing has been achieved previously[8,24].

Although using a pair of different electrodes has been proved to mix NPs (cf. Section 5.2)[8,24], the associated interpretations are hardly understood. This chapter examines the internal NP mixing obtained by vaporizing the two electrodes of different materials used in spark discharges in both theoretical and experimental manner. Spark discharges form periodically between the gap of the electrodes, which are associated with discharge current typically oscillating between its positive and

negative polarity at a frequency of ca. 1 MHz. This discharge current is termed as current oscillation from this point onwards. The spark oscillatory behaviour determines the mixing ratio of NPs, which has remained an unexplored feature up to now[24]. In order to understand the relation between electrical parameters and the NP mixing ratio, Section 5.3 develops a model that links the current oscillation to the relative ablation of the two electrodes, gravimetrically determined in Section 5.4. The mass ablation ratio determines the mean particle composition from any electrode combination, because the ablated materials essentially convert to NPs. Section 5.5 shows that this ratio can be controlled by the electrical parameters in the spark circuit. Model predictions are validated with measurements of the ablated ratio of the electrodes, determined by weighing the electrodes before and after sparking, and compared with chemical analysis obtained by energy-dispersive X-ray spectroscopy (EDX) and inductively coupled plasma mass spectrometry (ICP-MS), which were reported previously[8,25]. Since the vapours generated from the two electrodes may not be completely mixed, Section 5.6 further investigate the composition distribution of the resulting NPs, the broadness of which can be controlled by the process parameters.

5.2 Interpreting NP mixing based on earlier work[8]

The concept of mixing NPs by spark ablation, using different materials for the anode and the cathode, leads to vapour clouds that are initially not completely mixed and go through the first steps of homogeneous nucleation independently before they mix, thereby resulting in a composition distributions of the final particles. The NP composition can be determined by means of EDX, ICP-MS, and gravimetric measurements of the electrodes before and after sparking. Figure 5.1 shows the composition of a number of NPs, produced by spark ablation using electrodes of different matter (i.e., Pd and Au), as determined by EDX in a scanning transmission electron microscope[8]. Because the number of detected particles (6 and 7 particles in Figure 5.1a and b, respectively) is limited, these observations can only be considered as an approximation of the distribution of NP compositions.
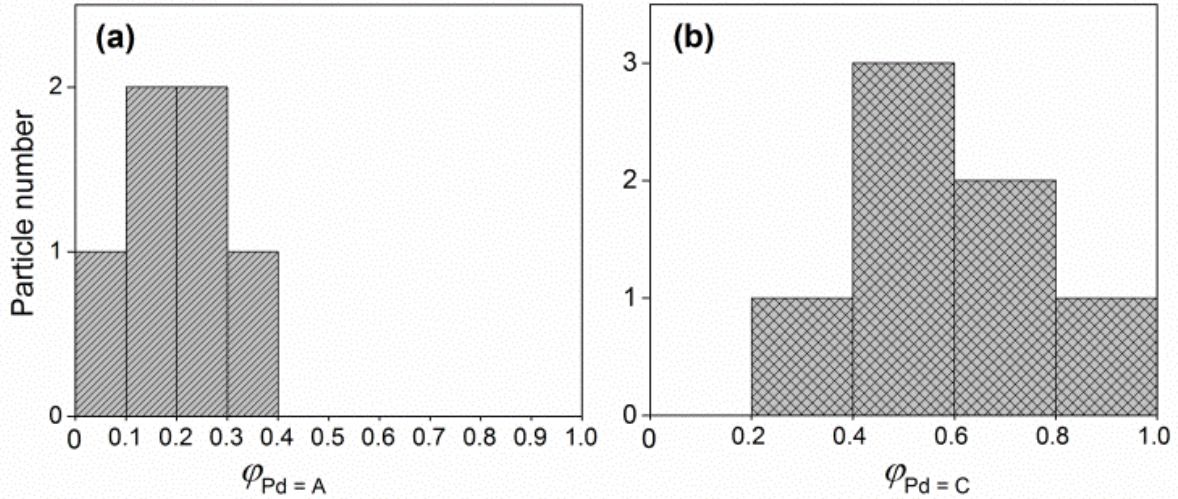
Figure 5.1 Distribution of the particle composition based on the data from Tabrizi *et al.*[4] determined by EDX on a random selection of (a) six particles produced using one Pd and one Au electrode, and (b) seven particles produced using one Pd and one Ag electrode. The compositions of the particles are defined with respect to Pd as $\varphi_{Pd=A} = \frac{m_{Pd=A}}{m_{Pd=A}+m_{Au=C}}$ and $\varphi_{Pd=C} = \frac{m_{Pd=C}}{m_{Pd=C}+m_{Ag=A}}$. Sample standard deviations σ_{sp} are 0.10 for Pd-Au (a) and 0.20 for Pd-Ag (b).

Tabrizi *et al.*[8] showed that the mean particle composition depends on the cathode material. The corresponding data is assembled in Table 5.1 and they were determined by ICP-MS. Based on the energy balance of the process[26], the total mass of both electrodes ablated per spark Δm at a given spark energy E can be estimated as[9]:

$$\Delta m \approx \alpha E C_m \tag{5.1}$$

Here α is a material-independent parameter representing the fraction of spark energy consumed for material evaporation, whereas C_m is a material constant representing the mass evaporated per unit of energy absorbed by the electrodes, estimated as[9,26]:

$$C_m \approx \left(c_{ps}(T_b - T_c) + H_m + H_e \right)^{-1} \tag{5.2}$$

where c_{ps} (J K⁻¹ kg⁻¹) is the heat capacity of the solid material; T_c and T_b (K) are the temperature of the carrier gas and the boiling point of the electrode

materials, whereas H_m and H_e (J kg^{-1}) are their enthalpies of melting and vaporization.

In this chapter, the subscript '=C' denotes that the material is used as the cathode, while '=A' represents that the material is used as the anode. For instance, $m_{Pd=C}$ is the mass portion of Pd in a particle when using Pd as a cathode.

Table 5.1 Mass ratios ablated from cathodes and anodes of different materials derived from Tabrizi *et al.*[4]. $m_{Au=C}/m_{Pd=A}$ denotes the mass ratio of NPs ablated from the cathode and the anode. These ratios were determined by means of ICP-MS. These values are equal to the ratio of $\Delta m_C/\Delta m_A$ (mass ablated per spark from the cathode to that of the anode), because the mass ablated from the electrodes is essentially converted to NPs[6].

$\dfrac{m_{Au=C}}{m_{Pd=A}}$	$\dfrac{m_{Pd=C}}{m_{Au=A}}$	$\dfrac{m_{Ag=C}}{m_{Pd=A}}$	$\dfrac{m_{Pd=C}}{m_{Ag=A}}$
2.9	0.6	0.7	1.7

A complication of using two different electrodes to mix NPs lies in the fact that the cathode is ablated more strongly than the anode[25]. This is because ablation is, at least in part, caused by the collisions of charge carriers with the electrodes. These charge carriers include the ionized gas atoms/molecules and free electrons. The higher the mass, the stronger is the ablation of the electrode attracting them. As the negatively charged species in the gas are, at least in part, electrons, the negative electrode is generally ablated more strongly than the positive one. The sparks obtained by the discharge of a capacitor are generally oscillatory as shown below, so that the electrodes take turns in experiencing strong ablation. Modifying the current oscillation by changing electrical parameters can therefore change the NP mixing ratio. For our further analysis, the cathode is defined as the electrode being negative during the period that most of the spark energy is dissipated.

The mass ablated from the cathode or the anode can be expressed separately using equation (5.1), if α is correspondingly replaced by the fraction of spark energy consumed for cathode ablation α_C or anode ablation α_A. The products of

these fractions and spark energy (i.e., $\alpha_C E$ and $\alpha_C E$) are then the energies dissipated by evaporating the associated electrodes. The ratio of energies absorbed by the cathode and the anode is expressed as:

$$k_r = \frac{\alpha_C}{\alpha_A} \tag{5.3}$$

It is worthwhile pointing out that k_r depends on the mass of the ions formed in the discharge due to their effect of sputtering the electrodes. Besides the characteristics of the oscillating discharge, the gas composition has an influence on k_r. For example, if both electrodes are ablated by positive and negative ions with identical mass and concentration, k_r will becomes unity. Ions from the evaporated material may also participate in ablation, but their contribution to vaporization is negligible, leading to a constant k_r under the same gas atmosphere and electrical spark characteristics, regardless of the electrode material combination. This assumption is consistent with the data of Tabrizi *et al.*[8] as shown below.

Substituting equation (5.3) to equation (5.1), the ratio of mass ablated per spark between the cathode (Δm_C) and the anode (Δm_A) can be calculated as:

$$\frac{\Delta m_C}{\Delta m_A} = k_r \frac{C_C}{C_A} \tag{5.4}$$

Equation (5.4) links a mass ratio of the ablated materials with k_r and material constants, which can be estimated by equation (5.2). This ratio is equal to the mean mixing ratio of NPs, which can also be experimentally determined, from either gravimetric measurements of the electrodes, EDX, or ICP-MS of the resulting NPs. Evidently, k_r is the mass ablation ratio when using the same electrode materials (i.e., $C_C = C_A$).

Applying equation (5.4) to the Au-Pd combination as shown in Table 5.1, yields:

$$\frac{m_{Au=C}}{m_{Pd=A}} \frac{m_{Pd=C}}{m_{Au=A}} = k_r^2 \frac{C_{Au}}{C_{Pd}} \frac{C_{Pd}}{C_{Au}} = k_r^2 \tag{5.5}$$

Substituting the values from Table 5.1 into equation (5.5), k_r = 1.3 is obtained for Au-Pd, and k_r = 1.1 for Ag-Pd. This discrepancy in k_r can be attributed to inaccuracies in the ICP-MS measurements. The empirical outcome suggests that k_r can be considered as being material independent. The average value of k_r = 1.2 was taken, because the same electrical circuit was used for the measurements used here[25]. In addition, using the same circuit gave a similar result for k_r, which was derived gravimetrically for identical electrodes[25].

Table 5.2 Comparison of the material constant ratios estimated when using different electrodes (the first and the second columns; cf. equation (5.4)) with those of using the identical electrodes (the third column; calculations are based on a number of gravimetric measurements for Au-Au and Pd-Pd combinations as well as Ag-Ag and Pd-Pd combinations)[23,25].

Material constant ratios	Different electrodes		Identical electrodes	Equation (5.2)
	Pd=A	Pd =C		
C_{Pd}/C_{Au}	0.4	0.5	0.5 [25]	0.5
C_{Pd}/C_{Ag}	1.7	1.4	1.6 [25]	0.7

Provided that the same spark circuit was used in this section (i.e., k_r = 1.2), equation (5.4) approximates the material constant ratios (C_C/C_A) when using two different electrodes. In the case of identical electrodes, the associated material constant ratios can be estimated from two subsequent gravimetric measurements of two electrodes' combinations (e.g., Pd-Pd & Au-Au; cf. details in the Supporting Information). The associated results for these coupled measurements are shown in Table 5.2 and are also compared with predictions using equation (5.2). Table 5.2 shows that the material constant ratios have the striking similarities regardless of whether different or identical electrodes were used. This supports the above assumption that the value of k_r (energy portions; cf. equation (5.3)) in the configuration using electrodes of the same material is representative for the case of different electrodes. Therefore, identical electrodes were used to investigate the relation between k_r and the electrical characteristics of the spark circuit.

Note that for C_{Pd}/C_{Ag}, there is a significant discrepancy between measurements and estimations using equation (5.2). This is probably due to the energy loss by thermal conduction of the electodes[9,10,25], which is not captured by equation (5.1), and the conductivity of Ag that is a factor of ca. 6 times higher than that of Pd.

5.3 Predicting NP mixing ratio
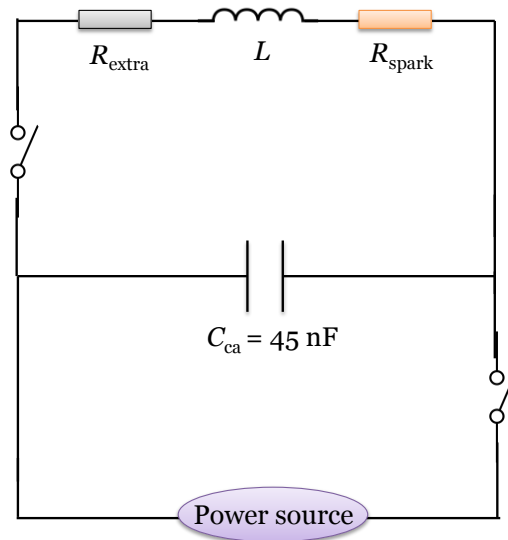
Figure 5.2. Simplified switching circuit used in the HFS. The initial potential difference U_C applied over the electrodes can be set independently of the breakdown voltage due to the decoupling of the charge cycle from the discharge[6]. Such separation is achieved by adding fast switches in the classical spark circuit[6,23]. Besides keeping a constant U_c, a low power source provides a continuous low current in the discharge gap. This low current reduces the breakdown voltage of the carrier gas, guaranteeing that U_c is always high enough to ignite the spark for the gap distances used here. Although the frequency of the HFS can go up to 25 kHz, the spark repetition frequency of 1 kHz was operated, at which there is no substantial electrode heating at the flow rate used in the experiment.

Figure 5.2 shows a simplified equivalent circuit of the high-frequency sparks (HFS) used in the present work[6]. Based on this circuit, a model is developed for linking the electrical parameters to the current oscillations, which in turn determines the ablation ratio of the electrodes. The spark discharge can be

considered as a constant resistance R_{spark} in the order of 1 Ω. Additional cable and electrode resistances can be neglected when using metal electrodes[27]. According to Kirchhoff's rules and the voltage-current relations for the inductance L_i, the total resistance $R_{tot}=R_{spark}+R_{extra}$ and the capacitance C_{ca}, one can write as:

$$L_i \frac{d^2I}{dt^2} + \left(R_{spark} + R_{extra}\right)\frac{dI}{dt} + \frac{1}{C_{ca}}I = 0 \tag{5.6}$$

Oscillations occur for the case of under damping $(R_{tot}^2 < \frac{4L_i}{C_{ca}})$, where equation (5.6) is solved to yield:

$$I = C_{ca}U_c\omega_f\left(1 + \frac{1}{\tau_D^2\omega_f^2}\right)\exp\left(-\frac{t}{\tau_D}\right)\sin(\omega_f t) \tag{5.7}$$

Here U_c is the initial voltage across the gap that is equal to the voltage over the capacitance igniting a spark discharge; $\tau_D = \frac{2L_i}{R_{tot}}$ is the damping factor; $\omega_f = \frac{1}{\sqrt{L_iC_{ca}}}\sqrt{1 - \frac{C_{ca}R_{tot}^2}{4L_i}}$ is the natural frequency of the oscillation.

The unknown parameters R_{spark} and L_i are derived from matching equation (5.7) with the measured current traces. If $R_{extra} = 0$, the spark energy ($E = \frac{1}{2}C_{ca}U_c^2$) can also be expressed as:

$$E = \int_0^\tau \left(R_{spark}\right)I^2 dt \tag{5.8}$$

In the oscillatory discharge, the electrodes take turns in having a negative and positive polarity. The electrode momentarily having the negative polarity is bombarded with positive ions, which have larger mass and carry more energy to the associated electrode than electrons, thereby emitting vapour. This brings about the assumption that the ablation only occurs on the electrode acting momentarily as the negative electrode. As a result, one electrode emits vapour during the initial negative-wave, whereas the other one takes over when the measured current becomes positive (cf. Figure 5.3). The cathode is defined as the electrode being negative during the time that most of the energy is

dissipated. For an under-damped oscillation, the cathode is the electrode that starts with the negative polarity. As the ablated mass is proportional to the spark energy (cf. equation (5.1)), the ablated mass of the cathode corresponds to the dissipated energy when $I < 0$, while the ablated mass of the anode is given by the dissipated energy when $I > 0$. According to equation (5.3), the ratio of the dissipated energies at the cathode and the anode is given by:

$$k_r = \frac{E\alpha_C}{E\alpha_A} = \frac{\int_0^\tau I^2 dt \ (I < 0)}{\int_0^\tau I^2 dt \ (I > 0)} \tag{5.9}$$

For electrodes of the same material ($C_A = C_C$), k_r can be determined by measuring the weight losses of both electrodes (cf. equation (5.4)), which essentially convert to the resulting NPs[6].

In accordance with mass conservation, the average particle composition can be determined gravimetrically (the weight losses of the anode and the cathode), , which are equal to the mass ablated per spark Δm from the respective electrode. The mean NP composition is expressed as (with respect to the cathode material):

$$\bar{\varphi}_C = \frac{\Delta m_C}{\Delta m_A + \Delta m_C} \tag{5.10}$$

Alternatively, $\bar{\varphi}_C$ can be formulated by substituting equation (5.4) to equation (5.10), which yields:

$$\bar{\varphi}_C = \frac{1}{1 + \frac{C_{mA}}{k_r C_{mC}}} \tag{5.11}$$

where the material term $\frac{C_{mA}}{C_{mC}}$ can be estimated by equation (5.2), while k_r is determined through equation (5.9). The unknown circuit elements, such as the spark resistance, can be derived by matching equation (5.7) with the current traces measured in this work.

5.4 Experimental section

In order to determine k_r by equation (5.9), a pair of identical Au electrodes (each rod having diameters of 3 mm and a length of 30 mm; 99.99% purity) was used in the HFS with a fixed capacitance of 45 nF. The gap distance between the electrodes was varied from 0.5 to 2 mm by a fine micrometre screw with a precision of 0.01 mm, while a He carrier gas (99.999% purity) was perpendicularly passed through this gap at a flow rate of 12.4 standard litres per min (slm). The potential difference between the electrodes U_c was manually set between 1.1 and 1.2 kV for the entire range of gap distances, thereby changing the spark energy. The spark repetition frequency was kept at 1 kHz throughout the measurements.

The amount of NP production was derived from weighing the electrodes before and after sparking, which was measured by an electric balance (AT201 Mettler Toledo) with a precision of 0.01 mg. In addition, the current traces were recorded by a Pearson Current Monitor (model 110), and an oscilloscope (Hameg HMO 1024) connected to the HFS using 1:100 High Voltage probes (Testec HV250).

5.5 Results and discussion

The electric circuit (cf. Figure 5.2) used for determining k_r assumes a constant spark resistance R_{Spark}, and this is justified by the perfect fit of the experimental current trace with the model predictions from equation (5.7) as shown in Figure 5.3(a). For $C_{ca} = 45$ nF, which leads to a fixed spark energy ($E = \frac{1}{2}C_{ca}U_c{}^2$), the damping behaviour is associated with R_{Spark} and the damping frequency mainly depends on L_i, so that both values can be derived accurately. Figure 5.3b reveals that R_{Spark} increases as the electrode gap distance increases, and the corresponding values are pointed out by the arrows in the figure (provided $L_i = 2.9$ µH). This provides a means of changing the total circuit resistance to influence the mixing ratio, as it follows from equations (5.4), (5.7) and (5.9). Because adding resistors to the circuit increases heat losses, it is in principle more efficient to change only the spark gap for varying the ablation

ratio. The parameter α embedded in equation (5.1) is a constant as discussed previously[9,25]. The results shown in Table 5.3 also validate this claim, showing that α is insensitive to both the electrode gap and spark energy.
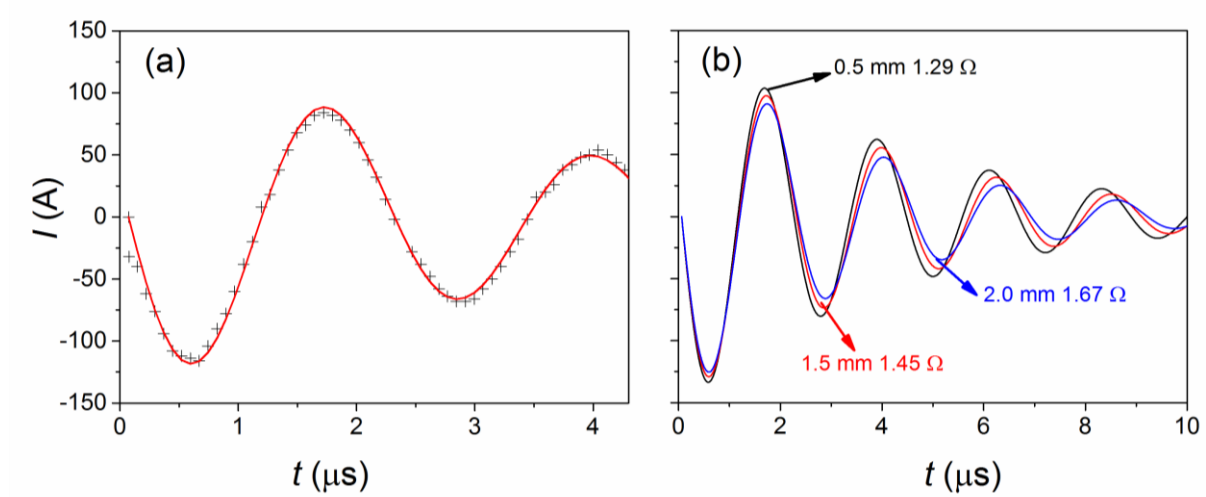
Figure 5.3 Current oscillations during a single spark between two electrodes at different gap distances. a), Current trace with a spark energy of 26.7 mJ and a gap distance of 1.5 mm. The symbols represent the measurements, while the curve is a fit of equation (5.7). b), Fits of equation (5.7) to measurements at different gap distances, yielding the corresponding values for L_i (2.9 µH) and R_{Spark} (i.e., 0.5 mm, 1.29 Ω; 1.0 mm, 1.45 Ω; 2.0 mm, 1.67 Ω).

Table 5.3 Dependence of α on gap distance and energy per spark.

Gap distance (mm)	$E = 26.3$ mJ	$E = 31.7$ mJ
0.5	0.116	0.122
1.5	0.110	0.119
2.0	0.120	0.122

The parameter k_r represents the energy ratio going in the ablation of the cathode and anode electrodes. The model in Section 5.3 links it to the electrical characteristics of the spark circuit (cf. Figure 5.2 and equation (5.9)). Table 5.4 compares the values of k_r and $\bar{\varphi}_C$ determined by equation (5.9) and (5.11) with those estimated by the gravimetric measurements at three different gaps. The results are in line with each other and reflect the same trend for increasing gap distance. Importantly, this correspondence verifies the assumption made in the

model: the material ablation is strongly dominated by the temporarily negative electrode within the spark oscillation.

Table 5.4 Comparison of k_r and the corresponding $\bar{\varphi}_C$ (equation (5.11) with $C_A = C_C$) determined by the gravimetric measurements (using equation (5.10)) and the model predictions using equation (5.9) (cf. E = 31.7 mJ, R_{extra} = 0).

	k_r		$\bar{\varphi}_C$	
Gap distance (mm)	Gravimetric measurements	equation (5.9)	Gravimetric measurements	equation (5.11)
0.5	1.5	1.7	0.60	0.63
1.5	1.6	1.8	0.62	0.64
2.0	1.7	1.9	0.63	0.66
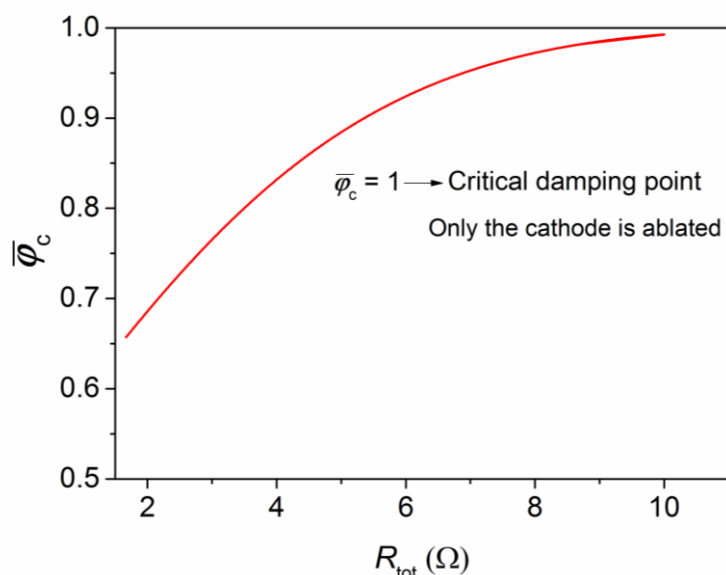
Figure 5.4 The mean mixing ratio $\bar{\varphi}_C$ as a function of the total resistance R_{tot} used in the spark circuit for $C_{mA} = C_{mC}$ (C_{ca} = 45 nF, L_i = 3 μH). When R_{tot} increases to a critical damping point ($R_{tot}^2 = 4L_i/C_{ca}$), no polarity reversal occurs, thereby only ablating the cathode.

Equations (5.7) and (5.9) imply that k_r is increased (more ablation from the cathode with respect to the anode), when L_i or C_{ca} is decreased. As C_{ca} also influences the spark energy, decreasing it is practical, but L_i could be decreased by careful design of the circuit (e.g. coaxial cables) and increased by adding an inductor. The simplest way of increasing k_r is to add a resistance R_{extra} to the circuit. However, the drawback of doing so lies in the reduction of energy

efficiency, because R_{extra} causes the reducing of energy efficiency from α to $\alpha \frac{R_{Spark}}{R_{Spark}+R_{Extra}}$. When R_{tot} (i.e., $R_{spark} + R_{extra}$) reaches the point of critical damping ($R_{tot}^2 = 4L_i/C_{ca}$), where no polarity reversal occurs and only the cathode is ablated.

Figure 5.4 shows the change in the mean composition $\bar{\varphi}_C$ as derived from equations (5.9) and (5.11) for the special case of $C_A = C_C$, which are representative for other material combinations as validated experimentally (cf. Section 5.2). The NP composition (i.e., $\bar{\varphi}_C$) has a broad range from 0.6 to 1.0. Note that the anode and cathode can be exchanged, covering also the composition range between 0 and 0.4.

As briefly mentioned above, another measure of controlling the particle composition is to adjust the spark gap, which directly relates to the length of the spark plasma, thereby determining the spark resistance. As confirmed by the data shown in Table 5.3, the energy efficiency α remains almost unchanged regardless of the gap distances. Table 5.4 shows that the electrode gap distance indeed has an influence on $\bar{\varphi}_C$. This influence, however, is small and control over the discharge becomes difficult with gaps larger than 2 mm.

5.6 Understanding the broadness of NP composition distribution

This section develops a general approach to predicting the composition broadness of NPs produced by spark discharges between two electrodes of different composition, which can be controlled by changing the operating parameters. According to the model described above and its consistency with the experiments, internal NP mixing can be controlled through the oscillatory behaviour of the discharge that makes electrodes take turns in emitting vapour clouds. The broadness of the particle composition distribution σ_{sp} shown in Figure 5.1 is attributed to partly mixed vapours of the two materials (the respective electrode surface) at the beginning, and/or their emissions at different times. The latter influence is negligible with respect to the spatial

separation, since the discharge oscillatory frequency lies at ca. 1 MHz. The dominance of the spatial separation of the two material sources implies that the spark gap should have an influence on σ_{sp}. Mixing is evidently incomplete in the initial phase of particle growth, but complete mixing subsequently does occur with the help of diffusion and turbulence during further NP growth. Particle formation can thus be modelled by a simplified process in which:

i. particles of one electrode material ('single-component particles') with diameter D_{pi} are first formed from the initial vapour clouds;

ii. subsequently, the resulting aerosols are completely mixed;

iii. particle-particle collisions contribute to their further growth.

The colliding particles fully coalesce below a critical size (i.e., primary particle size within agglomerates)[9] or their growth is interrupted by rapid dilution or deposition onto a substrate. Note that due to the initially unmixed growth, the final particles exhibit a spread of compositions, even if subsequent growth takes place under well-mixed conditions. The fraction of one component $\varphi_i = \frac{m_{Ai}}{m_{Ai}+m_{Bi}}$ in these final particles of diameter D_{pf}, can be described by Poisson statistics. Considering that the number of initial particles per final particles is $N = \frac{D_{pf}{}^3}{D_{pi}{}^3}$, the composition distribution can be approximated by Stirling's formula given by[28]:

$$f(\varphi') = \text{const} \exp\left(-\frac{(\varphi' - \overline{\varphi}')^2}{2\sigma_{sp}{}^2}\right) \qquad (5.12)$$

The standard deviation in equation (5.12) is given by[28]:

$$\sigma_{sp} = \sqrt{\frac{\overline{\varphi}'(1 - \overline{\varphi}')}{N}} = \sqrt{\frac{\overline{\varphi}(1 - \overline{\varphi}')}{\left(\frac{D_{pf}}{D_{pi}}\right)^3}} \qquad (5.13)$$

To determine σ_{sp} using equation (5.13), the composition $\overline{\varphi}$ can be estimated by gravimetric measurements (cf. equation (5.10)) or predicted by equation (5.11) using equation (5.9) for k_r and equation (5.2) for C_A/C_C.

This mixing model is simplistic because in reality there is an overlap between formation of the 'single-component particles' and the mixing phase, and because the particles have a distribution in size. Nevertheless, this analysis provides an estimate on how the process parameters influence the broadness of the NP composition distribution. The model can be tested by inserting σ_{sp} (cf. Figure 5.1) into equation (5.13). The primary particle diameters for the Pd-Au electrode combination are estimated from the corresponding micrographs[8] as $D_{pf} = 8$ nm and $D_{pf} = 5$ nm in the Pd-Ag case. Placing these diameters and the corresponding mean compositions $\bar{\varphi}$ into equation (5.13) yields the initial diameters of the 'single-component particles' D_{pi}. Importantly, both values of D_{pi} arrive at ca. 3 nm, which correlates well with the corresponding mean mass of electrodes ablated per spark as well as the electrode gap distance, implying a similar particle growth history for these two electrode combinations (Pd-Ag and Pd-Au)[10].

Supported by this qualitative consistency, equation (5.12) and (5.13) are key to predicting the influence of spark operating parameters on the broadness of the composition distributions in a qualitative sense. Quantitative predictions would require an appropriate value for D_{pi}. For example, equation (5.12) correctly predicts that the Pd-Ag distribution (cf. Figure 5.1b) is broader than that of Pd-Au (cf. Figure 5.1a). The main reason for this is the smaller D_{pf} for Ag-Pd. Another reason is that $\bar{\varphi}$ is closer to 0.5 (where $\bar{\varphi}(1-\bar{\varphi})$ has its maximum) as shown in Figure 5.1b for Pd-Ag.

In general, more turbulent mixing in the vicinity of the sparks should decrease D_{pi}. According to the particle growth model[10], a decrease in spark energy or an increase in the flow rate will also decrease D_{pi}, and therefore decrease σ_{sp}. Another alternative to reduce σ_{sp} is to increase D_{pf}, which is in turn closely associated with the temperature history and the surface state of the particles[6,9]. Finally, the dominance of the spatial separation of the two material sources over time effects ameliorated above implies that a larger distance between the electrodes is expected to extend the non-mixed period, thereby increasing D_{pi} and σ_{sp}.

5.7 Conclusions

This chapter has shown the influence of the oscillatory behaviour of a single spark on the relative ablation of the two electrodes, which can be used to change the mean mixing ratio $\overline{\varphi}_C$ of the resulting nanoparticles (NPs). The concept of separating the material-dependent and circuit-dependent contributions enables this work to determine the electrical parameter k_r by applying identical electrodes.

The model is based on previous observations where the cathode is more strongly ablated than the anode. In this model, assuming that only the electrode momentarily acting as negative polarity is ablated, is validated with the measurements. Tuning k_r, a ratio between the energy absorbed by the cathode to that absorbed by the anode, through the electrical parameters can be used to vary the particle composition within a broad range (cf. equation (5.7), (5.9) and (5.11)). Analysis of the data from former publications[8,25] confirms the assumption that the material dependence of the ablation rate from pairs of identical electrodes can be used to predict the ablation ratio of electrodes consisting of different materials.

The simplest way of varying the mean composition is to change the resistance in the circuit. The mean compositions $\overline{\varphi}_C$ predicted from equation (5.11) correlates well with the gravimetric measurements of the electrodes before and after sparking, and are consistent with results obtained in previous works[8,24]. Considering the broadness of NP composition distribution, a simple model proposed here serves as a basic guide for controlling it by altering the operating conditions.

The central results of this work provide a basic understanding of spark production of internally mixed NPs by using electrodes of different materials. The models developed here provide a tool for controlling the mean composition and broadness of the NP composition distribution. In combination with predicting the particle size and scaling up this production

method, the results can be used to expand the possibilities of novel nano-mixing toward industrial scale. The unique approach to internal NP mixing is stunningly attractive to produce nanoalloys, even if the raw materials do not form alloys in the macroscopic state or that need further powder mixing and sintering[13,14].

Supplementary Information in Chapter 5

Supplementary Information is provided in the following pages, including material constants and the experimental determination of material constant ratios

Table S5.1 Material constants for Au, Ag, Pd, Mg, and Al

Materials	H_e (J/kg)	H_m (J/kg)	c_{ps} (J/(kg K))	T_b (K)	$1/C_m$ (J/kg)
Au	1736041	63706	129	3243	2180296
Ag	2351852	104444	235	2435	2959666
Pd	3377358	157924	240	3236	4241603
Mg	5333333	353333	1020	1363	6778067
Al	10518519	396667	904	2743	13129985

Determining material constant ratios experimentally

Two different electrodes

This electrode configuration is simple, as one only need to determine the value of k_r by equation (S5.9) in the main manuscript. The experimental determination is also available using equation (S5.5). Doing so needs two consequential gravimetric measurements of the electrodes used. For example, we use Au-Pd electrode combination with known weight for each of them. First we use Au as the cathode to run spark for a certain time. Subsequently, we weigh the Au and Pd electrodes, which gives us the mass loss of each electrode after sparking. Second, we switch Au as the anode and repeat these experiments. We substitute the mass converted to NPs for each electrode to equation (S5.5), which gives the value of k_r. Equation (S5.4) is then used to estimate the material constant ratios.

Identical electrodes

In this case, the same gravimetric measurements are used to determine k. The only difference lies that we need to use two identical-electrode combinations. For example, to determine the material constant ratio between Ag and Pd, First we need

to do the gravimetric measurements for Ag-Ag electrode combination. Then we do the gravimetric measurements for Pd-Pd, provided that the same electrical circuit is used as that of A-Ag electrode combination. Considering that equation (S5.1) holds for using identical electrodes made from a wide range of materials, the material constant ration between Ag and Pd equals to the ratio of gravimetric measurements between Ag-Ag and Pd-Pd.
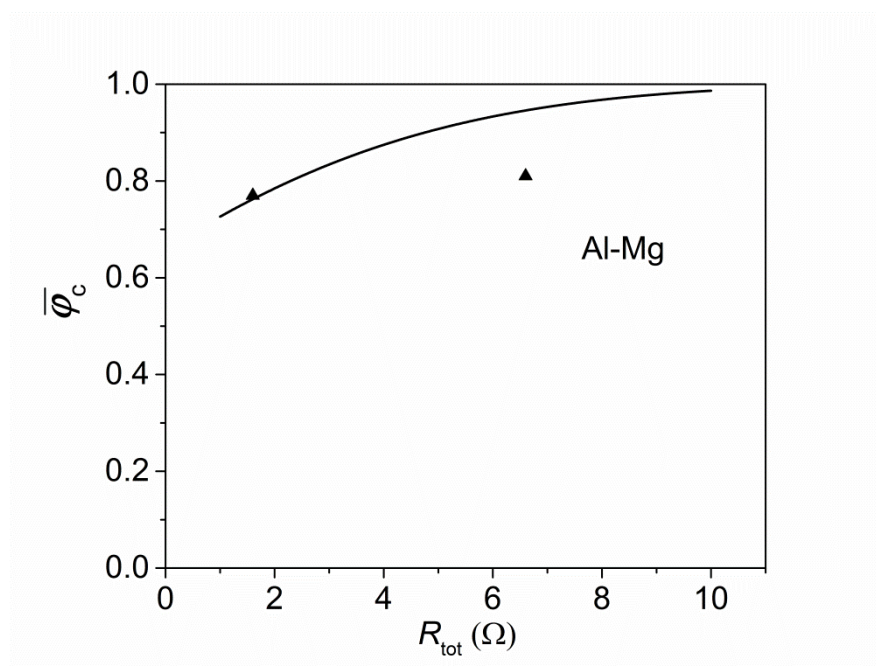
Figure S5.1 Ablation ratio ratio $\bar{\varphi}_C$ as as a function of the resistance in the spark circuit Al-Mg electrodes, where the curve is predicted by equation (S5.11), while the points are based on the data from Vons (C_{ca} = 20 nF, L_i = 2.0 µH, U_c = 1.3 kV, R_{extra} = 0 and 5 Ω)[24]. The predictions correspond well with the previous measurements for Al-Mg electrodes when using R_{extra} = 0 and 5 Ω.

References

1   C. A. Charitidis, P. Georgiou, M. A. Koklioti, A.-F. Trompeta and V. Markakis, *Manuf. Rev.*, 2014, **1**, 1–19.

2   V. Sebastian, M. Arruebo and J. Santamaria, *Small*, 2014, **10**, 835–853.

3   A. Tiwari, I. Mondal, S. Ghosh, N. Chattopadhyay and U. Pal, *Phys. Chem. Chem. Phys.*, 2016, **18**, 15260–15268.

4   R. Madhu, V. Veeramani, S.-M. Chen, P. Veerakumar, S.-B. Liu and N. Miyamoto, *Phys. Chem. Chem. Phys.*, 2016, **236**, 369–374.

5   M. Naqshbandi, J. Canning, B. C. Gibson, M. M. Nash and M. J. Crossley, *Nat. Commun.*, 2012, **3**, 1188.

6   J. Feng, X. Guo, N. Ramlawi, T. V Pfeiffer, R. Geutjens, S. Basak, H. Nirschl, G. Biskos, H. W. Zandbergen and A. Schmidt-ott, *J. Mater. Chem. A*, 2016, **4**, 11222–11227.

7   A. Maisser, K. Barmpounis, M. B. Attoui, G. Biskos and A. Schmidt-Ott, *Aerosol Sci. Technol.*, 2015, **49**, 886–894.

8   N. S. Tabrizi, Q. Xu, N. M. van der Pers, U. Lafont and A. Schmidt-Ott, *J. Nanoparticle Res.*, 2008, **11**, 1209–1218.

9   J. Feng, G. Biskos and A. Schmidt-Ott, *Sci. Rep.*, 2015, **5**, 15788.

10   J. Feng, L. Huang, L. Ludvigsson, M. E. Messing, A. Maisser, G. Biskos and A. Schmidt-Ott, *J. Phys. Chem. C*, 2016, **120**, 621–630.

11   J. H. Byeon, J. H. Park and J. Hwang, *J. Aerosol Sci.*, 2008, **39**, 888–896.

12   N. S. Tabrizi, Q. Xu, N. M. Pers and A. Schmidt-Ott, *J. Nanoparticle Res.*, 2010, **12**, 247–259.

13   D. Lahiri, B. Bunker, B. Mishra, Z. Zhang, D. Meisel, C. M. Doudna, M. F. Bertino, F. D. Blum, A. T. Tokuhiro, S. Chattopadhyay, T. Shibata and J. Terry, *J. Appl. Phys.*, 2005, **97**, 094304.

14   S. Xiong, W. Qi, B. Huang and M. Wang, *ChemPhysChem*, 2011, **12**, 1317–1324.

15   J. Feng, E. Hontañón, M. Blanes, J. Meyer, X. Guo, L. Santos, L. Paltrinier, N. Ramlawi, L. C. P. M. de Smet, H. Nirschl, F. E. Kruis, A. Schmidt-Ott and G. Biskos, *ACS Appl. Mater. Interfaces*, 2016, **8**, 14756–14765.

16　N. A. Isaac, P. Ngene, R. J. Westerwaal, J. Gaury, B. Dam, A. Schmidt-Ott and G. Biskos, *Sensors Actuators B Chem.*, 2015, **221**, 290–296.

17　A. Anastasopol, T. V Pfeiffer, J. Middelkoop, U. Lafont, R. J. Canales-Perez, A. Schmidt-Ott, F. M. Mulder and S. W. H. Eijt, *J. Am. Chem. Soc.*, 2013, **135**, 7891–7900.

18　J. H. Byeon and J. T. Roberts, *ACS Appl. Mater. Interfaces*, 2012, **4**, 2515–2120.

19　H. Kim, J. Kim, H. Yang, J. Suh, T. Kim, B. Han, S. Kim, D. S. Kim, P. V Pikhitsa and M. Choi, *Nat. Nanotechnol.*, 2006, **1**, 117–121.

20　S. M. Kang, S. Jang, J.-K. Lee, J. Yoon, D.-E. Yoo, J.-W. Lee, M. Choi and N.-G. Park, *Small*, 2016, **12**, 2443–2449.

21　S. Jang, J. Yoon, K. Ha, M. Kim, D. H. Kim, S. M. Kim, S. M. Kang, S. J. Park, H. S. Jung and M. Choi, *Nano Energy*, 2016, **22**, 499–506.

22　J. H. Byeon and J.-W. Kim, *J. Mater. Chem. A*, 2014, **2**, 6939–6944.

23　T. V. Pfeiffer, J. Feng and A. Schmidt-Ott, *Adv. Powder Technol.*, 2014, **25**, 56–70.

24　V. Vons, *PhD thesis*, Delft University of Technology, 2008.

25　N. S. Tabrizi, M. Ullmann, V. A. Vons, U. Lafont and A. Schmidt-Ott, *J. Nanoparticle Res.*, 2009, **11**, 315–332.

26　F. Llewellyn Jones, *Br. J. Appl. Phys.*, 1950, **1**, 60–65.

27　V. A. Vons, L. C. P. M. de Smet, D. Munao, A. Evirgen, E. M. Kelder and A. Schmidt-Ott, *J. Nanoparticle Res.*, 2011, **13**, 4867–4879.

28　I. N. Bronstein and K. A. Semendjajew, *Taschenbuch der Mathematik*, Deutsch Harri GmbH, Frankfurt, 1998.

6. Inhibition of 'Splashing' in High Frequency Sparks for Nanoparticle Synthesis

Current breakthroughs in green nanotechnology are capable of manufacturing industrial quantity of sub-10 nm nanoparticles (NPs) with improved uniformity. Newly developed high frequency sparks can yield sub-10 nm NPs with large quantities. In this method, fast quenching of the vapours generated from electrodes facilitates the formation of very small particles (< 10 nm). However, high repetition frequencies increase probability of striking the same hot-spots of the electrode surface, where molten pools are formed. Droplets are momentarily ejected from the microscopic pools and they are subsequently solidified by cooling, thereby forming 'splashing' particles that are larger than 100 nm. To supress the splashing while maintaining a high NP mass production rate, a permanent magnetic field is employed to deflect the a continuous glowing current, onto which sparks are superimposed. Inhibition of 'splashing' is expected to promote wide use of high frequency sparks for producing nanoscopic building blocks toward industrial scale.

Graphical Abstract
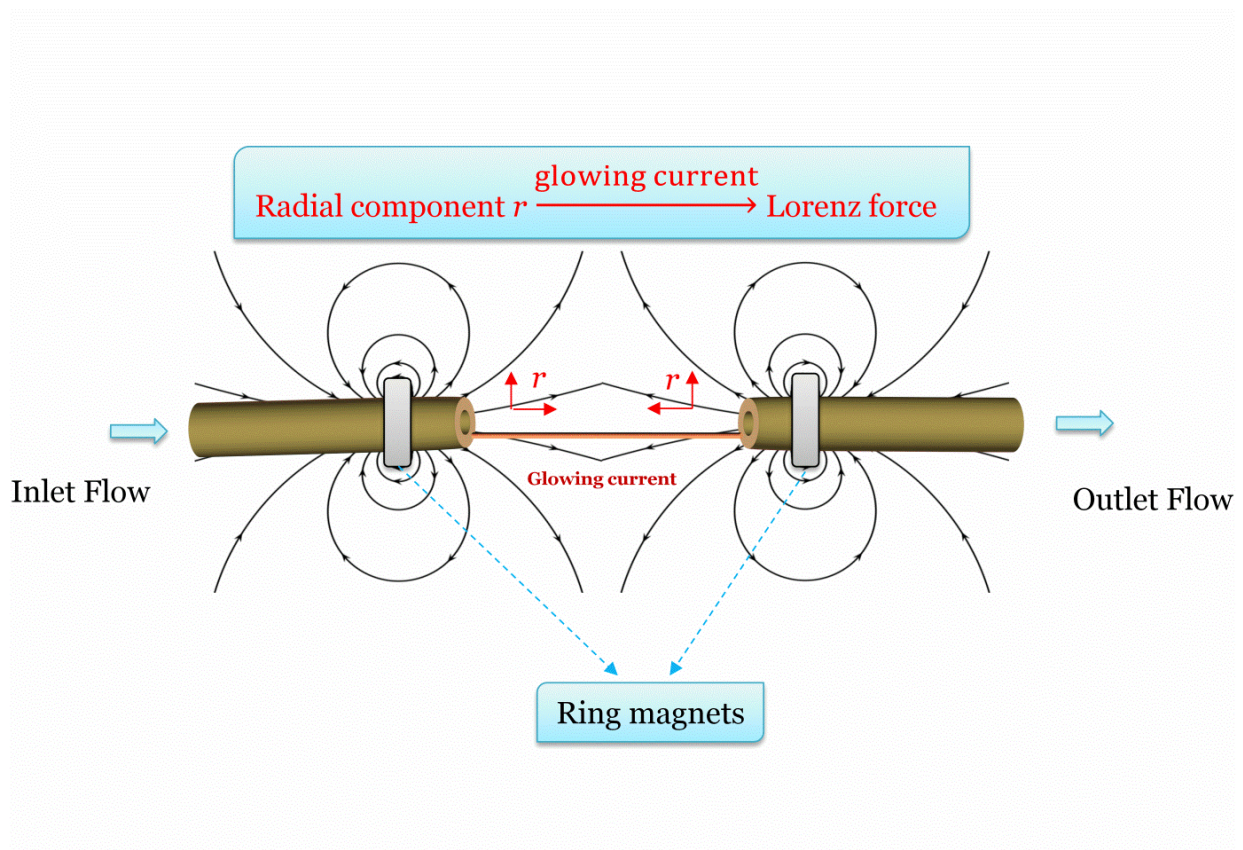
6. 1 Introduction

Apart from successful scaling up of spark ablation as described in Chapter 4, 'splashing' leads to forming particles having sizes larger than 100 nm, thereby exacerbating the properties of final products. To tackle the problem, this chapter aims at inhibition of 'splashing'.

Current breakthroughs in green nanotechnology are capable of manufacturing industrial quantity of sub-10 nm nanoparticles (NPs) with improved uniformity. These small NPs can be dispersed finely on a support, so that the associated high surface areas efficiently uses catalytically active components[1,2]. Minor changes in their composition or size can substantially influence the activity and selectivity of a reaction[1,2]. In addition to the fascinating catalytic properties, very small NPs exhibit a number of different optical, electronic and magnetic properties, as compared to their bulk counterparts[3]. The unique properties can be related to the surface atomic coordination[1], quantum confinement, and superatom potential[4].

The newly developed high frequency sparks (HFS), whose switching circuit was described in Pfeiffer's thesis[5], has been used to produce various monometallic and bimetallic NPs with sub-10 nm in size and well-defined chemical composition (cf. Chapter 5)[6]. Extremely fast quenching of the vapours generated from electrodes makes this method feasible to not only produce very small particles (< 10 nm), but also to rapidly mixing materials on an atomic scale (forming alloys; cf. Chapter 5)[7]. The latter has been identified to produce thermodynamically metastable NPs and nanoalloys that are converted from incompatible starting materials[8]. The unique feature gives birth to many applications in relation to growing demands for nanocomposites[9,10].

As compared to the production rate demonstrated in Chapter 4, HFS can reach higher mass production rates by further increasing the spark repetition frequency and/or the spark energy, which are, however, faced with two problems. The first one

lies in the fact that high repetition frequencies increases probability of striking the same hot-spots on the inter-electrode surface[11], where the energy is momentarily transferred to form molten pools. Such microscopic pools eject droplets under the action of electric and/or acoustic fields, as well as plasma pressure created by ion bombardment. Subsequent cooling solidifies the droplets, thereby forming undesired 'splashing' particles having sizes from 100 nm to a few microns. The second problem arises from the formation of splashing particles at a high spark energy, which can be inhibited by using a low spark energy (ca. 30 mJ) according to earlier work[6]. Splashing does not contribute to NP production, but leads to strong electrode erosion. As a result, it reduces converting efficiency of starting electrodes to NPs.

This chapter designs a system that is feasible to investigate the splashing particles generated by HFS with and without using of magnets around the electrodes. In the HFS, sparks are superimposed onto a low-power and continuous discharge, which enables magnetic deflection of the spark position, thereby avoiding successive sparks to strike the same spot on inter-electrode surface. Section 6.2 presents the experimental setup used for inhibition of 'splashing' particles. Section 6.3 compares the results of employing the magnets with those obtained from the experiments without using magnets. The particle samples were analysed by small- and wide-angle X-ray scattering (SWAXS), scanning electron microscopy (SEM) and transmission electron microscopy (TEM). Finally section 6.4 closes with a summary demonstrating that inhibition of splashing particles enhances the quality of the nanoscale building blocks at high yields and the converting efficiency of starting electrodes to sub-10 nm NPs.

6.2 Methods

6.2.1 Experimental setup

Figure 6.1 shows the schematic layout of the experimental setup used to identify the difference between using and not using magnets with respect to the splashing particles. It consists of a NP production system (i.e., the spark discharge generator; SDG), and collection systems (i.e., a filter, an impactor and a mini-particle sampler[12];

MPS). For all the experiments in Section 6.3, the energy per spark E was fixed to 32.4 mJ ($E =0.5\ C_{ca}U_C^2$, where C_{ca} = 45 nF, U_c =1.2 kV).
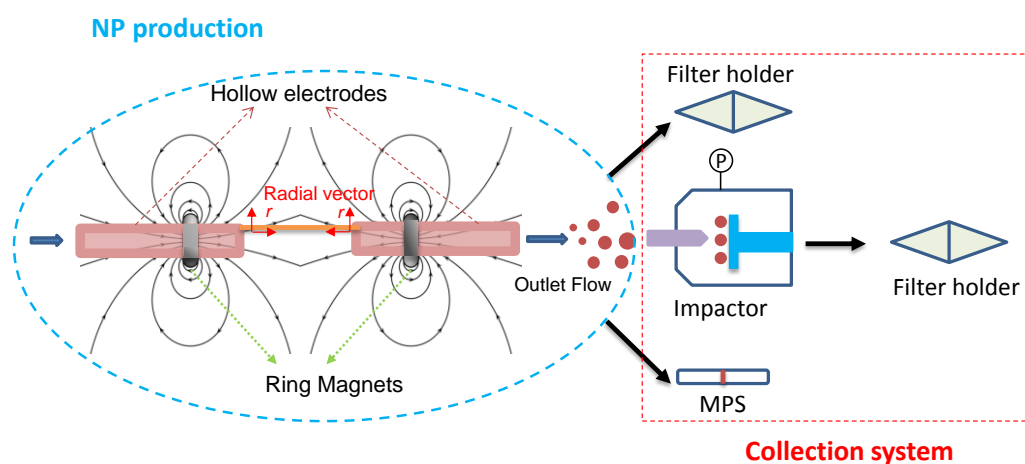
Figure 6.1 Schematic layout of the experimental setup and the configuration of ring magnets attached on the pair of hollow electrodes through which the coaxial flow passes. Key: DMA, differential mobility analyser; CPC, condensation particle counter; MPS, mini-particle sampler.

To keep the sparks at the circumference of rods and guarantee symmetry, the hollow electrodes (an inner and outer diameter of 6 and 8 mm, and a length of 20 mm; 99.99% purity) were used instead of solid ones. Two identical ring magnets were fixed around each hollow rod electrode. The carrier gas (Ar, purity 99.999%) passed through the hollow anode electrode and subsequently carried away the aerosols to the hollow cathode electrode and particle collection systems, having a flow rate of 10.5 slm. The magnets were mounted to avoid respelling each other, i.e. with identical poles facing. This caused the magnetic field lines to have a radial component between the magnets away from the horizontal (centre) axis where a low-power and continuous glowing current was formed and superimposed by sparks. As a result, a Lorentz force deflects the glowing current, positioning the superimposed sparks .

6.2.2 Particle collection and characterization

When the generated aerosols exited the hollow cathode electrode, MPS, impactor, and filter were placed downstream to collect the particles. TEM (JEOL JEM-1400) was utilized to exhibit both NPs and splashing particles. Both SEM (JSM 6300) and SAXS/WAXS measurements gave a comparison of the splashing particles produced

under the condition of using and without using the magnets around the electrodes. (1) The MPS was used to collect NPs onto the TEM grids with holes (S143-3 Q'foil 1.2/1.3 400 Cu)[12], through which the aerosol flow passed[12]. (2) Two custom-made filters were placed upstream and downstream of the impactor to collect particles on the commercial membrane filters (HVHP09050 Durapore PVDF 0.45 µm pore size, 90 mm diameter). The particle samples were analyzed by SAXS/WAXS. (3) A custom-made impactor (low-pressure of 70 mbar, a nozzle with a diameter of 3.5 mm at a flow rate of 0.63 slm, Stokes number = 0.01 for 100 nm Au NPs when the carrier gas is Ar with purity of 99.999%) was used to sample the splashing particles onto the impaction plate[13]. A piece of membrane filter (with a dimension of 1.5 × 1.5 cm²; cut from the commercial ones) was glued on the centre of the impaction plate, where particles were deposited. In addition, silica wafers (1 × 1 cm²) were also placed on the impaction plate to collect particles. The former was used for SAXS/WASX measurements[14,15], while the latter was characterized by SEM.

6.3 Results and discussion

Figure 6.2 shows SEM images of Au splashing particles with and without using magnets over the hollow electrodes. In the absence of magnets, there is an increased probability of repeated spark discharges striking the same spot on the inter-electrode surface, thereby causing the formation of splashing particles with sizes larger than 100 nm. To suppress splashing without reducing the production rate, a magnetic field was applied to deflect the continuous glowing current[5,16], onto which a spark is superimposed. This avoids repeatedly striking the same spot on electrode surface.
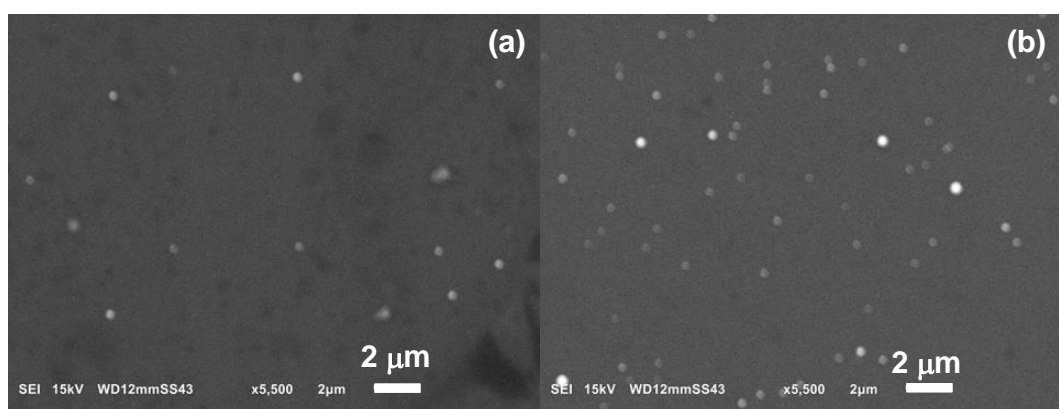
Figure 6.2 SEM images of Au splashing particles produced using hollow electrodes at f = 1 kHz. Au splashing particles collected on the impaction plate by the impactor

for 10 min with a flow rate of 0.63 slm and a deposition pressure of 70 mbar, with magnets (a) and without magnets (b).

The SEM images indicate that the amount of splashing particles is dramatically reduced when using the magnets, as shown in Figures 6.2a, whereas Figure 6.2b shows the splashing particles collected in the absence of magnets. By statistic counting of the splashing particles on many SEM images, it is shown that the splashing particles are supressed by about a factor of five at 1 kHz when using magnets in the system.
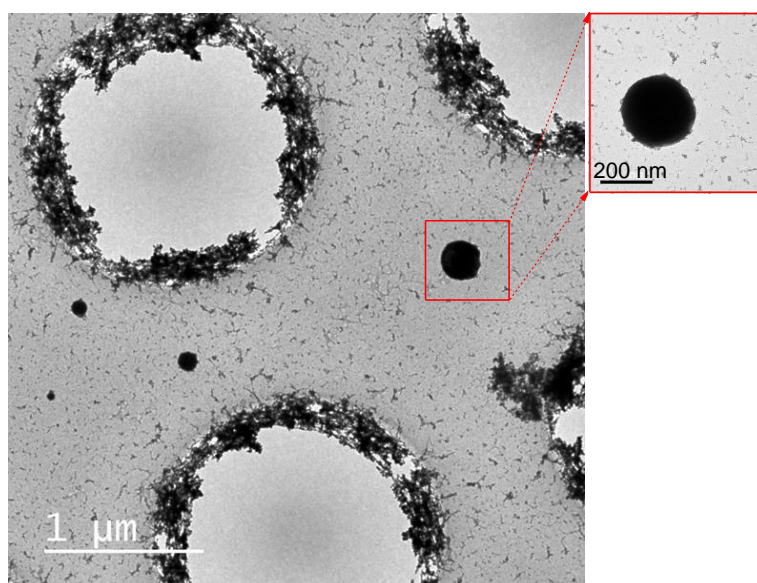
Figure 6.3 TEM images of the Au splashing particles and agglomerates.

Interestingly, the gravimetric measurements of the electrodes did not show the difference between the case of using magnets and without using magnets. Based on Figure 6.2b, assuming that all the splashing particles were deposited on the impaction plate, their number presented in the observation area, which is based on many SEM images, is estimated to be on the order of 10^5 particles/mm^2 during 10 min impaction. The total mass of splashing particles can be estimated to the order of 10^{-4} mg for 200 nm (10^{-2} mg for particles of 500 nm). The mass production rate of Au NPs reported in Chapter 4 (cf. Figure 4.1) is ca. 8 mg for 10 min. As a result, gravimetric measurements can hardly identifies such a small mass fraction, from 0.01 wt.% (e.g., 200 nm) to 0.1 wt.% (e.g., 500 nm). Although the mass fraction of splashing particles remains low, the higher frequency is expected to form more

splashing particles. Therefore, to supress the splashing is essentially necessary to improve the NP uniformity and to enhance the converting efficiency of starting electrodes to sub-10 nm NPs .
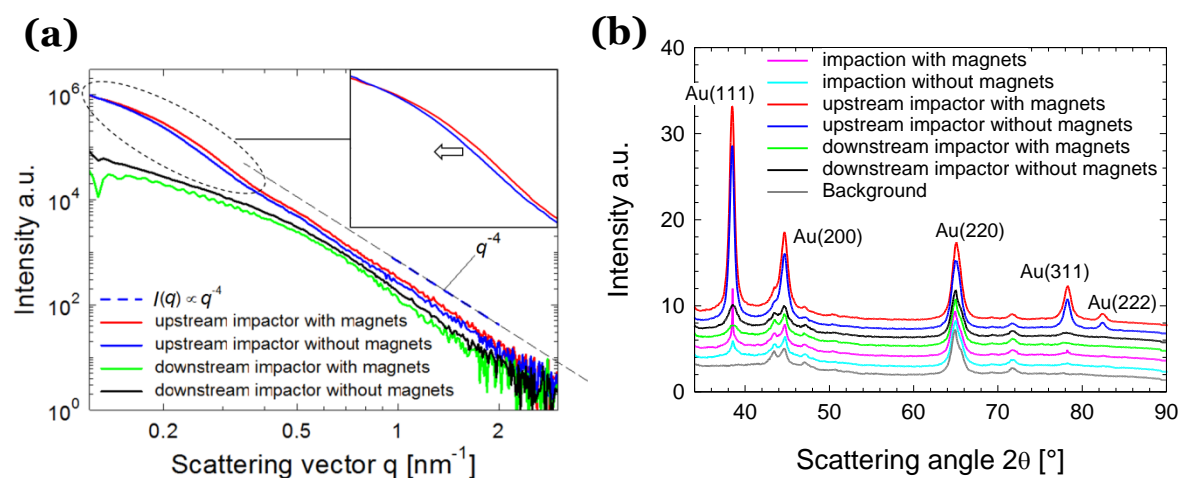
Figure 6.4 SAXS/WAXS measurements of Au particles. SAXS curves of Au particles collected upstream and downstream of the impactor (a). WAXS curves of Au particles collected on the impaction plate, downstream and upstream of the impactor, respectively (b).

By analysing the SEM images, the concentration of splashing particles is ca. 10^3 particles/cm³, which is in line with the estimation from the TEM images shown in Figure 6.3. Comparing the number concentration of splashing particles observed by SEM with the total number concentration measured by SMPS (10^7 particles/cm³, see Figure 5.2 in Chapter 5), it indicates that the number fraction of the splashing particles produced by the spark is approximately 0.01 % (number based). This small fraction justifies the conclusion that the splashing particles are also hard to be measured by the SMPS.

Figure 6.4 shows detailed SAXS/WAXS data of the Au particles collected at different locations, namely upstream, downstream of the impactor and on the impaction plate. The SAXS curves (cf. Figure 6.4a) show that the scattering intensity follows the power law in the large q region, i.e., the intensity is proportional to q^{-4}, which implies that the Au particles have smooth surfaces with d_s of 2.0. As displayed in the inset of Figure 6.4a, the 'shoulder' in the SAXS curve of the particles collected upstream of the impactor without using the magnetic field is shifted to the left, as compared to the particles collected at the same location while employing the magnets. For the

particles collected upstream of the impactor, in the case of not using the magnets, the mean size of 32 nm is larger that of 29 nm using the magnets. This comparison suggests that more splashing particles were produced in the absence of magnets, as also confirmed by SEM images (cf. Figure 6.3b).

For the particles collected downstream of the impactor, the two samples (with and without using the magnetic field) were analysed by SAXS/WAXS (cf. the lower two curves shown in Figure 6.4a). The almost overlapping SAXS curves exhibit similar structural information. These Au NPs have a mass fractal dimension of 2.02, a mean size of 11 nm, and a surface fractal dimension of 2.0. At wide angles, some peaks corresponding to gold crystal phases (111), (200), (220), (311) and (222) are visible (cf. Figure 6.4b), as compared to the background measurement (the Au peak at (220) probably results from the sample substrate and the camera system itself). The peaks of these Au NPs are relatively weaker and broader than those samples collected upstream of the impactor, implying that these particles are smaller or have smaller crystals. The comparison of the samples placed downstream and upstream of impactor validates the assumption that all of the splashing particles are collected on the impaction plate.

For the particles deposited on the impaction plate, due to their relatively large sizes, the main peaks Au (111) in WAXS curves are narrower than those collected downstream of the impactor (cf. Figure 6.4b). Therefore, the SAXS/WAXS analysis allows qualitatively distinguishing the difference of splashing particles produced with and without using the magnets, in good consistency with the observation by electron microscope (cf. Figure 6.2).

6.4 Conclusion and future applications

The central results here are to show that the splashing particles have been successfully suppressed by employing permanent magnets around the electrodes. This chapter used a fixed spark repetition frequency at 1 kHz, showing that splashing particles can be supressed by a factor of five. The associated magnetic deflection of the continuous glowing current allows positioning the superimposed sparks. As a result, the probability of striking the same spot on the inter-electrode surface is

decreased in the HFS. These results can therefore serve as a basic guideline for improving the uniformity of the resulting NPs and enhancing the converting efficiency of starting electrodes to sub-10 nm NPs. In relation to creating 3D nanostructures by focused aerosol deposition[17–20], the technique described here can be implemented to avoid the splashing particles to block the open structure of a patterned 'mask', which allows depositing aerosol NPs.

References

1   R. Reske, H. Mistry, F. Behafarid, B. R. Cuenya and P. Strasser, *J. Am. Chem. Soc.*, 2014, **136**, 6978–6986.

2   E. C. Tyo and S. Vajda, *Nat. Nanotechnol.*, 2015, **10**, 577–588.

3   F. E. Kruis, H. Fissan and A. Peled, *J. Aerosol Sci.*, 1998, **29**, 511–535.

4   D. E. Bergeron, A. W. Castleman, T. Morisato and S. N. Khanna, *Science*, 2004, **304**, 84–87.

5   T. V. Pfeiffer, *PhD thesis*, Delft University of Technology, 2014.

6   J. Feng, X. Guo, N. Ramlawi, T. V Pfeiffer, R. Geutjens, S. Basak, H. Nirschl, G. Biskos, H. W. Zandbergen and A. Schmidt-ott, *J. Mater. Chem. A*, 2016, **4**, 11222–11227.

7   J. Feng, N. Ramlawi, G. Biskos and A. Schmidt-Ott, *J. Nanoparticle Res.*, 2016 (under review).

8   V. Sebastian, M. Arruebo and J. Santamaria, *Small*, 2014, **10**, 835–853.

9   J. Chen, J. Zheng, E. A. Decker, D. J. McClements and H. Xiao, *RSC Adv.*, 2015, **5**, 73892–73900.

10   M. Naqshbandi, J. Canning, B. C. Gibson, M. M. Nash and M. J. Crossley, *Nat. Commun.*, 2012, **3**, 1188.

11   J. Feng, G. Biskos and A. Schmidt-Ott, *Sci. Rep.*, 2015, **5**, 15788.

12   B. R'mili, O. L. C. Le Bihan, C. Dutouquet, O. Aguerre-Charriol and E. Frejafon, *Aerosol Sci. Technol.*, 2013, **47**, 767–775.

13   V. Vons, *PhD thesis*, Delft University of Technology, 2008.

14   X. Guo, A. Gutsche and H. Nirschl, *J. Nanoparticle Res.*, 2013, **15**, 2058.

15   X. Guo, M. Wagner, A. Gutsche, J. Meyer, M. Seipenbusch and H. Nirschl, *J. Aerosol Sci.*, 2015, **85**, 17–29.

16   T. V. Pfeiffer, J. Feng and A. Schmidt-Ott, *Adv. Powder Technol.*, 2014, **25**, 56–70.

17   H. Kim, J. Kim, H. Yang, J. Suh, T. Kim, B. Han, S. Kim, D. S. Kim, P. V
      Pikhitsa and M. Choi, *Nat. Nanotechnol.*, 2006, **1**, 117–121.

18   H. Lee, S. You, P. V. Pikhitsa, J. Kim, S. Kwon, C. G. Woo and M. Choi, *Nano
      Lett.*, 2011, **11**, 119–124.

19   K. Jung, H.-J. Song, G. Lee, Y. Ko, K. Ahn, H. Choi, J. Y. Kim, K. Ha, J. Song,
      J.-K. Lee, C. Lee and M. Choi, *ACS Nano*, 2014, **8**, 2590–2601.

20   S. Jang, J. Yoon, K. Ha, M. Kim, D. H. Kim, S. M. Kim, S. M. Kang, S. J. Park, H.
      S. Jung and M. Choi, *Nano Energy*, 2016, **22**, 499–506.

Part C

Application of NPs

7. Scalable and Environmentally Benign Process for Smart Textile Nanofinishing

A major challenge in nanotechnology is that of determining how to introduce green and sustainable principles when assembling individual nanoscale elements to create working devices. For instance, textile nanofinishing is restricted by many constraints of traditional pad-dry-cure processes, such as the use of costly chemical precursors to produce nanoparticles (NPs), the high liquid and energy consumption, the production of harmful liquid wastes, and multi-step batch operations. By integrating low-cost, scalable, and environmentally benign aerosol processes of the type proposed here into textile nanofinishing, these constraints can be circumvented while leading to a new class of fabrics. This one-step textile nanofinishing relies on the diffusional deposition of aerosol NPs onto textile fibres. As proof of this concept, Ag NPs are deposited onto a range of textiles and their antimicrobial properties are assessed in relation to two strains of bacteria (i.e., *Staphylococcus Aureus*, *Klebsiella Pneumoniae*). The antimicrobial activity (AA) reaches as high as ca. 5.5 when the loading is one order of magnitude less (10 ppm; i.e., 10 mg Ag NPs per kg textile) than textiles treated by wet-routes. The AA does not increase in proportion to the Ag content above 10 ppm as a consequence of a 'saturation' effect. Such low NP loading on antimicrobial textiles minimizes the risk to human health and ecosystem, as well as it reduces potential changes in colour and texture of the resulting textiles. After three washes, the release of Ag lies in the order of 1wt.%, comparable to textiles nanofinished with wet-routes. Interestingly, the washed textiles exhibit almost no reduction in AA, much as those of as-deposited samples. Considering that a realm of functional textiles can be nanofinished by aerosol deposition, this chapter demonstrates that the proposed approach, which is universal and sustainable, can lead to a wide number of textile-based applications.

Graphical Abstract
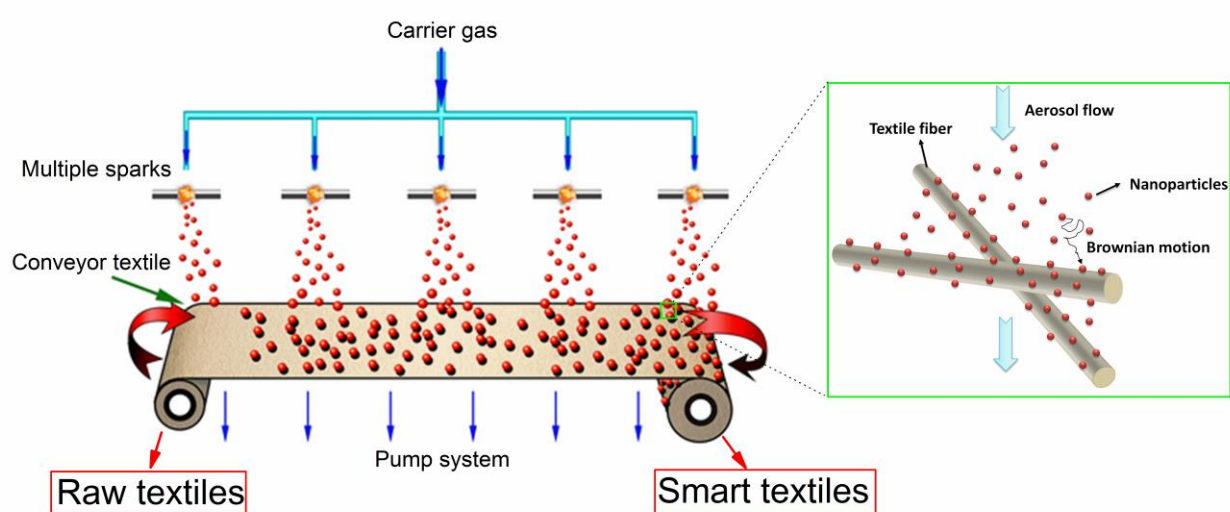
7.1 Introduction

Fundamental studies and scaling up of spark ablation have been demonstrated in Parts A and B. From this chapter onwards, the focus is shifted to the application of NPs. Chapter 7 proposes a new process for smart textile nanofinishing, showing antimicrobial activities of the textiles.

Implementing nanotechnology to make "smart textiles" is evinced growing interest[1–3], which together with bioinspired fibres and coatings represent cutting-edge advancement in the field of textile-based products. For instance, the aesthetic appreciation of fashion will acquire new dimensions, if the optical appearance of fabrics can be manipulated by utilizing the surface plasmons of coated nanoparticles (NPs)[4]. In combination with sensor technologies, colour-changing fabrics will enable adaptation to surroundings thereby advancing camouflage techniques[3]. What is more, integrating NPs into textiles can also introduce antimicrobial[5–7], flame retardant[8,9], self-cleaning[3], and UV protective properties[10], while simultaneously helping in the development of wearable devices (e-Textiles)[11–13], and exerting chemical softening effects to textile fibres. Despite this tremendous range of applications, the dispersion, impregnation, distribution, and immobilization of low NP loads onto textile fibres in a controlled environment remain major challenges, especially when considering the increasing demands for green and sustainable techniques.

Producing functional textiles is currently based on conventional pad-dry-cure processes, which have many shortcomings. Such wet-finishing processes rely on chemical reactions in a liquid medium and the use of surfactants. This, in turn, requires reducing agents or templates for the synthesis of colloidal nanomaterials, inevitably resulting in surface contamination on the final nanomaterials[14]. Squeezing out the excess solution from the padded fabric produces liquid waste products, some of which are detrimental to the

environment. In addition, if uncontrolled evaporation of the solvent occurs during the drying process, it can cause inhomogeneous distribution of NPs on the fibres due to migration phenomena[15]. This drying procedure also limits the roll-to-roll speed of the textile finishing line. Another drawback of the wet-finishing process is that the reproducibility and controllability of nanomaterial deposition are frequently inhibited by the batch-type operation[16]. The nanofinished textiles, for instance, can receive high nanomaterial loading in an uncontrolled fashion with respect to their concentration profile within the textiles. In combination with polymeric binding, which exacerbates fabric texture and comfort, these high loadings raise many concerns in relation to nanomaterial release during washing and disposal[17,18].
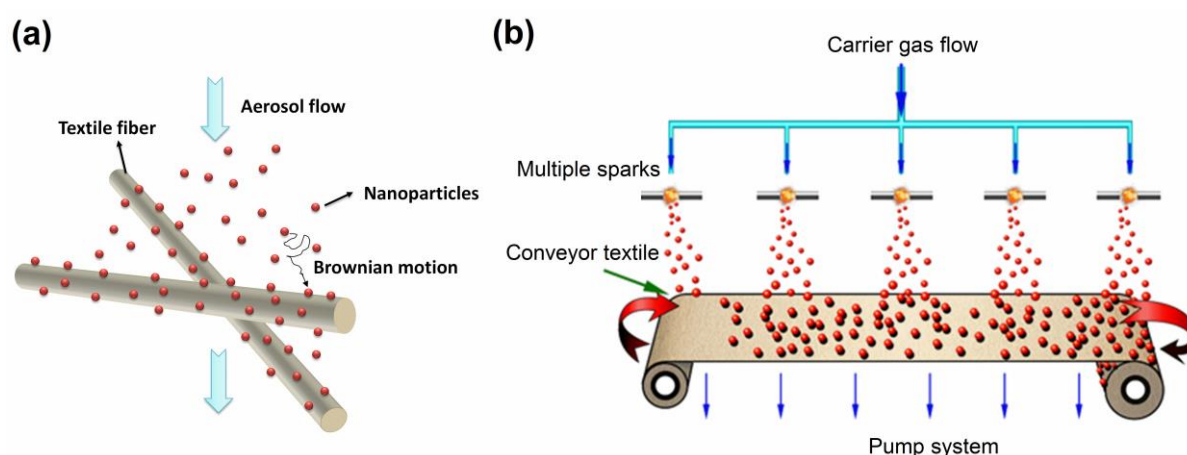
Figure 7.1 Illustration of the nanofinishing process. (a) An aerosol flow is passed through the textile, where the NPs collide and stick to the fibres by van der Waals forces. The NP-fibre collisions are caused by the Brownian motion of the NPs. (b) Conceptual design of a simple, scalable and green route for textile nanofinishing achieved by integrating electrical discharges for the synthesis of NPs into roll-to-roll textile production.

The advancement of textile nanofinishing not only requires the implementation of a sustainable technology producing complex nanomaterials for enhancing performance and extending the functions of the final product[1], but also it needs to guarantee financial and environmental viability. This chapter proposes a sustainable and universal approach to textile nanofinishing that relies on a single-step NP synthesis and deposition process. Among the aerosol processes, electrical discharges allow the high-yield synthesis and direct deposition of a wide range of

well-defined NPs[19–24] (with respect to NP concentration, size[25,26], crystallinity[27], and chemical composition[28,29]) that can be directly deposited onto textile fibres by diffusion (cf. Section 7.2), in a green and universal manner.

The uniqueness of the proposed process lies in that diffusional deposition can be easily integrated into textile nanofinishing while providing a controlled loading profile within the textiles. In addition to these unique features, the proposed NP synthesis method yields sub-5 nm singlet particles[26,30,31], whose size can be tuned even down to that of atomic clusters (i.e., of the order of a few Å). Particles in this size range not only provide an extremely large surface area for sufficiently high mass specific activity and diffusional deposition efficiency, but they also guarantee strong adhesion to fibers (given that agglomeration is avoided), thus minimizing their release. Since the NP synthesis method is fully compatible with commercial roll-to-roll textile production as illustrated in Figure 7.1, the nanofinishing process proposed here is amenable to upscaling (cf. Figure S7.6 in the SI). Although the applications of the proposed method can be numerous, as a proof of the concept, this chapter uses it here to fabricate antimicrobial textiles and test their activity and washing durability. Antibacterial textiles have been commercialized by using the wet-finishing processes[32]. Therefore, this dry approach, which is simple, green and scalable, is expected to draw considerable attention from these industrial partners. With some adaptations and modifications, the process proposed here can be directly deployed in these sectors.

7.2 Results

7.2.1 Particle size distributions in the gas phase

A scanning mobility particle sizer (SMPS)[33] was used to determine the size distributions of the Ag NPs generated by spark ablation. A tube (with a length of 32 cm and an inner diameter of 4 mm) transfers the aerosol NPs from the depositing point (i.e., the textile sample) to the measuring point (i.e., the SMPS). To account for the particle coagulational growth in the sampling tube, theoretical calculations were used to estimate their size distributions of the

particles when they arrive at the surface of the textile (cf. Supplementary Section S7.1).

Figure 7.2a and b show lognormal particle size distributions (PSDs) measured by the SMPS (black curves) at two different quenching gas flow rates (Q_q = 20 and 50 standard litres per minute (slm)). The geometric mean diameter (d_p) and the geometric standard deviation (σ_g) of the PSDs of the generated NPs are summarized in Table 7.1. The size of the particles produced by spark ablation can be easily controlled by varying Q_q [26]. When Q_q increases from 20 to 50 slm, d_p decreases from ca. 3.6 to ca. 1.5 nm, which is corroborated by model predictions[30]. Interestingly, an increase in Q_q does not diminish the deposition efficiency of the NPs significantly (cf. Supplementary Section S7.2).

As the NP mass production rate is unaffected by the gas flow rate, increasing Q_q only decreases the particle size (i.e., resulting in an increase of the total particle surface area) and therewith the mass specific activity. This observation simplifies the scalability of the proposed textile nanofinishing methodology with respect to NP synthesis. The size distribution (with d_p = 3.6 nm; cf. Figure 7.2c) derived from analysing the TEM image is similar to the estimation based on the SMPS measurements (d_p = 3.9 nm; cf. red curve in Figure 7.2a,). Most of the deposited particles shown in the TEM image (inset in Figure 7.2c) are non-agglomerated singlet particles. This is highly desirable as singlets have stronger adherence to the fibres than agglomerates, which also simplifies the modelling of NP deposition onto the textile fibres.

Table 7.1 Mean size d_p and geometric standard deviation σ_g of Ag NPs generated by spark ablation in Ar (purity 99.999%).

Q_q (slm)	d_p (nm)		σ_g	
	SMPS measurements	Deposition on textile[26,30]	SMPS measurements	Deposition on textile[26,30]
20	9.7	3.6	1.53	1.35
50	7.6	1.5	1.48	1.35
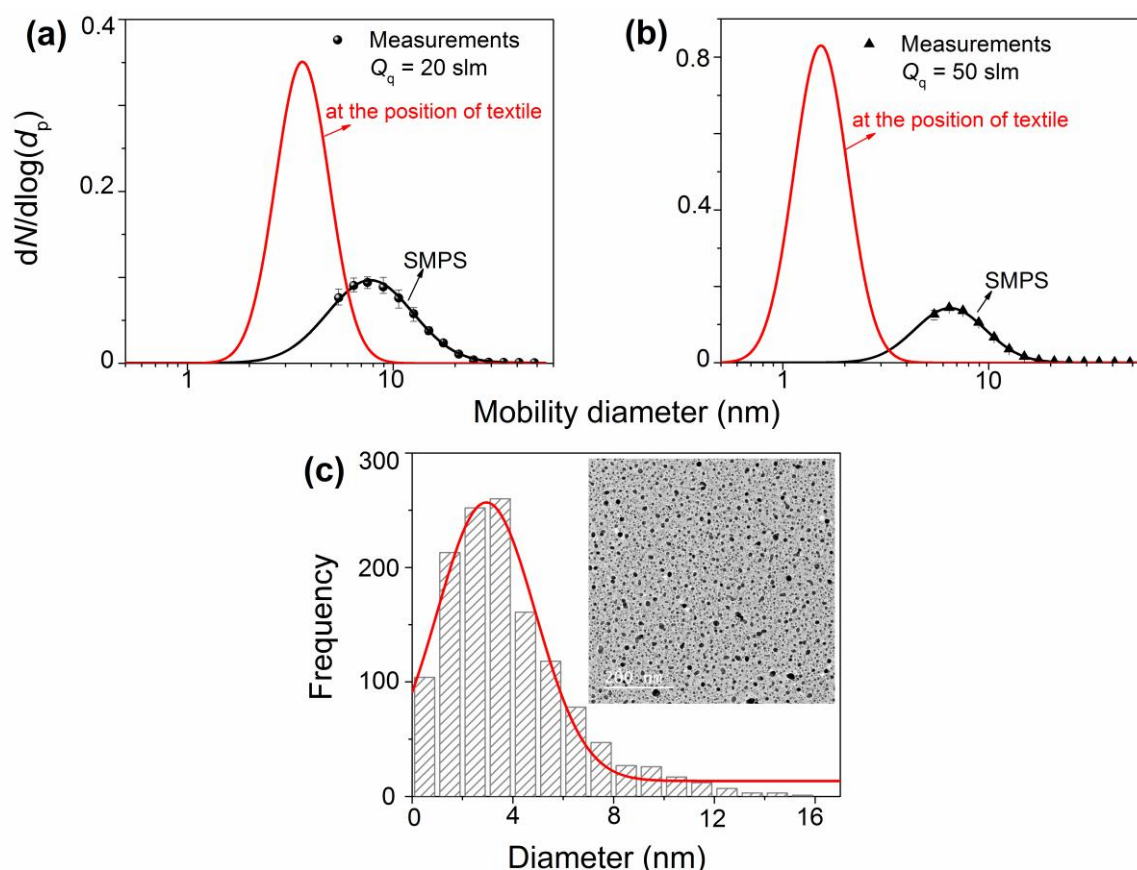
Figure 7.2 Particle size distributions at quenching gas flow rates of (a) Q_q = 20 slm; (b) Q_q = 50 slm. The black symbols and curves correspond to the particle size distributions measured directly by the SMPS and to the fitted lognormal distributions, respectively, while the red curves correspond to the particle size distribution at the location of the textiles as estimated by considering the growth of the particles along the sampling line to the SMPS. (c) the particle size distribution is based on the TEM image (Q_q = 20 slm).

7.2.2 Particle deposition on textiles

The deposition efficiency of the particles onto the textile fibres depends on the particle size, the textile characteristics, and the flow rate through the fabric. Figure 7.3 shows all the predicted and measured size-dependent deposition efficiencies of the particles onto different textiles (namely Acrylic-Polyester-Cotton-Polyamide (APCP), Polyester (PES), and Cotton; cf. Supplementary Table S7.1 for more details) as a function of particle diameter. Diffusional deposition is the dominant mechanism for NPs smaller than 5 nm (cf. Figure 7.2 and Supplementary

Section S7.2)[34]. The deposition efficiency E_{dep} for any given textile with an averaged solidity α_s, thickness L, and fibre diameter d_f can therefore be estimated as[34]:

$$E_{dep} = 1 - \exp\left(\frac{-10.8\alpha_s L D^{\frac{2}{3}}}{\pi(1-\alpha_s)d_f^{\frac{5}{3}}U^{\frac{2}{3}}}\right) \tag{7.1}$$

where $U = Q_q/A$ (A is the deposition area); U is a face velocity, and D is the diffusion coefficient of the particles, which can be determined by equation (S7.8) given in the SI. For a fixed U, E_{dep} solely depends on the particle size.
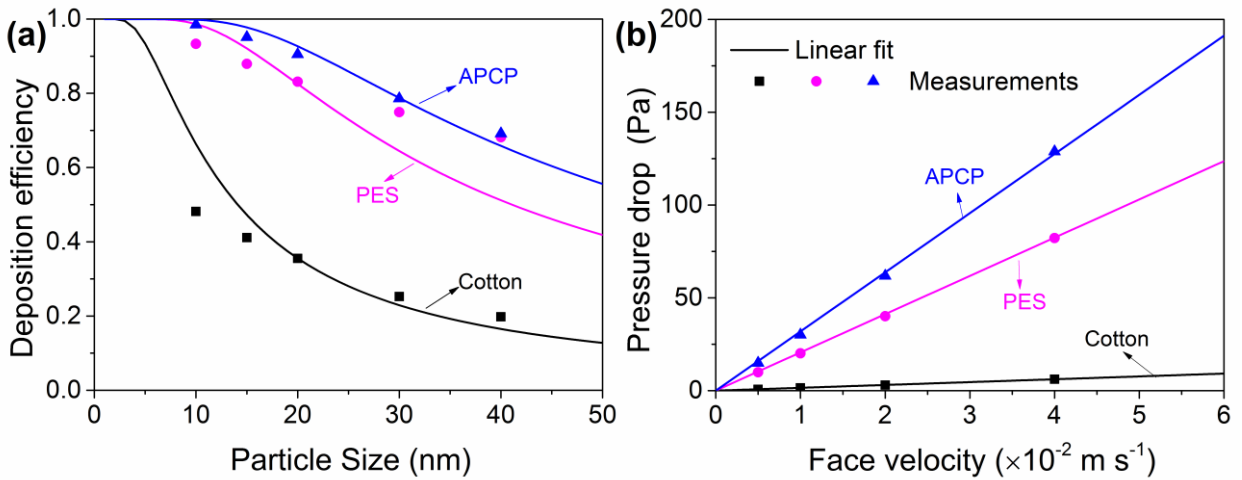
Figure 7.3 Filtration performance of the textiles. (a) deposition efficiency as a function of particle diameter for a face velocity of 0.02 m s^{-1}. The curves represent predictions using equation (7.1), whereas the symbols correspond to the deposition measurements. (b) flow pressure drop across the textiles as a function of face velocity.

For any given mass production rate and deposition time, equation (7.1) can be used to estimate the NP loading on the textiles[26]. Predictions by equation (7.1) are validated with inductively coupled plasma mass spectrometry (ICP-MS) (cf. Table S7.2). The agreement between measurements and predictions has a practical value, especially when it comes to scaling up the process and building an online system to monitor the NP loading of the treated textile. Another interesting feature is that the NP loading decays exponentially as a function of the depth of the textile (L_d)[35], determined by face velocity during deposition. As a result, the concentration/loading profile can be tuned (cf. equation (7.1)) depending on the applications.

Observed discrepancies between predictions made by equation (7.1) and the measurements can be caused by the inhomogeneity of the textiles, which strongly influence the collection efficiency of a filter medium[36]. This is especially true for the Cotton and PES textiles that have impermeable multi-filamentary fibres (i.e., only few fibres extend into the permeable pore structure). APCP textile mainly consists of a "hairy" tuft of individual fibres (oriented along the upstream side during filtration) which more closely resemble a conventional depth filter structure.

A pressure drop is caused by the combined effect of each fibre resisting the gas flow. Figure 7.3b shows that the measured pressure drop is linearly dependent on the flow face velocity (cf. Supplementary Equation (S7.15))[34]. Since the NP loading does not introduce additional resistance (at least regarding the loading range intended here), the pressure drop for the raw (without aerosol deposition) and nanofinished textiles (with aerosol deposition) collapses into one single curve as shown in Figure 7.3b (cf. Supplementary Table S7.2).

7.2.3 Surface chemistry and morphology of Ag NPs on textile fibres

The primary particle size, the surface property, and the crystal phase of the Ag NPs are determined by small- and wide-angle X-ray scattering (SAXS/WAXS). The scattering intensity I_i of the raw and nanofinished Cotton textile was recorded as a function of the scattering angle 2θ or the scattering vector $q = (4\pi \cdot \sin\theta)/\lambda$ (using X-ray (Cu K_α radiation) wavelength $\lambda = 0.154$ nm).

 Figure 7.4 shows the SAXS/WAXS data for the nanofinished Cotton textile. The scattering intensity follows a power law ($I_i \propto q^{-4}$) when q ranges from 0.5 to 2 nm^{-1}, which implies that the Ag NPs have a smooth surface with a surface fractal dimension d_s of 2.0. In the range of q smaller than 0.5 nm^{-1}, their radius of gyration R_g was found to be 5.4 nm, which corresponds to a mean diameter d_p of 13.9 nm[37]. This diameter is significantly larger than that estimated by the SMPS measurements (i.e., the red curve in Figure 7.2b). Such a discrepancy can be attributed to the strong coalescence of high-purity singlets on fibres during deposition[37]. The coalescence ceases when the NPs reach a critical size beyond which agglomerates become dominant[26]. Another reason for this discrepancy lies in the fact that the low loading of Ag NPs in the textile leads to

large scattering in SAXS measurements, causing large deviations in data fitting. Comparing the peaks of the WAXS curves corresponding to the raw fabric with those of the nanofinished fabric, an additional peak at $2\theta = 37.1^\circ$ is related to crystalline phase Ag (111). The acquired signals are relatively weak due to the low NP loading on the fabric (cf. Supplementary Table S7.3).
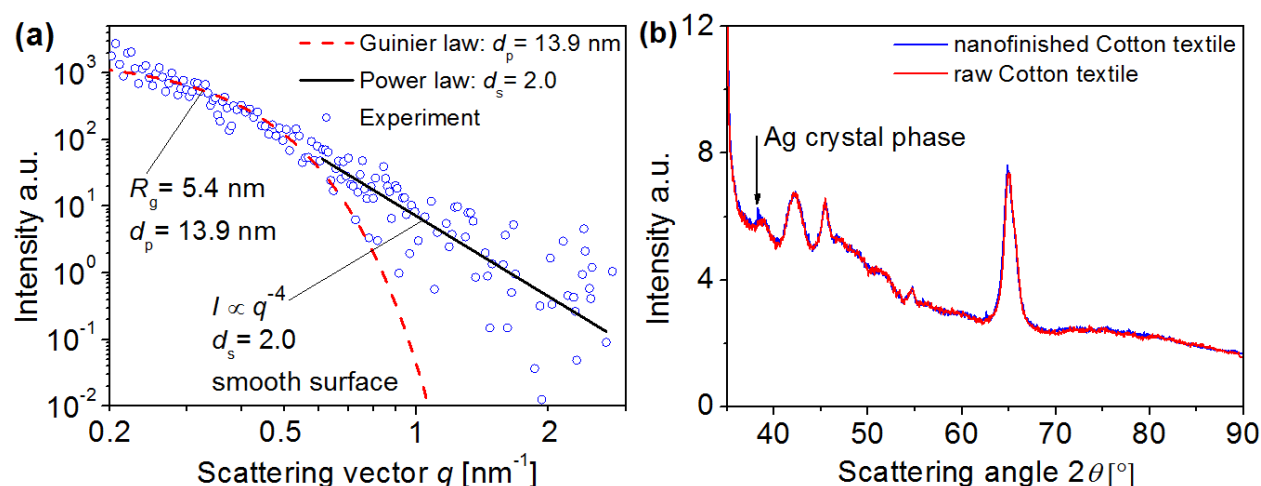
Figure 7.4 SAXS/WAXS data for Cotton textile. (a) SAXS data for Cotton textiles treated with Ag NPs. (b) the WAXS patterns seen in raw and nanofinished Cotton.

XPS confirms the existence and chemical state of the surface of the three nanofinished textiles. These textiles were examined with XPS on the front side: which was directly facing the aerosol flow during deposition, and the backside, which was in close contact with the textile sample holder. The absence of any additional peaks in the XPS measurements performed on the backside of the nanofinised textiles, as compared to those on the raw textiles indicates the absence of silver on this side. This is in line with the predictions of equation (7.1) and the deposition measurements shown in Figure 7.3a, which indicate that the majority of the particles (depending on their size) are being deposited at the front side of the textiles as the aerosol flows from one side to the other. Consequently, the concentration of the deposited particles decreases with increasing fabric depth. Sub-10 nm particles have 100% deposition efficiency, implying that no Ag particles are present at the backside of the fabric (i.e., all of them are deposited before the flow reaches the backside), as confirmed by the XPS measurements (cf. red curve in Figure 7.5a).
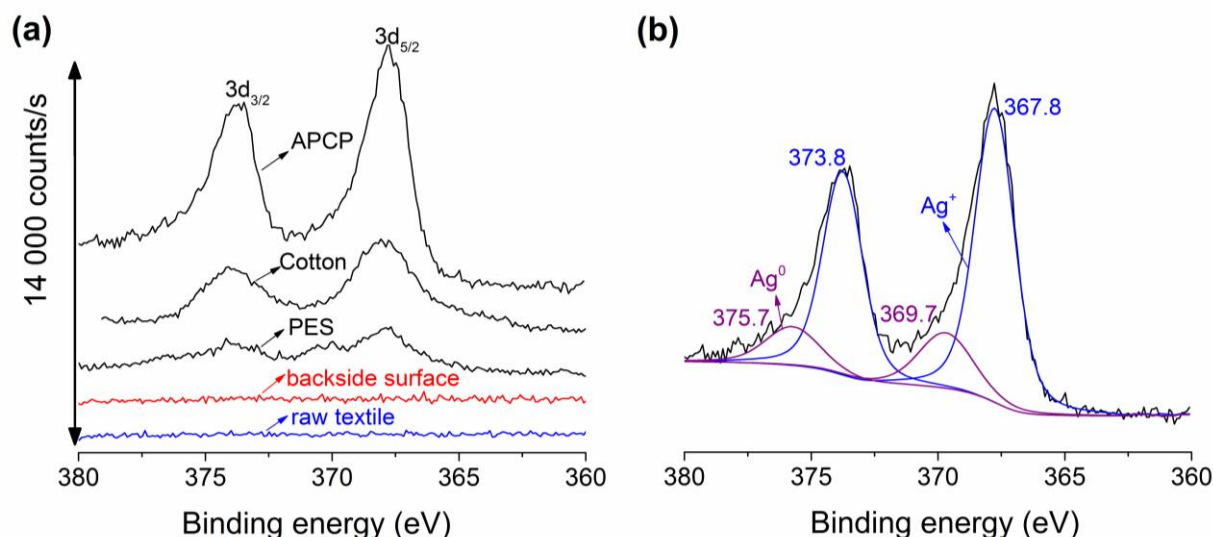
Figure 7.5 Compositional characterization of Ag NPs deposited on textiles. (a) High-resolution Ag 3d ($3d_{5/2}$ and $3d_{3/2}$) XPS region spectra of APCP, Cotton, and PES textiles, including the front side surface (black curves) and the back side surface (red line) of the nanofinished fabrics, as well as the surface of the raw textiles (blue line). As all the three raw textiles and their backsides have flat lines, the red and blue lines are valid for all these three textiles. The total intensity of the two peaks reflects the different contents of Ag on the nanofinished textiles, in line with the ICP-MS measurements (Supplementary Information Table S7.3). (b) the deconvolution of the Ag 3d peaks for the nanofinished APCP textile.

On the front side, the peaks at 369.7 and 375.7 eV are assigned to the binding energies of Ag $3d_{5/2}$ and Ag $3d_{3/2}$ of metallic Ag^0. The 367.8 and 373.8 eV peaks correspond to the binding energies of Ag $3d_{5/2}$ and Ag $3d_{3/2}$ of Ag^+ (Ag_2O) or to the surface charges of the NPs. A number of studies have reported on the shift of XPS core levels to higher binding energies for sub-10 nm Ag NPs[39,40]. Considering also the (small) difference in the internal standard, the binding energy identified in the measurements suggests that the NPs are smaller than 20 nm in diameter, which is in line with the SMPS results. The chemical state ratio of Ag^+/Ag^0, estimated by the deconvolution of the Ag 3d peaks (cf. Figure 7.5b), is ca. 3.9 (which is similar to that reported Prieto *et al.*[39]). This is understandable because the surface of Ag NPs undergoes oxidation (also confirmed by the presence of Ag MNN peak in the Auger region[41]) when exposed to the atmosphere.

The low amount of NPs deposited in the textiles (cf. Table S7.3) is responsible for the invisible peak of silver oxides in the WAXS curve (cf. Figure 7.4b). Note that the positive charges of the Ag NPs could also contribute to Ag$^+$: they electrostatically attract the negatively charged bacterial cell membranes thereby promoting antibacterial activity[17,42].

7.2.4 General macroscopic properties of the nanofinished textiles

The colour of the nanofinished textiles depends on the types of fabrics (cf. Figures 7.6 a, e and i) and on the NP loading (Figures 7.6b, f and j). SEM images with two different magnifications for each textile sample are presented in the last two columns of Figure 7.6 (c, d, g, h, k, and l). Magnified images show the singlet and agglomerated Ag NPs attached to the surface of the fibres. As shown in Figure 7.2, the NPs suspended in the gas phase remain non-agglomerated singlets. Particles agglomerate at a later stage after coalescence via collisions with arriving aerosol NPs. Moreover, NP depositions of low loading did not change the woven structure of the fabrics, which indicates that the air-breathing properties that are so vital to textile comfort are preserved.

7.2.5 Antimicrobial properties of the nanofinished textiles

Ag NPs have been widely shown to exhibit antimicrobial activity[17,43]. Although the exact mechanisms of their antimicrobial action is still subject to debate[44], it is believed that Ag ions released by the NPs interfere with bacterial cell functions upon contact[43,45–49]. The Ag ions penetrate the bacterial cell wall, and subsequently bind with DNA molecules, leading to a loss of the ability to replicate. At the same time, Ag NPs inactivate and denaturate proteins because they tend to have a greater capacity to react with sulphur-containing proteins and phosphorous-containing DNA. These phenomena lead to the degradation or death of the microorganisms[46,47]. Electrostatic attraction between bacterial cells and particles can also have an impact on antibacterial activity (AA)[47–49], whereas reactive oxygen species can damage lipids, proteins, and the DNA of microorganisms[45].
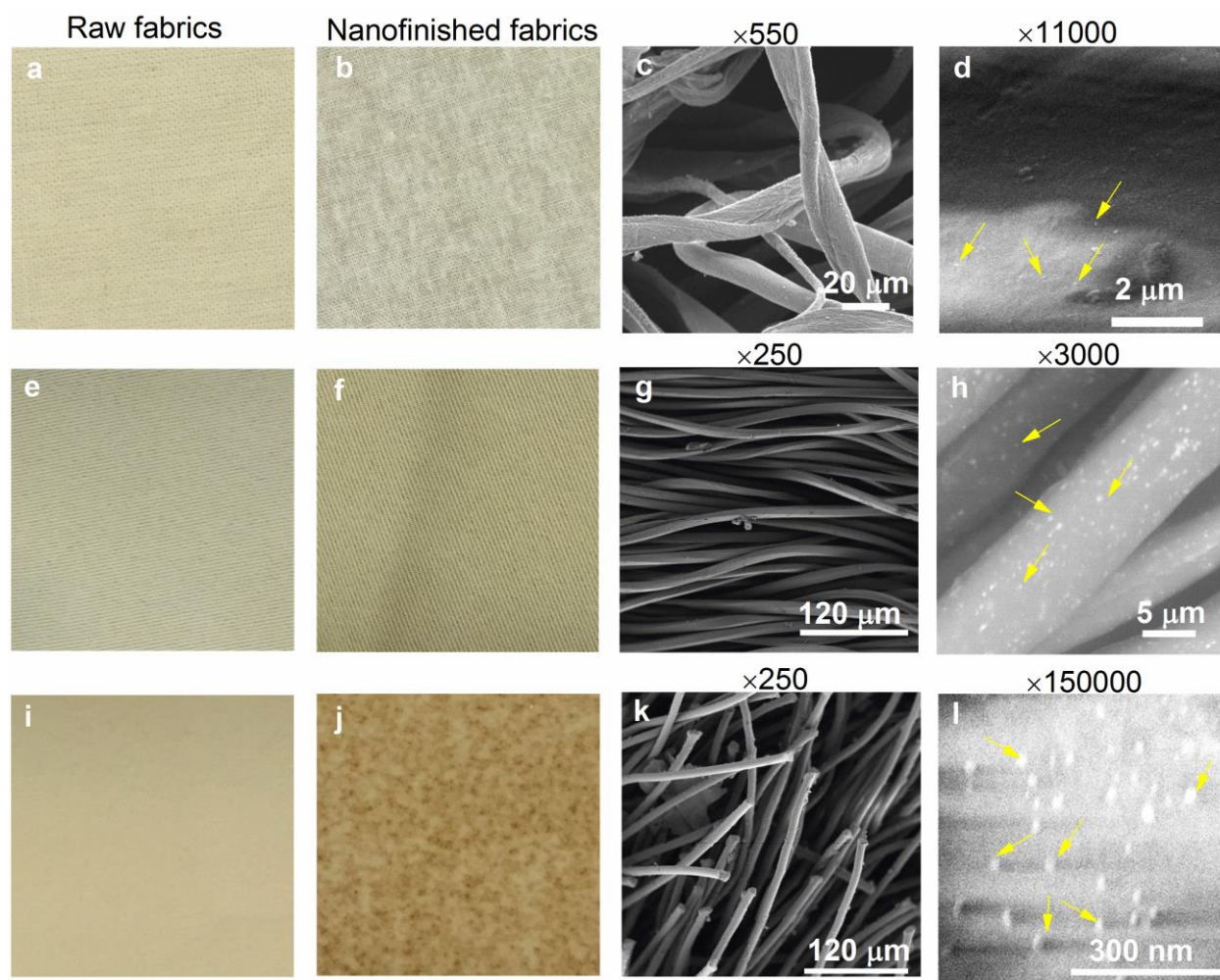
Figure 7.6 Visual change of the fabrics before and after the deposition of Ag NPs (first two columns) and SEM images of the nanofinished textiles (last two columns). (a-d) Images of raw and nanofinished Cotton fabrics, together with two sets of SEM images with magnifications of ×550 (acceleration voltage: 5 kV) and ×11000 (acceleration voltage: 3 kV). (e-h) Images of raw and nanofinished PES fabrics, together with two sets of SEM images with magnification of ×250 (acceleration voltage: 5 kV) and ×3000 (acceleration voltage: 3 kV). (i-l) Images of raw and nanofinished APCP fabrics, together with two sets of SEM images with magnifications of ×250 (acceleration voltage: 5 kV) and ×150000 (acceleration voltage: 3 kV).
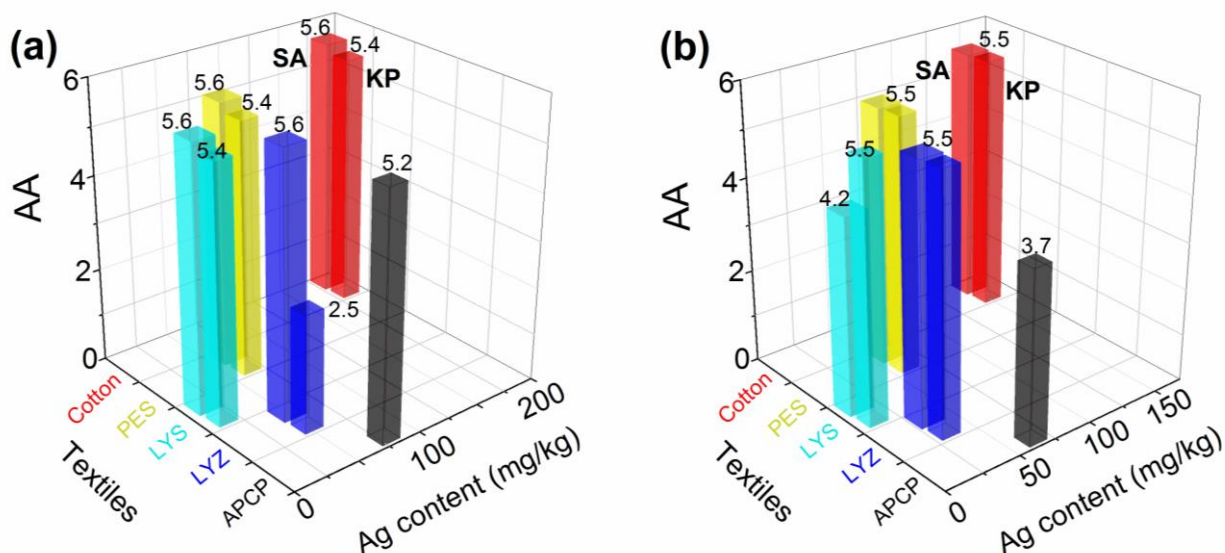
Figure 7.7 Antibacterial activity (AA) of the textiles treated with Ag NPs against *Staphylococcus aureus* (SA), and *Klebsiella pneumonia* (KP), represented, respectively, by the left and right rectangular columns of the same textile. (a) Antibacterial activity of nonwashed textiles versus Ag content; (b) antibacterial activity of washed textiles (three cycles for Cotton, PES, LYS, and LYZ, and five cycles for APCP) versus Ag content.
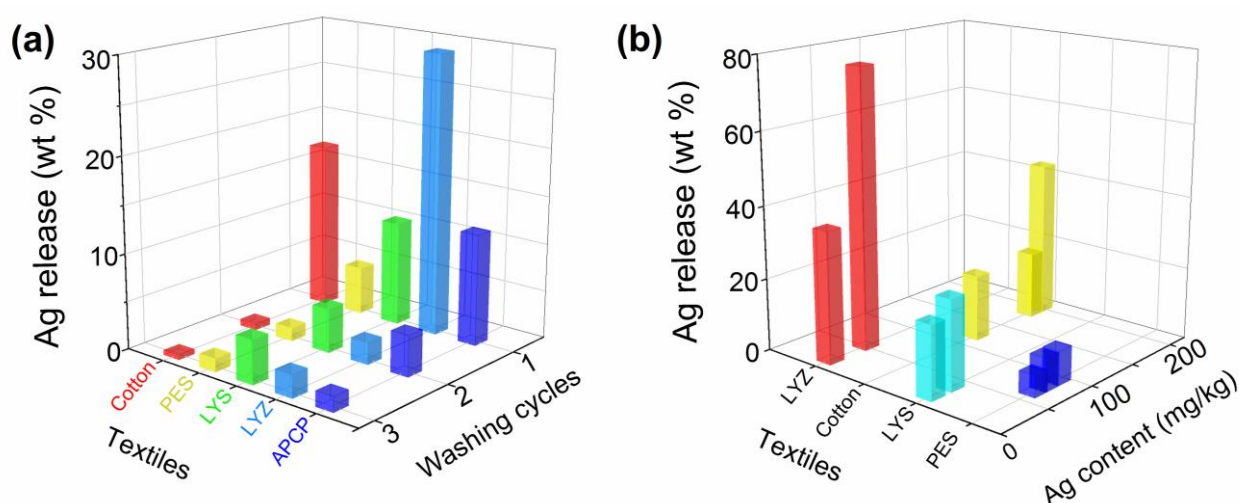
Figure 7.8 Ag NP release from the nanofinished textiles as a function of (a) washing cycles and (b) Ag content.

The AA of the nanofinished textiles was assessed in accordance with the International Standard ISO20743 (quantitative method). All the nanofinished textiles assessed in this work exhibit strong AA (≥3). An AA of ca. 5 is equivalent to a colony forming unit (CFU) reduction efficiency of 99.96% (see Methods). The high AA values shown in Figure 7.7a can be attributed to the

large specific surface area and to the associated fast ion release rate of the NPs that were synthesized and used here[43]. In contrast to traditional wet-finishing processes[17,50,51], the textiles with such low Ag NP loading (in the order of 10 ppm) still have high antimicrobial efficiency (against *Staphylococcus Aureus* (SA) and *Klebsiella Pneumoniae* (KP), as shown respectively by the left and right bars corresponding to each experiment). Minor differences in AA against SA and KP can be explained by the dissimilar defence systems of the two species against Ag ions[46]. Viability assays show no statistically significant change in the AA of the textiles with concentrations above ca. 15 ppm. Changes above this limit cannot be determined by standard method employed to test the AA (cf. Methods), due to 'saturation' of the method[44]. This means that by exceeding a NP loading level, the CFU reduction efficiency remains roughly 100% (more specifically, 99.96% for AA of 5).

The AA values of the different nanofinished textiles after washing are presented in Figure 7.7b. Interestingly, the AA remains as high as 5.5 after three washing cycles. The decreased AA of nanofinished LYS (from 5.6 to 4.2; Lyocell Safari in Supplementary Table S7.1) is attributed to its lower Ag content (12 ppm) which is not sufficient to achieve the saturation point. Though this Ag content is ca. 50 times lower than that reported in previous work[50], a high AA is still retained[52]. The comparatively low Ag content required to achieve high AA values when dry deposition is used, may be attributed to the homogenous NP coverage, the size of NPs which is in the sub-10 nm range, and the faster ion release. In contrast to the results reported by Hebeish *et al.*[53], the AA of LYZ (Lyocell Zen; cf. Supplementary Table S7.1) textile is higher in the washed rather than the in the unwashed samples. A possible reason for this is that the pH of the detergent used for washing considerably promotes Ag ion release[43]. On the other hand, compounds (e.g., starch, protein derivatives, fats and oils) typically used on the textiles that serve as nutrients for the bacteria are easily washed away, thereby resulting in an increased AA after washing.

7.2.6 Washing durability of the nanofinished textiles

In connection with the release of Ag NPs from textiles, the laundering durability is of paramount importance for their reuse. To determine that, this chapter carried out a mechanical washing test following the standard method ISO 105-C06:2010. A high NP release was observed for the first washing cycle (ca. 5-33%). Less Ag was released in the second wash (< 5 %) gradually decreased to ca. 1 wt.% after three washing cycles (one order of magnitude lower than that seen in commercial fabrics[51]), indicating good washing durability. The higher release of Ag in the first wash is ascribed to the agglomerates formed in the very first layers of the fabric facing the aerosol flow (cf. Supplementary Figure S7.4). Such agglomerates easily become detached from the fibres during washing[51]. Even after three washing cycles, virtually no reduction is observed in the AA of the nanofinished textiles, implying that a lower amount of Ag NPs (ca. 10 ppm) would be sufficient to achieve an AA value of ca. 5. To reduce the release of Ag while still retaining high AA, the nanofinished textiles can be appropriately washed before use.

Lower NP loading can prevent the formation of agglomerates on the fibres while maintaining high AA, as demonstrated by Lok *et al.*[54]. Particle size distribution measurements (cf. Figure 7.2) confirm that the NPs remain non-agglomerated singlets when suspended in the gas[26]. Depositing such singlets should decrease particle release in conjunction with strong particle adhesion to the fibres when compared to larger particles or agglomerates. Both enhanced adhesion and a large exposed surface can thus be achieved by making the particles small[54]. Deposition of NPs deeper within the textiles, which should also reduce their release during mechanical washing, can be achieved by simply increasing the quenching gas flow rate Q_q as indicated by equation (7.1) (cf. Figure S7.5). The size of the resulting Ag NPs also reduces to the sub-5 nm, which helps in realizing a minimum deposition level. Ultimately, this low NP loading can reduce the potential environmental and human health impacts while guaranteeing the comfort of textiles as their texture will remain unchanged[55]. Apart from the influence of particle size on the release, the type of textiles also plays a role as indicated by the leaching test shown in Figure

7.8a. In addition, the formation of agglomerates on the front layers of the fabric, due to the longer deposition as discussed above, contributes substantially not only to the high Ag content but also to the imminent release in the mechanical washing process (cf. Figure 7.8b).

7.3 Discussion

This chapter has combined, for the first time, NP synthesis in the gas phase with diffusional deposition to realize a novel pathway for the next generation of multifunctional textiles. Put briefly: sub-10 nm NPs carried by a gas flow are passed through the fabric, where they rapidly diffuse and attach to the textile fibers. This approach does not require any stabilization steps or reducing agents, does not produce any effluents, and has low energy consumption, thereby gaining financial and environmental benefits. In addition, the fast kinetics of NP formation in the gas phase represents a dramatic increase in the process throughput, which addresses one of the bottlenecks seen in large-scale textile nanofinishing.

As proof of this concept, among the numerous potential applications of the functionalized textiles, this chapter shows that the antimicrobial activity of a number of textiles nanofinished with Ag NPs is high. Although the NP loads used here were one order of magnitude lower than those used in traditional wet-finishing routes, they were shown to be sufficient for achieving high antibacterial activity even after three washing cycles. The antimicrobial textiles outperform those reported in the literature due to the particle size which lies in the sub-10 nm range, the good mechanical durability, the absence of liquid precursors, the desired finishing surface, the easy scalability, and the virtually unlimited mixing combinations of NPs.

Investigating the size-effect of the NPs can also provide an opportunity to improve fundamental understanding of particle-cell interactions, which have been impossible to investigate up until now. Despite the small NP loadings (even in the order of 10 ppm), compared to those used in other studies, the plateau ("saturation effect") in the antimicrobial activity of the nanofinished fabrics reported here can be attributed to the size and the composition of the particles employed. To reveal the NP size-dependent effects in future work, one will have to use even smaller loadings and also

avoid the formation of agglomerates on the fibers, thus minimizing their release due to the strong adhesion of the singlets to the fibers. The low loading of NPs on textiles can also maintain conformal contact with the human body in a non-invasive way.

Apart from the aforementioned advantages of depositing singlets on textile fibers, their deeper deposition within textiles can improve the washing durability. This can be achieved by increasing the face velocity of aerosol flow, associated with increased pressure drop (cf. Figure 7.3b). The pressure drop can be estimated theoretically, thereby providing the basis for designing a system that bears with such high pressure when scaling up the nanofisnihing process. In order to allow the high pressure, which forces the aerosol flow passing through the fabrics, the whole system (roll-to-roll) must be sealed, which can be realized by employing standard vacuum components and flanges. Therefore, one has to design an enclosure for the fabric rolls and seals for the slits that are the interfaces with the aerosol deposition environment and the ambient air.

When agglomerates cannot be avoided, to improve the washing durability of the nanofinished fabrics, one can bind them to the textile fibers by introducing covalent linkage (e.g., thiol group) to textile fibers[45,56]. Surface area of the agglomerates is approximately equal to the sum of individual particles, thus providing comparable antimicrobial properties. The reason for not fabricating NP surface is to maintain the simplicity of the NP production method. Another reason is that the non-fabricated NPs tend to further agglomerate when released in an aquatic environment. These large agglomerates are no longer able to cross biological barriers, such as the blood-brain or placenta barrier[55]. The risks are consequently eradicated as compared to those linked to using surfactants to prevent further agglomeration[55].

Nanofinished textiles can release a fraction of the deposited NPs upon washing, thereby reducing their antimicrobial activity and having an impact on the environment[57]. Because the NP release mechanism can vary depending on the temperature and the pH of the detergent[58–61], this chapter used the standard ISO 105-C06:2010 washing method at the most harsh conditions[62], which fixed the pH within the range 6.5–7.0 and temperature at 90 °C. Doing so facilitates

comparison with other studies[51] and maintains textile properties (e.g., color, comfort, and texture) for long-term use. Despite the tremendous global market of smart textiles[62], the major concern lies in their potential release of the NPs to the environment[57]. Ag NPs, or ions released from their surfaces, that end up to the wastewater can inhibit the growth of bacteria in treatment plants and/or become toxic to aquatic life[63]. Future life cycle evaluations should also take into account the type of nanomaterials, their solubility, and oxidizing capacity.

7.4 Conclusions

This chapter has presented a universal and sustainable way for one-step textile nanofinishing by incorporating aerosol NP production and deposition onto fibres. This enables the proposed approach to stand out from all the multi-step finishing processes employed so far. As proof of the concept, this work has studied the antibacterial activity of a number of textiles loaded with Ag NPs at concentrations in the order of 10 ppm. These textiles exhibited AA of ca. 5.5 (logarithmic reduction in bacterial count) which corresponds to a CFU reduction efficiency of ca. 99.96%. This high AA is maintained even after three washing cycles. Although Ag release by mechanical washing is one order of magnitude lower than that of commercial nanofinished textiles, the washing durability can still be enhanced by introducing covalent linkage between Ag NPs and thiol-modified cellulose fibres. The proposed approach also allows tuning the depth profile and the size of the NPs deposited in textiles, which lies beyond the capabilities of pad-dry-cure processes and can be used to further improve the washing durability. Although this study demonstrates the antimicrobial properties of the nanofinished textiles with Ag NPs, the concept can be extended to diverse material combinations for the preparation of multifunctional textiles. Since the performance of nanofinished textiles still needs to be further investigated and improved, concerted effort is still required to understand the impact that released nanomaterials can have on humans and ecosystems.

7.5 Methods

7.5.1 Nanoparticle synthesis

Electrical discharges were used to produce Ag NPs[64,65]. In spark ablation, a spark discharge is initiated by a self-pulsed circuit operating in parallel with a capacitor bank and with two electrodes (two identical 99.99% pure Ag rods with a diameter of 3 mm and a length of 30 mm; MaTecK GmbH, Germany) placed next to each other forming a gap through which the carrier gas (Ar purity 99.999%) flushes through. In the arc discharge, one is made of tungsten (with a diameter of 1.6 mm, purity 99.95%, Goodfellow Cambridge Ltd., UK), and the other is made of Ag (with a diameter of 9.5 mm, purity 99.9%, Goodfellow GmbH, Germany). In a similar manner with spark ablation, a carrier gas of N_2 (purity 99.999%). In these methods, the Ag electrode evaporates due to the energy delivered by the discharge. The vapors are quenched by the carrier gas, leading to the formation of NPs through homogeneous nucleation, and subsequent condensation.

7.5.2 Particle size distributions measurements

A scanning mobility particle sizer (SMPS) was used to measure the size distribution of the particles[33]. The system consists of a differential mobility analyzer (DMA), and a Faraday cup aerosol electrometer (AEM). The DMA selects particles based on their electrical mobility, whereas the AEM counts the charged monodisperse particles downstream of the DMA.

7.5.3 Textile Nanofinishing by aerosol deposition

The textile performance was evaluated by measuring the filtration efficiency and the pressure drop. When the aerosol flow passed through the textile, the latter acts as a filter. The textiles (Cotton, PES, and APCP) consisted of a mat of fine fibres arranged perpendicularly to the aerosol flow direction and all had a fibre diameter of ca. 20 μm. The face velocity ranged from 0.5 to 4 cm s^{-1}. Because the aerosol NPs were very small, their Brownian motion guarantees the collision with the fibre while flowing around in a non-intercepting

streamline, whereas upon collision van der Waals forces ensure that NPs stick to the fibres.

7.5.4 Filtration properties of the textiles

To investigate the filtration efficiency of NPs (sintered, size-classified Ag spheres) for different textiles, their concentrations at the inlet and outlet of the textile holder were measured using two condensation particle counters (CPC Model 3775, TSI). The filtration efficiency results were calibrated for particle losses in the tubing and textile holder as well as for differences in the counting efficiencies of the each CPC, based on reference measurements with no textile samples in the holder. The filter pressure drop Δp at various face velocities (0.5, 1, 2, 4 cm s^{-1}) was measured using a sensitive handheld differential pressure transducer (Testo Model 521-3) connected to the upstream and downstream ports of the textile holder. Δp across the filter was obtained by subtracting the measured pressure drop across the empty textile holder from that using the entire holder and textile assembly. Details of the setup are shown in Supplementary Figure S7.3.

7.5.5 Analysis of the fabric Ag content by means of ICP-MS

Three replicates of 0.2 ± 0.04 g from each textile were digested with 3 ml HNO$_3$ (65%, Fluka) and 1.5 ml HCl (95%, Sigma–Aldrich), and were attained in a microwave digestion system (ULTRAWAY of MILESTONES). The Ag content of the digests was quantified by means of inductively coupled plasma mass spectroscopy (ICP-MS Perkin-Elmer OPTIMA 7700), which was calibrated with a silver standard solution (AgNO$_3$ in 5 M HNO$_3$, 1000 mg L^{-1}, Merck).

7.5.6 Antimicrobial activity of the nanofinished textiles

The antibacterial activity of the fabrics was tested according to a standard method (ISO 20743: 2013) using the Gram-negative bacterium *Klebsiella pneumonia* ATCC 4352 (LMG 3128) and the Gram-positive bacterium *Staphylococcus Aureus* ATCC 6538 (CECT 239). All textiles used in this work were placed into 0.2 mL of inoculum (1~3×10^5 CFU mL^{-1}) and 20 mL of neutralizing agent per 0.4 g of fabric. This standard always made use of a

reference fabric (C values). The antimicrobial activity (AA) was determined by counting the number of bacterial colonies and was calculated according to the logarithm reduction of CFU given by:

$$AA = \log\left(\frac{C_t/C_0}{T_t/T_0}\right) \tag{7.2}$$

where C_0 and C_t are the CFU of control/untreated samples at times 0 and 18 h; T_0 and T_t are the CFU of test/treated (or nanofinished) samples at times 0 h and 18 h. In the standard method to determine AA, the CFU was always below 2000, and thus changes exceeding this limit cannot be determined. In order to obtain an averaged AA, the tests were repeated three times. Each measurement used two control samples (raw fabric) for reference purposes and two test samples (treated fabrics). According to Annex F of ISO 20743: 2013, the antibacterial property of the test fabric can be considered as "significant" when $2 \leq AA < 3$ and "strong" when $AA \geq 3$.

7.5.7 Washing durability of the nanofinished textiles

The washing procedure was conducted according to a standard method (ISO 105-C06:2010). A washing machine (ATLAS Linitest) equipped with steel vessels that had a capacity of 550 ml and a motor speed of 40 ± 2 rpm was used for all the tests. Ten steel balls previously cleaned in HNO_3 (65%) were used to exert mechanical stress. It was ensured that the detergent/container volume ratio (0.279) was the same as that in the steel vessel. The detergent was prepared by dispersing 4g L^{-1} ECE 98-standard washing powder in distilled water (composition: 9.7% LAS, 5.2% non-ionic surfactant, 3.6% soap, 4.5% antifoam, 32.5% zeolite, 11.8% carbonate, 5.2% acrylic acid, 3.4% Na-silicate, 1.3% CMC, 0.8% phosphonate, 9.8% sulphate, 12.2% others/water)[60]. The textiles (2 samples; area of 40×100 mm²) were washed for 55 min at 90 °C. Acid-cleaned polyethylene bottles (100 ml) were used to recover the detergent from the washing machine. The detergent was analysed by means of ICP-MS to determine the Ag content embedded in the textiles (mg/kg). This study performed three cycles for Cotton, PES, LYS, and LYZ nanofinished textiles, while the APCP nanofinished textile was washed five cycles.

7.5.8 Surface chemistry and morphology of the nanofinished textiles

A transmission electron microscopy (TEM, Philips CM30T and Philips CM12) and a scanning electron microscopy (SEM, Hitachi S-3400N and Hitachi S-4500) were used to image the particles in order to determine their size, structure and morphology. For the TEM measurement, a mini-particle sampler was used to collect the particles on the TEM grids (Van Loenen Instruments, S143-3 Q'foil 1.2/1.3 400 Cu) by filtration[66].

Detailed information on the structure of the particles found on the fibres was obtained by small- and wide-angle X-ray scattering (SAXS/WAXS). Non-invasive measurements were performed using a custom-made laboratory SAXS/WAXS camera with Cu-Kα radiation ($λ = 1.54$ Å), as described elsewhere[67]. To obtain sufficiently accurate statistical results, each sample, having an area of ca. $0.5 × 1.5$ cm² was positioned inside the SAXS/WAXS measuring chamber and illuminated by an X-ray beam. The scattering signals were simultaneously recorded within a detection angle of 90°.

X-ray Photoelectron Spectrometer (XPS; Thermo Fisher Scientific Kα model) examination was carried out for the elemental analysis of the nanofinished textiles. A monochromatic Al Kα X-ray source having a spot size of 200 μm at a pressure of 10^{-8} mbar and a constant pass energy of 10 eV was used; the flood gun was turned on during the measurements in order to compensate the potential charging of the surface. The peak positions in the narrow scan spectra were adjusted according to the internal standard C1s peak at 284.5 eV, with an accuracy of ± 0.05 eV.

Supplementary Information in Chapter 7

The SI of this chapter contains the following contents: the calculation of particle size distribution at the location of textiles, modelling NP deposition onto textile fibres, the characteristics of some textiles, the filtration properties of a number of textiles, the estimation of NP loading on textiles, the visual layout of the particle deposition on one single fibre, the layout and a photograph of experimental setup.

S7.1 Particle size distribution at the position of textiles

The size distributions of NPs at the position of the textiles (Figure 7.2a and 7.2b in the main manuscript) take into account the particle growth between the fabric holder and the DMA. The mean particle size can be calculated by extrapolating the size distributions measured by the SMPS measurements to those at the position of the fabric in the holder.

The total particle number concentration can be estimated by:

$$N(t_f) = \frac{N(t_M)}{\exp\left(-K_{df}\frac{\pi d_{tube}{}^2 x}{4Q_a}\right)(1+\omega) - \omega} \tag{S7.1}$$

where $\omega = \frac{\beta N(t_M)}{2K_{df}}$ is a dimensionless quantity, β the coagulation coefficient, K_{df} the diffusional deposition rate, Q_a the aerosol flow rate, d_{tube} the inner diameter (4 mm) and x is the length of the tube connected to textile holder and the DMA (x = 32 cm; cf. Figure S7.1); $N(t_M)$ and $N(t_f)$ are the total number concentration measured by SMPS and the location where NPs are deposited onto the textiles.
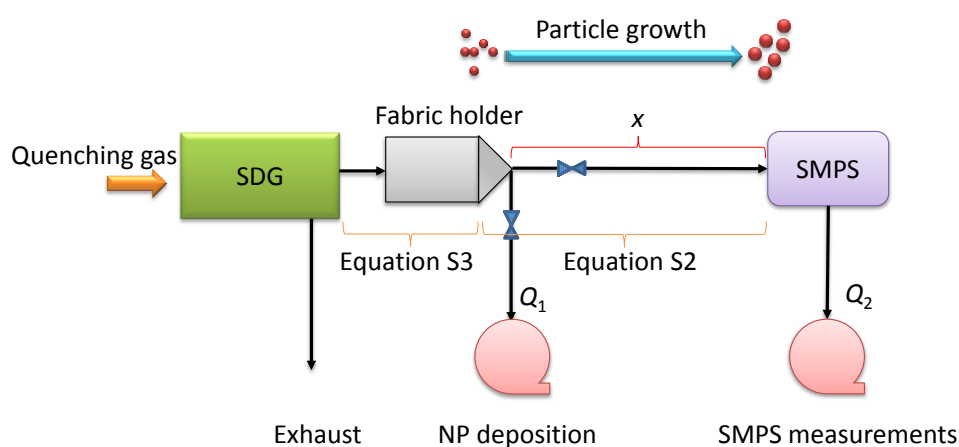
Figure S7.1 Schematic illustration of the setup for nanoparticle (NP) deposition and measurements.

The mean particle size at the location of textile is given by:

$$d_p(t_f) = \frac{d_p(t_M)}{\left(\left(\dfrac{\omega}{\dfrac{1}{\exp\left(K_{df}\dfrac{\pi d_{tube}{}^2 x}{4Q_a}\right) - 1} - \omega} + 1\right)\right)^{\frac{1}{3}}} \tag{S7.2}$$

where $d_p(t_M)$ is the mean particle sizes measured by SMPS measurements and and $d_p(t_f)$ are calculated on the basis of work shown before[26,30].

The mean size determined by equation (S7.2) is not the one corresponding to the fabric deposition. This is because an aerosol flow rate of 8.5 slm (i.e., face velocity ca. 2 cm s⁻¹ at a circular textile with a diameter of 8 cm) was used for textile nanofinishing, while the aerosol flow rate for SMPS measurements was 1.1 slm.

 To account for the different flow conditions, different particle growth has to be considered. The particle size depends on mass production rate and Q_q for a given particle generator as follows:

$$d_p = \left(\frac{3\beta V_{eff}\dot{m}}{\rho\pi Q_q{}^2}\right)^{1/3} \tag{S7.3}$$

where β is the coagulation coefficient, V_{eff} the volume of fabric holder, $\dot{m}$ the mass production rate through the fabric holder. Note that for the mass production rate through the fabric holder the exhaust flow needs to be excluded. The difference between conditions during the fabric deposition process and the SMPS measurements are reflected through the flow rate (SMPS: Q_2 = 1.1 slm; Fabric deposition: Q_1 = 8.5 slm) and $\dot{m}$ (e.g., for the quenching gas flow rate of Q_q = 20 slm, the mass production rate in the fabric holder for SMPS: $Q_2/Q_q\,\dot{m}$; fabric deposition: $Q_1/Q_q\,\dot{m}$) of equation S7.3.

The mean size d_{pf} at the position of the fabrics is thus calculated as:

$$d_{pf} = \left(\frac{Q_2}{Q_1}\right)^{1/3} d_p(t_f) \tag{S7.4}$$

S7.2 Modelling of NP deposition onto textiles

In the particle generation process, a higher flow rate leads to smaller particles. In the subsequent deposition step, decreased particle sizes lead to higher deposition efficiency, while an increased flow velocity reduces the deposition efficiency. The combined effect of these opposing trends still results in enhanced collection, as can be concluded from the considerations that follow:

Increasing the volume flow Q_q decreases the particle size d_p according to [26]:

$$d_p \propto Q_q^{-\frac{2}{3}} \tag{S7.5}$$

As shown in the main manuscript, the resulting NPs deposited on the textiles are smaller than 5 nm, and thus have extremely high diffusion coefficient (cf. equation (S7.7)). The Brownian motion of small NPs is sufficient to greatly enhance the probability of their hitting a fibre while travelling past a fibre while travelling passed it on a non-interception streamline. A simple filtration model accounting only for diffusional deposition of the particles can be applicable to estimate the deposition efficiency in our case. According to that, the aerosol flow passes through the pores between the fibers. The diffusion deposition efficiency E_{dep} is given by[68]:

$$E_{dep} = 1 - \exp\left(\frac{-10.8\alpha_s L D^{\frac{2}{3}}}{\pi(1-\alpha_s)d_f^{\frac{5}{3}}U^{\frac{2}{3}}}\right) \tag{S7.6}$$

where α_s is the volume fraction of fibres, which is also called solidity; where L is the thickness of the fabrics; d_f is the effective fibre diameter; D is the diffusion coefficient; U is the face velocity. Most of the parameters used in equation (S7.6) can be determined experimentally. The face velocity is given by:

$$U = \frac{Q_q}{A} \tag{S7.7}$$

where A is deposition area of the fabrics.

D is given by

$$D = \frac{kTC_{\text{c}}}{6\pi\mu d_{\text{p}}} \tag{S7.8}$$

where k is Boltzmann's constant, T the absolute temperature, μ the viscosity of the gas medium. C_{c} is the slip correction factor given by

$$C_c = 1 + \frac{\lambda_{\text{m}}}{d_{\text{p}}}\left(2.34 + 1.05\exp\left(-0.39\frac{d_{\text{p}}}{\lambda_{\text{m}}}\right)\right) \tag{S7.9}$$

The flow velocity U used in the model is 2 cm s⁻¹, corresponding to an aerosol flow rate of 8.5 slm passing through a circular fabric with a diameter of 8 cm.

Equation (S7.6) can be rewritten as[34]:

$$E_{\text{dep}} = 1 - \exp\left(-\underbrace{\frac{4\alpha L}{\pi(1-\alpha)d_{\text{f}}}}_{f'}\cdot\underbrace{2.7\left(\frac{D}{d_{\text{f}}U}\right)^{\frac{2}{3}}}_{\eta_{\text{D}}}\right) = 1 - \exp(-f'\cdot\eta_{\text{D}}) \tag{S7.10}$$

where f' combines all specific parameters of filter media (here is the textile), and η_{D} is the single fiber collection efficiency for diffusional collection, which includes, besides others, all process variables relevant for the deposition; in the diffusional regime, this included velocity U and diffusion coefficient D. Thus, the deposition efficiency E increases with increasing single fiber collection efficiency η_{D}.

The single fiber collection efficiency can be related to D and U as:

$$\eta_{\text{D}} \propto \left(\frac{D}{U}\right)^{\frac{2}{3}} \tag{S7.11}$$

In the free molecule range, D can be related to d_{p} as:

$$D \propto d_{\text{p}}^{-2} \tag{S7.12}$$

Given that U scales with Q_{q}, we finally arrive at

$$\eta_{\text{D}} \propto Q_{\text{q}}^{\frac{2}{9}} \tag{S7.13}$$

which means, η_D increases with higher flow rates, and thus, an increase of Q_q improves the NP deposition on the fabrics.

Equation S7.13 implies that an increase of Q_q does not diminish the NP deposition on the fabrics. The positive consequence of increasing Q_q lies in that the particle size is accordingly decreased (cf. equation S7.5), while the mass production rate of NPs is unaffected.[26] This unique feature enables the deposition of sub-5 nm NPs, thereby maximizing the surface area and minimizing the NP loading on textiles. It is worthwhile pointing out that this advantageous capability also facilitates a fast and efficient deposition of even smaller particles (going down to the atomic cluster regime) on the fibers of the textiles only with the implementation of a single step.
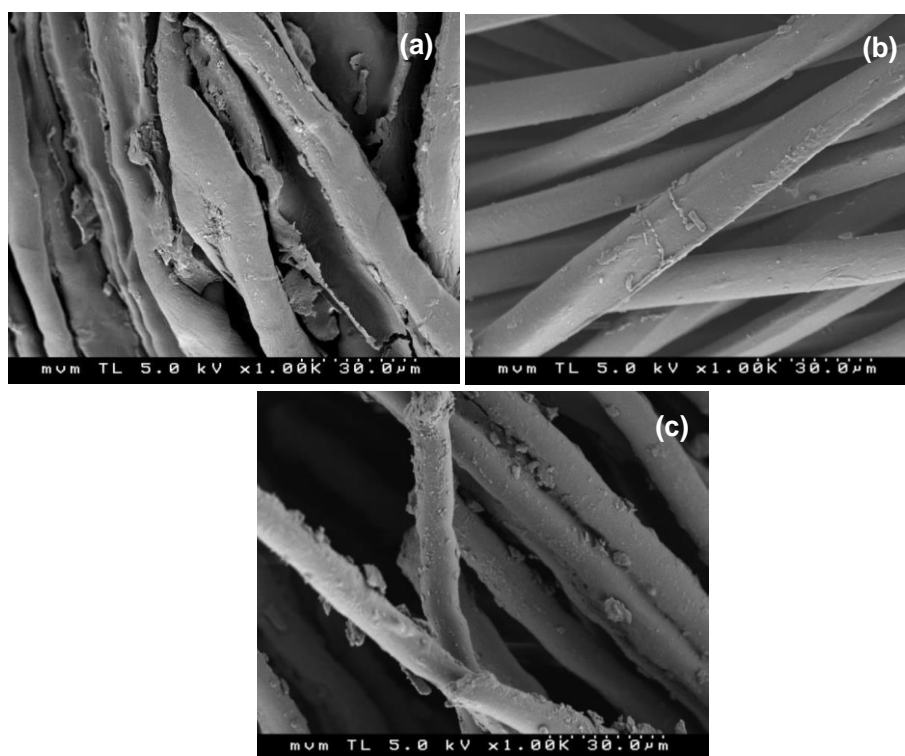
Figure S7.2 SEM images for the determination of the fibre diameter of different textiles. (a) Cotton; (b) PES; (c) APCP.

This chapter only considers the diffusional deposition. Other deposition mechanisms (e.g., inertial impaction, interception and gravitational settling), which are not captured by equation (1), become influential when particles get larger. However, even for the largest NPs investigated here, the other effects contribute negligible to deposition as indicated by the associated Stokes number *St* and interception

parameter R (for the 50 nm Ag NPs at 2 cm s^{-1}, St is in the order of 0.0001, and R is below 0.005)[69].

Table S7.1 Characteristics of some textiles used in Chapter 7

Textile	Composition (wt.%)	Weight (g m^{-2})	SEM d_f (µm)	Thickness L (mm)	Solidity α_s
Cotton	100 Cotton	140-150	25	0.35	0.10
PES	100 Polyester	200	20.6	0.55	0.17
APCP	40Acrylic20Polyester20cotton10polyamide	400-500	23	0.90	0.19
LYS	100 Lyocell rayon (Safari)	225	-	-	-
LYZ	100 Lyocell rayon (Zen)	130	-	-	-

Table S7.1 shows the characteristics of the textiles shown in the model. d_f is estimated from the SEM measurements, while L is an averaged value among the measurements using a calliper at different positions of a specific textile. α_s can be calculated and compared to values obtained by fitting predictions from equation S7.6 to deposition efficiency experimentally obtained (Figure 7.3a). The fitted values are in line with the reported solidity for these textiles[70], and α_s also fulfils the requirement:

$$\alpha_s = \frac{M_A}{L\rho} \tag{S7.14}$$

where M_A is the mass per unit area of the textile (kg m^{-2}; supplied by the manufacturer), and ρ is the density of the fibres (kg m^{-3}).

The pressure drop represents the total drag force of all the fibres given by[34]:

$$\Delta p = \frac{\mu L \left(64\alpha_s{}^{1.5}(1 + 56\alpha_s{}^3)\right)}{d_f^2} U \tag{S7.15}$$

Pressure drop is thus directly proportional to L, U and inversely proportional to d_f^2.

S7.3 Measuring deposition efficiency E_{dep} and pressure drop Δp for the textile samples

Figure S7.3 shows the setup used to determine E_{dep} and Δp for different particle sizes at various face velocities. This setup includes a section for particle generation, size selection and sintering, for independent flow rate adjustment, and for the actual deposition process including the measurement equipment for particle concentration and pressure drop, respectively. Table S7.2 shows pressure drop of the raw and nanofinished textiles, respectively.

Table S7.2 The pressure drops of the raw and nanofinished textiles with Ag NPs

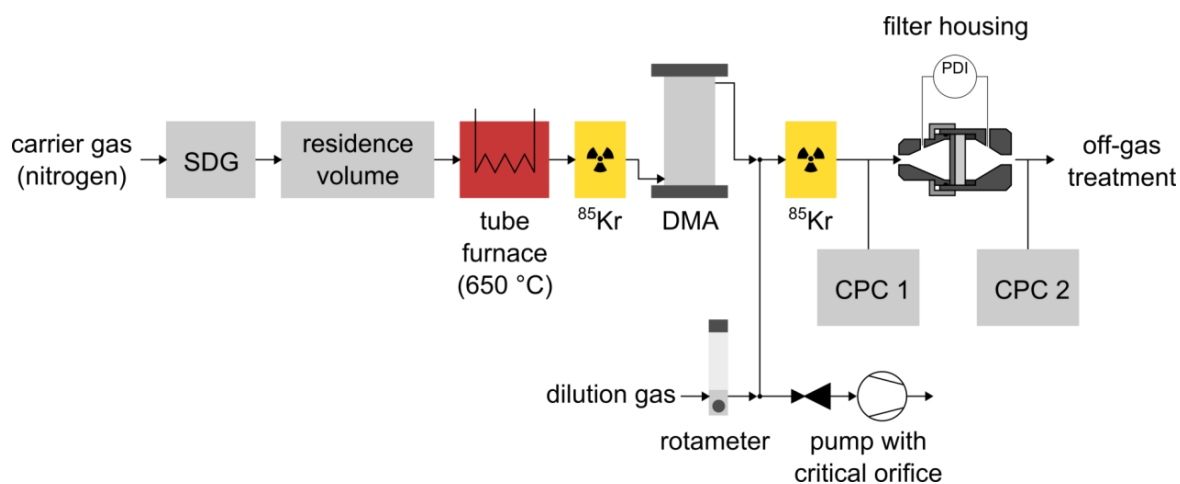| Face velocity (cm/s)	Cotton (Δp, pa)		PES (Δp, pa)	
	raw	nanofinished	raw	nanofinished
0.5	0.7	0.8	9.9	10
1.0	1.5	1.5	20.1	19.9
2.0	3.0	3.0	40.1	40.4
4.0	6.2	6.2	82.2	81.9

Figure S7.3 Schematic layout of the setup used for the determination of E_{dep} and Δp.

S7.4 Estimation of Ag NP loading on the textiles

Inductively coupled plasma mass spectrometry (ICP-MS) was used to determine the NP loading on the textiles. In addition, we also employ the deposition model to estimate the NP loading, which shows good consistency with those of determined by ICP-MS. The results are summarized in Table S7.3. The unit of ppm here means 1 mg of Ag NPs is deposited on 1 kg of textile. The model predictions are higher than that determined by ICP-MS. This is attributed to the loss of a certain amount of NPs on the walls of the containers used during ICP-MS measurements. Another possible reason is that the model predictions neglect the diffusional losses to the walls of the ducts in the production line. Although Figure 7.3a shows that the deposition efficiency of NPs on Cotton textile is low, the collection time was varied in order to demonstrate the influence of the NP loading on the antibacterial activity. This is verified by the determinations of NP loads using ICP-MS and XPS.

Table S7.3 Comparison of the NP loading determined by ICP-MS and deposition model.

Textiles	Q_q (slm)	ICP-MS (ppm)	Deposition model (ppm)
Cotton	50	108	121
	20	120	162
	40[a]	186	-
PES	50	92	121
	20	65	162
	40[a]	65	-
APCP	50	76	121
	20	79	162
LYS	40[a]	15	-
LYZ	40[a]	51	-

[a] the particles were produced by arc discharge (current 15 A) and used N_2 as carrier gas. The other samples were prepared by means of spark ablation and Ar as carrier gas.

Table S7.4 shows the atomic composition of C, O, N and Ag for the textile samples determined by XPS. Due to the inhomogeneities of the three textiles, some deviations exist in the XPS measurements from textile to textile. In order to qualitatively compare the Ag loading of these three textiles, we use C 1s as a reference signal. We obtain that the order of textiles with increasing Ag contents is as follows: Cotton > APCP > PES (cf. Table S7.4). This qualitative comparison is in correspondence with

the ICP-MS measurements and the estimation from the deposition model (cf. Table S7.3).

× 5000
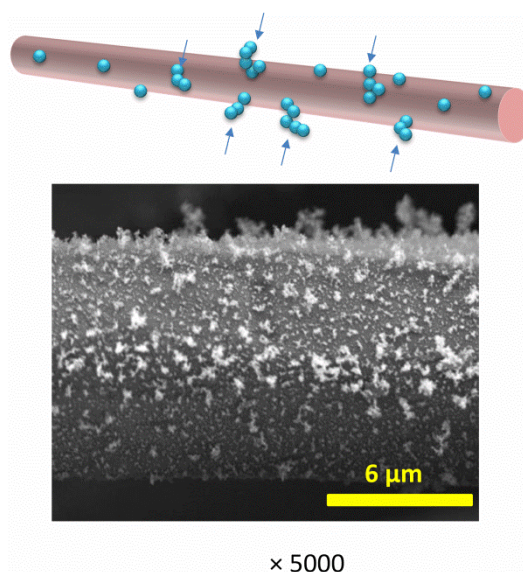
Figure S7.4 Agglomerated NPs on the textile fibre at extended deposition time. When the deposition time increases, agglomerated NPs are observed by low resolution SEM.

Table S7.4 Atomic composition of C, O, N and Ag for the textile samples. The values are presented with a standard deviation averaged on three spots for each textile sample. Nanofinished and raw textiles were measured. The nanofinished textiles were measured on both sides, namely the front surface (facing aerosol) and back surface side.

	Sides	C 1s (%)	O 1s (%)	N 1s (%)	Ag 3d (%)
Nanofinished Cotton	front	63.7 ± 0.9	34.1 ± 0.6	-	2.2 ± 0.3
	back	64.1 ± 0.7	35.9 ± 0.7	-	-
Raw Cotton	--	86.6 ± 0.3	13.4 ± 0.3	-	-
Nanofinished PES	front	67.4 ± 1.0	24.8 ± 0.3	-	0.8 ± 0.2
	back	71.4 ± 0.8	22.1 ± 0.6	-	-
Raw PES	--	68.7 ± 1.0	28.4 ± 0.6	-	-
Nanofinished APCP	front	79.5 ± 1.3	15.1 ± 1.1	3.5 ± 0.3	2.0 ± 0.2
	back	72.0 ± 1.4	27.2 ± 0.9	1.0 ± 1.0	-
Raw APCP	--	70.7 ± 1.2	27.4 ± 0.4	1.8 ± 0.01	-

Figure S7.4 shows that the agglomerated particles are formed due to extending the deposition time. These agglomerates are easily to be detached during washing, explaining the high release rate for the first washing cycle. In order to reduce their release, we can bind them to the textile fibers by introducing covalent linkers (e.g., thiol groups) to the fibers[45,56].

In order to probe the depth profile of NP deposition within the textiles, we employ XPS-etching for the textile samples. Figure S7.5 show shat the Ag content gradually decreases as the etching time (i.e., depth) increases.
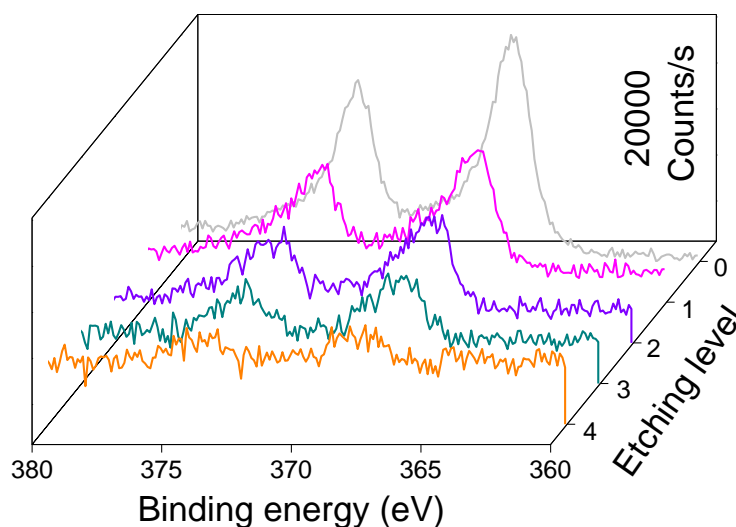
Figure S7.5 The depth profile trend of Ag for APCP obtained with a sequence of four etching levels (220 etching-time s[-1]; beam energy 1000 eV).

S7.5 Particle production and measurements

Electrical discharges (i.e., spark discharges and arcs) were applied as particle sources for textile nanofinishing. The experimental setup consists of components for generation (particle generator), collection (a mini-particle sampler, MPS; textile holder), and online measurements (a scanning mobility particle sizer; SMPS). More details on the experimental setup can be found elsewhere[26,71]. The layout and a photograph of these systems are shown in Figure S7.6. Four parallel particle generators were used to produce NPs, which can be deposited onto textiles. This process, in principle, can be integrated in a closed loop system using recycling gas flow (cf. Figure S4.3 in the SI of Chapter 4). In order to integrate the conveyor textile mode into the recycling systems, one has to design an enclosure for the fabric rolls

and seals for the slits that are the interfaces with the aerosol deposition environment and the ambient air.

Figure S7.6. Schematic illustration (a) and the photograph (b) of the experimental setups for textile nanofinishing using four spark ablation systems for producing the NPs. Key: MPS: mini-particle sampler; DMA: differential mobility analyzer; AEM: aerosol electrometer.

References

1   R. F. Service, *Science*, 2003, **301**, 909–911.

2   M. Hamedi, R. Forchheimer and O. Inganäs, *Nat. Mater.*, 2007, **6**, 357–362.
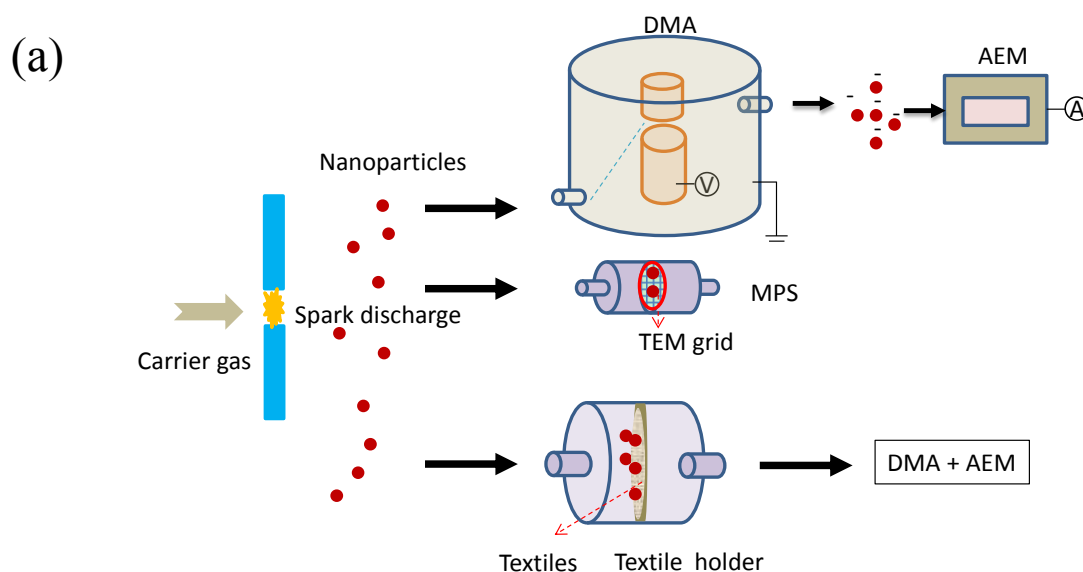
3   E. Dolgin, *Nature*, 2015, **519**, S10–S11.

4   J. P. Hinestroza, *Mater. Today*, 2007, **10**, 56.

5   M. B. Dickerson, A. A. Sierra, N. M. Bedford, W. J. Lyon, W. E. Gruner, P. A. Mirau and R. R. Naik, *J. Mater. Chem. B*, 2013, **1**, 5505.

6   A. Zille, M. M. Fernandes, A. Francesko, T. Tzanov, M. Fernandes, F. R. Oliveira, L. Almeida, T. Amorim, N. Carneiro, M. F. Esteves and A. P. Souto, *ACS Appl. Mater. Interfaces*, 2015, **7**, 13731–13744.

7   X. Deng, A. Yu Nikiforov, T. Coenye, P. Cools, G. Aziz, R. Morent, N. De Geyter and C. Leys, *Sci. Rep.*, 2015, **5**, 10138.

8   T. Mayer-Gall, D. Knittel, J. S. Gutmann and K. Opwis, *ACS Appl. Mater. Interfaces*, 2015, **7**, 9349–9363.

9   S. Chen, X. Li, Y. Li and J. Sun, *ACS Nano*, 2015, **9**, 4070–4076.

10   X. Xiao, X. Liu, F. Chen, D. Fang, C. Zhang, L. Xia and W. Xu, *ACS Appl. Mater. Interfaces*, 2015, **7**, 21326–21333.

11   L. Liu, Y. Yu, C. Yan, K. Li and Z. Zheng, *Nat. Commun.*, 2015, **6**, 7260.

12   M. Stoppa and A. Chiolerio, *Sensors*, 2014, **14**, 11957–11992.

13   L. Hu, M. Pasta, F. La Mantia, L. Cui, S. Jeong, H. D. Deshazer, J. W. Choi, S. M. Han and Y. Cui, *Nano Lett.*, 2010, **10**, 708–714.

14   A. Verma and F. Stellacci, *Small*, 2010, **6**, 12–21.

15   N. von Goetz, C. Lorenz, L. Windler, B. Nowack, M. Heuberger and K. Hungerbühler, *Environ. Sci. Technol.*, 2013, **47**, 9979–9987.

16   V. Sebastian, M. Arruebo and J. Santamaria, *Small*, 2014, **10**, 835–853.

17   A. P. Richter, J. S. Brown, B. Bharti, A. Wang, S. Gangwal, K. Houck, E. a. Cohen Hubal, V. N. Paunov, S. D. Stoyanov and O. D. Velev, *Nat. Nanotechnol.*, 2015, **10**, 817–823.

18　T. Walser, L. K. Limbach, R. Brogioli, E. Erismann, L. Flamigni, B. Hattendorf, M. Juchli, F. Krumeich, C. Ludwig, K. Prikopsky, M. Rossier, D. Saner, A. Sigg, S. Hellweg, D. Günther and W. J. Stark, *Nat. Nanotechnol.*, 2012, 7, 520–524.

19　A. Anastasopol, T. V Pfeiffer, J. Middelkoop, U. Lafont, R. J. Canales-Perez, A. Schmidt-Ott, F. M. Mulder and S. W. H. Eijt, *J. Am. Chem. Soc.*, 2013, **135**, 7891–7900.

20　K. Han, W. Kim, J. Yu, J. Lee, H. Lee, C. Gyu Woo and M. Choi, *J. Aerosol Sci.*, 2012, **52**, 80–88.

21　C. Boissiere, D. Grosso, A. Chaumonnot, L. Nicole and C. Sanchez, *Adv. Mater.*, 2011, **23**, 599–623.

22　J. H. Byeon and J.-W. Kim, *J. Mater. Chem. A*, 2014, **2**, 6939–6944.

23　J. H. Byeon, J. H. Park, K. Y. Yoon and J. Hwang, *Nanoscale*, 2009, **1**, 339–343.

24　M. Heurlin, M. H. Magnusson, D. Lindgren, M. Ek, L. R. Wallenberg, K. Deppert and L. Samuelson, *Nature*, 2012, **492**, 90–94.

25　S. K. Sengar, B. R. Mehta, R. Kumar and V. Singh, *Sci. Rep.*, 2013, **3**, 2814.

26　J. Feng, G. Biskos and A. Schmidt-Ott, *Sci. Rep.*, 2015, **5**, 15788.

27　P. Grammatikopoulos, C. Cassidy, V. Singh and M. Sowwan, *Sci. Rep.*, 2014, **4**, 5779.

28　J. H. Byeon, J. H. Park and J. Hwang, *J. Aerosol Sci.*, 2008, **39**, 888–896.

29　J. H. Byeon and J.-W. Kim, *ACS Appl. Mater. Interfaces*, 2014, **6**, 3105–3110.

30　J. Feng, L. Huang, L. Ludvigsson, M. E. Messing, A. Maisser, G. Biskos and A. Schmidt-Ott, *J. Phys. Chem. C*, 2016, **120**, 621–630.

31　E. C. Tyo and S. Vajda, *Nat. Nanotechnol.*, 2015, **10**, 577–588.

32　Yuan Gao and R. Cranston, *Text. Res. J.*, 2008, **78**, 60–72.

33　S. C. Wang and R. C. Flagan, *Aerosol Sci. Technol.*, 1990, **13**, 230–240.

34　W. C. Hinds, *Aerosol Technology: Properties, Behavior, and Measurement of Airborne Particles*, John Wiley & Sons, New York, 1999.

35　D. Thomas, P. Penicot, P. Contal, D. Leclerc and J. Vendel, *Chem. Eng. Sci.*, 2001, **56**, 3549–3561.

36　E. Schweers and F. Löffler, *Powder Technol.*, 1994, **80**, 191–206.

37   G. Beaucage, *J. Appl. Crystallogr.*, 1995, **28**, 717–728.

38   J. Sun, L. He, Y.-C. Lo, T. Xu, H. Bi, L. Sun, Z. Zhang, S. X. Mao and J. Li, *Nat. Mater.*, 2014, **13**, 1007–1012.

39   P. Prieto, V. Nistor, K. Nouneh, M. Oyama, M. Abd-Lefdil and R. Díaz, *Appl. Surf. Sci.*, 2012, **258**, 8807–8813.

40   I. Lopez-Salido, D. C. Lim and Y. D. Kim, *Surf. Sci.*, 2005, **588**, 6–18.

41   A. Scandurra, G. F. Indelli, N. G. Spartà, F. Galliano, S. Ravesi and S. Pignataro, *Surf. Interface Anal.*, 2010, **42**, 1163–1167.

42   C. Levard, E. M. Hotze, G. V Lowry and G. E. Brown, *Environ. Sci. Technol.*, 2012, **46**, 6900–6914.

43   Z. Xiu, Q. Zhang, H. L. Puppala, V. L. Colvin and P. J. J. Alvarez, *Nano Lett.*, 2012, **12**, 4271–4275.

44   J. R. Morones, J. L. Elechiguerra, A. Camacho, K. Holt, J. B. Kouri, J. T. Ramírez and M. J. Yacaman, *Nanotechnology*, 2005, **16**, 2346–2353.

45   B. Simoncic and D. Klemencic, *Text. Res. J.*, 2016, **86**, 210–223.

46   Q. L. Feng, J. Wu, G. Q. Chen, F. Z. Cui, T. N. Kim and J. O. Kim, *J. Biomed. Mater. Res.*, 2000, **52**, 662–668.

47   I. Sondi and B. Salopek-Sondi, *J. Colloid Interface Sci.*, 2004, **275**, 177–182.

48   P. K. Stoimenov, R. L. Klinger, G. L. Marchin and K. J. Klabunde, *Langmuir*, 2002, **18**, 6679–6686.

49   J. S. Kim, E. Kuk, K. N. Yu, J.-H. Kim, S. J. Park, H. J. Lee, S. H. Kim, Y. K. Park, Y. H. Park, C.-Y. Hwang, Y.-K. Kim, Y.-S. Lee, D. H. Jeong and M.-H. Cho, *Nanomedicine*, 2007, **3**, 95–101.

50   N. V. K. Thanh and N. T. P. Phong, *J. Phys. Conf. Ser.*, 2009, **187**, 1–7.

51   C. Lorenz, L. Windler, N. von Goetz, R. P. Lehmann, M. Schuppler, K. Hungerbühler, M. Heuberger and B. Nowack, *Chemosphere*, 2012, **89**, 817–824.

52   S. Gavanji, *Appl. Sci. Reports*, 2013, **1**, 50–56.

53   A. Hebeish, *Int. J. Biol. Macromol.*, 2015, **72**, 1384–1390.

54   C.-N. Lok, C.-M. Ho, R. Chen, Q.-Y. He, W.-Y. Yu, H. Sun, P. K.-H. Tam, J.-F. Chiu and C.-M. Che, *J. Biol. Inorg. Chem.*, 2007, **12**, 527–534.

55   C. Som, P. Wick, H. Krug and B. Nowack, *Environ. Int.*, 2011, **37**, 1131–1142.

56   X. Deng, A. Yu Nikiforov, T. Coenye, P. Cools, G. Aziz, R. Morent, N. De Geyter and C. Leys, *Sci. Rep.*, 2015, **5**, 10138.

57   R. B. Reed, T. Zaikova, A. Barber, M. Simonich, R. Lankone, M. Marco, K. Hristovski, P. Herckes, L. Passantino, D. H. Fairbrother, R. Tanguay, J. F. Ranville, J. E. Hutchison and P. K. Westerhoff, *Environ. Sci. Technol.*, 2016, **50**, 4018–4026.

58   K. Kulthong, S. Srisung, K. Boonpavanitchakul, W. Kangwansupamonkon and R. Maniratanachote, *Part. Fibre Toxicol.*, 2010, **7**, 1–9.

59   A. B. Stefaniak, M. G. Duling, R. B. Lawrence, T. a. Thomas, R. F. LeBouf, E. E. Wade and M. Abbas Virji, *Int. J. Occup. Environ. Health*, 2014, **20**, 220–234.

60   L. Geranio, M. Heuberger and B. Nowack, *Environ. Sci. Technol.*, 2009, **43**, 8113–8118.

61   D. Pohle, C. Damm, J. Neuhof, A. Rosch and H. Munstedt, *Polym. Polym. Compos.*, 2007, **15**, 357–363.

62   A. K. Yetisen, H. Qu, A. Manbachi, H. Butt, M. R. Dokmeci, J. P. Hinestroza, M. Skorobogatiy, A. Khademhosseini and S. H. Yun, *ACS Nano*, 2016, **10**, 3042–3068.

63   C. Bianco, S. Kezic, M. Crosera, V. Svetličić, S. Šegota, G. Maina, C. Romano, F. Larese and G. Adami, *Int. J. Nanomedicine*, 2015, **10**, 1899–908.

64   S. Schwyn, E. Garwin and A. Schmidt-Ott, *J. Aerosol Sci.*, 1988, **19**, 639–642.

65   E. Hontañón, J. M. Palomares, M. Stein, X. Guo, R. Engeln, H. Nirschl and F. E. Kruis, *J. Nanoparticle Res.*, 2013, **15**, 1957.

66   B. R'mili, O. L. C. Le Bihan, C. Dutouquet, O. Aguerre-Charriol and E. Frejafon, *Aerosol Sci. Technol.*, 2013, **47**, 767–775.

67   X. Guo, M. Wagner, A. Gutsche, J. Meyer, M. Seipenbusch and H. Nirschl, *J. Aerosol Sci.*, 2015, **85**, 17–29.

68   Y. S. Cheng and H. C. Yeh, *J. Aerosol Sci.*, 1980, **11**, 313–320.

69   T. Müller, J. Meyer and G. Kasper, *J. Aerosol Sci.*, 2014, **77**, 50–66.

70   K. Pietrzak, B. Gutarowska, W. Machnowski and U. Miko ajczyk, *Text. Res. J.*, 2016, **86**, 812–822.

71   E. Hontañón, E. Kruis, L. Santos, L. Ludvigsson, A. R. Persson and M. E. Messing, *Proc. World Congr. New Technol.*, 2015, 1–4.

8. Conclusions and Recommendations

8. 1 Concluding remarks

In view of the new aspects explored in this thesis, this section sets out to summarize the striking findings as follows. These findings extend the knowledge of spark produced NPs associated with their applications.

- ✓ A new 'singlet' concept has been introduced to challenge the paradigm of 'NP synthesized in the gas phase leads to agglomerates' in Chapter 2. Atomic clusters and smallest NPs formed at the early stages of spark ablation are liquid-like even at room temperature, and therefore fully coalesce into singlets when colliding with each other. Growth of the singlets to a critical size above which coalescence only partly occurs or ceases, signals the onset of agglomeration, which leads to non-spherical/agglomerated particles. This concept can be generally applied to synthesize non-agglomerated singlets ranging from single atoms to particles in the nanometre range.

- ✓ A simple yet versatile semi-empirical model has been developed for predicting the size distribution of singlet particles as a function of the process conditions in Chapter 3. The model provides a simple and practical tool that can be generally used to design and control point vapour source reactors for the synthesis of singlets with tunable sizes starting from that of a single atom.

- ✓ Chapter 4 have demonstrated that a newly developed HFSs (see more details about its electrical circuit[1]), quenched by a high purity carrier gas, yields large quantities of various monometallic and mixed bimetallic NPs with sub-10 nm primary particle size and well-defined chemical composition (mixed on an atomic or nanoscale). Carbon black, silica and titania particles have been produced on an industrial scale by using aerosol technologies[2–8]. Besides their large volume production, one bottleneck lies in that elemental compositions have limited controllability, such as unavoidable oxides. This work likely breaks the inherent limitations of low production rate of very small NPs with high purity and easy-to-control compositions.The HFSs therefore provides a

green, sustainable, and versatile platform for manufacturing a number of different key building blocks.

✓ Chapter 5, for the first time, theoretically explains the concept of spark mixing using a pair of electrodes consisting of different materials. The ablation ratio of two electrodes can be tuned by adjusting the oscillatory behaviour of a single spark discharge. In connection with this oscillatory behaviour, a simple model has been developed to estimate the ablation ratio of two electrodes. This way of mixing NPs enables the possibility of manufacturing complex nanocomposites using incompatible starting electrodes.

✓ Chapter 6 pioneers a way of suppressing splashing particles in the HFSs. Put briefly: the low-power and continuous glowing current are deflected by the Lorentz force, so that the superimposed sparks onto the continuous current can also be positioned desirably. This reduces the probability of striking the same spot on the electrode surface by the high frequency sparks, thereby inhibiting the formation of splashing particles.

✓ Chapter 7, for the first time, integrates a scalable and environmentally benign aerosol process into textile nanofinishing. The unique feature of the proposed method lies in that a loading profile of NPs within textiles can be controlled. Antimicrobial properties of the nanofinished textiles with Ag NPs were assessed in relation to two strains of bacteria, showing high antibacterial activity despite one order of magnitude lower amount of Ag content than that of undergone traditional wet-routes. The new textile nanofinishing process can be expanded to other types of smart textiles, such as colour-changing clothes, and self-cleaning upholsteries.

8.2 Recommendations

This dissertation has thrown up much potential in need of further investigation, which can be undertaken in the following bullet points:

• The singlets have been successfully deposited at the substrate on a low coverage. To achieve a thicker coverage while maintaining these separated singlets, one should immobilize them at surface. The roughness of a substrate may play a role for immobilization of the NPs that are deposited. Another

option is to introducing chemical bonds between the singlets and substrates. This, however, may contaminate or change the chemical state of the singlets, as they possess the large number of high-reactivity surface atoms. In addition, the coalescence depends on the temperature. Therefore, 'freezing' these singlets is a good alternative to prevent further coalescence upon collisions. Continued efforts are needed to make these recommendations more accessible to deposit separated singlets on substrates with high coverage.

- Without any additional treatment, avoiding the formation of agglomerates on substrate can be directly achieved by depositing a low coverage of singlets on the surface of substrates. This should be quantified by providing NP coverage density as well as associated properties in applications. Especially, Chapter 4 has demonstrated that non-agglomerated particles are initially formed in gas phase, which is in line with the singlet concept proposed in Chapter 1.

- Future research should be carried out to establish a numerical solution for monitoring the self-organization of small particles at surfaces (cf. Figure 8.1). Apparently, the material of the substrate is also a major determinant of the particle self-organization at surface[9,10]. Further studies regarding the dependence of substrate materials would be worthwhile. It is also strongly recommended to extend further investigation and experimentation into the dependence of annealing conditions (e.g., time and temperature) on particle morphologies[11], since very small singlets can be mobilized by using high temperature. The associated graphical abstract is shown in Figure 8.1. The preliminary experimental results are presented in Figure 8.2.

- Difficulties of avoiding agglomeration arise, when the system achieves high mass production rates. A strong dilution can, however, be imposed to prevent such agglomeration, as shown in Chapter 2. In the case of forming agglomerates, aerosol deposition is emerged as powerful platforms for creating 3D patterned nanostructures. Recent developments in 3D nanostructures have led to renewed applications in many fields[12–19].

- Model predictions show that one can control the ablation ratio of two electrodes consisting of different materials by changing the electrical parameters in HFS. The evaporated species are rapidly mixed in the explosive vapour expansion process before condensation, thereby facilitating internal

mixing. As a result, this model can also predict the mean composition of the resulting NPs. Further investigation and experimentation into nanocomposite analyse is thus strongly recommended. Applications of these unique mixed nanoparticles should also be explored.
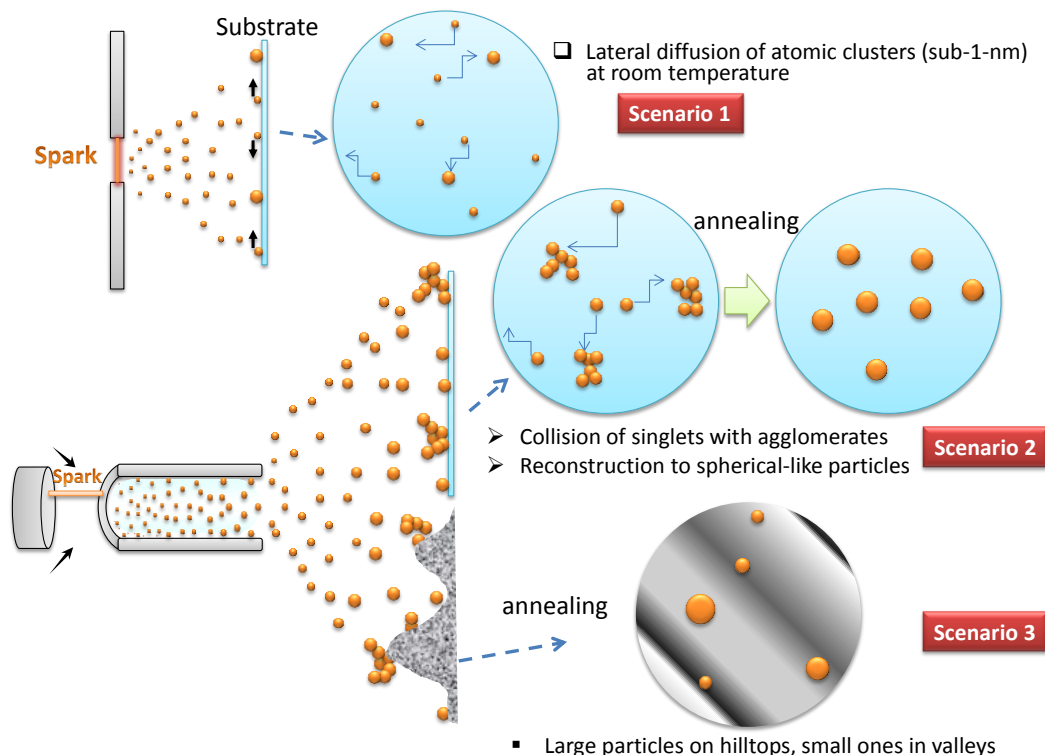

Figure 8.1 Self-organization of NPs on substrates described in three scenarios. Rapid diffusion of the NPs in the gas phase guarantees their efficient deposition onto substrates, followed by their transport at surface, which is based on a 2D random walk. After deposition, the collision of sub-1-nm particles leads to forming their big counterparts, which do move laterally. This is the Scenario 1 described at room temperature. Proceeding collisions contributes to further particle growth accompanied by instantaneous coalescence, depending on the temperature, the roughness and the material of the substrate. When the complete coalescence ceases after collisions, it triggers the formation of agglomerates. With the help of annealing in Scenarios 2 and 3, these agglomerates reconstruct to spherical-like particles. Meanwhile, the deposited sub-10-nm singlets also execute a 2D random walk on substrates at high temperature, acting similarly to the sub-1 nm particles at room temperature. The final size of the NPs on substrates depends on the mass loading per unit area, which can be controlled by varying the deposition time,

and the annealing conditions (e.g., time and temperature). The scenarios proposed here can be constructed to deposit aerosol NPs on substrates having desirable sizes and/or diverse nanostructures at surface, fulfilling the requirements of potential end-users (e.g., nano-catalysis).
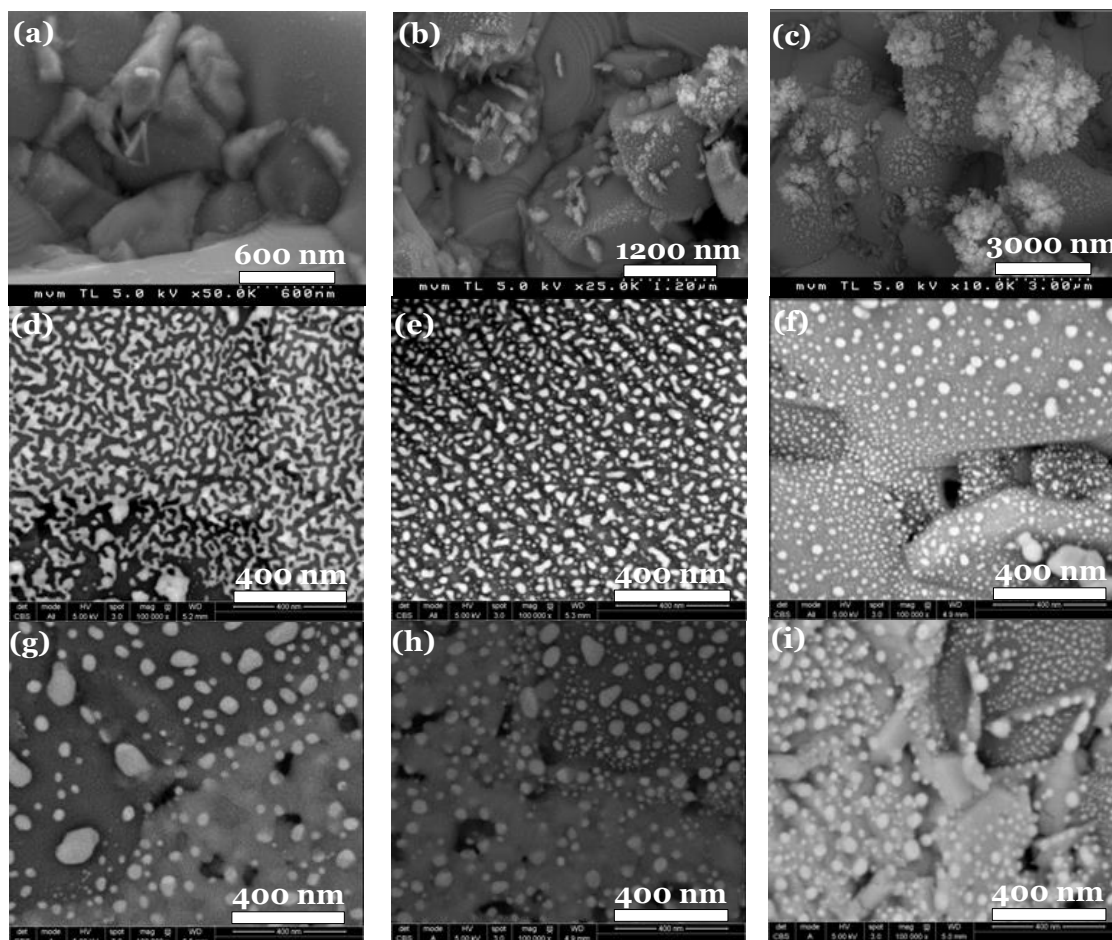
Figure 8.2 HRSEM images of Ni NPs deposited on ceramic discs. Images assembled in the first row (a-c) are as-deposited samples with various deposition durations of 10, 100, 1000 min, corresponding to the first, the second, and the third column. The images assembled in the second row show that the samples were annealed at 700 °C for 1 h, while 900 °C for 100 h was set to anneal the samples presented in the third row.

Figure 8.2 reveals that the resulting particle size after annealing essentially depends on the deposited mass per unit area and the annealing conditions (e.g., temperature and time). This serves a basic guide for investigating the size dependence on an optimum catalytic activity. Annealing to required reaction temperatures for methane reforming at 700 °C for 1 h (cf. the second row in

Figure 8.2) and at 900 °C for 100 h (cf. the third row in Figure 8.2) in Ar/H$_2$(96/4%) atmosphere results in coalescing the primary particles to form larger round units.

- A single spark event is complicated multi-scale processes, which take place simultaneously. One of the BOUNAPAR-E project partners has proposed main physical mechanisms involved in one spark, streamer propagation, electrical current oscillations, Joule heating, ion bombardment, electrode evaporation, the associated vapour expansion. Notably, the fraction of spark energy used for electrode evaporation has not been understood theoretically. Therefore, profound knowledge of this point should be acquired.

- To improve the washing durability of nanofinished textiles, a deeper deposition of NPs within textiles can be facilitated through adjusting the operating conditions of gas phase NP syntheses (cf. increasing flow rate). In addition, preventing agglomeration or depositing very small singlets can also strengthen the sticking of NPs on textile fibres.

- When the agglomerates are difficult to avoid, covalent linkage between the NPs and textile fibres should be introduced. For instance, the thiol group can be added to textile fibres during its production, so that Ag NPs are firmly bound to textile fibres, reducing NP release during washing. Other types of functional textiles of using different NPs can also selectively choose the associated chemical bonds between particles and fibres.

- Some gaseous chemicals can be mixed with the carrier gas to form a protective layer on particle surface. This layer, on one hand, can be easily 'digested' in the applications. On the other hand, it also plays a role of preventing further agglomeration upon collisions.

- Aerosol NP production should be integrated into the existing fabrication lines. For instance, the aerosol NPs used as nanocatalysis can be directed to a fluidic reactor to promote gaseous chemical reactions due to their high diffusivity and large ratio of surface atoms.

- Besides the high-yield synthesis of engineered NPs, great efforts are needed to ensure an efficient collection method and/or a compatible processing line.
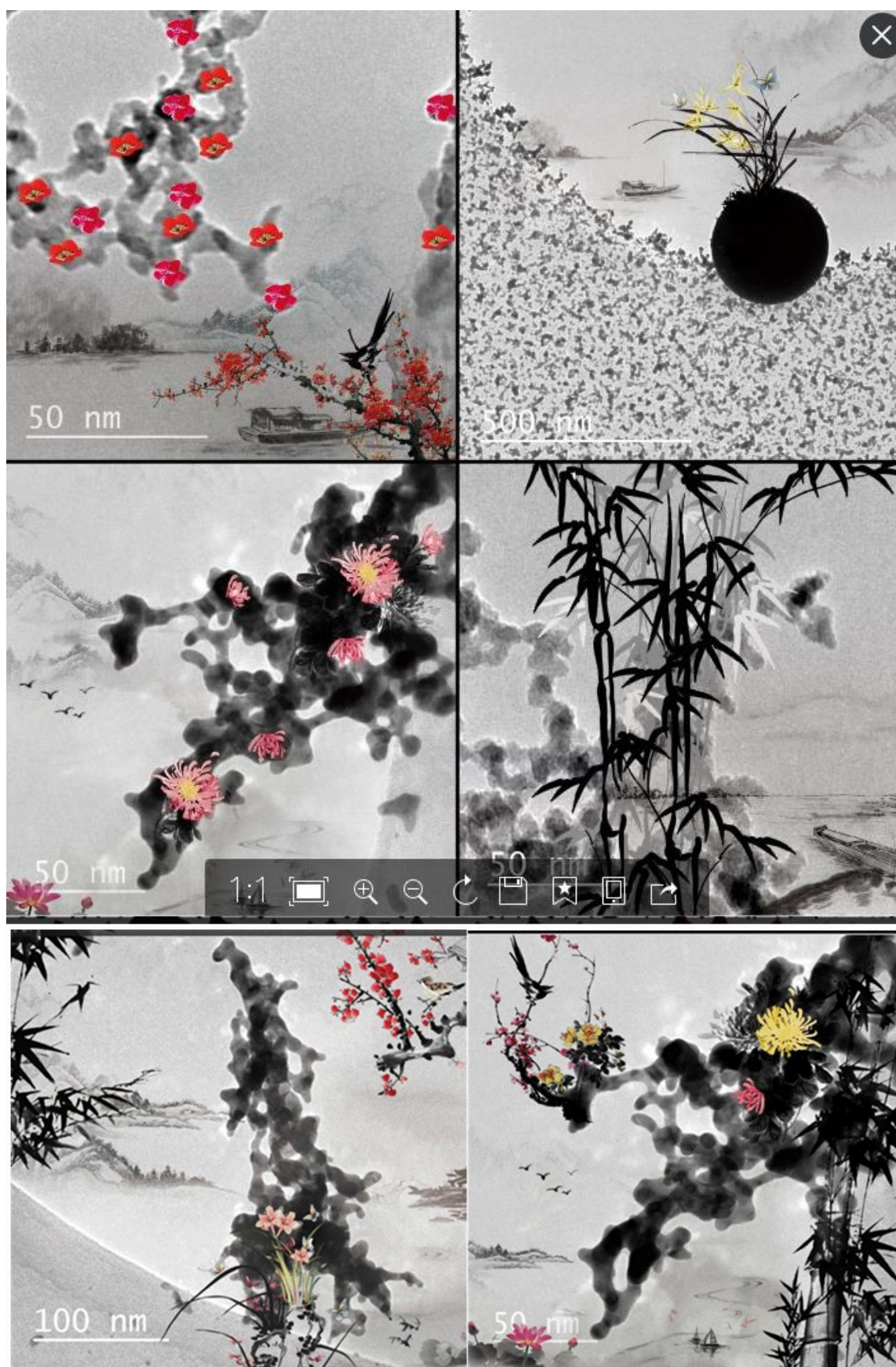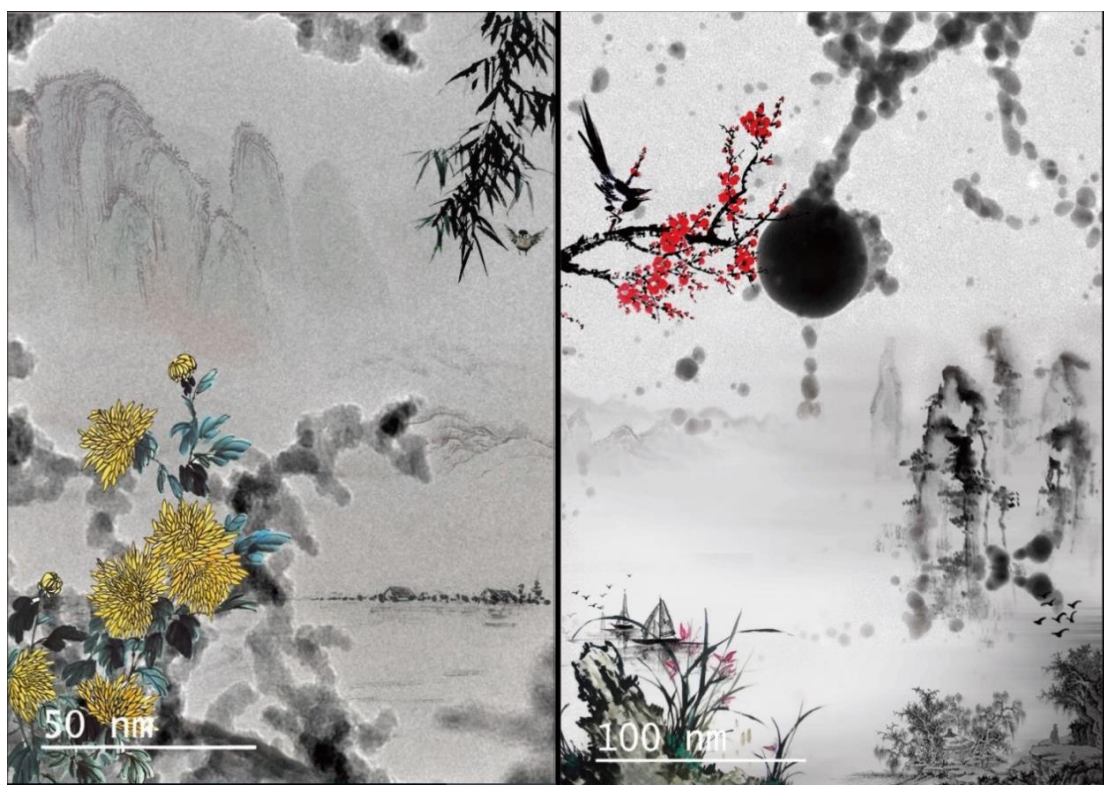
Figure 8.3 Chinese Four Gentlemen are blooming on the nano-agglomerates. Chinese art uses four plants: the plum blossom, the orchid, the bamboo, and the chrysanthemum to represent four gentlemen, which are in line with Confucianist gentlemen.

• Another possible area of future research would be to combine nanoscience with arts. For example, beautiful agglomerates can be painting base to create new depictions with the help of Chinese calligraphy (cf. Figure 8.3), which belongs to the ink and wash painting. The dissertation cover is designed in accordance with this notion. Figure 8.3 shows some other example paintings on the basis of deposited NPs on TEM grids.

Figure 8.3 belongs to the type of Chinese Ink and Washing Painting, which was developed in the most prosperous era of Tang Dynasty. Chinese painting can be classified on the basis of topics into Chinese Figure Painting, Chinese Landscape Painting, and Chinese Flower-and-Bird Painting.

• Magnetic alloy NPs have enabled stronger, lighter and more efficient materials for energy or biomedical related applications. However, the formation of alloy

NPs in traditional wet-chemistry commonly encounters impurities due to the use of precursors, thereby degrading the magnetic response. In addition, the size and composition of resulting NPs are difficult to control in a reproducible manner. Spark ablation was nominated to be capable of converting a bulk alloy electrode into NPs, retaining the composition and crystal lattice structure of the starting alloy. Both experimental evidence and theoretical understanding of the formation of nanoalloys should be provided, especially in connection with their applications, such as drug delivery, magnetic refrigerants. This work has been undertaken to complete a scientific publication.

References

1   T. V. Pfeiffer, *PhD thesis*, Delft University of Technology, 2014.

2   C. A. Charitidis, P. Georgiou, M. A. Koklioti, A.-F. Trompeta and V. Markakis, *Manuf. Rev.*, 2014, **1**, 1–19.

3   R. Mueller, L. Mädler and S. E. Pratsinis, *Chem. Eng. Sci.*, 2003, **58**, 1969–1976.

4   S. E. Pratsinis, *Prog. Energy Combust. Sci.*, 1998, **24**, 197–219.

5   H. K. Kammler, L. Mädler and S. E. Pratsinis, *Chem. Eng. Technol.*, 2001, **24**, 583–596.

6   R. Strobel and S. E. Pratsinis, *J. Mater. Chem.*, 2007, **17**, 4743.

7   R. S. Windeler, S. K. Friedlander and K. E. J. Lehtinen, *Aerosol Sci. Technol.*, 1997, **27**, 174–190.

8   J. J. Helble and A. F. Sarofim, *J. Colloid Interface Sci.*, 1989, **128**, 348–362.

9   J. V Barth, G. Costantini and K. Kern, *Nature*, 2005, **437**, 671–679.

10   Z. Zhang, *Science*, 1997, **276**, 377–383.

11   a. Herz, a. Franz, F. Theska, M. Hentschel, T. Kups, D. Wang and P. Schaaf, *AIP Adv.*, 2016, **6**, 035109.

12   K. Jung, H.-J. Song, G. Lee, Y. Ko, K. Ahn, H. Choi, J. Y. Kim, K. Ha, J. Song, J.-K. Lee, C. Lee and M. Choi, *ACS Nano*, 2014, **8**, 2590–2601.

13   H. Choi, S. Kang, W. Jung, Y. Jung, S. J. Park, D. S. Kim and M. Choi, *J. Aerosol Sci.*, 2015, **88**, 90–97.

14   K. Jung, J. Hahn, S. In, Y. Bae, H. Lee, P. V Pikhitsa, K. Ahn, K. Ha, J.-K. Lee, N. Park and M. Choi, *Adv. Mater.*, 2014, **26**, 5924–5929.

15   S. Jang, J. Yoon, K. Ha, M. Kim, D. H. Kim, S. M. Kim, S. M. Kang, S. J. Park, H. S. Jung and M. Choi, *Nano Energy*, 2016, **22**, 499–506.

16   S. You, K. Han, H. Kim, H. Lee, C. G. Woo, C. Jeong, W. Nam and M. Choi, *Small*, 2010, **6**, 2146–2152.

17   H. Kim, J. Kim, H. Yang, J. Suh, T. Kim, B. Han, S. Kim, D. S. Kim, P. V Pikhitsa and M. Choi, *Nat. Nanotechnol.*, 2006, **1**, 117–121.

18   J. J. Cole, E. C. Lin, C. R. Barry and H. O. Jacobs, *Small*, 2010, **6**, 1117–1124.

19   J. Byeon, D. Park and J. Kim, *Nanoscale*, 2015, **7**, 2271–2275.

Summary

Commercial production of high-performing nanomaterial-based applications such as smart textiles, nanocatlysis, and drug delivery and therapy requires scalable fabrication processes that are simple and do not use expensive and toxic chemicals. Employing green techniques that avoid the use of poisonous and expensive chemicals has been realized as a necessity for the production of NPs on an industrial scale. Making products/business by going green will be the mainstream in the future. This dissertation strives to contribute to demonstrate this practicability.

The applied NP synthesis method is spark ablation, which has been greatly advanced in this dissertation. The spark ablation, which is operated at ambient pressure, is rapidly quenched by a high purity gas. It provides great versatility in the synthesis of inorganic NPs consisting of a wide variety of conducting or semiconducting materials including rare earths (that are difficult to produce with traditional wet-chemistry methods), thermodynamically unstable materials[1], and alloys (e.g., steel) with virtually unlimited mixing possibilities[2–6]. In addition, the method offers good control over particle size which can range from that of atomic clusters to that of singlets or agglomerates consisting of primary particles a few nm in diameter (cf. Chapters 2 and 3)[3,7,8]. This technique can produce oxide and non-oxide NPs, when appropriate gases and electrodes are available. As a result, recent research efforts have focused on fabricating NPs using spark ablation for a number of new applications (Table S4.1 presented in Chapter 4)[2,3,5,8–23].

This dissertation was divided into three main parts, namely fundamental studies (Part A; cf. Chapters 2 and 3), scaling-up (Part B; cf. Chapters 4~6), and some applications (Part C; cf. Chapter 7). The fundamental studies endeavour to provide future users a versatile tool for the design of a particle generator and a process line,

which are compatible with existing fabrication processes. Subsequently, Part B demonstrates the scalability of this method, including internal NP mixing and inhibition of 'splashing'. To show the applications of the generated NPs, Part C proposes a new process for smart textile nanofinishing.

Chapter 2 introduces a new and scalable concept of "singlet" particle production. Vapours are produced by localized material ablation using lasers or electric discharges. The vapours are strongly quenched by an inert gas flow of variable temperature, thereby producing particles by condensation. As the supersaturations reached in the rapidly quenched vapour cloud are extremely high, the critical nucleus size is pushed down to the atomic scale. As a result, the growth governed by particle-particle collisions can be considered to start from the atomic scale, and therefore particle-particle collisional growth represents a valid model for the description of the size distribution evolution. The atomic clusters and smallest nanoparticles that are formed at the early stages of the process are liquid-like even at room temperature, and therefore fully coalesce into singlets when colliding with each other. Growth of singlets to a critical size above which coalescence only partly occurs or ceases for the selected operating temperature, signals the onset of agglomeration which leads to non-spherical/agglomerated particles. For drastically quenched processes, the temperature in the particle growth phase can be decoupled from the localized vaporization, and can be set to a value guaranteeing complete coalescence. This feature provides great flexibility in controlling the size of the resulting nanoparticles.

Chapter 3 presents a simple, yet versatile approach that can generally be used to describe the evolution of particle size and concentration from rapidly-quenched point vapor sources such as spark discharges. The mean size of singlet NPs can be easily controlled by adjusting the operating conditions. The experiment shows that the size distributions can all be fitted to log-normal functions and that the self-preserving geometric standard deviation of ca. 1.35 is reached at a size of ca. 6 nm, which can be regarded as a general feature. The approach described in this work is versatile and applicable to the singlet NPs of any material; it is also compatible with existing fabrication processes, thereby enabling a non-disruptive methodology for the generation of functional materials.

After the fundamental studies have been described in Part A, the scaling-up of NP production is studied in a greater depth as compared to the previous work[2,24]. A newly developed HFS allows the preparation of an extensive variety of inorganic NPs of well-defined primary particles size and composition at yields of up to 130×10^{-3} g h^{-1} (operated at 3 kHz). Such yields of small NPs have never been achieved before by gas-phase spark ablation. The mass production rates for the NPs consisting of different materials increase linearly with spark frequency. As a result, HFS can achieve NP mass production rates of the order of 1 g h^{-1} as extrapolated from the results presented in Chapter 4. Considering that the generic process is easily scalable by parallelizing, the HFSs can achieve mass production rates to meet industrial demands. Besides the production capacity, the method also maintains consistency in product quality attributed to good kinetic control. In addition, the fast quenching makes this method feasible to produce thermodynamically metastable materials and to achieve efficient mixing on the atomic or nanometer scale. In contrast to chemical routes, the system avoids using any precursor solutions, thereby allowing single-step synthesis of complex multicomponent nanomaterials with high purity in a predictable and green manner. These findings pave the way of upscaling an extensive variety of nanomaterial syntheses, providing a green and versatile approach to nanofabrication. The produced NPs (many types, desirable composition) will be of interest to diverse fields such as material science, chemistry, and physics as well as applications from industrial partners.

In addition to scaling-up, Chapter 5 theoretically explains the concept of spark mixing using a pair of electrodes consisting of different materials. The ablation ratio of two electrodes, which is equal to the mean composition of resulting NPs, can be tuned by adjusting the oscillatory behaviour of a single spark discharge. In connection with such an oscillatory behavior, a simple model is developed to estimate the ablation ratio of two electrodes. This way of mixing NPs enables the possibility of manufacturing complex nanocomposites using incompatible starting electrodes.

Chapter 6 explores the feasibility of using permanent magnets in the HFS to inhibit the formation of splashing particles. High repetition frequencies increase probability of striking the same hot-spots of the electrode surface, where molten pools are formed. Droplets are momentarily ejected from the microscopic pools and they are

subsequently solidified by cooling, thereby forming 'splashing' particles that are larger than 100 nm. To suppress the splashing while maintaining a high NP mass production rate, a permanent magnetic field is employed to deflect the a continuous glowing current, onto which sparks are superimposed.

After presenting the fundamentals and scaling-up in Parts A and B, the applications of the generated NPs are also investigated (cf. Chapter 7). Integrating low-cost, scalable, and environmentally benign aerosol processes into textile nanofinishing, the constraints encountered in wet finishing processes can be circumvented while leading to a new class of fabrics. As proof of this concept, Ag NPs are deposited onto a range of textiles and their antimicrobial properties are assessed in relation to two strains of bacteria, exhibiting high antibacterial activity even when the Ag loading is one order of magnitude less than in the textiles treated by traditional wet-routes. Such low loading for antimicrobial textiles minimizes the risk to human health (during textile use) and to the ecosystem (after textile disposal), as well as it reduces the changes in colour and texture of textile products. Interestingly, the washed textiles exhibit almost no reduction in antimicrobial activity, much as those of as-deposited samples. Considering that a realm of functional textiles can be nanofinished with the help of aerosol deposition, the proposed universal and sustainable approach can potentially lead to a wide number of applications.

Samenvatting

Commerciële productie van nanomaterialen gebaseerd op toepassingen met een hoog rendement, zoals intelligent textiel, nanokatalyse en medicijnafgifte en drugstherapie, vereisen schaalbare productieprocessen die simpel zijn en geen kostbare en toxische chemicaliën gebruiken. Het toepassen van groene technieken die giftige en dure chemicaliën vermijden zijn erkent als een noodzaak in de productie van nanodeeltjes op industriële schaal. Groene productieprocessen zullen in de toekomst alledaags zijn en deze thesis streeft bij te dragen aan de uitvoerbaarheid en deze te demonstreren.

De toegepaste synthesemethode van nanodeeltjes is vonkablatie, een methode waarin veel vooruitgang is geboekt in deze thesis. Deze methode omvat het snelle koelen met zeer zuiver gas en vind plaats bij atmosferische druk. Het verschaft veel veelzijdigheid bij de synthese van anorganische nanodeeltjes bestaande uit brede selectie geleidende en halfgeleidende materialen waaronder zeldzame aardmetalen (hetgeen moeilijk is te verwerken met gebruikelijke methodes), thermodynamisch onstabiele materialen, en legeringen (e.g. staal) met praktisch onbeperkte mengmogelijkheden. Bovendien, de methode biedt goede controle over de deeltjesgrootte van deeltjes met groottes van atomaire clusters tot singlets en agglomeraten, bestaande uit primaire deeltjes met diameters van enkele nanometers. Deze techniek kan oxide en non-oxide nanodeeltjes produceren zolang geschikte gassen en elektrodes beschikbaar zijn. Als gevolg wordt vonkablatie recentelijk onderzocht voor verscheidene nieuwe toepassing.

Deze thesis bestaat uit drie delen, fundamental studies (deel A; cf. hoofdstuk 2 en 3), scaling-up (deel C; cf. hoofdstuk 4~6) en some applications (deel C; cf. hoofdstuk 7). Het fundamentele onderzoek streeft er naar om toekomstige gebruikers te voorzien van een veelzijdig gereedschap voor het ontwerpen van een deeltjesgenerator en proceslijn die compatibel zijn met bestaande fabricageprocessen.

Hoofdstuk 2 introduceert een nieuw, het schaalbare concept van singlet deeltjesproductie. Dampen worden geproduceerd door gelokaliseerde materiaalablatie met behulp van lasers of elektrische ontladingen. De dampen worden afgeschrikt door een inert draaggas met bepaalde temperatuur en deeltjes resulteren via condensatie. De oververzadiging die tijdens het koelen wordt bereikt is zeer hoog en de kritieke deeltjesgrootte bereikt de atomaire schaal. Vanuit dit oogpunt kan de groei van deeltjes via botsingen tussen deeltjes beschouwd worden als iets dat begint vanaf de atomaire schaal. Het model voor groei via botsingen tussen deeltjes is om deze reden gangbaar voor het beschrijven van de evolutie van de grootteverdeling. De atomaire clusters en kleinste nanodeeltjes die vormen tijdens de vroege stadia van het proces zijn zelfs bij kamertemperatuur vloeistofachtig en smelten samen wanneer ze met elkaar botsen. Groei van singlets naar een kritische grootte waarboven samensmelting tussen botsende deeltjes maar gedeeltelijk gebeurt of volledig stopt bij een gegeven temperatuur, kondigt het begin van agglomeratie aan die zal leiden tot niet-sferische deeltjes/agglomeraten. Voor processen die zeer snel gekoeld zijn kan de temperatuur tijdens de groei van de deeltjes worden ontkoppeld van de gelokaliseerde verdamping en worden ingesteld op een waarde die volledige samensmelting garandeert. Dit kenmerk verschaft flexibiliteit bij de controle over de grootte van de resulterende nanodeeltjes.

Hoofdstuk 3 stelt een eenvoudige, maar veelzijdige benadering voor, die over het algemeen gebruikt kan worden om de evolutie van deeltjesgrootte en concentratie vanaf snel gekoelde damp puntbronnen zoals vonkverdamping. De gemiddelde grootte van singlet nanodeeltjes kan eenvoudig worden beïnvloed door operationele parameters te wijzigen. Het experiment laat zien dat alle grootteverdelingen met een lognormale functie kunnen worden benaderen en dat de zelfbehoudende geometrische standaarddeviatie van ong. 1.35 wordt bereikt bij een grootte van ong. 6 nm. Dit kan worden beschouwd als een algemeen kenmerk. De benadering die is hier beschreven is veelzijdig en toepasbaar voor singlet nanodeeltjes van elk materiaal; het is ook toepasbaar bij bestaande fabricageprocessen, dit staat een onverstoord proces methodologie toe bij het genereren van functionele materialen.

Na de fundamentele onderzoeken, beschreven in deel A, wordt de scaling-up van de productie van nanodeeltjes wordt diepgaander onderzocht vergeleken met

voorafgaand werk. Een recent ontwikkelde HFS (high frequency spark) maakt de bereiding van een uitgebreid assortiment anorganische nanodeeltjes met goed gedefinieerde grootte en samenstelling van primary nanodeeltjes mogelijk met obrengsten tot 130×10^{-3} g h^{-1} (bij 3 kHz). Dergelijke opbrengsten van kleine nanodeeltjes bij vonkontladingen in de gasfase zijn nooit bereikt. De massaproductie snelheid voor nanodeeltjes bestaande uit verschillende materialen neemt lineair toe met vonkfrequentie. Hieruit volgt dat HFS productiesnelheden kan bereiken in de orde van 1 g h^{-1}, geëxtrapoleerde met resultaten uit hoofdstuk 4. Het generische proces kan is eenvoudig geschaald worden door verschillende HFS's parallel te koppelen. Ergo, de HFS's kunnen voldoen aan de industriële eisen. Behalve de productiecapaciteit, houdt de methode ook productkwaliteit in stand, iets wat wordt toegeschreven aan de goede kinetische controle. Bovendien zorgt het afschrikken ervoor dat deze methode ook fungeert voor thermodynamisch instabiele materialen en efficiënt mixen op atomaire of nanoschaal behaald. Contrasterend met de chemische routes vermijdt het systeem precursor oplossingen, waardoor single-step synthese van complexe multicomponent nanomaterialen met hoge zuiverheid mogelijke zijn op een voorspelbare en groene manier. Deze bevindingen maken de weg vrij voor opschalen van een uitgebreid assortiment nanomateriaal syntheses en verstrekken een groene een veelzijdige benadering voor nanofabricage. De geproduceerde nanodeeltjes (vele types, gewenste samenstelling) zijn interessant voor diverse disciplines zoals materiaalwetenschappen, scheikunde en natuurkunde evenals toepassingen voor industriële partners.

Naast opschalen, richt hoofdstuk 5 zich op het optimaliseren van de HFS's, waarbij het theoretische onderzoek van nanomixen door het afstellen van het oscillerende gedrag van een enkele vonkontlading en het verhinderen van splash deeltjes zijn geïncludeerd. Het eerste blijft theoretisch, terwijl het tweede succesvol bereikt wordt met behulp van een permanent magnetisch veld in de vonkbrug.

Na de fundamenten en het opschalen in delen A en B te hebben voorgelegd worden de toepassingen van de gegenereerde nanodeeltjes ook onderzocht. Door goedkope, opschaalbare en milieuvriendelijke aerosol processen te integreren in textiel nanoafwerking kunnen beperkingen, ondervonden in natte afwerking processen, worden omzeild en een nieuwe soort textiel ontwikkeld. Als proof of concept worden

zilver nanodeeltjes afgezet op verschillende textielsoorten en de antibacteriële eigenschappen voor twee bacteriestammen worden vastgesteld. Hoge antibacteriële activiteit is aanwezig zelfs als de zilver dekking een orde van grootte minder is dan in textiel behandeld via traditionele natte routes. Dergelijke lage bedekkingen voor antibacterieel textiel minimaliseren risico's voor de menselijke gezondheid (tijdens gebruik van het textiel) en het ecosysteem (na het weggooien) en reduceert ook mogelijke veranderingen in kleur en textuur van textielproducten. Het wassen van het textiel resulteert in minimale afname in antibacteriële activiteit, vergelijkbaar met de referentie stalen. Gezien dat een significant aantal functionele textielsoorten nanoafgewerkt kunnen worden met behulp van aerosol depositie, demonsteren onze resultaten dat de voorgestelde universele en duurzame benadering potentieel kan leiden tot vele toepassingen.

(Translated by Sander Boeree)

Acknowledgements

After long 'travelling' in this thesis 'sea', I would like to kindly offer a land for some leisure by variously expressing my grateful thanks to my colleagues, supportive friends, and beloved family.

In 2012, I was so excited to receive an offer from Andreas Schmidt-Ott and George Biskos, who deserve my grateful thanks for your enthusiastic support and strict requirements in the past four-year PhD project. You gave me complete freedom to independently conduct my research and deal with all the issues related to European project and paper submissions. From this comprehensive training, I indeed became stronger than ever. In our regular meetings, we drew out so many brainwaves, which cannot be all covered by this thesis in the present form.

I also would like to thank my co-workers in the Nanolab, such as Konstantinos Barmpounis, Spyros Bezantakos, Anne Maisser, Nishchay Isaac, Borja Rodríguez, Penelope Ioannidou, Kelly Nitos, Maria Pap, Marco Valenti, Tobias Pfeiffer, Bendikt Fraters, and Dirk Brossell. Without your company, this thesis wound stand lonely. Especially thank Konstantinos, Anne, Isaac, and Spyros for helping me to tackle some tough problems. Your constructive advice is very valuable to make me strong enough to confront those difficulties. Kelly, you did great job in the beach volleyball in Valencia. Many enjoyable parties and activities with some of you cannot be fully described here.

It is highly desirable to open one independent paragraph to acknowledge all the people involved in BUONAPART-E. The research leading to these results has received funding from the European Union's Seventh Framework Program under Grant

included in this dissertation though. A big thanks to all of you and your great collaborations in your thesis projects. Without your help, my thesis cannot be so plentiful.

I also thank all the present and former people in MECS group most sincerely. Bernard Dam, thank you for the valuable remarks raised in the group meetings. Joost Middelkoop, I have to thank you a lot for the TEM work and great support for arranging the exhaust ducts for my experimental system. Thanks are also for other MECSers for making the lunch, coffee break, and borrel a moment of fun and relax.

Michiel Makkee, my great mentor, I wish to thank you for the compassion and care during my long PhD project. It is a great help having you around. Your prompt response and valuable advice/suggestion deserve my grateful thanks. Thanks go to Ans van Schaik, a great faculty graduate school member, for addressing all the documents promptly and carefully. Willy Rook's help for using electric balance in Catalysis Engineering group has to be thanked greatly.

The biggest thanks to Yingying Zhao, you are definitely the first to be acknowledged among all my friends. You cooked more than 1000 times for me. The miles for you to travel to me are comparable to the number of words included in this lengthy thesis. I also greatly appreciate that you took care of me when I got surgery in the summer of 2014. Thank you for listening to my tough stories and for encouraging me to go on.

Many thanks go to other friends Shuhao Cao, Ming Ma, Hua Dong, Sander Boeree, Anping Cao, Fahimeh Nafezarefi, Wuyuan Zhang, Bo Qu, Zhen Liu, Liangyong Chu, Xiaohui Sun, Quan Pan, Kai Zhang, Min Qu, Haikuan Li, Meiling Liu, Ryan G. A. Bos... for all the joyful memories we spent together, and also for listening to me during my difficult and happy times. Give heartfelt thanks to Deshu Qu for designing some layouts. Sander Boeree's generosity for translating my summary to Dutch deserves my grateful thanks most sincerely. I would like to profusely thank Liangjun Yin, Liangyong Chu, Ming Ma, Peng Lu and Gang Chen for your generous help for the move from Delft to Leiden. I thank my ardent paranymphs: Anping and Fahimeh.

The most important acknowledgements are truly to my beloved family. I went abroad to do my PhD in a non-disturbed manner, because you created such a good environment. I am deeply indebted to my three sisters and brothers-in-law who took

a constant and affectionate care of my lovely mother. Such appreciations are certainly not adequate to thank you. My heartiest gratitude is deserved to my dear mother for your endless encouragement, strong support, and kind understanding, especially my absence during your surgery. Although I could not come back to take care of you, I am missing you so much every day. My dear nephews and nieces, Jing Lv, Xiaolei Wang, Tingjie Lv, Guangda Shen, Xichao Wang, Guangheng Shen, I am very proud of you. Heartfelt thanks to my family again for all your understanding, patience, and love which kept me going on...

馮繼成

Jicheng Feng

Delft, March 2016

Publications

➢ **Feng, Jicheng**, Biskos, G. & Schmidt-Ott, A. Toward industrial scale synthesis of ultrapure singlet nanoparticles with controllable sizes in a continuous gas-phase process. *Sci. Rep*., **5,** 15788 (2015).

➢ **Feng, Jicheng**, Huang, L., Ludvigsson, L., Messing, M.E., Maisser, A., Biskos, G. & Schmidt-Ott, A. General approach to the evolution of singlet nanoparticles from a rapidly quenched point source. *J. Phys. Chem. C,* **120,** 621–630 (2016).

➢ **Feng, Jicheng**, Hontañón, E., Blanes, M., Meyer, J., Guo, X., Santos, L., Paltrinier, L., Ramlawi, N., de Smet, L., Nirschl, H., Kruis, F.E., Schmidt-Ott, A. & Biskos, G. Scalable and environmentally benign process for smart textile nanofinishing. *ACS Appl. Mater. Inter*., **8** (23), 14756-14765 (2016).

➢ **Feng, Jicheng**, Guo, X., Rawlawi, N., Pfeiffer, T.V., Geutjens, R., Basak, S., Nirschl, H., Biskos, G., Zandbergen H.W. & Schmidt-Ott, A, Green manufacturing of metallic nanoparticles: facile and universal approach to scaling up. *J. Mater. Chem. A,* **4**, 11222-11227 (2016).

➢ **Feng, Jicheng**, Ramlawi, N., Biskos, G., Schmidt-Ott, A., Internal nanoparticle mixing by oscillatory spark ablation between electrodes of different materials 2016 (under review)

➢ **Feng, Jicheng**, Nguyen, T.V., Geutjens, R., Li, J., Basak, S., Zhu, Q., Galbács, G., Guo, X., Zandbergen, H.W., Brück, E.H., Schmidt-Ott, A., Room-temperature magnetic materials: new route towards efficient cooling or heating through ternary alloy nanoparticles (under preparation).

➢ **Feng, Jicheng**, Ramlawi, N., Biskos, G., Schmidt-Ott, Self-organization of nanoparticles at surfaces (under preparation)

➢ Pfeiffer, T. V., **Feng, Jicheng** & Schmidt-Ott, A. New developments in spark production of nanoparticles. *Adv. Powder Technol.* **25,** 56–70 (2014).

➢ Hontañón, E., **Feng, Jicheng**, Blanes, M., Guo, X., Santos, L., Schmidt-Ott, A., Nirschl, H., Kruis, F.E. Aerosol Route to Antibacterial Nanosilver Coating of Cotton Fabrics. *in proceeding of the international conference Nanomaterials:applications and properties* 01001 (Sumy State University, 2014).

➢ **Feng, Jicheng**, Zhao, J., Tang, B., Liu, P. & Xu, J. The electrochemical performance of ordered mesoporous carbon/nickel compounds composite material for supercapacitor. *J. Solid State Chem.* **183,** 2932–2936 (2010).

➢ **Feng, Jicheng**, Tang, B., Zhao, J., Liu, P. & Xu, J. Preparation of Ni/Mn compounds/ordered mesoporous carbon composite for use in an electrochemical supercapacitor. *J. Appl. Electrochem.* **41,** 901–907 (2011).

➢ **Feng, Jicheng**, Zhao, J., Liu, P., Tang, B. & Xu, J. Preparation and Electrochemical Characterization of Ordered Mesoporous Carbon/PbO Host-guest Composite Electrode Materials for Supercapacitor. *J. new Mater. Electrochem. Syst.* **13,** 321–326 (2010).

Highlights in Newsletters/Magazines

- ➢ 'Revolutionizing smart textile nanofinishing in a green fashion' is live on Nanowerk

  http://www.nanowerk.com/spotlight/spotid=44013.php

- ➢ '智能纺织品纳米整饰的绿色革命化' 在线发表在 科学网

  http://paper.sciencenet.cn//htmlpaper/20168114254158440316.shtm

- ➢ 'Smarter textile nanofinishing' is published on T.EVO

  http://www.tevonews.com/research-news/425-smarter-textile-nanofinishing

International Conferences

➢ **Feng, Jicheng**, Maisser, A., Pfeiffer, T. V., Biskos, G. & Schmidt-Ott, A. Size Controlled Synthesis of Spherical Nanoparticles by Spark Discharge. *The 2013 European Aerosol Conference (*Prague, Czech), poster presentation.

➢ **Feng, Jicheng**, Huang, L., Maisser, A., Pfeiffer, T. V., Biskos, G. & Schmidt-Ott, A. A Simple Model for Nanoparticle Formation by Spark Ablation. *The 2014 International Aerosol Conference (*Busan, South Korea), oral presentation.

➢ **Feng, Jicheng**, Biskos, G. & Schmidt-Ott, A. Controlling the size of singlet nanoparticles in spark ablation. *Aerosol Technology 2015 (*Tampere, Finland), oral presentation.

➢ **Feng, Jicheng**, Denonvile, C., Fontaine, M., Fjeld, H., Azar, A.S. & Schmidt-Ott, A. Toward industrial scale incorporation of nanoparticles onto catalytic membrane by aerosol route. *Aerosol Technology 2015 (*Tampere, Finland), oral presentation.

➢ **Feng, Jicheng**, Messing, M.E., Biskos, G. & Schmidt-Ott, A. Depositing particles on a substrate during their liquid-like phase of growth. *The 2015 European Aerosol Conference (*Milan, Italy), oral presentation.

➢ **Feng, Jicheng**, Biskos, G. & Schmidt-Ott, A. Achieving high yields of nanoparticles and suppressing 'splashing' in high frequency sparks. *The 2015 European Aerosol Conference (*Milan, Italy), poster presentation.

➢ **Feng, Jicheng**, Hontañón, E., Blanes, M., Meyer, J., Guo, X., Santos, L., Paltrinier, L., Ramlawi, N., de Smet, L., Nirschl, H., Kruis, F.E., Schmidt-Ott,A. & Biskos, G. Nanofinishing antimicrobial textiles by means of aerosol filtration. The 2016 European Aerosol Conference (Tours, France), oral presentation.

Jicheng FENG

01-04-1985	Born in Shandong, China

Professional Experience

04/2016~present	Post-doctoral fellowship at Leiden University
04/2012~04/2016	PhD researcher at Delft University of Technology
10/2010~04/2012	Technical Supervisor at SINOPEC of Shanghai Leader Catalyst Co. Ltd.

Education

09/2008~10/2010	MSc in Materials Processing and Engineering, Shanghai University of Engineering Science, *MSc with distinction*
09/2004~07/2008	BSc in Chemical Engineering and Technology, Qingdao University of Science and Technology

Honours & Awards

05/2013	2012 Graduate Recipient of Shanghai Outstanding Achievement Award, MSc with distinction in Shanghai
11/2011	2011 Social Entrepreneurship Business Competition (CEO&CTO)
09/2011	'Jili Cup' National Entrepreneurship Business Competition for College Students (CEO&CTO), Second Prize, € 8000
11/2010	The National Entrepreneurship Business Competition: 'Win in Changshu' (CEO&CTO), Second prize, € 15 000
10/2010	The Seventh 'Challenge Cup' National Entrepreneurship Business Competition (CEO&CTO), Third prize
04/2010	The Eighth Tan Kah Kee Young Inventor's Award
12/2009	The Sixth 'Zhangjiang High Tech.' Entrepreneurship Business Competition (CEO&CTO), Second prize
12/2009	The 'Academic Star' of Shanghai Graduate Students
03/2010-03/2011	Vice Chairman of the Society for Advanced Materials and Processing Engineering (SAMPE): Shanghai Branch

Part-time Job

10/2008~04/2012	Work Safety Supervision Bureau in Shanghai

Voluntary Experience

08/2010~09/2010	Shanghai World EXPO 2010 ICP

Jicheng Feng is now a postdoctoral researcher at Leiden University. He is involved in a project financed by Dutch Technology Foundation STW, aiming at developing a new electrochemical method for the preparation of (metallic) nanoparticles dispersed in solution.

In his PhD (2012-2016) at Delft University of Technology, he was involved in a European research project co-financed by the European Commission (no. 280765). This project gathers 21 partner institutions from all over Europe, aiming at developing industrial quantities of well-defined nanoparticles in a green manner to fulfil the customer demands. In this project, he led and organized many international collaborations: with PALAS in Germany to develop a flexible device for future scaling up, with FOMENTEX in Spain to pioneer a way of smart textile nanofinishing, with SINTEF in Norway to produce nanocatalysis for methane reforming, and with RID in the Netherlands to create 'switchable' magnetic nanoparticles toward biomedical applications and/or magnetocaloric refrigerants. Notably, some of his work has been highlighted in newsletters and magazines.

Before his PhD, he worked for SINOPEC (2010-2012), as part of the Research and Development Department. He participated in testing bench & pilot-scale treatability for polyethylene catalysts, and worked in the front-line for almost one year where he accumulated valuable experience and knowledge in industrial production lines.

During his master (2008-2010), he initiated several projects and attended the most well-known Entrepreneurship Business Competition events in China. He, as a CEO and a CTO, led almost 20 people in a team, who had different expertise. A great number of prizes, among which there are four National-level and three Provincial-level awards, were obtained, the total grant accounting to approximately 30 000 €. One of these was '*The Eighth Tan Kah Kee Young Inventor's Award*'. Besides his MSc graduation with distinction (Cum laude, 96.2/100), he also received '*2012 Graduate Recipient of Shanghai Outstanding Achievement Award*' in May 2013.

Appendices

Simulation Codes

1. Particle Evolution Code used in Chapter 3

Main Script

```matlab
1  tic
2  clc
3  clear
4  %% Input Parameters
5  q=6.0; % Quenching flow rate [ lpm ] ;
6  E=15.74; % Spark Energy [mJ/ spark ]
7  sigmag=1; %Particle size distribution factor
8  %% Model Code
9
10 for i =1:3
11 tspan1=2.4/q ; % Residence time in Stage 1 and it is strongly depends on the geometry
dimensions of the generators.  Here Veff=40 cm3 is used.
12 tspan2 =0.181; % Residence time in Stage 2
13 dp0=135e-12; % Diameter of Gold atom
14 if E>2 % Spark energy should reach a certain value,
otherwise there is no particle generation
15
16 delta_m_Electrode =8.33046153846154e-13*E-1.64123076923078e-12; % Mass loss of
electrode per spark
17 N0=3.41554153928098e23*power (delta_m_Electrode, 0.25 ) ;
% Particle (atom) concentration at t=0
18 % This is the optimized power relation
19
20 % due to two fitting variables in V_0=deta /M*power ( deta_m
, 0.25)
21 % N0=3.41554153928098e23*power (deta_m_ Electrode, 0.25 )=
N_A/M/V_0*power (detam , x )
22 % solve the above equations when detam=1.1488 e-11 kg . x
=0.337
23 % now the N0=N_A/M*power ( detam, x )
```

```
24
25 % ODE solver for Stage 1, initial condition is dp0
and N0 , para is the parameter
26 y01=[N0 dp0 ] ;
27 options = optimset ( 'Display ' , ' off ' ) ;
28 [T1 Y1]=ode15s (@dpNfun1 , [ eps tspan1 ] , y01 , options , q ,
sigmag ) ;
29
30 % ODE solver for Stage 2, initial condition is the
the termination condition in Stage 1
31 y02=[Y1( length (Y1) , 1 ) Y1( length (Y1) , 2 ) ] ;
32 dp=Y1 ( : , 2 ) ;
33 [T2 Y2]=ode15s (@dpNfun2 , [ tspan1 tspan1+t span2 ] , y02 ,
options) ;
34
35 % Generated Result
36
37 T=[T1 ;T2 ] ; % Total residence time
38 N=[Y1 ( : , 1 ) ;Y2 ( : , 1 ) ] ; % Particle concentration evolution
39 D=[Y1 ( : , 2 ) ;Y2 ( : , 2 ) ] . * 1 e9 ; % Particle diameter evolution
40
41
42
43 else
44
45 ' Spark Energy Too Low! '
46 T=0;
47 N=0;
48 D=0;
49
50 end
51 end
52 %% Output
53 Dfinal=D( end )% Dfinal is the mobility diameter at the end of the evolution for the three
chosen flow rates: 2.1, 25 and 40
```

Functions

Diffusion

```
1 % This function is used for calculating the diffusion coefficient in Stage 2.
2 % k_diff is the desired variable to be solved in function "dpNfun2" by
3 % fsolve. Time ( t ) , diffusion coefficient (D) and diameter of the tube in
4 % stage 2 ( dtube ) is the parameter in the equation .
5 function y=Diffusion ( k_diff, para)
6 t=para ( 1 ) ; % Time , [ s ]
7 D=para ( 2 ) ; % diffusion coefficient of aerosol particles , [m
^2/ s ]
8 dtube=para ( 3 ) ; % Diameter of the tube in Stage 2 , [m]
9
10 y=4* sqrt (D/( pi* t ) ) /dtube*exp ( t* k_diff)-k_diff;
11 end
```

dpNfun1

```
1 % This function is used for modeling the particle evolution in Stage 1. It is a
2 % time dependent ODE and is solved by ODE15s in the main function .
3 function dy=dpNfun1 (t , y , q , sigmag)
4 N=y ( 1 ) ; % Particle concentration , [#/m^ 3 ]
5 dp=y ( 2 ) ; % Particle size, [m]
6 % k_tot =0.12*(q-8) ; % Total influence factor of dilution and turbulent diffusion in stage 1,
[ s ^-1]
7 k _tot=0.1089*q ;
8 dy = zeros ( 2 , 1 ) ; % Initialization of  the output
9
10 T=293; % Ambient Temperature, [K]
11
12 kb=1.3806488e-23; % Boltzmann constant, [m2 kg s-2 K-1]
13 eta=1.75e-5; % Viscosity, [ kg m-1 s-1]
```

```
14
15  % Cunningham correction factor
16  lambda=0.066e-6; % mean free path, [m]
17  if dp<=0.1e-6
18  cc=1+lambda/dp *(2.34+1.05 * exp (-0.39 * dp/lambda ) ) ;
19  else
20  cc=1;
21  end
22  D=kb*T*cc /(3 * pi * eta * dp) ; % Diffusion coefficient, [m2 s -1]
23
24  rho_p=19.32 e3 ; % Density of gold particles, [ kg/m^ 3 ]
25
26  % Coagulation coefficient beta
27  c=sqrt ( (48 * kb * T) /( pi ^2* rho_p*dp^3) ) ;
28  rc=dp / 2 ;
29  l=8 * D/( pi * c) ;
30  g=(1/(6* rc * l ) ) * ( (2*r c+l )^3-power ( (4* rc ^2+l ^2), 3/2) ) - dp ;
31  epsilon =2.2;
32  b=(( sigmag-1) /(1.5-1) )*(0.7663-0.7071) +0.7071;
33  phi=3 * sqrt ( 3 ) * b * ( ( ( eta ^2*2* rc ) /( rho_p*kb*T) ) ^(1/2) )* ( exp ( (25 * log
    ( sigmag) ^2) /8)+2 * exp ( ( 5 / 8 ) * log ( sigmag) ^2)+exp ( ( 1 / 8 )* log ( sigmag ) ^2) ) ;
34  beta=8*pi * epsilon*phi*D*dp/(dp/(dp+g )+8 * D/( c * dp) ) ;
35
36  dy ( 1 )=-1/2*beta*N^2-k_tot*N; % dN/dt
37  dy ( 2 )=1/6*beta*N*dp ; % d(dp) /dt
38  end
```

dpNfun2

```
1  % This function is used for modeling the particle evolution in Stage 2. I t is a
2  % time dependent ODE and is solved by ODE15s in the main function.
3  function dy=dpNfun2 ( t , y )
4  N=y ( 1 ) ; % Particle concentration, [#/m^ 3 ]
5  dp=y ( 2 ) ; % Particle size, [m]
```

```
6 dy = zeros ( 2 , 1 ) ; % Initialization of the output
7
8 % Cunningham correction factor
9 lambda=0.066 e-6; % mean free path, [m]
10 if dp<=0.1e-6
11 cc=1+lambda/dp*(2.34+1.05*exp (-0.39*dp/lambda ) ) ;
12 else
13 cc=1;
14 end
15
16 kb=1.3806488 e-23; % Boltzmann constant , [m2 kg s-2 K-1]
17 eta=1.75 e-5; % Dynamic viscosity, [kg m-1 s-1]
% http :/ /www. lmnoeng.com/Flow/GasViscosity.php
18 T=293; % Temperature, [K]
19
20 D=kb*T*cc /(3*pi* eta*dp) ;% Diffusion coefficient, [m2 s -1]
21
22 dtube2=4e-3; % Diameter of the tube in Stage 2, [m]
23
24 rho_p=19.32 e3 ; % Density of gold particles, [
kg/m^ 3 ] % http : / /www. chemicool.com/elements/gold.html
25
26 % Coagulation coefficient beta
27 c=sqrt ( (48*kb*T) /( pi ^2* rho_p*dp^3) ) ;
28 rc=dp/2 ;
29 l=8*D/( pi*c) ;
30 g=(1/(6*rc*l ) )*( ( 2*rc+l )^3-power ( ( 4*rc ^2+l ^2) ,3/2) )-dp; %
31 beta=8*pi*D*dp/(dp/(dp+g )+8*D/( c*dp) ) ;
32
33 % k_diffusion in Stage 2
34 para0=[ t ,D, dtube2 ] ;
35 options = optimset ( ' Display ' , ' off ' ) ;
36 k_diff = fsolve ( @Diffusion , 1 , options , para0 ) ;
37
38 dy ( 1 )=-1/2*beta*N^2-k _diff*N; % dN/dt
39 dy ( 2 )=1/6*beta*N*dp ; % d(dp) /dt
```

```
40 end
```

Testing

```
1 %Input1
```

% this testing is strongly dependent on the geometrical dimensions of the spark discharge generator. One should adapt these parameters accordingly in order to use the model.

```
2 q=6.0; % Quenching f low rate [ lpm ] ;
3 E=15.74; % Spark Energy [mJ/ spark ]
4 sigmag=1; % Particle Size Distribution Factor
5 %Output1
6 Dfinal =6.3; % nm
7
8
9 %Input2
10 q=25; % Quenching f low r a t e [ lpm ] ;
11 E=15.74; % Spark Energy [mJ/ spark ]
12 sigmag=1; % Particle Size Distribution Factor
13 %Output2
14 Dfinal= 3.5; % nm
15
16
17 %Input3
18 q=40; % Quenching f low rate [ lpm ] ;
19 E=15.74; % Spark Energy [mJ/ spark ]
20 sigmag=1; % Particle Size Distribution Factor
21 %Output3
22 Dfinal =3.0; % nm
```

2. Current Oscillation Fitting Code used in Chapter 5

Main Script

```
1 format long
%%%% Input Parameters%%%
3 n=60; %number of Data Points to use
4 file=' SampleDataFile.csv ' ; % Choose Current Data file name
5 C=44*10^-9; % the value of capacitance in the high frequency spark circuit
6 Vo=-1200; % Interval to search for the correct voltage in
7 R=0.1 : 0.01:6 ; % Interval to search for the resistance in
8 L=2.9; %  Interval to search for the correct inductance in
9
10 %%%% Fitting Script %%%%%
11 M=importdata ( file ) ;
12
13 tI=M. data ( : , 1 ) ;
14 I=-M. data ( : , 2 ) ;
15 I=I +1.816*ones ( length ( I ) , 1 ) ;
16 startTime=5.4*10^-8;
17 endTime=4.54*10^-6;
18 i=find ( ( t I>s tar tTime ) ,1 , ' first ' ) ;
19 j=find ( t I>endTime , 1 , ' first ' ) ;
20 tI=t I ( i : j ) ;
21 I=-I ( i : j ) ;
22
23 tI=takein ( tI , n) ;
24 I=takein ( I , n) ;
25 I=I*10;
26
27 L=L*10^-6;
28 temp=1000000; % dummy variable
29 y=[ ] ;
30 for i =1: length (Vo)
```

```
31      for j =1: length (L)
32          for k=1: length (R)
33              if (R( k ) ^2-4*L( j ) /C) < 0
```
34 % E=costI (tI , I , [Vo(i) ,L(j) ,R(k)] ,C)+costV (tv ,V

, [Vo(i) ,L(j) ,R(k)] ,C) ;
```
35              E=costI ( t I , I , [ Vo( i ) ,L( j ) ,R( k ) ] ,C) ;% choosing the c
```
36 %
```
37              if E<temp
38                  temp=E;
39              y ( 1 )=Vo( i ) ;
40              y ( 2 )=L( j ) ;
41              y ( 3 )=R( k ) ;
42                  end
43              end
44          end
45      end
46 end
```
47 [e2]= checkfit (y , tI , I ,C) ;% show the current fit plot and calculate the relative error

48 % Solution is stored in variable y in the form y (1) i s

Voltage /y (2) i s

49 % Inductance /y (3) is Resistance

50

51 [e , rCathode]=energy (y , tI ,C) ;% Finding rCathode from the

oscillations. e is the relative error of the fits

Functions

CostI

1 % calculate the error between the model and current data points

2 function e=costI (t , I , y ,C)

3 t=t-t (1)*ones (length (t) , 1) ;

4 x (1)=y (1) ;

5 x (2)=2*y (2) /y (3) ;% R:Y(3) ////// L:Y(2)

```
6 x ( 3 )=(1/ sqrt ( y ( 2 )*C) )* sqrt (1-C*( y ( 3 ) ^2) /(4*y ( 2 ) ) ) ;
7 x ( 4 )=atan (1/( x ( 2 )*x ( 3 ) ) ) ;
8 E=(I-C* x( 1 )*x ( 3 ) . *( 1 +(1/((x ( 2 ) ^2) .* ( x ( 3 ) ^2) ) ) ) . *exp(-t . /
x ( 2 ) ) . *s i n ( x ( 3 )* t ) ) ; %. / I ;
9 e=0;
10    for i =1: length ( t )
11        e=E( i )^2+e ;
12    end
13 e=e / length ( t ) ;
14 end
```

CheckFit

```
1 % Plot the experimental data next to the model and calculate the relative
2 % error of the fits
3 function [ e2 ]= checkfit (y , t I , I ,C)% tv ,V, t I , I ,C)
4 % figure
5 % plot ( tv ,V, ' ro ' ) ;
6 % hold on
7 % plot ( tv , v o l t a g e (y , tv ,C) ) ;
8 figure ( 2 )
9
10 plot ( t I , I , ' ro ' ) ;
11 hold on
12 plot ( tI , current ( t I , y ,C) ) ;
13 hold off
14 xlabel ( ' time ( s ) ' )
15 ylabel ( ' current (A) ' )
16 % e1=costV ( tv ,V, y ,C) ;
17 e2=costI ( t I , I , y ,C) ;
18 % e=e1+e2;
19 end
```

Energy

```
1
2  % Caculate r_cathode based on the model parameters during oscillations
3  function [E , rc ]=energy (y , tv ,C)
4  E=0;
5  E1=0;
6  E2=0;
7  Cmc=1;
8  Cma=1;
9  P=current ( tv , y ,C) . ^ 2*y ( 3 ) ;
10 C=current ( tv , y ,C) ;
11 for i =1: length ( tv ) - 1
12 E=E+P( i ) * ( tv ( i +1) - tv ( i ) ) ;
13 end
14
15 for i =1: length ( tv )-1
16
17 if C( i )>= 0
18
19 E1=E1+P( i ) * ( tv ( i +1) - tv ( i ) ) ;
20 else
21 E2=E2+P( i ) * ( tv ( i +1) - tv ( i ) ) ;
22      end
23
24 end
25 E1=E1* (Cmc/Cma) ;
26 rc=E2/(E1+E2) ;
27
28
29 end
```

Current

```
1 % Calculate the current based on parameters in the oscillation model
2 function I=current ( t , y ,C)
3 t=t - t ( 1 ) * ones ( length ( t ) , 1 ) ;
4 x ( 1 )=y ( 1 ) ;
5 x ( 2 )=2 * y ( 2 ) /y ( 3 ) ;% R:Y( 3 ) ///// L:Y( 2 )
6 x ( 3 )=(1/ sqrt ( y ( 2 ) * C) ) * sqrt (1- C * ( y ( 3 ) ^2) /(4 * y ( 2 ) ) ) ;
7 x ( 4 )=atan (1/( x ( 2 )  * x ( 3 ) ) ) ;
8 I=C * x ( 1 ) * x ( 3 ) .* (1+1/( ( x ( 2 ) ^2) . * ( x ( 3 ) ^2) ) ) .* exp( - t . / x ( 2 ) )
. * sin ( x ( 3 ) * t ) ;
9 end
```

TakeIn

```
1
2 % Take a certain number of data points from the full current trace measured by the
oscilloscope
3 function V=take in (v , n)
4 V=ones (n , 1 ) ;
5 V( 1 : 8 )=v ( 1 : 8 ) ;
6 io=ceil (8 * n/ length ( v ) ) ;
7 for i =3:n
8
9 V( i )=v ( ceil ( io * length ( v ) /n) ) ;
10 io=io +1;
11 end
12 end
```

3. Fabrics Code used in Chapter 7

Main Script

```
1  format long
2  sol =[ ] ;
3  clearall
4  %%%Input%%%
5  P= . . . % Penetration matrix (column vector for each velocity
6  [
7  0.518116305
8  0.589007697
9  0.644686649
10 0.74743302
11 0.80204612
12 0.865895106
13 0.894514192
14 0.911414944
15 0.933706281
16 0.96640386
17
18 ] ;
19 dp=. . . % Particle diameters vector corresponding to each of the penetration values above
20 [
21 10
22 15
23 20
24 30
25 40
26 60
27 80
28 100
29 125
```

```
30 150
31 ] ;
32 alpha =0 . 0 5 : 0 . 0 0 1 : 0 . 3 ; % Choose alpha range
33 dens =1 . 1 : 0 . 0001 : 3 ; % Choose the Fiber Density Range
34 dw= 10 * 10^ - 6:0.01 * 10^ - 6:2.5 * 10^ - 5; % Choose fiber diameter range
35
36 for s=3 % Choose for which velocity from the U vector or set of velocities one wants to fit
(provide index or index vector)
37
38 U=. . .% Provide velocity vector
39 [
40 0.5
41 1
42 2
43 4 ] ;
44 U=U * 10^ - 2;
45 deltaP =. . . % Provide deltaP vector (only relevant if the two equations are fitted)
46 [
47 0.7
48 1.5
49 3
50 6.2
51
52 ] ;
53
54
55
56 dp=dp * 10^ - 9;
57 T=298; % Temperature (K)
58 q=s ; % choose velocity value (1 2 3 4 )
59 visc =22.6 * 10^ - 6; % viscosity ( pa . s )
60 mfp=68.33 * 10^ - 9; % Mean Free Path (m)
61 k=1.3806488e10^ - 23; % Boltzmann Constant
62 Cc= 1+dp.^(-1) . * ( 0.234e1+0.105e1 . * exp ( 1 ) .^( ( - 0.39E0) . * dp
 . * mfp.^(-1) ) ) . * mfp ;
```

```
63 D=(k * T. * Cc ) . / ( 3 * pi *visc * dp) ;
64 x0=[0.055 , 2.5*10^ - 4 1.5 * 10^ - 5] ; % Initial Guess
65 c=1;
66 temp=100;
67 for i =1: length ( alpha )
68     for j =1: length ( dens )
69         for k=1: length (dw)
70             L=(0.13 * 10^ - 3) . / ( alpha ( i ) * dens ( j ) ) ;
71             E= costP (D,P, alpha ( i ) ,L,dw( k ) ,U( q ) ) ;
72
73             if E<temp
74                     temp=E;
75                 x ( 1 )=alpha ( i ) ;
76                 x ( 2 ) =(0.13 * 10^ - 3) . / ( alpha ( i ) * dens ( j ) ) ;
77                 x ( 3 )=dw( k ) ;
78             end
79         end
80     end
81 end
82
83
84 f igure ( 1 )
85 hold off
86 plot (dp*10^9 , ones ( length (P) , 1 ) - P, ' ro ' )
87
88
89 dp1=transpose ( 1 : 1 : 200 ) *10^ - 9;
90 hold on
91 k=1.3806488 e 10^- 23;
92 Cc1= 1+dp1 .^( - 1) . * ( 0 . 2 3 4E1+0.105E1 . * exp ( 1 ) .^( ( - 0.39E0) . *
dp1 . * mfp.^(- 1) ) ) . * mfp ;
93 D1=(k * T. * Cc1 ) . / ( 3 * pi * visc * dpl ) ;
94
95 plot ( dp1 *10^9 , ones ( length (D1) , 1 ) − penetration (x ,D1 ,U( q ) ) ) ;
96 axis ( [ 0 200 0 1 ] )
```

97 end

98 %%%Output Solution

99 solution =x ;

Functions

Penetration

1 % Calculate the penetration from the fabric parameters

2 function P= penetration (x ,D,U)

3 P= exp ((- 10.8 * x (1) . * x (2) . * D. ^ (2/3)) . / (pi . * (1 - x (1)) * (x (3) ^(5/3) * U^(2/3))))) ;

4 end

costP

1 % Calculate the error between the experimental data and the results from the model simulations

2 function E= costP (D, P, alpha , L, dw, U)

3 f= (P+(- 1) . * exp (1) .^((- 0.343775E1) .* (1+(- 1) . * alpha) .^(-1) . * alpha . * D. ^ (2 / 3) . * dw.^(- 5/3) . * L . * U.^(- 2/3))) . /P;

4

5 E=0;

6 for i =1: length (D)

7 E = E+ f (i) ^ 2 ;

8 end

9 E=E/ length (D) ;

10 end

4. Particle Size Distribution Codes used in Chapters 2, 3, 4, 7

Functions

PSDn

1 function [DISTR]= PSDn(V, neutr , gasneut r , DMA, PS , gasdma , qpoly , qsheath , AEMCPC)

2 % calculate DN/ddp for a given combination of DMA and AEM or CPC

3 % voltages . if a neutralizer is specified, this file also calculates the

4 % charge distribution and applies that to DN/ddp .

5 %

6 %

7 % function [DISTR]= PSDn(V, neutr , gasneut r , DMA, PS , gasdma , qpoly ,

8 % qsheath , AEMCPC)

9 %

10 %

11 % V=[Vdma (1 array) Vaemcpc (x arrays)]

12 % Vdma: dma set voltage (V)

13 % Vaemcpc : measured voltage for aerosol electrometer or CPC (V)

14 %

15 % neutr : indicate whether or not a neutralizer is used

16 % 1=neutralizer (any other # means no neutr .)

17 % gasneut r : gas used in neutralizer

18 % 1=He

19 % 2=Ar

20 % 3=N2

21 % 4=Air

22 %

23 % DMA: DMA used

24 % 1=TSI 3071

25 % 2=Long French

```
26  % 3=Short French
27  % PS: DMA Power supply type (-1 f o r negative , +1 for positive  )
28  % gasdma : gas used in dma
29
30  % gas=[M( kg/mol ) m+(kg/mol ) m - (kg/mol )
31  % Z+(m2/V * s ) Z - (m2/V * s ) eta (Pa * s ) sigma (m2) ]
32  % 1=He
33  % 2=Ar
34  % 3=N2
35  % 4=Air
36
37
38  % qpoly : DMA sample f lowrate (SLM) assumes that
39  % polydisperse=monodisperse and monodisperse= aem flow
40  % qsheath : DMA sheath air flow rate (SLM)
41  %
42  % AEMCPC: indicate whether AEM or CPC is used
43  % 1=CPC TSI
44  % 2=CPC Grimm (any other # means AEM)
45
46
47
48
49  [ n ,m]= size (V) ;
50  nn=n - 1;
51  % nn=n ; % in orde r to match other docs
52  Vdma=V( 1 : nn , 1 ) ;
53  Vaemcpc=V( 1 : nn , 2 :m) ;
54
55  %Vdma to dp conversion
56  DP=dma(Vdma, gasdma , DMA, qsheath , qpoly ) ;
57  dp=DP( : , 1 ) ; % in nm
58  ddp=DP( : , 4 )  * ones ( 1 ,m□1) ;
59  dpupper=DP( : , 3 ) ;
60  dplower=DP( : , 2 ) ;
61
```

```
62 % particle concentration
63 Vaem=Vaemcpc ;
64 el =1.6021765 e-19;
65 Raem=1e11;
66 %Raem=1.3 e12 ; depends on the resistance of the AEM
67 Qaem=qpoly * 1000/60; % aem f low in ccm/ s
68 I=abs (Vaem) /(Raem * e l * Qaem) ; % measured particle concentration
 ( part /ccm)
69
70 if AEMCPC==1
71 Vcpc=Vaemcpc ;
72 % I =10.^(Vcpc - 3) ; % measured particle concentration ( part /ccm)
73 I=1e6 * Vcpc ;
74 end
75 if AEMCPC==2
76 I=Vaemcpc * 1 e6 ; % Grimm measured particle concentration ( part /ccm)
77 end
78
79
80 DN=2* I ; % actual particle concentration in ddp ( part /ccm)
81
82 %charge distribution
83 if neutr = = 1
84 % q=3;
85 q=3;
86 Fn=charge (dp , 3) ;
87 FN=Fn ( 1 : nn , q+1- PS) * ones ( 1 ,m-1) ;
88 % DN=2 * I . /FN; % actual particle concentration in ddp ,
89 DN=1.5*2* I . /FN; % corrected for charge distribution ( part /ccm)
90 end
91 DNddp=DN. / ddp ; % deltaN/ de ltadp ( part /ccm*nm)
92
93 % interval
94 Int=zeros (nn , 1 ) ;
95 N=[2:nn-1 ] ' ;
```

```
96 Int (N)=ddp (N) +0.5 * ( dplower (N)-dpupper (N-1) ) +0.5*( dplower (
N+1)-dpupper (N) ) ;

97 Int ( 1 )=ddp ( 1 ) +0.5*( dplower ( 2 )-dpupper ( 1 ) ) ;

98 Int (nn)=ddp (nn) +0.5*( dplower (nn)-dpupper (nn-1) ) ;

99

100 Intm=Int * ones ( 1 ,m-1) ;

101

102 DNtot=DNddp. * Intm ; % total particle concentration  per interval ( part /ccm)

103 Ntot=sum(DNtot ) ; % total particle concentration ( part /ccm)

104

105 dpm=dp * ones ( 1 , m-1) ;

106

107 dpNmean=exp ( sum( log (dpm) . * DNtot ) . / Ntot ) ; %
number mean particle count (nm)

108 %

109 % dpNmean=sum(dpm. *DNtot ) . / Ntot ;

110

111 dpNmeanm=ones (nn , 1 ) * dpNmean ;

112

113 % VarN=sum( ( (dpm-dpNmeanm) . ^ 2 ) . * DNtot ) . / Ntot ; % number
variance (nm2)

114 % StDevN=VarN. ^ 0 . 5 ; % standard deviation (nm)

115 StDevN=exp ( ( sum( ( ( log (dpm)-log (dpNmeanm) ) . ^ 2 ) . * DNtot ) . /
Ntot ) . ^ 0 . 5 ) ; % number variance (nm2)

116 % standard deviation (nm)

117

118 distr =[dp ddp ( 1 : nn , 1 ) DNddp ] ;

119 [ o , p]= size ( distr ) ;

120 s t=[Ntot ; dpNmean ; StDevN ] ;

121 ST= [ zeros ( 3 , p-(m-1) ) st ] ;

122 DISTR=[ distr ; ST ] ;

123

124 plot (DP( 1 : nn , 1 ) , distr ( 1 : nn , 3 :m+1) )

125 hold on

126

127 x l a b e l ( ' mean mobility size (nm) ' )
```

```
128  ylabel('nDeltaN/nDeltadp ( part /( ccm*nm) )')
129  %
130  % legend ('2.1 slm','6 slm','9.9 slm','13.8 slm','17.7
slm','21.5 slm','25.4 slm','29.3 slm','33.2 slm','37.1
slm','41 slm','44.9 slm')
131
132  grid on
```

Ztodp

```
1   function [ J]=Ztodp (Zdma , gas )
2   % this function is used to calculate particle size from electrical mobilities .
3
4   % ZDMA: ( vertical ) vector containing the electrical mobilities
5   % (m2/V* s )
6
7   % gas=[M( kg/mol ) m+(kg/mol ) m-(kg/mol )
8   % Z+(m2/V* s ) Z-(m2/V* s ) eta (Pa* s ) sigma (m2) ]
9   %1=He
10  %2=Ar
11  %3=N2
12  %4=Air
13
14
15  % qsheath : DMA sheath flowrate (SLM) (=excess flow rate )
16  % qpoly : DMA sample flowrate (SLM) (=monodisperse flow rate )
17
18  % [ 1 ] Atkins , P.W. , (1998) , Physical chemistry (6 th ed . ) ,
Oxford Uni v e r s i t y
19  % Press , Oxford , p . 30
20  % [ 2 ] TSI 3080 DMA manual , www. TSI . com
21  % [ 3 ] Hoppel , W.A. , (1978) , J . Aerosol Sci . , vol . 9 , 41
22
23  % gas properties
24  G=gasprop ( gas ) ;
```

```
25 e ta=G( 6 ) ; % gas viscosity (Pa*s )

26 sigma=G( 7 ) ; % collision cross section (m2 ) [ 1 ]

27

28

29

30 % constants

31 P=1.013E5 ; % gas pressure (Pa)

32 T=293; % temperature (K)

33 R=8.3145; % gas constant ( J/molK)

34 Na=6.02214 e23 ; % Avogrado ' s constant (1/mol )

35 e l =1.6021765 e-19; % elementary charge (C)

36 k=R/Na ; % Boltzmann ' s constant ( J/K)

37

38 % mean free path gas

39 l=k*T/ ( ( 2 ^ 0 . 5 ) *P* sigma ) % gas mean free path (m) [ 1 ]

40

41 % particle size singly charged particles

42

43 % slip correction (Cc ) factor parameters

44 % Cc=1+2* l /x * ( a+b * exp(-c * x /(2 * l ) ) ) % [ 2 ]

45 a=1.142;

46 b=0.558;

47 c=0.999;

48 D=3 * pi * eta ;

49

50 n=length (Zdma) ;

51 for N=1:n

52

53 de s t=e l /(D * Zdma(N) ) ; % first estimate of the

54                          % particle size ,

55                          % disregarding the slip

56                          % correction factor  (m)

57

58 %  solver for particle size

59 B=@( x ) e l * (1+2* l /x * ( a+b*exp(- c * x /(2 * l ) ) ) ) ) /(D * x )-Zdma(
N) ;
```

```
60 d=fzero (B, dest*10) ;
61 dp(N)=d/1e-9;
62
63
64
65 end
66
67 J=[dp ' ] ;
```

Gasprop

```
1 function [ gas ]=gasprop (N)
2 %N:
3 %1=He
4 %2=Ar
5 %3=N2
6 %4=Air
7
8 %gas=[M( kg/mol ) m+(kg/mol ) m-(kg/mol ) Z+(m2/V* s ) Z-(m2/V*
s ) eta (Pa * s ) sigma (m2) ]
9 % M: molecular mass of the gas ( kg/mol )
10 % m+: molecular mass of positive ion ( kg/mol )
11 % m-: molecular mass of negative ion ( kg/mol )
12 % Z+: positive ion mobility (m2/V* s )
13 % Z-: negative ion mobility (m2/V* s)
14 % eta : viscosity (Pa * s )
15 % sigma: collision cross section (m2) [ 1 ]
16
17 % The ion data on is not reliable , mainly an extrapolation based on
18 % Romay and Pui (1992) and the approach of Wiedensohler and Fissan (1991) .
19 % No experimental data on the BIPOLAR charging in Helium is available. Use
20 % the argon bipolar charge distributions instead.
21 % Ion properties for argon, nitrogen and air are based on Wiedensohler and
22 % Fissan (1991)
23
```

```
24 % [ 1 ] Wiedensohler , A. and Fi s san , H. , (1991) , Aerosol Sci . Technol . , vol .
25 % 14 , 358
26 % [ 2 ] Romay , F. J . and Pui , D.Y.H. , (1992) , Ae rosol Sci . Technol . , vol . 17 ,
27 % 134
28
29
30 GASPROP=[ 4.00 e-3 0.008 0.0043 17.2 e-4 20. 9e-4 1.863e-5 2.1e-19;
31 39.95e-3 0.110 0.060 1.4e-4 1.7 e-4 2.217e-5 3.6e-19;
32 28.02e-3 0.110 0.060 2.0 e-4 2.15e-4 1.77e-5 4.3e-19;
33 29.56e-3 0.140 0.101 1.4 e-4 1.6 e-4 1.73e-5 4.3e -19] ;
34
35 [ n ,m]= size (GASPROP) ;
36 gas=GASPROP(N, 1 :m) ;
```

Dmaprop

```
1 function [DMA]=dmaprop (N)
2 % DMA=[L(cm) r1 (cm) r2 (cm) ]
3 % 1=TSI 3071
4 % 2=French ( long )
5 % 3=French ( short )
6
7 DMAPROP=[44.369 0.937 1 .961 ;
8 37.5 0.935 1.96 ;
9 10.585 0.935 1.96 ] ;
10
11 [ n ,m]= size (DMAPROP) ;
12
13 DMA=DMAPROP(N, 1 :m) ;
```

Cma

```
1 function [ J ,K]=dma(VDMA, gas , dma , qsheath , qpoly )
2 % this function is used to calculate particle size from DMA voltage and DMA properties
3 %
```

```
 4 %
 5 % [ J ,K]=dma(VDMA, gas , dma , qsheath , qpoly )
 6 %
 7 %
 8 % VDMA: ( vertical) vector containing the DMA voltage setpoints
 9 %
10 % gas=[M( kg/mol ) m+(kg/mol ) m-(kg/mol )
11 % Z+(m2/V*s ) Z-(m2/V* s ) eta (Pa * s ) sigma (m2) ]
12 %1=He
13 %2=Ar
14 %3=N2
15 %4=Air
16
17 % DMA=[L(cm) r1 (cm) r2 (cm) ]
18 % 1=TSI 3071
19 % 2=French ( long )
20 % 3=French ( short)
21
22 % qsheath : DMA sheath flow rate  (SLM) (=excess flow rate)
23 % qpoly : DMA sample flow rate (SLM) (=monodisperse flow rate)
24
25 % [ 1 ] Atkins , P.W. , (1998) , Physical chemistry (6 th ed . ) ,
Oxford University
26 % Press , Oxford , p . 30
27 % [ 2 ] TSI 3080 DMA manual , www. TSI . com
28 % [ 3 ] Hoppel , W.A. , (1978) , J . Aerosol Sci . , vol . 9 , 41
29
30 % gas properties
31 G=gasprop ( gas ) ;
32 eta=G( 6 ) ; % viscosity (Pa * s )
33 sigma=G( 7 ) ; % collisional cross section  (m2 ) [ 1 ]
34
35 Vdma=abs (VDMA) ; % DMA voltage
36
37 % constants
```

```
38 P=1.013E5 ; % gas pressure (Pa)

39 T=293; % temperature (K)

40 R=8.3145; % gas constant ( J/molK)

41 Na=6.02214e23 ; % Avogrado ' s constant (1/mol )

42 e l =1.6021765 e-19; % elementary charge (C)

43 k=R/Na ; % Boltzmann ' s constant ( J/K)

44

45 % DMA properties

46 H=dmaprop (dma) ; % properties of the DMA ( from DMAprop.m)

47 L=H( 1 ) /100; % DMA length (m)

48 r1=H( 2 ) /100; % inner radius DMA (m)

49 r2=H( 3 ) /100; % outer radius DMA (m)

50 Qsheath=qsheath /(60*1000) ; % sheath flow rate (m3/ s)

51 Qpoly=qpoly /(60*1000) ; % polydisperse aerosol flow rate (m3/ s )

52

53 % mean free path

54 l=k*T/ ( ( 2 ^ 0 . 5 ) *P* sigma ) ; % gas mean free path (m) [ 1 ]

55

56 % singly charged particles

57

58 % slip correction (Cc ) factor parameters

59 % Cc=1+2*l /x *( a+b*exp(-c*x /(2 * l ) ) ) [ 2 ]

60 a=1.142;

61 b=0.558;

62 c=0.999;

63

64 D=3* pi * eta ;

65 n=length (VDMA) ;

66 dp=ones (n , 1 ) ; % [m]

67 dppl=ones (n , 1 ) ; % [m]

68 dpmi=ones (n , 1 ) ; % [m]

69 LAM=L/ log ( r2 / r1 ) ; %Shape factor DMA

70 Zdma=Qsheath . / ( 2 * pi *Vdma*LAM) ; % mobility that is set in DMA (m2/V* s ) [ 2 ]

71

72 RelTol=1e-10;
```

```
73 Cc=ones (n , 1 ) ;
74
75 %Solve for dp ( and Cc ) by iteration
76 dpold=zeros (n , 1 ) ;
77 while max( abs (dp-dpold ) . / abs (dp) )>RelTol
78 dpold=dp ;
79 dp=e l *Cc/3/ pi / eta . /Zdma ;
80 Cc=1+2 * l . / dp . * ( a+b*exp(-c * dp/2/ l ) ) ;
81 end
82
83 % DMA resolution
84 DZdma=Qpoly/Qsheath*Zdma ; % Ful l
Width Hal f Mean o f
85                              % the DMA transfer function
86                              % (m2/V* s) [ 3 ]
87
88 Zpl=Zdma+DZdma; % maximum mobility
89                    % particles coming out o f
90                    % DMA for given voltage
91                    % (m2/V * s)
92
93 Zmi=Zdma - DZdma; % minimum mobility of
94                      % particles coming out of
95                      % DMA for given voltage
96                      % (m2/V * s )
97
98
99 %Solve for upper and lower limits of dp ' s
100 dpold=zeros (n , 1 ) ;
101 while max( abs ( dppl-dpold ) . / abs ( dppl ) )>RelTol
102 dpold=dppl ;
103 dppl=e l * Cc/3/ pi / eta . / Zpl ;
104 Cc=1+2 * l . / dppl . * ( a+b*exp(-c * dppl /2/ l ) ) ;
105 end
106
107 dpold=zeros (n , 1 ) ;
```

```
108  while max( abs (dpmi-dpold ) . / abs ( dpmi ) )>RelTol
109  dpold=dpmi ;
110  dpmi=e l * Cc/3/ pi / eta . / Zmi ;
111  Cc=1+2* l . / dpmi . * ( a+b*exp(-c *dpmi/2/ l ) ) ;
112  end
113
114  ddp=dpmi-dppl ;
115
116  J=[dp dppl dpmi ddp ] ;
117  J=J . * 1 e9 ; % convert to [nm]
118  K=[Zdma Zpl Zmi DZdma ] ;
```

Charge

```
1   function [ ch]=charge (dp , gas )
2   % this function is used to calculate the steady state bipolar charge distribution for
3   % a given particle size dp (n by 1 vector ) and a given gas-type , based on
4   % the Fuchs theory as described in :
5   %
6   % [ 1 ] Fuchs , N.A. , (1963) , J . Pure and Appl . Geophys . , vol . 56 , 185
7   % [ 2 ] Adachi , M. e t . a l . , (1985) , J . Aerosol . Sci . , vol . 16 , 109
8   % [ 3 ] Reischl , G. e t . a l . . (1996) , J . Aerosol Sci . , vol .27 , 931
9   % [ 4 ] Wiedensohler , A. and Fissan , H. , (1991) , Aerosol Sci . Technol . , vol .
10  % 14 , 358
11  % [ 5 ] Romay , F. J . and Pui , D.Y.H. , (1992) , Aerosol Sci . Technol . , vol . 17 ,
12  % 134
13  %
14  % gas=[M( kg/mol ) m+(kg/mol ) m-(kg/mol ) Z+(m2/V* s ) Z-(m2/V* s ) ]
15  % 1=He
16  % 2=Ar
17  % 3=N2
18  % 4=Air
19  %
20  % The ion data on helium is NOT reliable , mainly an
```

extrapolation based on

21 % Romay and Pui (1992) and the approach of Wiedensohler

and Fissan (1991) .

22 % No experimental data on the BIPOLAR charging in Helium is available. Use

23 % the argon bipolar charge distributions instead.

24 % Ion properties for argon, nitrogen and air are based on Wiedensohler and

25 % Fissan (1991)

26 %

27 % indexes: pl for positive ions , mi for negative ones

28

29

30 a=(dp*1e-9) / 2 ; % particle radius (m)

31

32 q=3; % maximum particle charge

33

34 % charge of the particle, p is considered positive if ion and particle

35 % charge are of the same sign.

36 ppl=[-q : q] ; % for positive ions

37 pmi=-1*ppl ; % for negative ions

39 %gas properties

40 G=gasprop (gas) ;

41 M=G(1) ; % molecular mass of the gas (kg/mol)

42 mpl=G(2) ; % molecular mass of the positive ion(kg/mol)

43 mmi=G(3) ; % molecular mass of the negative ion (kg/mol)

44 Zpl=G(4) ; % positive ion mobility (m2/V * s)

45 Zmi=G(5) ; % negative ion mobility (m2/V * s)

46

47 % constants

48 P=1.013e5 ; % gas pressure (Pa)

49 T=293; % temperature (K)

50 R=8.3145; % gas constant (J/molK)

51 Na=6.02214e23 ; % Avogrado ' s constant (1/mol)

52 el =1.6021765e-19; % elementary charge (C)

53 k=R/Na ; % Boltzmann ' s constant (J/K)

54 e0=8.855e-12; % dielectric constant (F/m)

```matlab
55
56 % mean ion thermal speed (m/ s )
57 cpl=(8 * k * T/( pi * (mpl/Na) ) ) ^ 0 . 5 ;
58 cmi=(8 * k * T/( pi * (mmi/Na) ) ) ^ 0 . 5 ;
59
60 %  diffusion coefficient of ion (m2/ s )
61 Dpl=k*T*Zpl / el ;
62 Dmi=k*T*Zmi/ el ;
63
64 % ion mean free path (m) as given by Re ischl e t . a l . ,equation ( 4 )
65 lpl =16*2^0.5/(3* pi ) * Dpl/ cpl * (M/(M+mpl ) ) ^ 0 . 5 ;
66 lmi =16*2^0.5/(3* pi ) *Dmi/cmi * (M/(M+mmi) ) ^ 0 . 5 ;
67
68 % alternatively mean free path as given by Adachi et . a l .
69 %lpl =1.329* Zpl / el * ( k*T*mpl*M/ ( (M+mpl ) * Na) ) ^0. 5
70 % lmi=1.329*Zmi/ el * ( k*T*mmi*M/ ( (M+mmi) * Na) ) ^0. 5
71
72
73 % Knudsen number for ions (-)
74 Knpl=lpl . / a ;
75 Knmi=lmi . / a ;
76
77 % delta : limiting sphere (m)
78 Ap=1+Knpl ;
79 Bp=1+Knpl . ^ 2 ;
80 Am=1+Knmi ;
81 Bm=1+Knmi . ^ 2 ;
82
83 delpl=(a . ^ 3 ) . / ( lpl . ^ 2 ) . * ( 1/5 *Ap. ^ 5 - 1/3*Bp. * Ap. ^ 3 +2/15* Bp . ^ 2 . 5 ) ;
84 delmi=(a . ^ 3 ) . / ( lmi . ^ 2 ) . * ( 1/5 *Am. ^ 5 -1/3* Bm. *Am. ^ 3 +2/15* Bm. ^ 2.5 ) ;
85
86 % ion potential at delta
87 [A,PPL]=ndgrid ( a , ppl ) ;
88 [A,PMI]=ndgrid ( a , pmi ) ;
89 [DELPL,PPL]=ndgrid ( delpl , ppl ) ;
90 [DELMI,PMI]=ndgrid ( delmi , pmi ) ;
```

91

```
92 phidelpl=(PPL* el ^2) . / ( 4 * pi * e0 *DELPL)- e l ^2/(8* pi * e0 ) *(A
. ^ 3 ) . / (DELPL. ^ 2 . * (DELPL.^2-A. ^ 2 ) ) ;
93 phidelmi=(PMI* el ^2) . / ( 4 * pi * e0 *DELMI) - e l ^2/(8 * pi * e0 ) * (A
. ^ 3 ) . / (DELMI . ^ 2 . * (DELMI.^2-A. ^ 2 ) ) ;
94
95 % the integral of exp ( phi ( a/x ) /kT) from x=0 to x=a/ delta
96 n=length (dp) ;
97 m=length ( ppl ) ;
98
99 Ipl=zeros (n , m) ;
100 Imi=zeros (n ,m) ;
101
102 D=( el ^2) /(4 * pi * e0 ) ;
103 E=1/(k*T) ;
104
105 for N=1:n ;
106     an=a (N) ;
107     delpln=delpl (N) ;
108     delmin=delmi (N) ;
109
110      for M=1:m;
111          pmpl=ppl (M) ;
112          pmmi=pmi (M) ;
113
114          Fpl=@( x ) exp ( pmpl*D*E/an*x-D/2*E/an*x.^4/(1-x . ^ 2 )) ;
115          Fmi=@( x ) exp (pmmi*D*E/an*x-D/2*E/an*x.^4/(1□x . ^ 2 )) ;
116
117          Gpl=an/ delpln ;
118          Gmi=an/ delmin ;
119
120 %  quad is the bounded MATLAB integration algorithm
121          ipl=quad ( Fpl , 0 , Gpl ) ;
122          Ipl (N,M)=ipl ;
123
124          imi=quad (Fmi , 0 , Gmi ) ;
125          Imi (N,M)=imi ;
```

```
126
127        end
128  end
129
130  % alpha : striking coefficient ([ 1 ] ) , or the fraction of
131  %  ions entering the limiting sphere that actually reach the particle
132
133  % cgs units
134  elcgs= 4.80E-10;
135  kcgs= 1.38E-16;
136
137  H=2/(3* kcgs * T) ;
138  J=elcgs ^ 2 ;
139
140  ALPHAPL=zeros (n ,m) ;
141  ALPHAMI=zeros (n ,m) ;
142
143  n=length (dp) ;
144  m=length ( ppl ) ;
145
146  for N=1:n ;
147        acgsn=a (N) * 100; % in cm
148        delplcgsn=delpl (N) *100; %in cm
149        delmicgsn=delmi (N) *100; %in cm
150
151        for M=1:m;
152            pmpl=ppl (M) ;
153            pmmi=pmi (M) ;
154
155            c =[ 0.005 : 0.005 : 1 ] ' ;
156  rpl=(delplcgsn-acgsn ) * c+acgsn ;
157  rmi=(delmicgsn-acgsn ) * c+acgsn ;
158
159  %
160  %
161  %
162  %
```

```matlab
163 b2pl=rpl .^2+H*( pmpl*J/ de lplcgsn-J/2* acgsn ^3/(delplcgsn ^2*( deplcgsn ^2-acgsn
^2) ) ) . * rpl .^2-H*pmpl*J . * rpl+(H*J/2* acgsn ^3) . / ( rpl .^2-acgsn ^2) ;
164 b2minpl=min ( b2pl ) ;
165
166 alphapl=b2minpl /( delplcgsn ^2) ;
167
168 %
169 %
170 if alphapl <0;
171 alphapl=0;
172 end
173
174 %  if the calculated alpha is larger than zero, all ions entering the
175 % limiting sphere reach the particle, and the actual alpha should be 1
176
177 if alphapl >1;
178     alphapl=1;
179 end
180
181 ALPHAPL(N,M)=alphapl ;
182
183 % same approach for negative ions
184 b2mi=rmi .^2+H*(pmmi*J/ delmicgsn-J/2* acgsn ^3/( delmicgsn ^2*( delmicgsn^2-acgsn
^2)) ) ) . * rmi .^2-H*pmmi*J .* rmi+(H*J/2* acgsn ^3) . / ( rmi .^2-acgsn ^2) ;
185 b2minmi=min ( b2mi ) ;
186
187 alphami=b2minmi /( delmicgsn ^2) ;
188
189 if alphami <0;
190     alphami=0;
191   end
192
193 if alphami >1;
194     alphami=1;
195   end
196
197 ALPHAMI(N,M)=alphami ;
```

```matlab
198
199    end
200 end
201
202 % combination probability [ 2 ]
203
204 exppl=exp(-phidelpl/( k*T) ) ;
205 expmi=exp(-phidelmi /( k*T) ) ;
206
207 etapl=pi *cpl *ALPHAPL.*DELPL. ^ 2 . * exppl ./(1+ exppl * cpl . *
ALPHAPL.*DELPL. ^ 2 . / ( 4 * Dpl . *A) . * Ipl ) ;
208 etami=pi *cmi*ALPHAMI. *DELMI . ^ 2 . * expmi ./(1+expmi*cmi . *
ALPHAMI. *DELMI . ^ 2 . / ( 4 *Dmi . *A) . * Imi ) ;
209
210 % Finally, the calculation of the bipolar charging steady state. This is
211 % based on balance equations over Np, with p the particle charge, and
212 % taking positive ion concentration to be equal to negative ion
213 %  concentration, and set Nq+1, N_q-1 to zero .
214
215 opl =[1: q ] ' ;
216 N=[1:n ] ' ;
217
218 etaplpo s (N, opl )=etapl (N, q+opl ) ;
219 etamipos (N, opl )=etami (N, q+opl+1) ;
220
221 etaratiopos=etaplpos . / etamipos ;
222
223 omi= -1*[-q : -1 ] ' ;
224 etaplne g (N, opl )=etapl (N, omi ) ;
225 etamineg (N, opl )=etami (N, omi+1) ;
226
227 etarationeg=etamineg . / etaplneg ;
228
229 Npos=cumprod ( etaratiopos , 2 ) ;
230 Nneg=cumprod ( etarationeg , 2 ) ;
231
232 Npart=ones (n ,m) ;
```

```
233
234 Npart (N, q+1+opl )=Npos (N, opl ) ;
235 Npart (N, opl )=Nneg (N, omi ) ;
236
237 Ntot=sum(Npart , 2 ) * ones ( 1 ,m) ;
238
239 ch=[Npart . / Ntot ] ;
```